Walker, John Scott (2018) *Dynamic loading and stall of clean and fouled tidal turbine blade sections.* PhD thesis.

https://theses.gla.ac.uk/8715/

Dynamic Loading and Stall of Clean and Fouled Tidal Turbine Blade Sections

John Scott Walker

Submitted in fulfilment of the requirements for the
Degree of Doctor of Philosophy

Aerospace Sciences Research Division
School of Engineering
College of Science and Engineering
University of Glasgow

January 2018

ABSTRACT

The current drive to generate energy from sustainable renewable resources has led to an increased interest in generating power through exploiting the kinetic energy in faster flowing tidal streams. Much of the knowledge gained from the development of wind turbines has been applied to the tidal stream turbine. However, the hostile marine environment introduces new technological challenges. The tidal turbine operates under highly unsteady, turbulent flow conditions and the occurrence of marine biofouling adds further complication to the issue. The main objective of the present work is to advance the understanding of the effect marine fouling has on the unsteady hydrodynamic loading and performance of tidal turbine blade sections.

To investigate this challenging fluid phenomenon, a series of two-dimensional static and unsteady experiments were designed and conducted in the dynamic stall test rig at the University of Glasgow's Handley Page wind tunnel facility. The test matrix was constructed to cover the full operating envelope of a blade from MW-scale turbines, and included three thicker, cambered blade sections from two radial positions on the blade – a NACA 63-619 and two proprietary AHH designs. Chordwise integrated force and pitching moment coefficients were obtained from surface pressure measurements for three representative blade fouling configurations: an aerodynamically clean baseline; a light level of widely distributed microfouling roughness; and the addition of macrofouling with a single instrumented barnacle protuberance.

This work has generated what is believed to be a unique database of unsteady tidal turbine blade section performance and, more importantly, the negative impact marine biofouling is likely to have on these investigated parameters. The approach followed through the work has been to assess the impact of marine biofouling on the individual blade sections and then assess the consequences of marine biofouling on the turbine by combining the blade section findings in a BEMT numerical performance model.

KEYWORDS: tidal turbine, marine biofouling, unsteady, blade section, performance.

CONTENTS

LIST OF FIGURES

LIST OF TABLES

PREFACE

This thesis presents work carried out by the author in the Aerospace Sciences Research Division at the University of Glasgow during the period from February 2013 to August 2017, supervised by Dr Richard Green and Dr Eric Gillies. The work is part of a University of Glasgow College of Science and Engineering Industrial Scholarship in collaboration with tidal developer ANDRITZ HYDRO Hammerfest (AHH) and the Energy Technology Partnership (ETP). Industrial supervision has been provided by Dr Catriona Phillips. Acknowledgement is given to the National Wind Tunnel Facility, EPSRC Grant Number EP/L024888/1, for the provision of experimental equipment.

AUTHOR'S DECLARATION

"I declare that, except where explicit reference is made to the contribution of others, that this dissertation is the result of my own work and has not been submitted for any other degree at the University of Glasgow or any other institution."

Printed Name: _____

Signature: _____

Date: _____

NOMENCLATURE & ABBREVIATIONS

UNITS

All units of measurement throughout this thesis conform to the *Système Internationale*, with deviations from this rule noted where appropriate.

SYMBOLS

The following symbols are used throughout this thesis. Where a symbol is used only briefly, it is defined at the appropriate point in the text.

LATIN

a	Axial induction factor
a'	Tangential induction factor
B	Rotor blade count
c	Aerofoil chord
C_c	Axial force coefficient
C_d	Drag force coefficient (Due to pressure)
C_l	Lift force coefficient
C_m	Pitching moment coefficient (Around local pitch axis)
C_n	Normal force coefficient
C_p	Pressure coefficient
C_P	Turbine power coefficient
C_Q	Turbine torque coefficient
C_T	Turbine thrust coefficient

C_w	Work coefficient
D	Blade drag force
h	Water depth
k	Reduced frequency
p	Pressure
P	Turbine power output
q	Dynamic pressure
Q	Turbine torque
r	Radial position
R	Turbine rotor radius
Re	Reynolds number
S	Sensitivity
t	Time
T	Turbine thrust force
U	Fluid flow speed
V	Voltage
x/c	Non-dimensional aerofoil chordwise position

GREEK

α	Angle of attack
$\dot{\alpha}$	Linear pitch rate
$\dot{\alpha}_{\text{red}}$	Reduced pitch rate
$\Delta()$	$()_n - ()_{n-1}$
θ	Pitch angle
λ	Tip speed ratio
μ	Dynamic viscosity
Ξ	2D aerodynamic cycle pitch damping coefficient
ρ	Fluid density

σ	Cavitation number
σ'	Rotor solidity
ϕ	Inflow angle
ψ	Turbine blade azimuth angle
ω	Model oscillatory frequency
Ω	Turbine rotational speed

SUBSCRIPTS

∞	Freestream
0	Mean
1	Amplitude
Com	Command (Input) signal
ds	Dynamic stall
hub	Turbine hub height position
max	Maximum
min	Minimum
Off	Offset
Pos	Position (Feedback) signal
n	n^{th} term
r	Local radius
rel	Relative
ss	Static stall
x, y, z	Axial, lateral, vertical

ABBREVIATIONS

ADC	Analogue-to-digital converter
ADCP	Acoustic Doppler current profiler
AHH	ANDRITZ HYDRO Hammerfest
AWG	Arbitrary wave generator

BEMT   Blade element momentum theory

CFD   Computational fluid dynamics

EMEC   European Marine Energy Centre

ETP   Energy Technology Partnership

FSS   Full scale span

LE   Leading edge

NACA   National Advisory Committee for Aeronautics

NASA   National Aeronautics and Space Administration

NREL   National Renewable Energy Laboratory

PCB   Printed circuit board

PID   Proportional-integral-derivative

RIB   Run information block

RSME   Root square mean error

TE   Trailing edge

UoG   University of Glasgow

CHAPTER 1

INTRODUCTION

1.1 THE DRIVE TOWARDS RENEWABLE ENERGY

An ever increasing production of global carbon emissions from electricity generation, transportation and heating has been recognised as a main contributor to both climate change and increased air pollution levels (IEA, 2016). The primary means of generating energy are heavily reliant on the burning of energy-dense fossil fuels, including oil, coal and natural gas, and the generation of electricity and heat alone is attributed to approximately 40 % of the global energy-related carbon dioxide emissions (Ang and Su, 2016). The UK annual contribution in 2014 has been estimated at 145.3 million tonnes of CO_2 – around 35 % of the total UK carbon emissions. However, alongside the impact of carbon emissions on the climate, the burning of finite fossil fuel resources to generate energy is not a sustainable solution and extraction methods can be very damaging to the local environment. Therefore, steps must be taken to decarbonize global energy production and move towards a so-called greener economy, with an aim of reducing carbon emissions and pollution, and reducing the global dependency on the diminishing raw finite energy resources. This has led to an increased interest in generating energy through the development of both existing and emerging renewable energy technologies.

In 2009, the European Union published the Renewable Energy Directive 2009/28/EC (European Union, 2009), mandating levels of renewable energy usage and carbon emission reductions for all EU Member States. The targets are for 20 % of the gross final energy consumption to come from renewable energy sources and a consequent 20 % reduction in carbon dioxide emissions by 2020, but applied collectively across all Member States. In response to this directive, the UK Government published the National Renewable Energy Action Plan (DECC, 2010), committing the UK to produce 15 % of all energy from renewable resources by 2020. This is broken down as: 30 % of electricity generation; 12 % of heating; and 10 % of transport fuels. By 2016 the UK

was producing 24.6 % of electricity, 6.2 % of heat, 4.5 % of transport fuels and 8.9 % overall, and although on track to meet the electricity generation target, the heat and transport targets are in doubt (BEIS, 2017).

In terms of electricity generation, the Scottish Government has set an additional target of generating the equivalent of 100 % of Scotland's gross annual electricity consumption from renewable resources by 2020 (Scottish Govt, 2011). This is a more stringent target than that set by the UK government, but reflects the biased distribution of renewables resources across the country (Carbon Trust, 2011). Efforts to advance energy production from renewable resources has been supported by the United Nations Framework Convention on Climate Change (UNFCCC) Paris Agreement 2015 (United Nations, 2015) aiming to hold the increase in global average temperature to well below 2 °C above pre-industrial levels, and pursue efforts to limit temperature increase to 1.5 °C above pre-industrial levels. At time of writing, 153 UNFCCC members have ratified the agreement, including the UK.

For 2016, the annual total UK electricity consumption amounted to 339.4 TW h, of which approximately 26 % was generated from renewables, with the majority generated from coal (9 %), gas (42 %) and nuclear (21 %) (BEIS, 2017). The dominant renewable resources for electricity generation remain wind and bioenergy, contributing 49 % and 36 % to the renewables' share respectively (BEIS, 2017). However, as well as focussing on generating energy from sustainable resources, perhaps an increased emphasis should be placed on the energy required through the life cycle of a product and not just the consumption at point of use.

The wind turbine is the technology probably most associated with renewable electricity generation, but other technologies, including solar photovoltaic and hydro, and especially bioenergy, are seen to contribute significantly to the overall renewables' share. Although not currently generating significant quantities of energy, tide and wave based marine energy devices have the potential to emulate offshore wind devices and are expected to become more popular as the technology matures and the associated costs begin to decrease.

1.2 MARINE RENEWABLE ENERGY

Marine renewable energy is a sustainable energy source which is derived from natural processes that are constantly replenished (Borthwick, 2016), and exploits the movement of the tides and action of the wind, both in the air and in the creation of waves, to generate energy. An overview of marine energy technology classifications is shown in Figure 1.1, covering the major areas of tidal energy, wave energy and ocean thermal energy conversion, and includes offshore wind.

The challenges facing marine renewable energy technologies are summarised by Borthwick (2016) and include: how to extract, convert, store and export the
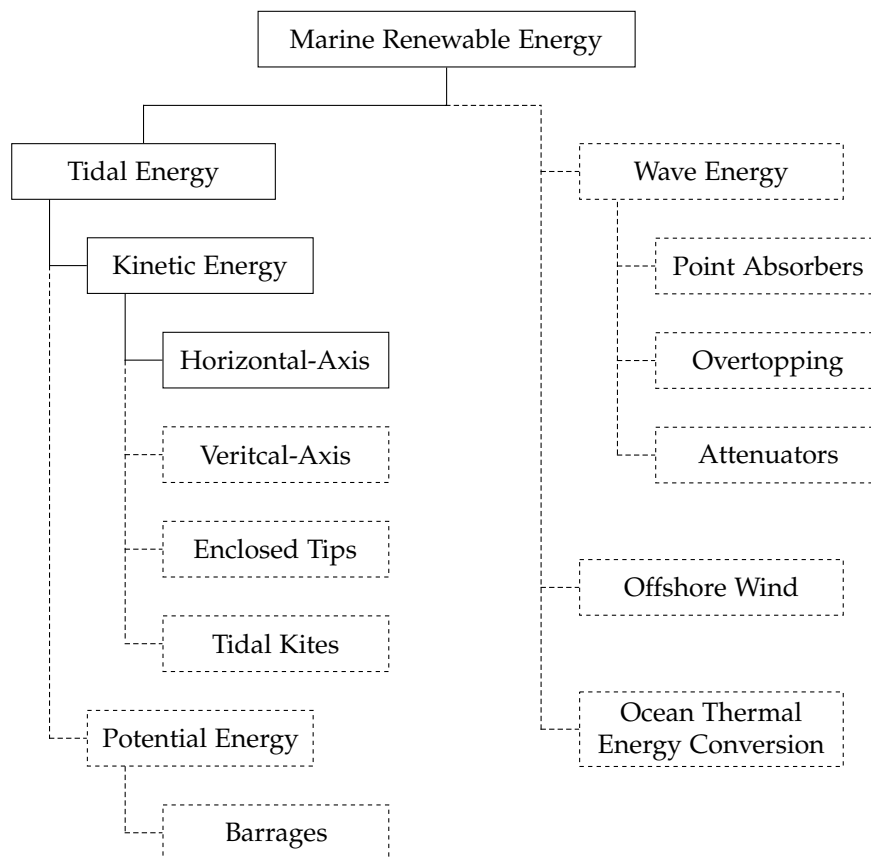
Figure 1.1: Breakdown of marine renewable energy technologies.

energy; technology advancement; infrastructure issues; cost reduction and investment; environmental impact assessment; and legal aspects. Apart from offshore wind, which has benefited from the technology development of onshore wind, marine renewable energy is still very much at an early stage of development. To highlight this point, during Q1 2017 UK offshore wind provided just over $5\,\mathrm{TW\,h}$ of electricity of the Grid, with a load factor of $43.2\,\%$, compared to close to zero for both tidal and wave combined (BEIS, 2017). There are two approaches to generating electricity from the tides: tidal potential, or range, devices which utilise a static pressure head produced between high and low tides; and tidal kinetic, or stream, devices which utilise the flow of underwater tidal current streams (Roberts et al., 2016). The focus for the present work are the underwater turbines being developed to extract energy from tidal streams.

The relative motion of the Earth and Moon around the Sun, and the associated imbalance of gravitational and centripetal forces, give rise to long-period waves which travel through the oceans. The tidal crests and troughs circulate in an anti-clockwise direction around the oceans, restricted by the continental land masses, and what is observed as high and low tide on the coastline, alternating approximately every six hours, are the result of each crest and trough travelling up the continental shelf (MacKay, 2009). The vertical motion of the tidal cycle on the coastline results in a

horizontal movement of the water, hence creating currents – a flood current on the rising tide and ebb currents on the falling tide. These currents are augmented by the local bathymetry and passages between islands and around headlands, giving locations with faster tidal currents which are ideal for siting tidal stream devices (Adcock et al., 2015; Neill et al., 2017).

Tidal currents and direction are periodic, but highly predictable, with variations in the tide linked to the daily tidal cycle and monthly lunar cycle. However, using the UK as an example, positioning arrays of tidal devices along the length of the country would take advantage of the tidal phase (Roberts et al., 2016), giving a cumulative averaged output from multiple out-of-phase inputs.

A major problem for marine-based renewables still to overcome is access to the Grid (Rourke et al., 2010) – the Grid is designed to send power out to remote areas, where marine renewable devices are located, not the opposite direction. Although tidal stream technologies have a lower impact than conventional energy resources (Rourke et al., 2010), particularly by removing the visual impact associated with onshore wind turbines (Premalatha et al., 2014), consideration must be made to the environmental interaction of the turbines. However, turbines do generally tend to operate in zones of higher flow and sediment disturbance, and any physical impact of smaller-scale projects has been shown to be reversed after decommissioning activities (Frid et al., 2012).

The current direction of the industry is towards larger scale devices, likely due to the cost of entry to the market and the need to generate a financial return. However, this limits the number of potential sites as a minimum flow condition is required for optimum turbine operation. The focus on a minimum tidal flow requirement for the existing technology has perhaps led to tidal energy extraction at slower tidal sites, utilising alternative technologies, being overlooked. To exploit the full potential of tidal energy then a mix of both larger-scale commercial tidal arrays and smaller-scale community based arrays is a potential way forward and may remove some of the issues associated with supplying into the Grid.

1.2.1   Background to Tidal Energy

The history of extracting power from ocean tides stretches back to the Middle Ages when tidal mills were constructed along the European Atlantic coast and, in some cases, continued to operate into the mid 20th century (Charlier and Finkl, 2009). The 1960s saw the construction of the Rance Barrage in France (Andre, 1978), the world's first tidal power station. Although providing a template for future tidal barrage and lagoon schemes, only a limited number have been constructed, but have received recent attention with the announcement of the Swansea Bay Tidal Lagoon in the Severn Estuary (Waters and Aggidis, 2016).

The most significant progress in tidal energy over the last two decades has been

the focus on technology which extracts energy from faster flowing tidal streams (Ng et al., 2013). The UK has positioned itself as a leader in the development of tidal stream renewable energy technologies, as home to leading developers, test facilities and foremost tidal resources (Bahaj, 2011). This is alongside smaller developments in North America, including projects at the Bay of Fundy and Vancouver Island, and the Malay Archipelago. An overview of the tidal resources around Scotland is provided by Neill et al. (2017).

The UK has some of the best tidal resources in the world (DECC, 2013), with the majority concentrated in tidal zones around the Pentland Firth (Draper et al., 2013), Irish Sea and the Channel Islands, over which thirty individual practical tidal resource sites have been identified (Carbon Trust, 2011). It has been estimated that the Pentland Firth alone could generate up to 1.9 GW (Adcock et al., 2013), over 6000 GW h/yr (Carbon Trust, 2011). Leading the way in the development of tidal energy devices is the European Marine Energy Centre (EMEC, 2012), established in 2003 as the world's first marine energy test facility, allowing device developers to test full-scale grid-connected prototype devices. Other UK milestones in the industry include:

- 2008: Marine Current Turbines achieve the first commercial-scale grid-connected tidal turbine at Strangford Lough, Northern Ireland.

- 2011: World's first pre-commercial tidal turbine installed at EMEC.

- 2016: Nova Innovation install the first fully operational tidal turbine array at Bluemull Sound in the Shetland Islands.

- 2016: Atlantis Resources install the first commercial-scale operational tidal turbine array for the MeyGen project at the Inner Sound of the Pentland Firth.

- 2017: Scotrenewables Tidal Power achieve 2 MW rated power at EMEC, becoming the world's most powerful tidal turbine.

Table 1.1 summarises the status, capacity and commerciality of all UK tidal projects, where the values for devices tested at EMEC have been separated from the main data. Data for proposed future test sites and demonstration zones have been removed.

The tidal energy industry is still in relative infancy. Smaller kW-scale devices are now operating commercially, but larger MW-scale devices remain at the demonstration phase. To date, just over 10 MW of prototype or demonstration devices have been installed at EMEC and, at time of writing, a collective power output of 7 MW is being generated by operational devices at the MeyGen and Bluemull Sound tidal arrays. With each step towards commercial deployment an order of magnitude increase in total power capacity is expected to be realised, and over 1 GW of commercial power capacity will be achieved if all projects currently in planning, consented or under development are successfully deployed. Despite an outward public perception of a burgeoning, mainly homegrown, tidal energy industry, only a fraction of the potential

TABLE 1.1: Status, capacity and commerciality of UK tidal stream projects. Data taken from RenewableUK (2017).

Project Status	Capacity [MW]			Total [MW]
	Prototype	Demonstration	Commercial	
In Planning	–	20	320	340
Consented	0.5	12	80	92.5
Development	–	90	836	926
Construction	–	–	0.3	0.3
Operational	1.23	6	0.03	7.26
Cancelled	–	18	–	18
Other	0.44	3	–	3.44
EMEC	8.7	3	–	11.7
Total [MW]	10.87	152	1236.33	–

UK tidal resource is currently being exploited. Although progress in the sector is evident, technological challenges remain to be overcome before devices are deemed to be commercially viable. Until then, research and development will remain heavily reliant on government grants, venture capitalism and financial backing from larger multinationals (Fraenkel, 2014).

The majority of tidal stream devices have converged on a horizontal-axis arrangement, accounting for 76 % of all tidal device research and development (Magagna and Uihlein, 2015), but development continues on other approaches, particularly the enclosed tip (Venturi) and tidal kite configurations (Zhou et al., 2014). The leading tidal stream turbine technologies are shown in Figure 1.2.

As well as different approaches to generating power from fast flowing tidal streams, there are numerous terms, and associated acronyms, used in the literature to describe tidal stream turbines, including: tidal turbines; hydrokinetic turbines (HKTs); marine hydrokinetic turbines (MHKTs); tidal current turbines (TCTs); marine current turbines (MCTs); marine current energy devices (MCEDs); tidal energy conversion device (TECDs); and marine stream generators. The work presented in this thesis is focussed on the multi-blade MW-scale horizontal-axis tidal stream turbine configuration, but will be referred to throughout this thesis simply as a *tidal turbine*, *turbine* or the *device*.

1.2.2 THE HORIZONTAL-AXIS TIDAL STREAM TURBINE

The lift-based horizontal-axis tidal stream turbine is an axial flow, variable speed device which can be described crudely as a smaller scale wind turbine operating underwater. Early tidal turbine designs were heavily influenced by those of wind turbines (Batten et al., 2006) and, although sharing physical and operational similarities, the rotors experience very different loading and flow conditions (Rourke et al., 2010). As the density of seawater is much greater than that of air, tidal turbines can produce

(A) Horizontal Axis: AHH HS1000

(B) Helical Axis: ORPC TidGen

(C) Venturi: OpenHydro Open-Centre

(D) Tidal Kite: Minesto Deep Green

FIGURE 1.2: Overview of turbine types for extract energy from tidal streams.

comparable power outputs to wind turbines, but with a considerably smaller rotor swept area, while encountering more predictable and less varied flow conditions (Fraenkel, 2014).

The turbine rotor, which includes the hub and blades, sits in the vertical plane and rotates around the turbine central axis, parallel to the tidal stream. The nacelle houses the main gearbox, which is connected to the hub by the main shaft, and other ancillary equipment, but also carries all the turbine loads down towards the support structure and foundations. The foundations are usually of the monopile or gravity base type and a connection management system connects the turbine to the shore by a subsea cable. The turbine blades, typically manufactured from composite materials, are constructed from a series of defined hydrofoil blade sections. The blade shape is a function of the rotor tip speed ratio and solidity, and the blade thickness, chord and pre-twist angle vary along the blade span. Most larger-scale devices have a cylindrical root section and a thickness of around 15 % at the blade tip, and an approximate thickness of 30 % to 40 % at the inboard positions (Mycek et al., 2014).

The flow of the tidal stream generates a hydrodynamic lift force on each rotor blade, providing a driving torque to the turbine rotor. This rotation extracts kinetic energy from the fluid flow to be converted for electricity generation. As a consequence of the high dynamic pressure, the turbine blades are subjected to large thrust and torsion loads which lead to high in-plane and out-of-plane bending moments at the blade root (Milne, 2014). Therefore, the blade design process must account for both the hydrodynamic and structural performance of the blade, resulting in a relatively thick blade profile, particularly towards the blade root (Bir et al., 2011; Grogan et al., 2013). To regulate the rotor loads and maintain rated power output, most devices are

equipped with variable blade pitch control, although stall regulation is also possible (Whitby and Ugalde-Loo, 2014).

TIDAL TURBINE OPERATION

During the tidal cycle, the tidal stream flow speed varies with the ebb and flow of the tide. Therefore, the turbine must operate over a range of flow speeds and employs variable speed and pitch regulation to maximise the device efficiency across the flow speed distribution. A turbine rotor is designed to begin generating power at a minimum, or cut-in, speed of typically $1\,\text{m/s}$ to $2\,\text{m/s}$, and will achieve rated power at flow speeds between $2.5\,\text{m/s}$ and $4\,\text{m/s}$. These specific design points are determined from the expected flow distribution at each tidal site and the individual turbine design is tailored to meet the required specifications. Rated power is not normally achieved at the maximum flow speed for the site, but at some point between the minimum and maximum, or cut-out, speed, when the device is shut down to prevent excessive loading on the turbine components. However, at flow speeds above the rated case, blade pitch control is utilised to maintain the rated power output to the Grid (Whitby and Ugalde-Loo, 2014).

The turbines are deployed in water depths of between $20\,\text{m}$ and $50\,\text{m}$, and rotor diameters range from approximately $15\,\text{m}$ to $25\,\text{m}$ for MW-scale devices. The hub height – the position of the turbine axis from the seabed – is generally around $15\,\text{m}$ to $20\,\text{m}$. This allows the rotor to operate in the portion of the water column where the majority of the energy in the flow is located and away from fluid interactions at the seabed (Mason-Jones et al., 2012), but also leaves the upper level of the water column free for maritime traffic operating on the surface (Fraenkel, 2014). Some tidal turbines feature a yaw head allowing the rotor to rotate and face the second phase of the tide, or otherwise will operate in a reversed position, albeit at a reduced power output and efficiency.

CURRENT DESIGNS & CONCEPTS

Even within the horizontal-axis turbine type different approaches to power generation exist, with the major difference being the support structure and foundation type and rotor configuration. The principal specifications for a selection of the leading tidal stream turbine technologies are given in Table 1.2 and shown in Figure 1.3.

1.3 THE TURBINE MARINE OPERATING ENVIRONMENT

The tidal turbine operates in a very hostile marine environment, characterised by a highly turbulent flow velocity shear through the water column, and complicated by

TABLE 1.2: Technical specification overview for a selection of the leading deployed horizontal-axis tidal turbines. Images of each device can be found in Figure 1.3.

Parameter	Turbine Model			
	HS1500	SeaGen S	SR2000	Nova M100
Rotor Diameter [m]	18	20	16	9.5
No. of Rotors [–]	1	2	2	1
Blades per Rotor [–]	3	2	2	2
Rated Power [kW]	1500	2000	2000	100
Cut-In U_∞ [m/s]	1	1	1	–
Rated U_∞ [m/s]	3	2.5	3	–
Rotor Speed [rpm]	–	$4 - 11.5$	16 (Max)	–
Water Depth [m]	30	38 (Max)	25 (Min)	30
Foundation [–]	Gravity Base	Monopile	Floating	Gravity Base

(A) AHH HS1500/Atlantis AR1500

(B) MCT (Atlantis) SeaGen S

(C) Scotrenewables SR2000

(D) Nova Innovation Nova M100

FIGURE 1.3: Selection of the leading deployed horizontal-axis tidal turbines. The technical specification of each device can be found in Table 1.2.

the occurrence of marine biofouling on the tidal turbine structure and blades. These aspects of the marine environment are now described.

1.3.1 TIDAL FLOW CHARACTERISATION

Tidal turbines are situated at coastal sites where the geometry of the seabed results in increased tidal stream velocities, such as in tidal channels, at the tip of a headland or an oscillating shelf/bay arrangement (Adcock et al., 2015), in water depths between 20 m and 50 m. The magnitude and direction of the tidal streams are highly predictable, but will vary significantly from site to site. Therefore, each identified tidal project site
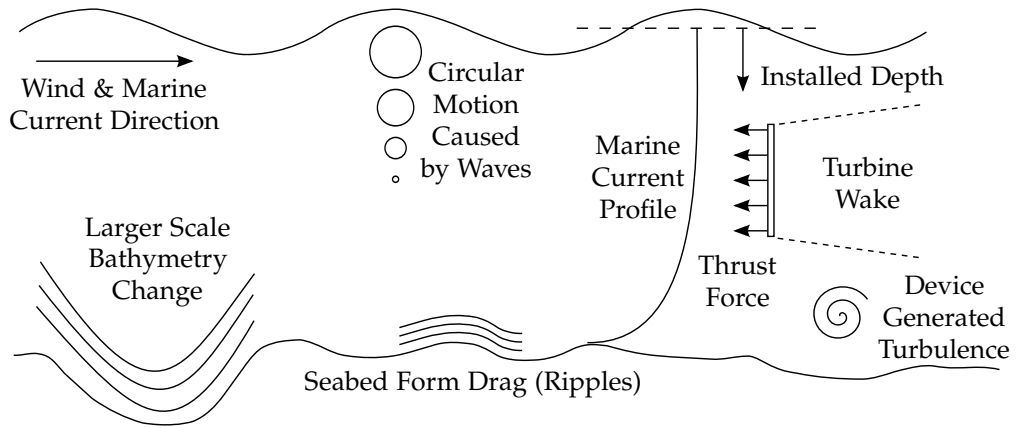
FIGURE 1.4: Variables influencing the flow around the tidal turbine. Adapted from Tatum et al. (2015).

requires detailed marine surveys to characterise the tidal resource (Gooch et al., 2009; Lewis et al., 2017).

Myers and Bahaj (2012) present the primary variables influencing the flow around the tidal turbine, particularly the wave-current interaction and and the flow velocity profile through the water column, both of which will contribute to fatigue loads on the turbine blades (Faudot and Dahlhaug, 2012), as shown in Figure 1.4.

The surface gravity waves descend through the water column in an orbital motion of decreasing magnitude, with increasing water depth, and penetrate to depths equal to half the wavelength of the surface wave, and the interaction with tidal currents stretch the motion into an elliptical trajectory (Tatum et al., 2015). Previous studies have investigated the effect of surface waves on the performance characteristic of tidal turbines using both numerical (Barltrop et al., 2007) and experimental (Luznik et al., 2013) methods.

The location of the deployed turbine relative to the seabed results in the turbine operating in a high shear velocity profile – or boundary layer – through the water column (Mason-Jones et al., 2012). This velocity profile arises from friction at the seabed reducing the tidal stream velocity at the bottom of the water column. The profile is characterised by a one-seventh power law, as described in Equation 1.1, which relates the profile velocity to the bed roughness and relative depth (Lewis et al., 2017). The variables z and h are the turbine draught and height from the seabed and the water depth respectively, $\bar{U}$ is the depth-averaged velocity and a bed roughness value of $\beta = 0.32$ is included.

$$U_z = \left(\frac{z}{0.32h}\right)^{1/7} \bar{U} \tag{1.1}$$

A more standard form of the one-seventh power law is given in Equation 1.2,

which relates the profile velocity to the conditions measured at the turbine hub height (Bryden et al., 2007).

$$U_z = U_{\text{hub}} \left(\frac{z}{z_{\text{hub}}} \right)^{1/7} \tag{1.2}$$

The positioning of the turbine rotor in the velocity profile also dictates the peak power the turbine can generate. Energy in the tidal stream is not evenly distributed through the water column, with 30 % of the available tidal stream energy located in the upper 50 % of the water column (Fraenkel, 2014). Therefore, for the same rotor geometry, the turbine sitting higher from the seabed will, in theory, generate a higher power output. Further to this, as the energy generated by the turbine is proportional to the velocity cubed (U^3), a 10 % variation in the average tidal stream velocity equates to an approximate difference of 30 % in the energy captured.

Turbulence levels in the tidal stream have not been widely reported in the literature, but Mycek et al. (2014) provides a summary of the limited studies available. Acoustic Doppler equipment and methods (ADCP and ADV) have assessed the following three-dimensional freestream turbulence intensity levels at different tidal sites: 7.9 % to 8.7 % at EMEC Falls of Warness (Osalusi et al., 2009); 9.5 % to 10.3 % at Sound of Islay (Milne et al., 2014); 6.6 % to 9 % at Puget Sound, WA (Thomson et al., 2012). These measurements are from the lower boundary layer level at around 5 m height from the seabed for freestream tidal velocities of 1.5 m/s, 2 m/s and 1.3 m/s respectively. The turbulence and velocity measurement differences from using an ADCP or ADV are discussed in Mycek et al. (2014).

Milne et al. (2014) provides further characterisation parameters for the tidal flow through the Sound of Islay. It is shown that turbulence parameters in the tidal flow are comparable to atmospheric turbulence spectral models, exhibiting a turbulence anisotropic ratio of 1 : 0.75 : 0.56 in the streamwise, traverse and vertical directions respectively. It is concluded that atmospheric boundary layer models are appropriate for modelling the tidal flow variations. Further to this, the averaged turbulent integral time and length scales in the streamwise direction were determined to be 6 s and 11 m to 14 m respectively at the maximum flow speed – the same order of magnitude to the turbine temporal and spatial scales, based on the turbine rotor diameter and time to complete a single rotation. The transverse and vertical turbulence scales were found to be significantly smaller. This suggests that turbulence in the tidal stream will have a significant impact on the turbine performance and the range of turbulence scales must be taken into account when considering tidal turbine blade loading (Blackmore et al., 2016).
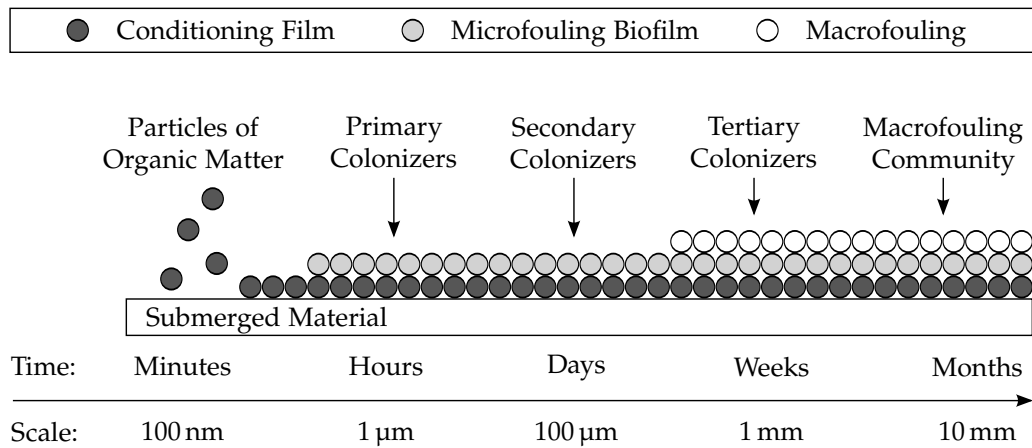
FIGURE 1.5: Schematic representation of the marine biofouling colonisation process on a submerged tidal turbine blade. Adapted from Martín-Rodríguez et al. (2015).

1.3.2 MARINE BIOFOULING

Marine biofouling is defined as the unwanted accumulation of biological material on submerged man-made surfaces, but will only begin to interfere with a technical process once a certain fouling threshold has been reached (Flemming et al., 2009, p.v). The development of the biofouled surface can be described as the layering of increasingly larger scale fouling organisms, as depicted in Figure 1.5.

An initial conditioning film composed of dissolved organic matter is absorbed onto the blade surface within minutes of entering the water. Over the following hours and days a microbial biofilm, consisting of microfouling organims including bacteria, microalgae and fungi, is gradually formed over the initial film and can reach $500\,\mu m$ thickness in some cases. From a period of weeks onwards, a macrofouling community develops in a third layer as the blade surface is colonized by invertebrate larvae. The macrofouling community is subdivided into soft fouling, including kelp and other algae, and hard fouling, including barnacles, mussels and bivalves (Callow and Callow, 2002; Martín-Rodríguez et al., 2015).

The specific fouling organisms and extent of the fouling on the turbine blade are influenced by a myriad of environmental and geographical factors. These include, but are not limited to: local flow speed and turbulence level; water quality, salinity, temperature and sunlight levels; the turbine blade substrate material; the physical turbine geographical location; meteorological seasons; and the fouling species breeding cycle (Cowie, 2010; Miller and Macleod, 2016). Additionally, the biofouling process is cumulative – once the blade surface is roughened or degraded to some extent by initial fouling or particulate erosion, the surface material will become more susceptible to further attack (Polagye and Thomson, 2010). Further to this, the formation and structure of the biofilm has also been shown to be dependent on the flow speed, with higher fluid flows resulting in thinner, denser biofilm structures consisting of

Image has been removed due to copyright restrictions	Image has been removed due to copyright restrictions
(A) Microfouling (Foreground)	(B) Barnacle Macrofouling
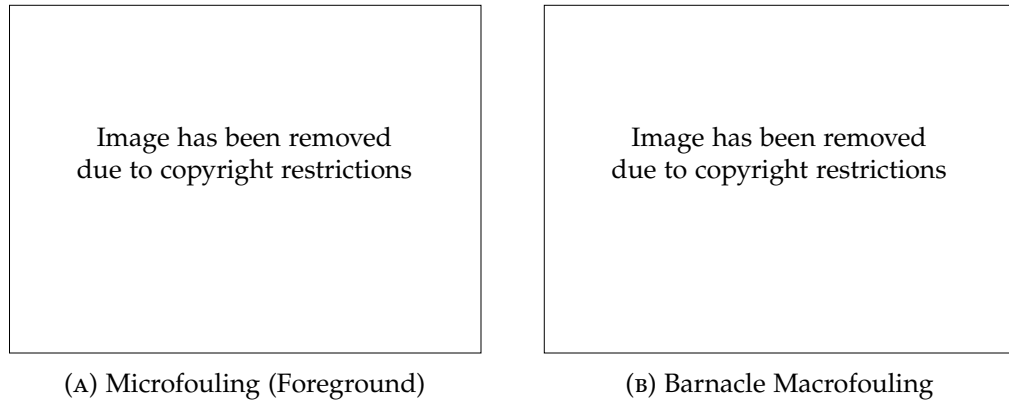
FIGURE 1.6: Examples of marine biofouling on a deployed tidal turbine blade. Images supplied by AHH.

cell clusters more resistant to detachment than a single cell (Melo, 2005). For sessile filter feeders, such as barnacles, a higher flow rate also improves the water column nutrient content which in turn influences the fouling community growth rate (Miller and Macleod, 2016), as do various other factors described by Crisp and Bourget (1985).

The principal macrofouler on a tidal turbine located in UK waters of approximately 40 m depth, has been identified as the barnacle species *Chirona hameri* (Vance et al., 2014). Other barnacle species, including *Balanus crenatus* and *Semibalanus balanoides* have also been identified in the fouling community. Like most barnacles, these species are sessile, benthic filter feeders and attach permanently to hard surfaces in subtidal zones at depths of between 20 m to 200 m (Southward, 2008). The process of barnacle adhesion is discussed in Khandeparker and Anil (2007). On detachment the calcareous basal disc will remain, but alongside other dead biomass provides a suitable surface and nutrient source for subsequent fouling organism attachment (Flemming et al., 2009, p.65). It is thought that algae macrofouling will not be a problem on tidal turbines as it is anticipated that higher tip blade speeds will dislodge or break the fouling at an early stage of growth (Bahaj and Myers, 2003). Examples of marine biofouling on a recovered tidal turbine blade are shown in Figure 1.6.

The increased blade thickness, weight and roughness due to marine biofouling have been identified as the fouling characteristics most likely to affect the efficiency of a marine device. A common approach to mitigate potential effects from fouling is to use protective anti-fouling coatings on the blade and account for the additional structural loading during the design phase (Miller and Macleod, 2016). However, considerable investigation into the issues surrounding device performance and marine biofouling is required.

All submerged structures will form a biofilm, hence further susceptibility to fouling, and presently anti-fouling coatings only delay the problem. Vance et al. (2014) presents the most recent assessment of tidal turbine protective coatings and Miller and Macleod (2016) presents initial work on mapping marine growth to provide developers with fouling characteristics for different device types and locations.

1.3.3 ROLE OF ROUGHNESS ON BLADE SECTION FLOW BEHAVIOUR

The effects of surface roughness were investigated in early experimental studies on turbulent flows through rough pipes (Nikuradse, 1933), and over flat plates (Prandtl, 1933) and aerofoils (Hooker, 1933; Jones and Williams, 1936), and demonstrated a pressure drop and corresponding drag increase attributed to the presence of the roughness elements. Moody (1944) combined the available results for the pressure drop in a pipe into a graphical format, relating the surface friction factor to a roughness size and roughness dependent Reynolds number, and the Moody diagram remains a commonly used engineering tool to this day.

The blade section roughness interacts with the boundary layer, leading to aerodynamic losses, in a process dependent on the roughness height – ordinarily presented as a fraction of the aerofoil chord length – boundary layer classification, hence ultimately the roughness chordwise location on the blade section, and Reynolds number (Klebanoff et al., 1992). For an increasing roughness level, the blade section will behave as aerodynamically smooth until a critical roughness height is reached. This point is determined from the critical Reynolds number based on the roughness height. Roughness forces a premature transition of the laminar flow boundary layer, but if a separated flow encounters a roughness elements then a reduced effect would be expected. Using roughness to force flow transition to the turbulent state can delay flow separation due to an increased resistance to the blade section adverse pressure gradient. Generally, rougher surfaces will have a thicker boundary layer, and higher Reynolds number flow will have an increased sensitivity to the roughness height (Kerho and Bragg, 1997). In addition, the effects of roughness on the flow are restricted to the inner layer, with the outer layer insensitive to roughness except for setting the length and velocity scales of the outer flow (Flack and Schultz, 2014).

Marine biofouling on the tidal turbine blades will gradually increase the roughness height, increasing the hydrodynamic blade losses, but also increasing the effective blade section thickness. The larger scale roughness level on the turbine blade is expected to be greater than the flow sub-layer close to the blade surface, and will be operating in a turbulent, high Reynolds number flow, hence the blade section lift and drag performance will be modified during the turbine life cycle as roughness due to biofouling develops on the blade surface. Roughness towards the leading edge of the blade section will pose a bigger problem than that at an aft chordwise position, but is dependent of the exact blade geometry, which can be designed to minimise the sensitivity to surface roughness.

1.3.4 BLADE SECTION DESIGN FOR ROUGHNESS INSENSITIVITY

In wind and tidal turbine applications contamination of the blade surface cannot be avoided. Unlike aircraft which can be easily and regularly maintained on the ground, the logistics of cleaning turbine blades are considerably more involved. Therefore, a

principal design consideration for modern turbine blade sections, alongside aerodynamic performance and structural requirements, is the sensitivity to surface roughness, particularly at the leading edge of wind turbines (van Rooij and Timmer, 2003). The same design objective applies to a tidal turbine, but roughness over the entire blade surface needs to be considered.

Somers (2005) describes the design approach to achieve these objectives for a wind turbine blade, by deducing a series of aerofoil pressure distributions for a required drag polar. The improved insensitivity to leading edge roughness is achieved by ensuring that, for aerofoil incidences close to maximum lift, the leading edge suction peak becomes sharper and moves quickly towards the leading edge with increasing lift. This results in transition on the upper surface to occur near the leading edge and maximum lift is generated with turbulent flow across the entire upper surface, hence improved sensitivity to leading edge roughness. If the transition movement is matched for all aerofoil sections comprising the turbine blade then each aerofoil section should display the same roughness insensitivity characteristics.

As well as for roughened aerofoils, thicker NACA sections have been shown to suffer from premature transition. Therefore, the modern families of turbine blade sections incorporate a profile to reduce the upper surface thickness, and circumvent the problem of premature transition. However, to counteract the resultant loss of lift, blade section designed specifically for tidal turbine applications include a characteristic s-shape profile on the lower surface profile towards the trailing edge to aft-load the blade section (Ahmed, 2012).

1.4 UNSTEADY LOADING ON TIDAL TURBINE BLADE SECTIONS

As described in Section 1.3, the tidal turbine operating environment is characterised by highly unsteady flow conditions. Therefore, on each rotation of the turbine rotor the individual blade sections will be subjected to a time-dependent variation in angle of attack. The two principal unsteady loading regimes on the blade section can be categorised with reference to the blade section incidence: lower angles of attack with fully attached flow; and higher angles of attack, beyond the static stall incidence, with time-dependent flow separation, where a fluid phenomenon called dynamic stall will occur (Leishman, 2000). The understanding of unsteady tidal turbine blade loading is largely derived from investigations on helicopter rotor performance and, more recently, the loading of wind turbine blades. This section will present an overview and implications of the unsteady fluid phenomenon occurring on the tidal turbine blade sections, starting with the parameters describing the blade motion. The terms *dynamic* and *unsteady* are used interchangeable when describing the blade section loading, as are *static* and *steady*.

Table 1.3: Reduced frequency flow regime definitions. Adapted from (Leishman, 2000, p.306).

Range	Description	Effect of Unsteady Terms
$k = 0$	Steady	None
$0 < k < 0.05$	Quasi-Steady	Small
$0.05 \leqslant k < 0.2$	Unsteady	Cannot be routinely neglected.
$0.2 \leqslant k$	Highly Unsteady	Dominate aerofoil behaviour.

1.4.1 Parameters Describing the Unsteady Blade Motion

During a complete revolution of the turbine rotor, each blade section will experience a varying local resultant flow velocity and incidence as the blade travels through the unsteady water column. The time-dependent blade section incidence forcing can be approximated as a single frequency sinusoidal variation in pitch around a mean incidence over the pitch cycle (Ramsay et al., 1995; Fuglsang et al., 1998b), as defined in Equation 1.3. The frequency of the blade pitch cycle oscillation is obtained directly from the turbine rotational speed, where each blade section pitch cycle corresponds to a complete revolution of the turbine.

$$\alpha = \alpha_0 + \alpha_1 \sin(\omega t) \tag{1.3}$$

In reality, the forcing experienced by a tidal turbine is comparable to an oscillatory plunge (Milne, 2014), but limitations of experimental facilities hinder the investigation of aerofoil plunging motions at appropriate length and flow scales. As a consequence of oscillatory forcing in pitch, the aerofoil leading edge pressure gradient is lower than for the equivalent oscillatory plunge case, hence flow separation will be delayed to slightly higher blade section incidences (Leishman, 2000). However, for practical engineering applications, particularly for cases investigating dynamic stall, aerofoil data obtained from oscillatory pitch tests can be assumed as representative of the oscillatory plunging case (Stepniewski and Keys, 1984, p.337).

The unsteady aerofoil response is dependent on both the magnitude and frequency of the oscillatory forcing, and the non-dimensional reduced frequency, defined in Equation 1.4, is used to indicate the degree of unsteadiness in the flow (Leishman, 2000). A summary of the reduced frequency flow regimes, and their influence on the unsteady aerofoil terms, is given in Table 1.3.

$$k = \frac{\omega c}{2 U_\infty} \tag{1.4}$$

For a fixed turbine operating condition, the turbine rotational speed fluctuations can be assumed to be negligible, but the resultant velocity at each blade section is constantly varying, hence a constantly varying reduced frequency. For the tidal

turbine it is appropriate to take an average over the cycle, or use the flow conditions at the turbine hub height, to obtain a single reduced frequency value as an indication of the flow unsteadiness level over a complete turbine rotation.

Similar terms can be obtained for the aerofoil pitch rate terms. An expression for the aerofoil time-dependent linear pitch rate is given in Equation 1.5, and the reduced pitch rate in Equation 1.6.

$$\dot{\alpha} = \alpha_1 \omega \cos(\omega t) \tag{1.5}$$

$$\dot{\alpha}_{\text{red}} = \frac{\dot{\alpha} c}{2 U_\infty} \tag{1.6}$$

Inboard blade sections have a lower resultant flow velocity and longer chord, hence a higher reduced frequency. It is likely that over the full span of a tidal turbine blade the full range of flow unsteadiness levels will be present, ranging from quasi-steady at the blade tip to highly unsteady at the blade root. Similarly, the mean blade section incidence will be higher towards the blade root as the blade pre-twist angles are generally higher at inboard positions (See Section 2.3).

1.4.2 DYNAMIC LOADING FOR ATTACHED FLOW

The unsteady forces acting on the blade section are comprised of both circulatory and non-circulatory components, and the presence of the unsteady effects results in moderate amplitude and phase differences in the aerofoil loads during the pitch cycle, when compared to the static case (Leishman, 2000). This is highlighted by an example unsteady case shown in Figure 1.7, where the direction of the pitch cycle is indicated on the figure.

Leishman (2000) describes these unsteady effects in greater detail. The unsteady circulatory component is a product of the circulation created around the aerofoil to satisfy the Kutta condition and is attributed to the dynamic response of vorticity being shed into the aerofoil wake. The unsteady non-circulatory component arises from flow acceleration effects, and are also referred to as the added mass terms. The motion of the aerofoil must accelerate the fluid volume surrounding the blade section, hence this added mass opposes the blade section motion. The non-circulatory forcing acts independently of the rotor wake and 180° out-of-phase to the aerofoil acceleration (Milne, 2014). The non-circulatory term can be estimated as the summation of the air mass within a cylinder diameter equal to the local chord length across the blade span, and has been shown not to be dependent on the rotor tip speed (Whelan, 2010). It is also interesting to note that the non-circulatory component can still exist even if the freestream velocity is zero. For the tidal turbine, the phase difference between the unsteady aerofoil forcing and aerodynamic response is primarily a function of

(A) Normal Force Coefficient   (B) Pitching Moment Coefficient
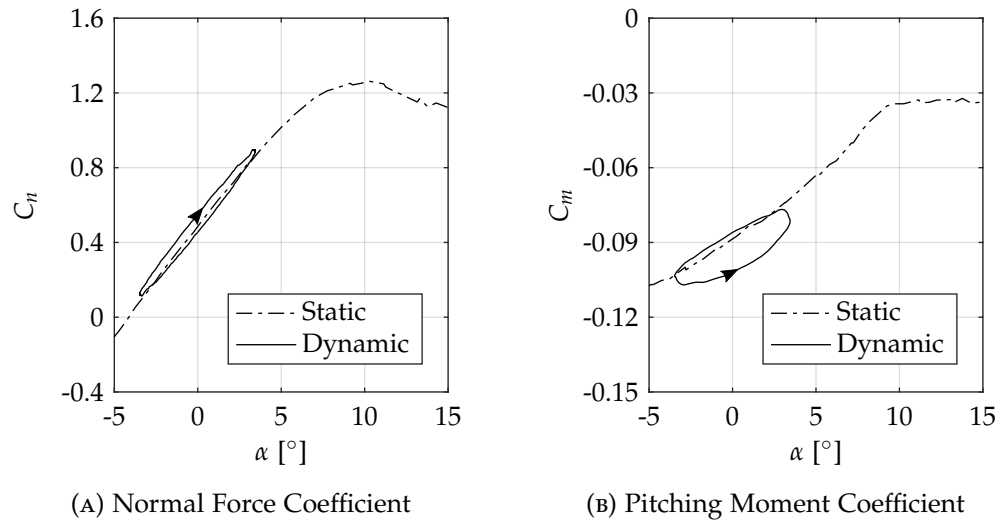
FIGURE 1.7: Unsteady blade section normal force and pitching moment coefficients for an example attached flow case compared to the static baseline.

reduced frequency, as compressibility effects can be ignored.

Methods for evaluating subsonic, incompressible unsteady blade section, and rotor, loading have their basis in the classical formulations originating from thin-aerofoil theory. Starting with the work of Theodorsen (1935), a model based on vortex theory in the frequency domain was presented for determining the unsteady response of a thin oscillating two-dimensional aerofoil, but assumed the forcing amplitude was small. The ambiguity of the reduced frequency when solving in the frequency domain necessitated a formulation in the time domain. The solution for the indicial (step input) response of a thin aerofoil from rest was found by Wagner (1925), with an exact solution to Wagner's function now known, and Küssner (1936) started the work completed by von Kármán and Sears (1938) which gives the indicial response to an aerofoil encountering a sharp-edged gust, such as that encountered in the rotor wake system. The derived indicial and lift deficiency functions continue to form the basis of widely used models for estimating unsteady blade section loading, such as the attached flow subsystem of the Beddoes-Leishman model (Leishman and Beddoes, 1989). If the indicial response function is known then the unsteady load response to any arbitrary aerofoil forcing can be determined.

Dynamic inflow models, such as those described by Peters and HaQuang (1988) and Peters (2009), provide an alternative time domain formulation to the problem, by modifying the flow through the rotor disk in a control volume, as opposed to at the blade section level. However, formulations and approximations in the available models based on thin-aerofoil or flat plate theories have not been validated for the thicker blade sections found on tidal turbines, as to date no unsteady experimental data for this aerofoil class has been freely available.

1.4.3 DYNAMIC STALL MECHANISM

The unsteady fluid phenomenon of dynamic stall occurs on rapidly pitching blade sections where the static stall incidence is being approached or exceeded during the pitch cycle. For a blade section operating under such conditions, flow separation is delayed to a higher angle of attack and a vortex is formed and shed from the aerofoil leading edge. The additional circulatory loading terms contribute to a lift overshoot, by up to as much as 100 %, and large changes to the pitching moment, but at an incidence greater than the aerofoil static stall angle. An excellent overview of the flow topology and characteristics of a two-dimensional blade section entering the dynamic stall regime is provided by McCroskey (1981), Carr (1988) and Leishman (2000). An example test case of a blade section entering the dynamic stall regime is shown in Figure 1.8, which highlights the considerable hysteresis in the pitch cycle loading when compared to the static case. The flow topology on the aerofoil upper surface is shown in Figure 1.9.

The unsteady flow features are now briefly described (McCroskey, 1981; Leishman, 2000). As the aerofoil incidence increases, on the pitch cycle upstroke, the static pressure in the boundary layer decreases causing the boundary layer flow to reverse. For the thicker sections used in tidal turbines the separation is likely to be dominated by flow separation at the trailing edge (A). A vortex forms at the aerofoil leading edge and the lift stall process is initiated by the moment stall event (B). The vortex convects along the blade section chord, inducing an additional lift term and moving the aerofoil centre of pressure aft (B to C). The vortex reaches the trailing edge and the aerofoil is now fully stalled. Large deviations in the lift and moment are identified at this point, although the changes do not happen concurrently (C to D). As the aerofoil incidence decreases, on the pitch cycle downstroke, the flow begins to reattach to the upper surface. If fully reattached before the following upstroke motion, the unsteady loading momentarily returns to those of the static state (E).

Having described the topology of the flow separation, the delayed onset of separation can be explained (Leishman, 2000): circulation shed in to the wake results in a reduction of lift and adverse pressure gradients compared to the equivalent static incidence; due to an induced camber effect, the leading edge pressure and pressure gradients are decreased by the positive pitch rate; and additional unsteady effects within the boundary layer, including flow reversal without significant separation, occur.

The dynamic stall regimes can be defined by the maximum blade section incidence ($\alpha_{\mathrm{max}} = \alpha_0 + \alpha_1$, where α_0 and α_1 are the mean incidence and pitch cycle amplitude respectively) during a pitch cycle with reference to the static stall incidence (McCroskey, 1981). The identified regimes are: no stall; stall onset; light stall; and deep stall. The inboard blade sections of the tidal turbine blade are expected to enter the deep stall regime during operation, while the outboard blade will enter the light stall regime.

(A) Normal Force Coefficient   (B) Pitching Moment Coefficient
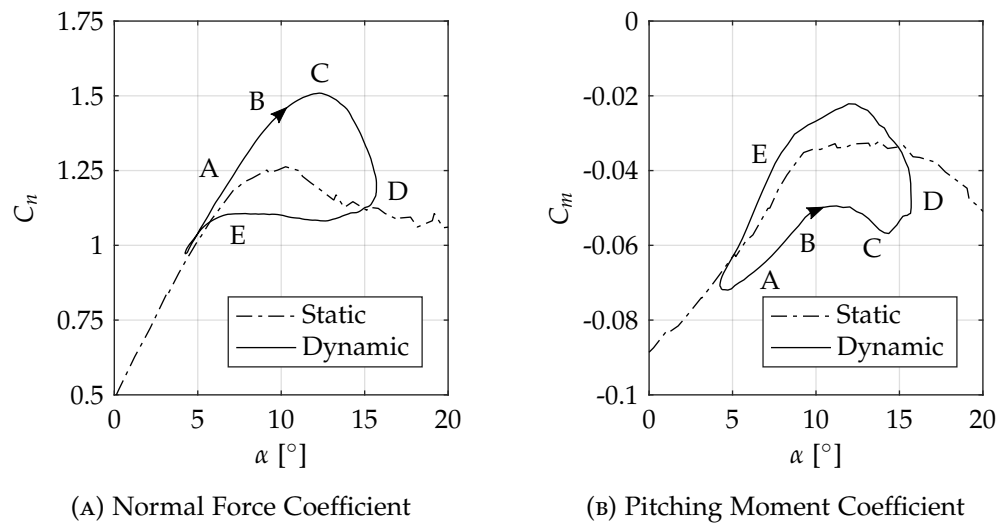
FIGURE 1.8: Unsteady blade section normal force and pitching moment coefficients for an example dynamic stall case compared to the static baseline. The highlighted points correspond to the features of the flow topology shown in Figure 1.9.
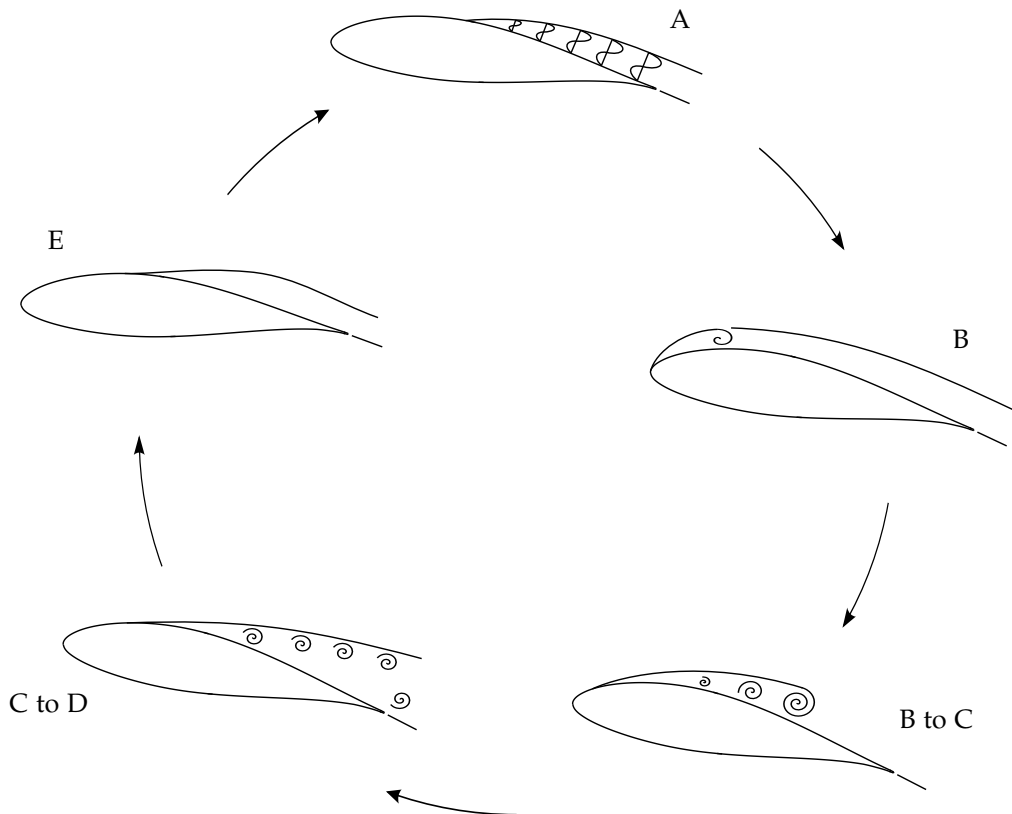
FIGURE 1.9: Schematic showing the key flow topology during dynamic stall of a two-dimensional blade section. Each step corresponds to the point highlighted in the loading cycles of Figure 1.8. Adapted from Leishman (2000, p.382).

Along with the reduced frequency, the maximum aerofoil incidence is a strong indicator of the blade section unsteady loading response. The higher the reduced frequency and level of stall penetration, the more unsteady the aerofoil loading response will become, resulting in larger magnitude hysteresis load loops. Similarly, an increase of reduced frequency, hence pitch rate, delays the flow separation to higher blade section incidences. Rotational and three-dimensional flow effects on the blade sections in a rotor need to be accounted for, but will require further investigation and are not included in the present work.

Semi-empirical dynamic stall models are available for predicting the unsteady loading on rotors, and have their roots in development of helicopter performance and analysis codes (Leishman, 2000, pp.390–393). The most widely used of these is the Beddoes-Leishman (Leishman and Beddoes, 1989) and is used for determining the indicial attached flow, non-linear separated, and vortex induced dynamic stall aerofoil loads by accounting for the time delay and deficiency functions associated with the boundary layer separation and dynamic stall vortex behaviour. This is the basis of the stall delay model utilised in Tidal Bladed (DNV GL, 2016) – the industry-standard software tool for simulating tidal turbine designs.

An advantage of semi-empirical models is that only limited data is required from unsteady aerofoil data, with the remaining inputs derived from static aerofoil performance tables. In the case of the Beddoes-Leishman model, only the four parameters to set the phase lag of the separation and vortex behaviour are obtained from unsteady data. However, this unsteady aerofoil data has to be available. As before, the systems within the semi-empirical models are based predominately on thin aerofoil theory and test data is required to show whether these assumptions remain valid for the case of a tidal turbine. Holierhoek et al. (2013) have presented a comparison of the Beddoes-Leishman model with the alternative ONERA and Snel unsteady numerical methods to assesses their applicability to wind turbine applications, but conclude that all three models show significant difference to test measurements particularly in the deep stall regime.

1.5   THESIS OVERVIEW

1.5.1   RESEARCH MOTIVATION, OBJECTIVES & RELEVANCE TO INDUSTRY

It has been established that the tidal turbine is required to operate in a highly unsteady flow environment, driven primarily by turbulence in the tidal stream (Milne et al., 2010), and, as such, the turbine blades will experience a high degree of dynamic loading. Blade failures on turbines have highlighted the likelihood of the unsteady blade loading being underestimated (Liu and Veitch, 2012), and have lead to conservative blade designs. The key design requirements of reliability and survivability (Blackmore et al., 2016) have resulted in turbine blades being over-engineering and including

safety factors of between 6 and 10 for normal operating conditions (Zeiner-Gundersen, 2015), reducing to 1 for the limiting load case. Ultimately, commercial technology innovation has to be financially viable (Carbon Trust, 2011), but to achieve an optimal design, and cost, the behaviour of the turbine blade loading must be understood.

- The first objective of this work is to investigate the unsteady hydrodynamic loading of tidal turbine blade sections under appropriate operating conditions.

Marine biofouling has been identified as a key concern across the marine energy industry, but the effects are varied and are often specific to individual device or component types (Miller and Macleod, 2016) – biofouling on the support structure, blade or wet connectors, for example, each present there own unique challenge. With regard to the turbine blades, the biggest impact of marine biofouling will be the effect of surface roughness on the blade hydrodynamic efficiency. There is believed to be no previously published investigations into the impact marine biofouling has on the unsteady hydrodynamic loading of tidal turbine blade sections.

- The second objective of this work is to investigate the effect a representative level of marine biofouling is having on the behaviour of the turbine blade section unsteady hydrodynamic loading.

The concept of generating power from the tide is not new, but the availability of fundamental research is limited (Luznik et al., 2013), as is both static and unsteady performance data for thicker aerofoil sections, especially with any surface roughness. Limited unsteady wind turbine blade section data, but with leading edge surface roughness, and static aerofoil and turbine scale-model tank testing with widely distributed roughness are available. The design of wind and tidal turbine blades often relies on proprietary blade sections. Therefore, due to the commercial nature of this data would not be published in the public domain.

- The final objective of this work is to apply the findings for the clean and fouled tidal turbine blade sections to a full turbine rotor model to assess the impact of marine biofouling on the turbine performance, particularly the turbine power output and rotor thrust loading.

The design life of a tidal turbine is between 20 and 25 years (Rourke et al., 2010), with a 5 year retrieval cycle for maintenance of the turbine rotational components (Zeiner-Gundersen, 2015). Therefore, the turbine must be designed to not only survive over this time frame, but also maintain a defined level of performance. It is not economically feasible for the turbine to be offline out with the designated periods of maintenance, or for the turbine performance to decline significantly. The operation of tidal turbines is already economically marginal with the current knowledge of the blade performance and it is expected that the effects of marine biofouling will reduce the margin further, both from the point of view of increased maintenance and, more importantly, reduced power production.

It is intended that this investigation will help inform the challenges of designing future tidal turbine technologies, but is also hoped that the findings can have an application across the wider marine energy industry. The ultimate objective of this work is to answer the question: what impact does marine biofouling have on the unsteady hydrodynamic loading of tidal turbine blade sections, and the consequential turbine performance?

1.5.2 METHODOLOGY & SCOPE

The performance of the selected tidal turbine blade sections has been evaluated from two-dimensional low-speed wind tunnel testing of the aerofoil models. Numerically integrated force and pitching moment data was obtained from chordwise surface pressure measurements. To quantify the effects of a light marine biofouling on the blade section two-dimensional performance, a representative level of artificial roughness was added to the model surface. In addition, the effects of barnacle macrofouling were investigated by including a pressure instrumented barnacle model on one of the two thinner blade sections. The experimental test matrix was determined from the analysis of tidal project site and turbine data, supplied by the project industrial sponsor, and the through the creation of a numerical geometry and flow model for a generic 1 MW tidal turbine. The consequences of the results obtained for the fouled blade sections on the full-scale turbine performance and blade loads has been assessed by means of a BEMT numerical model.

Due to the nature of experimental work, the scope of the project has been limited to the analysis of an isolated blade section subject to a resultant flow velocity. Spanwise flow effects arising from the influence of the turbine rotation and the rotor downstream wake structure have not been considered, and the turbine is assumed to have a rigid blade, no yaw misalignment, and fluid interactions with the turbine support structure have not been included. Further to this, computationally intensive methods, including CFD and inviscid vortex-based methods, have not been utilised to model the unsteady hydrodynamic blade loads.

1.5.3 RESEARCH ORIGINALITY & CONTRIBUTION

It has been identified that there is limited availability of both static and unsteady aerofoil performance data for the thicker aerofoil sections used in tidal turbine blades, which is required during the design of tidal turbine devices. In addition, there have been no investigations identified in the literature which tackle the problem of understanding how marine biofouling effects the unsteady hydrodynamic loading of the turbine blade sections. The major contribution of this thesis is to address this gap in the literature and provide new insights on the unsteady loading experienced by the turbine blades. It is hoped that the contributions highlighted in this thesis will

help inform the blade design of future tidal turbine devices. The main findings of this work have been summarised at the end of each results chapter.

1.5.4 THESIS STRUCTURE

Following this introduction to tidal energy technology and challenges facing the marine energy industry, the main body of the thesis is presented over four main chapters and additional appendices. The proceeding chapters are structured as follows.

Details of the experimental methodology are provided in Chapter 2, including a description of the wind tunnel test facility, model integration and data systems. A suitable experimental test matrix is developed from analysis of AHH supplied simulation data for three tidal project sites and confirmed by the creation of a described generic tidal turbine geometry and flow model. A discussion of the experimental errors and a justification of the method proposed for achieving the stated research objectives conclude the chapter.

The three main results chapter build on the work of the previous chapter, starting with the loading results for each investigated blade section and working towards the performance consequences on a full-scale tidal turbine. Each of the three results chapters begins with a review of the applicable literature.

Chapter 3 investigates the impact of light marine biofouling, or microfouling, on the static and unsteady hydrodynamic loading of three different tidal turbine blade sections – two aerofoils from an outboard blade position and one from an inboard blade position. Experimental results from static, oscillatory and transient load cases are all examined, followed by a discussion on the blade section pitching moments and damping considerations. Results for both the clean baseline design and the fouled rough blade section configurations are presented.

Chapter 4 expands on the analysis in the previous chapter by introducing barnacle fouling, or macrofouling, at a single chordwise location on one of the thinner outboard blade sections investigated. This provides a more representative example of biofouling on the turbine blade, which will include elements of both micro- and macrofouling. The effect of the barnacle on the integrated blade section loading for static and oscillatory test cases is presented. To conclude the chapter, the barnacle zone of influence on surface pressure in the vicinity of the protuberance is investigated.

The final results from this research are presented in Chapter 5, where the conclusions from the previous two chapters are combined and utilised in investigating the consequences of marine biofouling on key performance parameters of a full-scale tidal turbine. Three key areas are examined: the turbine power and thrust coefficient performance curves and the resultant turbine power output; the total blade drag increase due to barnacle fouling at discrete locations; and flow cavitation considerations.

Chapter 6 summarises the conclusions and contributions of the work described in this thesis and proposes future work to develop the presented findings and topics discussed, as well as recommendations to the marine energy industry to account for marine biofouling in future projects.

The appendices provide additional detail on the experimental methodology, in particular the technical specifications of the wind tunnel model design and instrumentation; information on the creation and simulation of the generic 1 MW tidal stream turbine geometry and simulation flow model; the structure of the experimental data files and a record of the run numbers for all investigated test cases; and finally, flow charts to describe the experimental procedures and routines to process the test data and details of a user interface developed to interrogate the experimental database.

CHAPTER 2

EXPERIMENTAL METHODOLOGY

A series of wind tunnel tests were conducted to investigate the influence of widely distributed surface roughness and section thickness on the steady and unsteady behaviour of three two-dimensional tidal turbine blade sections. The experimental tests were designed to consider static, oscillatory (sinusoidal) and constant pitch rate ramp (positive and negative) motions representative of different turbine operating conditions and events. The tests are conducted at a Reynolds number of 1.5×10^6. Time-series pressure and numerically integrated force and pitching moment data for each test case was obtained from measurement of the two-dimensional chordwise surface pressure distribution.

This chapter of the thesis details the experimental methodology of the test campaign, including: a description of the test facility; model design and integration, instrumentation and procedure; determining a suitable test matrix; processing and analysis of the experimental data; and a discussion of experimental accuracy and errors. Supplementary information is provided in Appendices A and B.

2.1   DESCRIPTION OF THE TEST FACILITY

2.1.1   THE HANDLEY PAGE WIND TUNNEL

All the experiments were conducted in the low speed 'Handley Page' wind tunnel (Hounsfield, 1940) at the University of Glasgow – originally built for the Handley Page Aircraft Company in 1938. An overview of the wind tunnel geometry is shown in Figure 2.1. The tunnel is of the closed return type and has an octagonal working section with major axis dimensions of width 2.54 m, height 1.61 m and length 2.74 m, giving a test section cross-sectional area of 3.14 m².

A nominal maximum flow speed of 65 m/s is achievable with the tunnel empty, but continuous running with a model installed is limited to approximately 45 m/s.
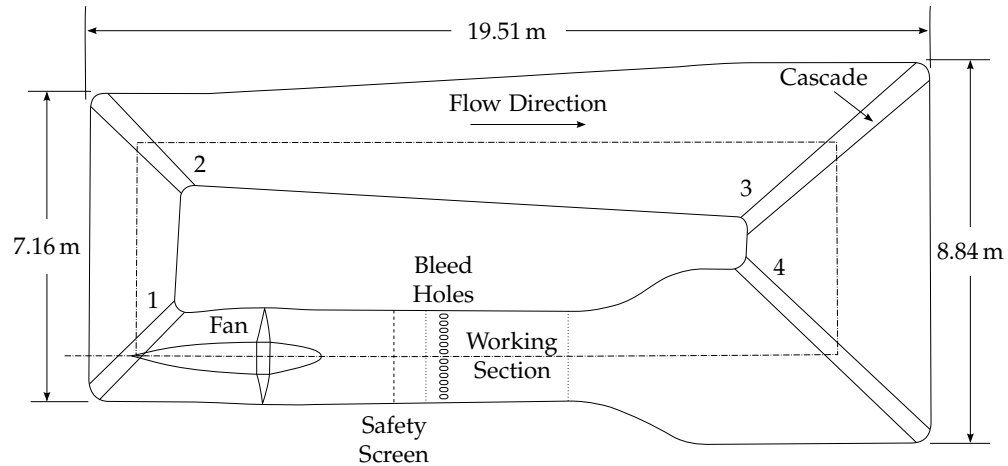
FIGURE 2.1: General arrangement of the Handley Page wind tunnel.

This results in a freestream Mach number of 0.12 and Reynolds number of 2.8×10^6 per metre chord. A pitot-static tube and thermocouple are positioned at the test section inlet for measuring the freestream flow speed and air temperature. At the downstream end of the working section, the tunnel is vented to the atmosphere through a ring of bleed holes, keeping the tunnel static pressure approximately equal to atmospheric pressure. A freestream turbulence intensity of 2.5 % at a flow speed of 45 m/s has been measured. Further details of the tunnel flow characteristics can be found in Appendix A.1.

The tunnel is of wooden construction with a steel primary structure, forming a continuous flow circuit of approximately 45 m, with total external dimensions of length 19.51 m and breadth 8.84 m. A cascade of turning vanes is located in each corner of the duct. The settling chamber to test section contraction ratio is 4:1, and to counteract boundary layer growth an expansion angle of 0.5° is included in the horizontal plane of the test section and the return leg has a divergence angle of 6° in both planes.

A 164 kW DC motor external to the tunnel drives the 2.29 m diameter fan, which is positioned 3.96 m downstream of the test section, in the divergent diffuser. The flow speed is adjusted by a manual fan speed controller. The speed controller does not include a temperature compensation system, therefore the tunnel speed requires manual correction to allow for tunnel temperature increases when running for longer time periods at higher flow speeds.

Figures 2.2 and 2.3 present historical images of the tunnel and the current dynamic stall aerofoil model installation.

2.1.2 THE DYNAMIC STALL TEST RIG

Integrated into the wind tunnel is the dynamic stall test rig, a hydraulic linear actuator and crank mechanism for controlling the aerofoil model position and motion, shown

(A) Testing of the Halifax bomber. © IWM   (B) Wind tunnel testing in the 1940s.

FIGURE 2.2: Historical images of the Handley Page wind tunnel.

FIGURE 2.3: Test aerofoil installed in the tunnel working section.

in Figure 2.4. The rig was originally developed in the 1980s (Leishman, 1984) and has been used extensively to investigate dynamic stall phenomena on helicopter and wind turbine rotor blades, but required significant refurbishment before beginning the experimental phase of the project to ensure the continued safe operation of the rig and integration with new devices. An updated hydraulic user interface module was designed and manufactured, with new safety features, allowing either manual user command inputs or automatic inputs from an AWG. Also, a MATLAB user interface was created to simplify and partially automate the routines required to operate the rig and collect the experimental data. The mechanical and electrical features of the rig are now described in more detail.
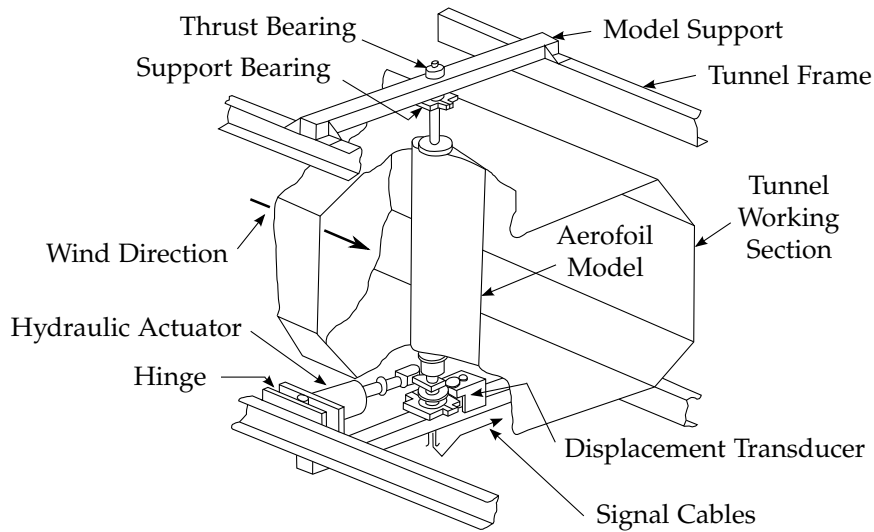
FIGURE 2.4: General arrangement of the dynamic stall test rig.

MECHANICAL FEATURES

The model is installed vertically in the tunnel working section and variation in the angle of attack, around the quarter chord position, is achieved with a hydraulic actuator and crank mechanism. The actuator, a UNIDYNE 907/1 type with a normal dynamic thrust of 6.1 kN operated at a supply pressure of 21 MPa, is mounted horizontally below the tunnel working section and pivots around a hinge at the supporting end. The crank arm, of length 0.125 m, is rigidly connected to the lower external spar connection. Below the crank arm is a fixed gear tooth which meshes with the displacement transducer gear. The displacement transducer is securely clamped to the lower support structure. An upper and lower self-aligning bearing assembly support the model and react the mechanical and aerodynamic loads through the transversely mounted support beams to the tunnel framework. The thrust force is transferred through the upper bearing assembly and model instrumentation cabling is routed out through the hollow axis of the lower external spar connection.

ELECTRICAL FEATURES

The hydraulic actuation system is controlled through a Star Hydraulics STE0005 single channel servo controller operating a Star Hydraulics 55x series electro-hydraulic servo valve. The hydraulic user interface unit processes the rig input signals, including the desired input command voltage (V_{Com}) and an enable signal to provide hydraulic pressure to the valve from the hydraulic pump. The position voltage (V_{Pos}) from the displacement transducer provides an instantaneous angle of attack signal, but also provides a feedback signal for the servo controller to determine the system error state.

The interface unit can operate in two different modes: manual for static cases; and
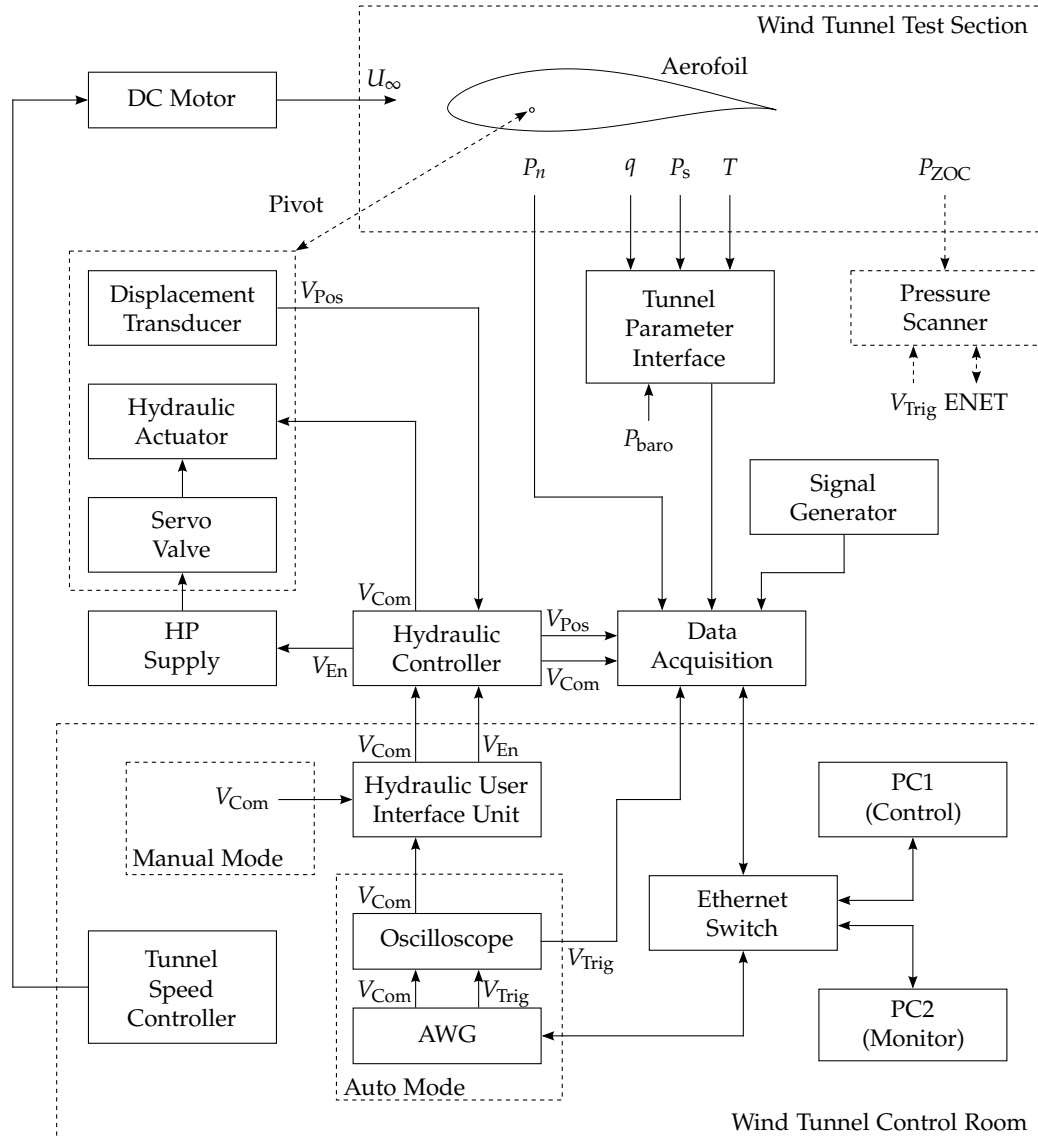
FIGURE 2.5: Schematic of the control and data acquisition system.

automatic for dynamic cases. In manual mode, the input voltage is adjusted by a multi-turn potentiometer and data acquisition is initialised by a software trigger, while in automatic mode, a D-TACQ Solutions ACQ1001Q 4 channel AWG device relays both the input voltage and a hardware trigger to the data acquisition unit. Timing of the dynamic test events is synchronised through the AWG internal 66 MHz clock chip, and signals are supplied to the controller at 2 kHz. Each AWG channel has a 250 kB internal memory buffer, providing a maximum run time of 64 s.

A schematic of the control and data acquisition system is shown in Figure 2.5.

RIG CALIBRATION

During installation of the test model, a calibration process was completed to determine the relationship between model angle of attack and both the servo controller input
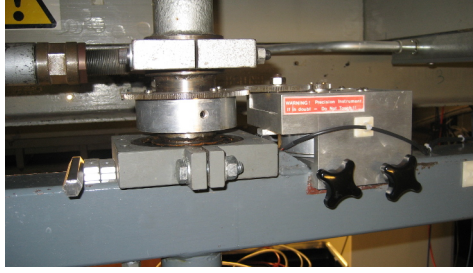
(A) Actuator and crank mechanism.

(B) Linear displacement transducer.

(C) Upper support and bearing assembly.

(D) Lower support and bearing assembly.

(E) Hydraulics user interface unit.
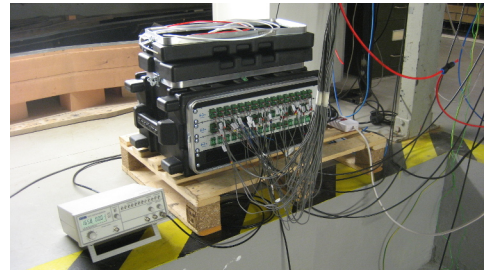
(F) D-TACQ data acquisition system.

FIGURE 2.6: Features of the dynamic stall test rig.

command voltage (V_{Com}) and the linear displacement transducer output position voltage (V_{Pos}). Running the rig in manual mode, the model trailing edge was positioned relative to the tunnel centreline – aided by angular increments marked on the tunnel floor – and the corresponding positions and command voltages were recorded. For both voltage variables, linear relationships, given in Equations 2.1 and 2.2, were found with minimum correlation coefficients of 0.999 and 1 for the command voltage and position voltage respectively. Due to transient conditions during power-up, no value for the command voltage offset ($V_{\text{Com}_{\text{Off}}}$) is stated as each test case will have a value recorded after the hydraulic system is enabled. A table of recorded calibration values is provided in Appendix A.2.

$$V_{\text{Com}} = S_{\text{Com}} \times (\alpha - \alpha_{\text{Off}}) + V_{\text{Com}_{\text{Off}}} \tag{2.1}$$

$$\alpha = \left(V_{\text{Pos}} - V_{\text{Pos}_{\text{Off}}} \right) / S_{\text{Pos}} \tag{2.2}$$

COMMENT ON CONTROLLER PID LIMITATIONS

The amplifier in the servo controller utilises full three-term PID control, with the gains adjusted manually with multi-turn potentiometers. However, this makes selecting and setting suitable gains for each set of test cases problematic. The test matrix covers a range of dynamic motion types, speeds and amplitudes (See Section 2.3) which would each require a set of gains to be determined. To avoid this difficulty the gains remained unchanged which resulted in the required model amplitude not necessarily being achieved for higher model pitch frequencies. The test matrix for the AHH 32 blade section was amended after taking this into consideration. The referencing of test cases refers to the input parameters, but obtained values are used when processing and analysing the datasets. Although the commanded model position may not be achieved in all cases, the actual position is always known from the displacement transducer.

2.2   MODEL DESIGN & INSTRUMENTATION

Selecting NACA 63-series aerofoils is a popular choice for the initial primary turbine blade shape (Whitby and Ugalde-Loo, 2014). They have good resistance to cavitation due to a relatively smaller minimum pressure coefficient and, compared to NACA 4-digit and 5-digit aerofoils, are less sensitive to leading edge roughness and have a delayed stall behaviour (Bir et al., 2011). Increasing the section camber not only improves the design lift coefficient, but also reduces the minimum pressure coefficient at a specific design point, hence improving cavitation resistance (Batten et al., 2006).

The model span, 1.61 m, is dictated by the model vertically spanning the test section and the model chord, 0.55 m, was determined by considering the balance between maximising the model chord and Reynolds number, but minimising the influence of solid blockage and interference effects (Leishman, 1984). The resulting model aspect ratio is 2.93.

2.2.1   AEROFOIL TEST SECTIONS

Three tidal turbine blade sections were selected for testing, one NACA 63-series section and two AHH proprietary sections, which cover the typical range of tidal turbine blade thickness. The two relatively thinner sections are located at the outboard portion of the turbine blade, where the majority of the rotor torque is generated (Manwell et al., 2002), and a thicker section from further inboard where blade structural considerations dominate (Grasso, 2012). To aid manufacturing of the model trailing edge, the rearward 5 % chord was modified to provide a trailing edge thickness of 2 mm (Ramsay et al., 1995). Due to the proprietary nature of the AHH test sections the coordinates cannot be published in this thesis. Therefore, a reduced set of coordinate
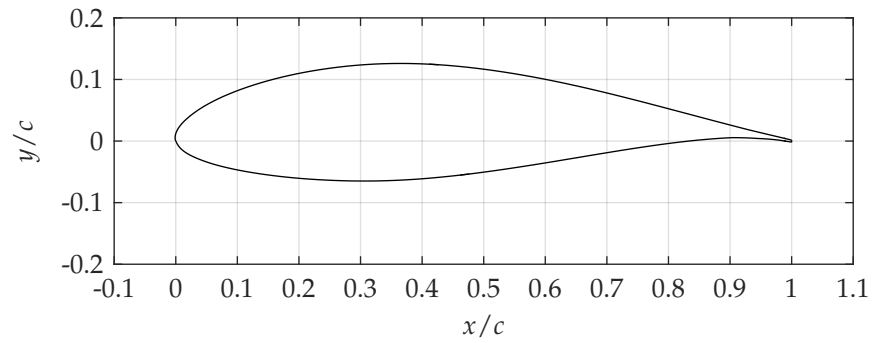
(A) NACA 63-619
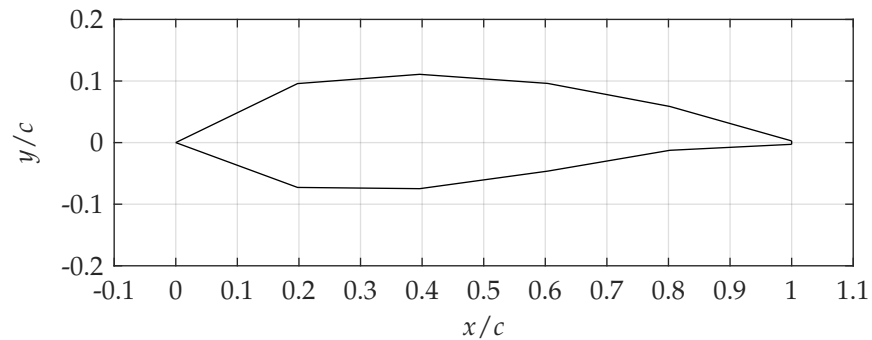
(B) AHH 19
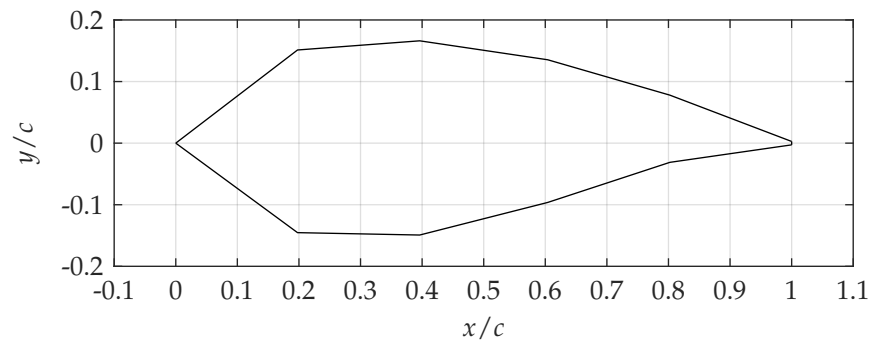
(C) AHH 32

FIGURE 2.7: Geometry coordinates for tested tidal turbine blade sections.

points for the AHH aerofoil geometries are provided for reference, but so that the full design cannot be obtained. The blade sections selected for test are outlined below and the aerofoil coordinates are presented in Figure 2.7.

- NACA 63-619: A 19 % thick section typically located at around 70 % blade span.

- AHH 19: An 18.8 % thick section located at approximately 75 % blade span.

- AHH 32: A 32.3 % thick section located at approximately 45 % blade span.

It is suggested (Barlow et al., 1999) that the ideal wind tunnel solid blockage value is between 0.01 and 0.10, with 0.05 being a typical value. For the three selected test sections the maximum solid blockages, at 25°, are 0.1286, 0.1259 and 0.1373, for the

NACA 63-619, AHH 19 and AHH 32 respectively. Over the typical operating range (See Figure 2.12) the corresponding solid blockages are 0.05 to 0.09, 0.05 to 0.09 and 0.09 to 0.12.

2.2.2 MODEL CONSTRUCTION, INTEGRATION & INSTRUMENTATION

The wind tunnel models are constructed from carbon fibre skins with an internal rib and spar structure, assembled and machined in negative moulds milled to the aerofoil geometry. The skins are fabricated from five layers of carbon fibre cloth (2/2 twill, 12k, 650 g) in a wet lay up and cold cure process. The ribs, manufactured from SikaBlock polyurethane tooling board (M940, density $1.2 \, \text{g/cm}^3$, and M330, density $0.24 \, \text{g/cm}^3$), are bonded with epoxy resin onto the composite skins. An internal aluminium spar, steel inserts and steel end plates transfer the aerofoil loads from the composite skin to the rig structure and also provide the connection interface between the model and actuation mechanism. An outlet in the lower rib and end plate allow the internal instrumentation cabling to be routed out of the model. Although not measured, the final section profile tolerance is expected to be equivalent to that of the mould machining process. The models have a total mass of approximately 20 kg and were finished by hand to give an aerodynamically smooth surface.

The model is connected into the test rig by four bolt connections on both the upper and lower end plates. The end plates sit in lubricated positioning rings in the tunnel floor and ceiling and form an air tight seal around the model. The vertical position of the model in the test section is set by adjusting a threaded rod on the thrust bearing. To prevent interference between the model and tunnel walls, there is a gap of 3.17 mm designed into the assembly. Barlow et al. (1999, p.350) suggest a maximum model gap of 1 mm to eliminate trailing vortices. Therefore, adhesive foam strip is applied around the model ends to seal the gap, but not restricting the model motion. Images of the model manufacturing process and tunnel integration are shown in Figure 2.8.

PRESSURE TRANSDUCERS

The chordwise surface pressure distribution was measured at the model midspan using an array of miniature amplified pressure transducers. First Sensor HDI series gage sensors were selected for offering a good balance of cost and performance. The sensors are temperature compensated with both a digital I^2C bus and 5 V bidirectional analogue signal output in a SMT housing. The maximum response time is 0.5 ms, giving a response frequency of 2 kHz.

For the leading edge region of the model ($x/c \leqslant 0.025$), ±200 mbar sensors were selected, corresponding to a maximum pressure coefficient of 15 at design conditions, and ±100 mbar sensors for the remaining locations. Each sensor was mounted on an individual in-house designed and manufactured PCB and powered from a 5 V DC

(A) Composite skin and spar assembly.
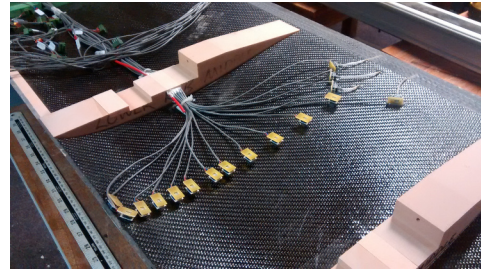
(B) Pressure transducer array.
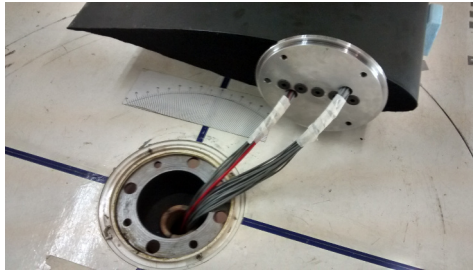
(C) End plates and instrument cabling.
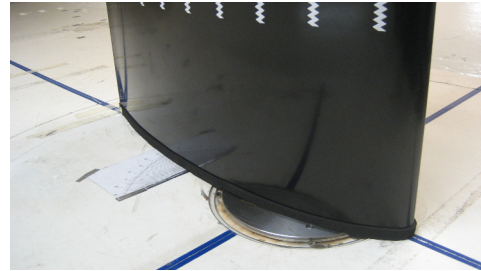
(D) Model located in positioning ring.

FIGURE 2.8: Wind tunnel model manufacture, assembly and integration.

excitation port on each data acquisition channel.

The surface pressure orifices of 0.9 mm inner diameter were machined normal to the model surface and positioned along the chord on the midspan centreline to minimise the effect of any spanwise pressure gradient on the measurements, and were biased towards the leading edge region where the aerofoil pressure and suction peaks are located. In order to minimise the pressure delay time (Whitmore et al., 1990), the pressure transducer ports were bonded into the skin surface behind the orifice. The exception to this was in the area around the trailing edge where the internal space did not permit this, so 0.9 mm inner diameter brass tubes were bonded to the skin and a length of pressure tube, no longer than 50 mm, connected the orifice to the sensor port. To minimise disruption from upstream taps and provide internal space for the sensor PCBs, the taps at the leading and trailing edges were staggered. The offset from the midspan did not exceed 60 mm. The central model volume was sealed during manufacture, to provide a common reference pressure to the gage sensors, and was vented to the tunnel static pressure.

A calibration procedure was carried out on the mounted sensors using a Druck DPI 610 portable pressure calibrator. Ten sensors of each specification were selected and calibrated over the operating pressure range, giving sensitivities of 20.4467 mV/mbar and 10.1950 mV/mbar, for the 100 mbar and 200 mbar specification respectively. Correlation coefficients of 1.0 were obtained for both calibration datasets.

All internal pressure instrumentation was tested after installation and prior to final model assembly. However, a handful of transducers over the three models did not function correctly during test. As the model internal volume was sealed

during assembly it was not possible to replace the defective sensors and a numerical correction was required. Towards the model trailing edge, linear interpolation of local pressure values was suitable for correcting the faulty pressure signal, but it was not possible to correct for a failed sensor close to the leading edge, on both the NACA 63-619 and AHH 19 models, due to the measurement being located in the proximity of the leading edge suction peak. The implications of this are discussed in Section 2.5.5.

Further details of the pressure transducer locations, specifications and calibration are provided in Appendix A.3.

MODEL STRUCTURAL INTEGRITY

A final structural check of the model design ensured the model structural integrity to extreme dynamic loading cases, particularly the model response to having the driving torque applied at only one end. A simplified model of the composite skin was constrained at each end to prevent displacement, but allow rotation, and carried all applied loads. The first case considered a uniform spanwise loading bending case, equivalent to $C_n = 2.2$ at a flow speed of $45\,\mathrm{m/s}$, and secondly a torsion case with the torque required to oscillate the model to an amplitude of 20° at a model frequency of $10\,\mathrm{Hz}$. Both cases are in excess of the expected model loading conditions and include a safety factor of 1.5. The bending deflection estimates are significantly below the limit of 0.1 % span and the maximum expected rotation is 0.037°, both minimising potential for spanwise pressure gradients and model structural failure. The results of this analysis are shown in Table A.4.

2.2.3   MODEL SURFACE ROUGHNESS

To simulate the biofouling conditions representative of a tidal turbine blade, two roughness configurations were considered. The first, investigated on all three models, imitates a microfouled blade, and the second, on the AHH 19 section only, includes a single macrofouled site. For both configurations the roughness application method on the two-dimensional models must be uniform, repeatable and measurable (Barlow et al., 1999, pp.306–311).

Transition is not intentionality fixed at any point on the aerofoil surface. Based on the model geometries and test Reynolds number, it can be inferred that the boundary layer over the aerofoil test sections is predominately turbulent, but a short chordwise region of laminar flow may exist at the aerofoil leading edge. With the addition of surface roughness, the first chordwise roughness element will transition the flow to a turbulent state, if not already transitioned, and the aerofoil will have a boundary layer, on the upper and lower surfaces, in a fully turbulent state.

(A) Spanwise limit of roughness.   (B) Zigzag turbulator tape dimensions.
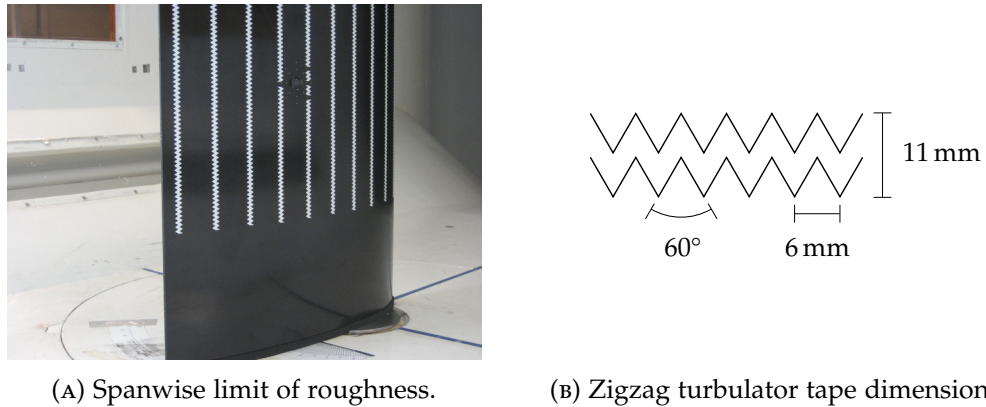
FIGURE 2.9: Application of widely distributed roughness to the model surface.

MICROFOULING: WIDELY DISTRIBUTED ROUGHNESS

To simulate the microfouled blade state, a 0.6 mm thick, 6 mm point to point, 60° zigzag turbulator tape was applied to the models. The selected ratio of roughness height to aerofoil chord was $0.0011c$, which corresponds to the light roughness configuration investigated previously by Walker et al. (2014). Ten strips of tape were applied to both the upper and lower surfaces, with the front edge of the tape positioned at spacial increments of $\Delta x/c = 0.10$ from $x/c = 0.05$ to $x/c = 0.95$ and over the central 75 % span. The zigzag turbulator tape distribution and dimensions are shown in Figure 2.9. The model span ends were left clean to account for the height of the tunnel wall boundary layer (Eckerle and Langston, 1986) and the tape was trimmed around any pressure tapping locations. This method resulted in a uniform roughness distribution over the aerofoil surface.

MACROFOULING: INSTRUMENTED BARNACLE

To represent the macrofouled case, an instrumented barnacle model was manufactured and attached to the AHH 19 model. The barnacle was positioned on the aerofoil upper surface at 60 % chord and 25 % span (400 mm from the tunnel floor), so as not to influence the main aerofoil pressure measurements at midspan.

Literature widely reports basal diameters of different species (Southward, 2008), but due to many influencing factors and ecological variation the height is rarely reported. Vance et al. (2014), as part of the ETI ReDAPT project, identified the acorn barnacle *Chirona hameri* as the dominant fouling species at the EMEC Walls of Warness tidal site, with a basal diameter of over 25 mm and in some cases reaching heights of 30 mm to 40 mm. Also in the fouling community were the smaller *Balanus crenatus* and *Semibalanus balanoides* species, which grow to diameters of 25 mm and 15 mm respectively. Barnes and Powell (1953) measured the length to height ratio of subtidal *Balanus crenatus* collected in the Firth of Clyde over a two year period, with a mean ratio of 2.9 for a 20 mm length. The widely referenced work of Orme

(A) Fouling colony on blade surface.   (B) Measurement of barnacle diameter.
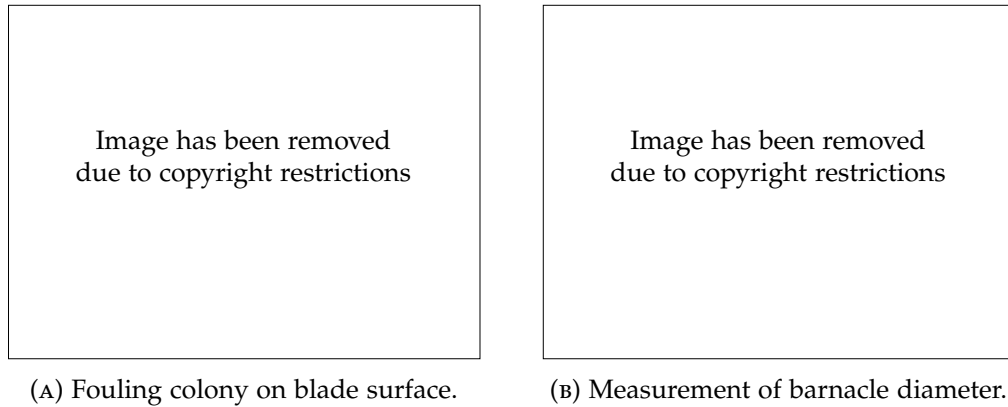
Figure 2.10: Barnacle biofouling on a deployed turbine blade. Images supplied by AHH.

et al. (2001) investigates a selection of barnacle sizes ranging from $0.0035c$ to $0.0285c$ for the roughness element height. A barnacle height of $0.02c$ was selected for this investigation.

Although the barnacle species on the AHH turbine blade (See Figure 2.10) was not confirmed, all observed specimens were a similar size with a measured diameter of approximately 25 mm. The barnacle model was based on a frustum (Sadique et al., 2015) with radii of 20 mm and 10 mm and height 11 mm, as shown in Figure 2.11, and included nine pressure orifices around the outer faces. A further sixteen orifices were included around the barnacle, on the model surface, on two concentric diameters of 40 mm and 60 mm. The orifices were 0.9 mm inner diameter brass inserts (Shaw, 1960) connected to a Scanivalve ZOC23b miniature pressure scanner by individual 1.5 m lengths of Saint-Gobain Tygon S3 flexible pressure tubing. Pressures were sampled at 125 Hz on a Scanivalve ERAD4000 Remote A/D, simultaneously with the principal experiments.

2.3   EXPERIMENTAL TEST MATRIX

This section details the creation and suitability of the experimental test matrix. To determine the range of turbine operating parameters, AHH supplied Tidal Bladed (DNV GL, 2016) simulation datasets. In addition to these datasets, a 1 MW tidal turbine was designed and simulated in a tidal flow to confirm the test matrix represented the expected operation of a typical turbine. The final blade parameter envelopes are presented in Figure 2.12, where the blade radial position is with respect to the turbine centre of rotation.
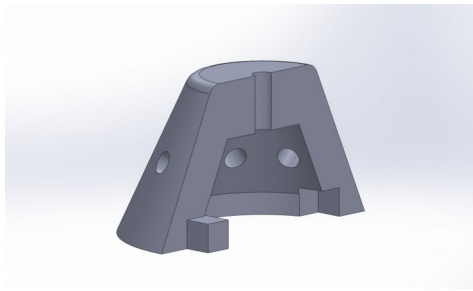
(A) SolidWorks part view.

(B) Barnacle components.
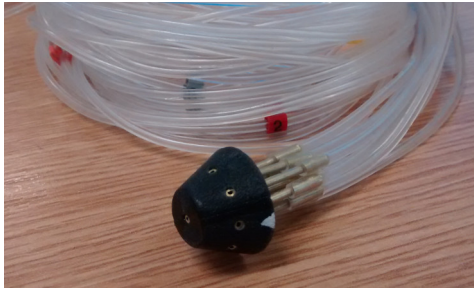
(C) Assembly of barnacle model.
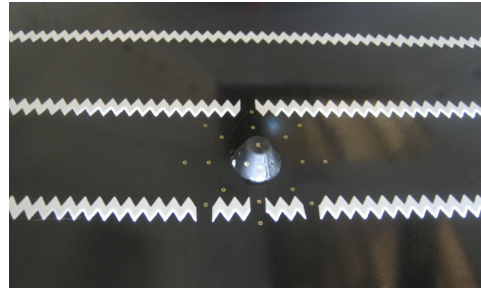
(D) Barnacle installed on test blade section.

FIGURE 2.11: Design, assembly and installation of 3D printed barnacle model.

2.3.1 ANALYSIS OF TIDAL SITE DATA

AHH SUPPLIED DATA

The AHH supplied datasets are from three different UK tidal project sites and included the rotor azimuth angle, angle of attack and relative flow velocity for a single turbine blade at discrete radial positions along the blade span. The simulation datasets are to demonstrate compliance with the applicable design load case standards (DNV GL, 2015b). The blade geometry, for the corresponding variant of the AHH HS1000 turbine, was also provided.

Each dataset covers 10 min of turbine operation, with a time step of 0.04 s or 0.02 s at three design speed ratings (first, variable and second). The site flow characteristics, including the tidal flow turbulence intensities, were based on detailed ADCP marine surveys, and the velocity profile is modelled on a standard one-seventh power law. In addition, the influence of the wave distribution and loading on the flow was accounted for with the significant wave height (H_s) and specified peak period (T_p) for a 50 year wave.

For each blade radial station, angle of attack and Reynolds number were calculated at each time step, while reduced frequency, reduced pitch rate, and collective and cyclic angle of attack were calculated over one complete revolution of the turbine. Results from the three speed ratings were combined to create a parameter envelope for each site and turbine variant.
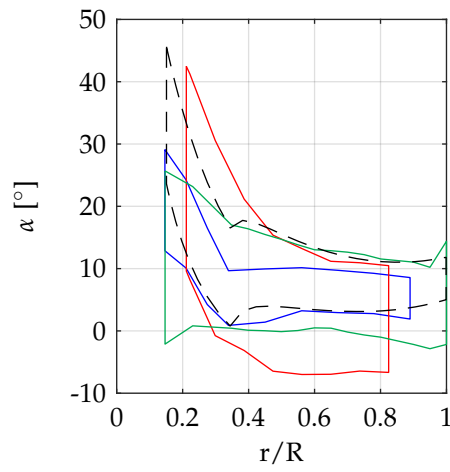
(A) Angle of Attack
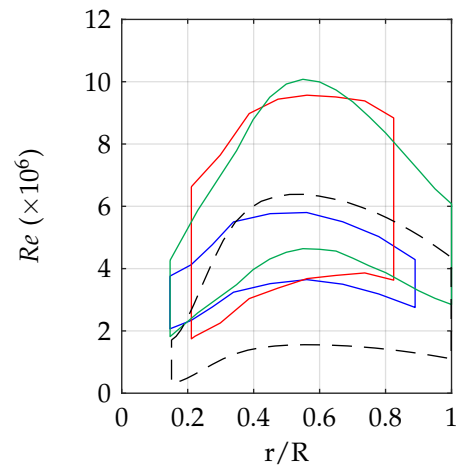
(B) Reynolds Number
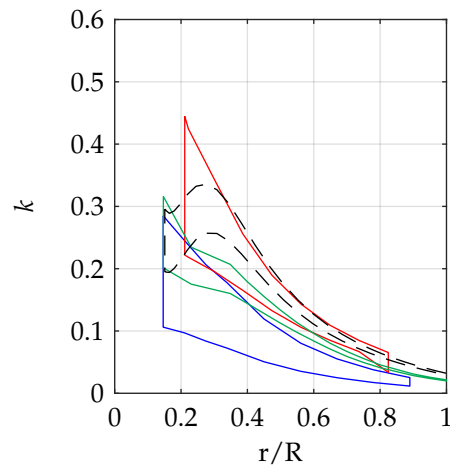
(C) Reduced Frequency
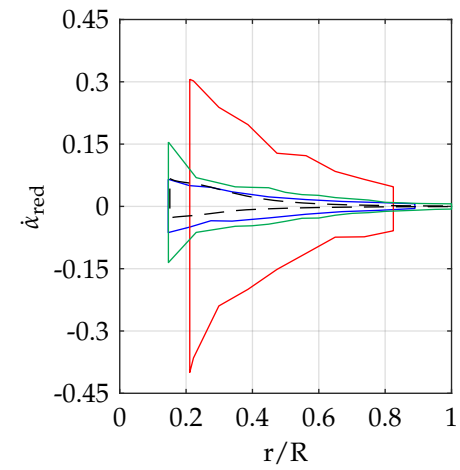
(D) Reduced Pitch Rate
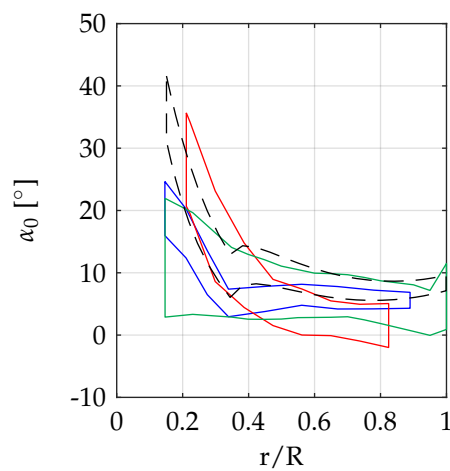
(E) Collective Angle of Attack
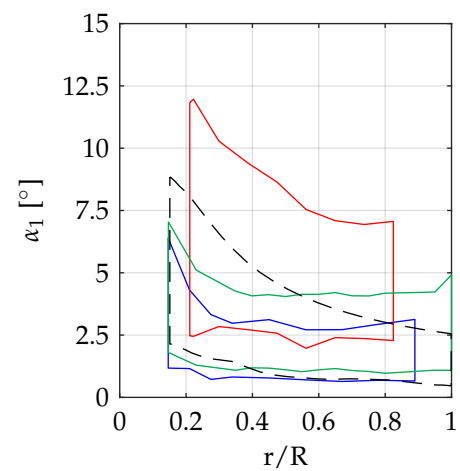
(F) Cyclic Angle of Attack

FIGURE 2.12: Blade parameters from AHH supplied data and 1 MW turbine model.

GENERIC 1 MW TIDAL TURBINE MODEL

To validate the AHH supplied data as a general case, a 1 MW horizontal-axis turbine model was created. Two aspects had to be considered: the design of an appropriate turbine blade geometry model; and the simulation of the design in a flow model. A summary of the model inputs and final geometry are presented in Appendix B.

Firstly, the blade geometry model. NREL HARP_Opt (Sale, 2014) is a multi-objective genetic algorithm turbine design tool based on blade element theory in a uniform steady flow. For a user defined turbine configuration and set of design parameter constraints, a turbine geometry is created which optimises the turbine efficiency. The turbine is variable speed and pitches to feather. For this analysis, the blade structural optimisation considerations were neglected.

Turbine parameter constraints were selected following a review of turbine designs in the available literature (Batten et al., 2007; Grogan et al., 2013; Mycek et al., 2014; Whitby and Ugalde-Loo, 2014), and a flow speed distribution for the EMEC tidal site (Melville, 2008) was utilised. Due to the limited availability of aerofoil data for the thicker sections, an aerofoil family for the turbine was created using FFA-W3-xxx and NACA 63-6xx aerofoil series data (Björck, 1990; Fuglsang et al., 1998b).

Secondly, the simulation flow model. A simple statistical flow model has been created which includes the tidal velocity modelled by the one-seventh power law and turbulent velocity components scaled from published tidal site turbulence measurements. It is assumed that the turbine yaw angle is 0°, the mean lateral and vertical velocities are 0 m/s, and the flow turbulence intensity does not change across the rotor face through the water column.

Work by Milne et al. (2014) presents turbulent flow data from the Sound of Islay and the turbulence anisotropic ratio $\sigma_u : \sigma_v : \sigma_w = 1.0 : 0.75 : 0.56$ describing the variation in axial, lateral and vertical velocity fluctuations. This allows the velocity fluctuations at any turbulence intensity to be estimated by scaling the standard deviation ratio, while maintaining an appropriate turbulence length and time scale. An axial turbulence intensity of 8 % was selected for this analysis (Thomson et al., 2012; Milne, 2014).

The model is time marched through a set number of flow cycles, equivalent to 10000 turbine rotations, with an updated blade azimuth angle and flow on each step. The time step is $\Delta t = 0.01$, giving an angular resolution of 0.67° at the fastest rotational speed. The thinking behind this simple model is that if the blade is rotated though the turbulent flow then with an increasing number of rotations, the blade should experience closer to the full range of possible velocity combinations at that point in the flow.

Further assumptions in the model are a fixed turbine rotational speed at each design point and the induction factors (a and a') are determined from the power

TABLE 2.1: Design parameters at the three defined design points.

Parameter	Design Point 1	Design Point 2	Design Point 3
C_P [–]	0.428	0.431	0.431
U_∞ [m/s]	0.6	1.6	2.4
Ω [rpm]	3.00	7.41	11.12

coefficient and local speed ratio. The relationship between the blade section angle of attack (α) inflow angle (ϕ) and pitch angle (θ) is given in Equation 2.3.

$$\alpha = \phi - \theta \tag{2.3}$$

As previously, the results of this analysis are combined into parameter envelopes and are included in Figure 2.12, and summarised in Table 2.1 for the three design points considered.

2.3.2 SCALING LAWS

Inferring the behaviour of a turbine blade section from a wind tunnel aerofoil model requires an understanding of the fluid flow and rotor motion, and the interdependency of these parameters. Ensuring that the principal parameters are scaled appropriately from the deployed turbine to the wind tunnel aerofoil model is essential.

Firstly, scaling the rotor blade motion and unsteadiness is considered. The reduced frequency, a fundamental non-dimensional parameter for characterising the unsteadiness of a single frequency oscillation (Leishman, 2000), is suitable for scaling the oscillatory frequency of a blade section (Milne, 2014), and scaled as described in Equation 2.4.

$$k_{\text{turbine}} = \frac{(\omega c)_{\text{turbine}}}{2U_{\text{water}}} = \frac{(\omega c)_{\text{model}}}{2U_{\text{air}}} = k_{\text{model}} \tag{2.4}$$

As the aerofoil behaviour is dependent on the angle of attack, the magnitude of the turbine blade section incidence is matched in the wind tunnel.

$$\alpha_{\text{turbine}} = \alpha_{\text{model}} \tag{2.5}$$

Similarly, the pitch rate can be scaled from the turbine to the aerofoil model by matching the reduced pitch rate terms.

$$(\dot{\alpha}_{\text{red}})_{\text{turbine}} = \frac{(\dot{\alpha} c)_{\text{turbine}}}{2U_{\text{water}}} = \frac{(\dot{\alpha} c)_{\text{model}}}{2U_{\text{air}}} = (\dot{\alpha}_{\text{red}})_{\text{model}} \tag{2.6}$$

Secondly, it is difficult to replicate the turbine Reynolds number in the wind

tunnel. However, a Reynolds number of 1.5×10^6, compared to a typical value of approximately 6×10^6 on the turbine, has been achieved during the experimental tests. Analysis of the three test sections in XFOIL (Drela and Youngreen, 2013) predict that the aerofoil loads are Reynolds number independent over the operating range, hence the results from the wind tunnel tests are comparable to the turbine rotor state.

2.3.3 SUMMARY OF THE TEST MATRIX

The final test matrix was selected with reference to the analysis presented in Figure 2.12 and with consideration to the operating capability and limits of the dynamic stall rig. Three different motion types were tested: static, oscillations in pitch, and constant rate ramp and hold. With reference to the turbine operation, static data is representative of the blade loads when the turbine is parked, while the oscillations are representative of normal operation. The ramp cases are most representative of fault cases, where the turbine must be shut down and parked, or the transient case during turbine start up (DNV GL, 2015b).

All the tests were conducted at a Reynolds number of 1.5×10^6 and the full test matrix was repeated for both the baseline clean and rough fouled blade configurations. A summary of the test cases is now presented and the full test matrix and corresponding data file names are given in Appendix C.

STATIC

A static polar was obtained for each test section, spanning an angle of attack range of −25° to 25° in 1° increments. The angular increment was reduced to 0.5° in regions of attached flow and positive static stall to ensure the salient flow features were acquired. A summary of the static test cases is given in Table 2.2.

TABLE 2.2: Summary of static test cases.

α_{min} [°]	α_{max} [°]	α_{inc} [°]	Aerofoil		
			NACA 63-619	AHH 19	AHH 32
-25	25	2	✓	✓	✓
-10	24	2	✓	✓	✓
-7.5	19.5	1	✓	✓	✓

OSCILLATORY PITCH CYCLES

The oscillatory angle of attack variation during one revolution of the turbine rotor can be approximated as a sinusoidal function, as described previously in Equation 1.3.

From the results presented in Figure 2.12, at approximately 75 % blade span, where the two thinner test sections would be located, the reduced frequency ranges from

0.02 to 0.1, the mean angle of attack from −1° to 10° and the angular amplitude from 1° to 7°. Similarly for the thicker inboard section, at approximately 45 % blade span, the respective ranges for k, α_0 and α_1 are 0.1 to 0.2, 2° to 12° and 1° to 9°. The test case parameters have been selected to cover these ranges, and a summary of the oscillatory test cases is given in Table 2.3.

TABLE 2.3: Summary of oscillation in pitch test cases.

k [–]	α_0 [°]	α_1 [°]	Aerofoil		
			NACA 63-619	AHH 19	AHH 32
0.025	0	$\begin{bmatrix} 2 & 4 & 6 \end{bmatrix}$	✓	✓	
	5		✓	✓	
	10		✓	✓	
0.05	0	$\begin{bmatrix} 2 & 4 & 6 \end{bmatrix}$	✓	✓	
	5		✓	✓	
	10		✓	✓	
0.1	0	$\begin{bmatrix} 2 & 4 & 6 \end{bmatrix}$	✓	✓	
	5		✓	✓	
	10		✓	✓	
	2	$\begin{bmatrix} 2 & 5 & 8 & 10 \end{bmatrix}$			✓
	8				✓
	12				✓
0.15	2	$\begin{bmatrix} 2 & 5 & 8 & 10 \end{bmatrix}$			✓
	8				✓
	12				✓
0.2	2	$\begin{bmatrix} 2 & 5 & 8 & 10 \end{bmatrix}$			✓
	8				✓
	12				✓

The chosen reduced frequency test parameters, for the two thinner test sections, cover the same range identified by Milne (2014) as the non-dimensional forcing parameter due to turbulence for a blade section at the $0.75R$ blade location. The additional cyclic angle of attack test point ($\alpha_0 = 10°$) for the AHH 32 section was included to overcome a limitation with the test hardware and was discussed previously on page 32.

CONSTANT RATE RAMPS

During a constant rate ramp and hold motion the model is pitched from an initial incidence (α_{init}) through an angular displacement (α_{arc}) at a pitch rate defined by the reduced pitch rate ($\dot{\alpha}_{\text{red}}$). The maximum linear pitch rate which the rig can achieve is 8.5 rad/s ($\dot{\alpha}_{\text{red}} = 0.052$ for the test conditions). A summary of the ramp test cases is given in Table 2.4.

TABLE 2.4: Summary of constant pitch rate rate ramp and hold test cases.

$\dot{\alpha}_{\mathrm{red}}$ [–]	α_{init} [°]	α_{arc} [°]	Aerofoil		
			NACA 63-619	AHH 19	AHH 32
0.0025			✓*		
0.005			✓*		
0.01	0	$\begin{bmatrix}10 & 15\end{bmatrix}$	✓*	*Baseline Config Only	
0.025			✓*		
0.04			✓*		
0.0025			✓	✓	✓
0.005			✓	✓	✓
0.01	0	$\begin{bmatrix}20 & 25\end{bmatrix}$	✓	✓	✓
0.025			✓	✓	✓
0.04			✓	✓	✓
-0.0025			✓	✓	✓
-0.005			✓	✓	✓
-0.01	$\begin{bmatrix}20 & 25\end{bmatrix}$	$\begin{bmatrix}-20 & -25\end{bmatrix}$	✓	✓	✓
-0.025			✓	✓	✓
-0.04			✓	✓	✓

2.3.4 LIKELIHOOD OF TEST CASE OCCURRENCES

An experimental test matrix has been defined, but it is of interest to understand the likelihood of each test case occurring on the turbine. An 'extreme' event occurring a few times on each tidal cycle is of greater concern than one which will only occur only on the odd occasion. The AHH supplied simulation data considers the design load case which captures the fifty year load effect. This statistically covers the effects of the majority of tidal flow and wave loading cases, but it is still possible to encounter higher flow cases, hence increased blade incidence and loading.

For each tidal project site, the probability of different angle combinations and reduced frequency occurring has been calculated across the turbine operating range, and presented in Figures 2.13 and 2.14. The width of the bin used for the angle analysis is 0.5° for the angular components (α_0 and α_1) and 0.005 for the reduced frequency. As the turbine blade thickness profile changes between turbines, the thinner section is assumed to be positioned at between 70 % and 85 % span, and the thicker section between 40 % and 50 % span.

2.4 DATA ACQUISITION & PROCESSING

2.4.1 DATA ACQUISITION SYSTEM

The wind tunnel data acquisition system is based around a portable 96 channel D-TACQ Solutions ACQ2006 networked DAQ appliance utilising 24 bit resolution
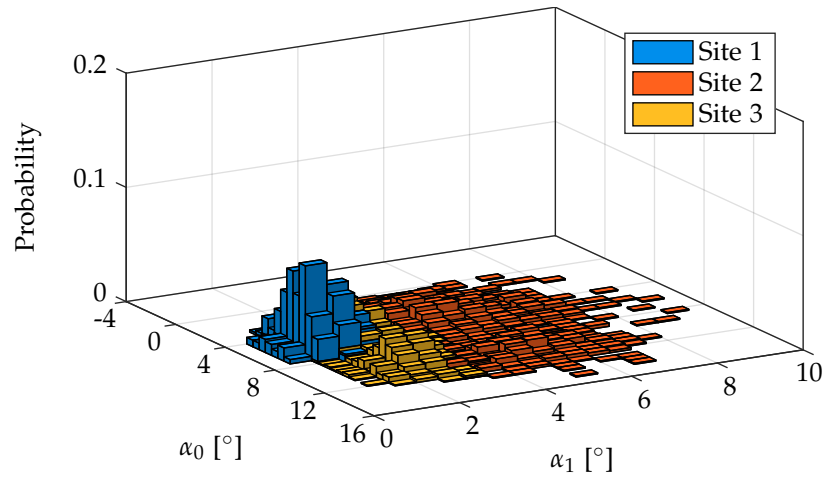
(A) Inboard (32 %) blade section.
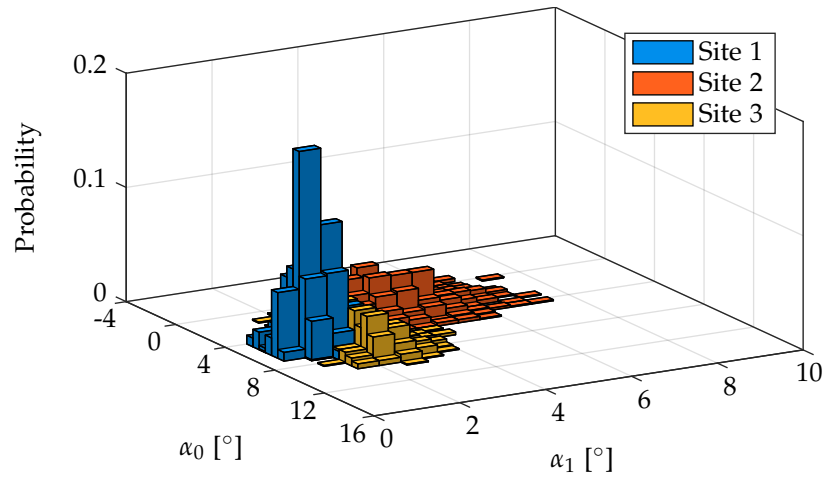
(B) Outboard (19 %) blade section.

FIGURE 2.13: Probability and variation of turbine blade section angle of attack.
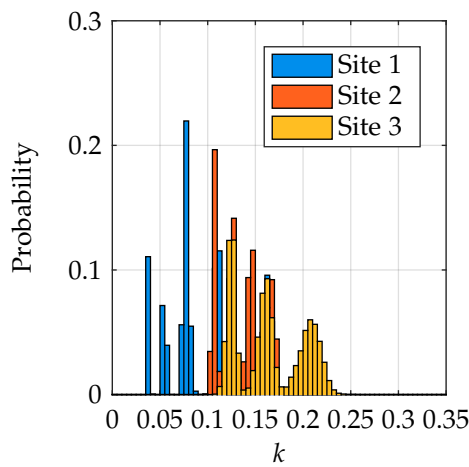
(A) Inboard (32 %) blade section.
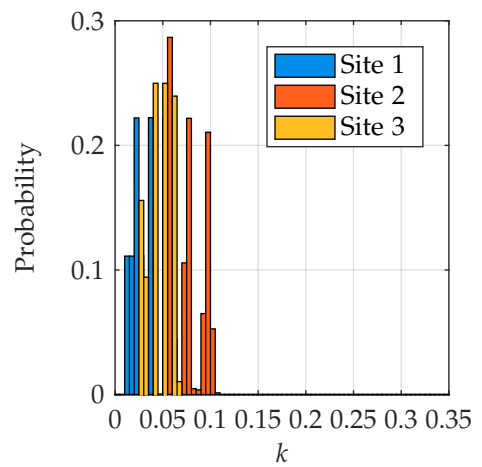
(B) Outboard (19 %) blade section.

FIGURE 2.14: Probability and variation of turbine blade section reduced frequency.

ACQ437ELF-16 ADC modules. Each acquisition channel is equipped with a dedicated 5 V DC power supply and inputs to the unit are connected by 4 port 3.81 mm pluggable terminal blocks. An overview of the acquisition channel map is given in Table A.7.

Experimental data was acquired at a sampling rate of 10 kHz, simultaneously on each connected channel, and the raw data was stored as voltage values in MATLAB MAT-file format. For each test case type a different sampling approach is employed: static test cases are sampled for 5 s at each test point; oscillatory test cases are sampled for the time taken to complete 10.5 cycles; and ramp test cases are repeated five times and sampled for 7 s, including a 2 s sample time before the model movement. For the oscillatory cases the motion amplitude was increased over 8 s and set in motion for a further 8 s before the data sampling was performed, starting on the motion upstroke at the model collective incidence.

The steps for processing the acquired experimental voltage data and converting to averaged engineering units for each test case type are now briefly described.

2.4.2 DATA PROCESSING

Measurements of the model surface pressures at each discrete chordwise location are reduced to the pressure coefficient, a parameter independent of body size, at the recorded angle of attack. The pressure coefficient is defined in Equation 2.7, where n is the transducer location.

$$C_{p_n} = \frac{p_n - p_\infty}{q} \tag{2.7}$$

MODEL INCIDENCE & TUNNEL PARAMETERS

The model angle of attack (Equation 2.2) and the corresponding parameters describing the flow in the wind tunnel (q, T, p_{baro} and p_{s}) were also obtained for each model position, as defined in Equations A.6 to A.9. The three tunnel pressures were obtained from the following sources: the flow dynamic pressure from a Furness MDC-FC002 micromanometer, connected to the tunnel pitot-static probe; the atmospheric pressure from a barometric pressure sensor (First Sensor 144S-PCB series); and the tunnel static pressure from a pressure sensor (First Sensor 144L-PCB series) with reference to atmospheric pressure. Expressions for converting the acquired voltages to engineering units are provided in Appendix A.5.

The processed experimental data is saved as a table in text DAT-file format and for each angle of attack includes the pressure coefficient at each transducer location, dynamic pressure, temperature, atmospheric pressure and tunnel static pressure. In addition, the header RIB provides details pertaining to that particular test case.

DATA PROCESSING: STATIC

Static test case raw voltage data is reduced to a sampling rate of 250 Hz using a two step filter. Every fifth term is retained to thin the dataset to 2 kHz then a twelfth order FIR filter is applied. The filtered dataset is numerically averaged for each angle of attack, discarding the first four samples of data to allow for any filter delay effects. During processing the three separate static test runs are combined into one output data file of increasing angle of attack.

DATA PROCESSING: OSCILLATIONS

Test data from the oscillatory test cases is also filtered to a reduced sampling rate, but ensemble-averaged using the data obtained from ten consecutive motion cycles. The additional half cycle in the data is present to ensure ten complete cycles are captured. A fixed reduced sampling rate would result in the higher reduced frequency tests having a higher data resolution. Therefore, the reduced sampling rate is scaled with the reduced frequency and set to $1000k$ Hz, resulting in approximately 400 samples per cycle for all test cases. Again, the dataset is thinned and then reduced with a twelfth order FIR filter. Filtering with a FIR filter introduces a time delay with respect to the input signal and is dependent on the frequency content of the output signal. It is acceptable to assume that the dominant frequency in all the output spectra is the model oscillatory frequency and all output signals will be shifted by the same time delay. As all the output data signals are filtered before the ensemble-averaging process, the delay effects are avoided as the first pitch cycle starts approximately 0.04 s after the acquisition trigger is received – a time delay longer than that introduced by the filter

The dataset block associated with each cycle is extracted, with the cycle position being identified from the angle of attack time history as the first sample greater than α_0 on the motion upstroke, and placed on a new cycle time base starting at $t = 0$. To give a common starting point for each cycle, the time base is shifted by Δt so that $\alpha = \alpha_0$ at $t = 0$. The time series dataset for each cycle is then interpolated onto a master time base and averaged across the ten cycles.

DATA PROCESSING: RAMPS

Similarly to the static and oscillatory test cases, the datasets for ramp cases are also thinned and then reduced with a twelfth order FIR filter to a final sampling rate of 500 Hz. The dataset block corresponding to 0.5 s before the motion trigger to 3 s after is extracted for each of the five repeats. This is sufficient time for the ramp arc to be be completed and for the augmented loads to return to the static equivalent state. Due to the high quality motion timing and trigger system, the time bases from the five

repeats are aligned and allow an average over the five repeats to be taken at each time step.

CALCULATION OF MODEL COEFFICIENTS

The x-component and y-component of the pressure force coefficient, with respect to the aerofoil body axes, can be calculated using Equations 2.8 and 2.9.

$$F_{x_n} = -C_{p_n} l_n \cos(\theta_n) \tag{2.8}$$

$$F_{y_n} = -C_{p_n} l_n \sin(\theta_n) \tag{2.9}$$

The parameter θ defines the angle of each discretised aerofoil panel the measured pressure is acting on. To simplify the calculation of the aerofoil load and pitching moment coefficients by ensuring the pressure force components are acting in the correct direction, the panel angles on the aerofoil upper surface have been rotated by 90° and those on the lower surface by 270°. The trigonometric functions in these terms have taken this angle transformation into account.

The aerofoil force and pitching moment coefficients, in the body axes reference system, can then be defined by Equations 2.10 to 2.12, where the limiting term i is the number of pressure transducers installed in the model. The obtained loads are two-dimensional aerofoil parameters and are described as a load coefficient per unit chord, where $(x/c)_{\mathrm{PA}}$ is the chordwise location of the blade section pitch axis.

$$C_n = \sum_{n=1}^{i} F_{y_n} \tag{2.10}$$

$$C_c = -\sum_{n=1}^{i} F_{x_n} \tag{2.11}$$

$$C_m = \sum_{n=1}^{i} \left(F_{y_n} \left((x/c)_n - (x/c)_{\mathrm{PA}} \right) + F_{x_n} (y/c)_n \right) \tag{2.12}$$

Similarly, the force coefficients in the flow axes reference system are defined by Equations 2.13 and 2.14.

$$C_l = -\left(\sum_{n=1}^{i} F_{x_n} \right) \sin(\alpha) + \left(\sum_{n=1}^{i} F_{y_n} \right) \cos(\alpha) \tag{2.13}$$

$$C_d = \left(\sum_{n=1}^{i} F_{x_n} \right) \cos(\alpha) + \left(\sum_{n=1}^{i} F_{y_n} \right) \sin(\alpha) \tag{2.14}$$

The evaluation of forces in this thesis are predominately presented as the normal and chordwise force coefficients, and the relationships between the body and wind axes reference system force components are given in Equations 2.15 and 2.16.

$$C_n = C_l \cos(\alpha) + C_d \sin(\alpha) \tag{2.15}$$

$$C_c = C_d \cos(\alpha) - C_l \sin(\alpha) \tag{2.16}$$

The air density is calculated by assuming an ideal gas, as defined by Equation 2.17, and the viscosity is calculated as a function of temperature in Equation 2.18 with Sutherland's Law (Sutherland, 1893), where the appropriate reference values for air have been substituted. Both parameters are obtained in SI engineering units.

$$\rho = \frac{RT}{p_{\text{baro}}} \tag{2.17}$$

$$\mu = 18.27 \times 10^{-6} \left(\frac{411.15}{T + 120} \right) \left(\frac{T}{291.15} \right)^{3/2} \tag{2.18}$$

2.4.3 WIND TUNNEL CORRECTIONS

The flow field around the aerofoil model in the closed wind tunnel test section is modified due to the presence of the tunnel walls (Glauert, 1933). For the infinite unbounded instance, in this case a tidal channel, the flow is free to expand, whereas the flow in the tunnel is constrained by the flow boundary at the wall. The proximity of the walls results in the alteration of the pressure and velocity field in the region local to the test section, hence a change to the measured pressures, forces and moments acting on the model, alongside small variations in the tunnel flow which can also have a significant influence on the measured parameters.

To compensate for the effects introduced by the tunnel wall boundary, a series of corrections can be applied to the measured data. Corrections for both static and dynamic test cases are outlined below.

STATIC CORRECTIONS

The corrections required for static wind tunnel tests consider the influence of streamline curvature, solid blockage and wake blockage, as described in *Low-Speed Wind Tunnel Testing* (Barlow et al., 1999). The effects of the tunnel buoyancy can be ignored for two-dimensional aerofoil testing and the wall effects on the lift distribution can also be neglected as the model chord is less than 70 % of the tunnel height.

   Due to the proximity of the model to the tunnel walls, the flow streamline curvature around the model is straightened, giving the effect of the aerofoil model having more camber than it actually does. Therefore, for a given angle of attack the test section will generate more lift and an increased pitching moment. At the same time, the flow passing the model is being constricted and by continuity the mass flow rate must be maintained, hence an increase in velocity in the region around the model. Similarly, the wake behind the test section will generate a zone of higher pressure, hence lower flow velocity. Again, to satisfy the continuity condition, the velocity in the freestream will increase, resulting in a pressure gradient across the model.

   All the static aerofoil data presented in this thesis has been corrected using the common two-dimensional wall corrections suggested by Barlow et al. (1999), and are presented in Equations 2.19 to 2.26. Subscript u denotes the uncorrected measurements and c/h is the ratio of the aerofoil model chord to the tunnel working section height. C is the test section cross-sectional area, which is $3.14\,\text{m}^2$ for the Handley Page wind tunnel. The processed data files are stored in an uncorrected state and require the stated static corrections to be applied when being used in the future.

$$\alpha = \alpha_\text{u} + \frac{57.3\sigma}{2\pi}\left(C_{l_\text{u}} + 4C_{m_\text{u}}\right) \tag{2.19}$$

$$C_l = C_{l_\text{u}}\left(1 - \sigma - 2\epsilon\right) \tag{2.20}$$

$$C_m = C_{m_\text{u}}\left(1 - 2\epsilon\right) + 0.25\sigma C_l \tag{2.21}$$

$$C_{d_0} = C_{d_{0_\text{u}}}\left(1 - 3\epsilon_\text{sb} - 2\epsilon_\text{wb}\right) \tag{2.22}$$

$$\sigma = \frac{\pi^2}{48}\left(\frac{c}{h}\right)^2 \tag{2.23}$$

$$\epsilon = \epsilon_\text{sb} + \epsilon_\text{wb} \tag{2.24}$$

$$\epsilon_\text{sb} = \frac{0.52 \times \text{Model Volume}}{C^{3/2}} \tag{2.25}$$

$$\epsilon_\text{wb} = 0.25\left(\frac{c}{h}\right)C_{d_\text{u}} \tag{2.26}$$

DYNAMIC CORRECTIONS

Correcting the measured model values for the effects of wall interference for the dynamic case is a greater challenge, which requires the time-dependent flow field variation to be considered, but has not been as thoroughly investigated compared to the static case. Ewald (1998) suggests unsteady wall corrections using both an analytical and panel method. However, the analytical method is limited to nearly quasi-steady behaviour ($0 < k \leqslant 0.05$) and the panel method requires a detailed understanding of the pressure distribution on the tunnel walls – something not available from the current investigation. This situation leads to the unsteady tunnel interference effects being routinely neglected.

Due to no viable correction method being available for unsteady wind tunnel testing (Choudhry et al., 2012), all dynamic data presented in this thesis has been left uncorrected and as measured. However, all static datasets presented in this thesis have had the static corrections described applied and uncorrected dynamic data is compared directly to the corrected static state.

2.5   MEASUREMENT ACCURACY, ERRORS & CONFIDENCE BOUNDS

2.5.1   ERROR ANALYSIS & CONFIDENCE BOUNDS

The measurement of a test variable will always have a certain level of uncertainty associated to the *measured* value and, as such, a *true* value cannot be obtained. Error analysis quantifies the parameter range around the measured value, for a given confidence bound or probability, in which the true value is likely to lie. The error analysis presented here is based on the methods detailed in the works of Coleman and Steele (2009) and Reddy (2011). All values presented in this error analysis are given for a 95 % confidence level and the variation of the experimental data is assumed to be described by a normal probability (Gaussian) distribution.

MEASURED VARIABLES

Measured variables are those obtained directly from test instrumentation, as opposed to calculated variables obtained from combining multiple measured variables in a data reduction equation. The overall uncertainty in the measurement of variable X consists of both a bias, or fixed systematic, error (b_X) and a random error (s_X), as described in Equation 2.27, where u_X is the overall uncertainty.

$$u_X = \sqrt{b_X^2 + s_X^2} \qquad (2.27)$$

The sources of bias error in the measurement system are present and equal in

all test cases, and include the uncertainties associated with calibration, and data acquisition, resolution and reduction. There are no statistical methods available for providing estimates of the individual bias error sources and the total bias error is determined from the individual sources, as described in Equation 2.28.

$$b_X = \sqrt{\sum_{n=1}^{i} b_{X_n}^2} \tag{2.28}$$

Conversely, the sources of random error are unpredictable and unknown, and are estimated from statistical methods. Random errors are not constant between consecutive readings or test cases, including effects such as sensor noise, and are estimated from the t-distribution for the defined confidence levels, and standard deviation and size of the measurement sample.

The fixed bias errors for the measured variables are summarised in Table 2.5, where the presented errors are determined from the available calibration data and sensor specifications.

TABLE 2.5: Bias error in measured variables.

α [°]	q [Pa]	T [°C]	p_{baro} [Pa]	p [Pa]
0.103	0.49	0.05	33.54	52.53

The random errors for the measured variables are summarised in Tables 2.6 and 2.7, for the static and unsteady oscillatory test cases respectively. The random errors for the static data are determined over 1250 individual samples (t-value of 1.96) at each model incidence. The largest random errors across the static parameter space are presented. For the oscillatory motion, the random errors are calculated based on the RMS parameter value for each of the ten individual pitch cycles (t-value of 2.23) before the ensemble-averaging routine. Values for the oscillatory motion with the highest level of unsteadiness and stall penetration are given (See Section 2.3.3). Due to the variation of the chordwise pressure distribution, the largest calculated error from the pressure transducer array is given as a percentage of either the static mean or oscillatory RMS value.

CALCULATED VARIABLES

The Taylor Series Method for the propagation of uncertainty in measured variables to calculated variables, by means of a data reduction equation, was used to evaluate the uncertainty of the obtained blade section pressure coefficients. This method is described in detail by Coleman and Steele (2009). The random errors are assumed to be uncorrelated and the uncertainty of the calculated pressure coefficients are summarised in Tables 2.8 and 2.9, for the static and unsteady test cases respectively.

TABLE 2.6: Random error in static measured variables.

Configuration	Parameter	Aerofoil		
		NACA 63-619	AHH 19	AHH 32
Baseline	α [°]	0.001	0.001	0.001
	q [Pa]	0.18	0.19	0.14
	T [°C]	0.001	0.001	0.002
	p_{baro} [Pa]	0.12	0.12	0.12
	p [%]	0.24	1.42	0.69
Rough	α [°]	0.001	0.001	0.001
	q [Pa]	0.28	0.25	0.15
	T [°C]	0.001	0.001	0.001
	p_{baro} [Pa]	0.19	0.17	0.14
	p [%]	0.30	0.37	2.02

TABLE 2.7: Random error in unsteady measured variables.

Configuration	Parameter	Aerofoil		
		NACA 63-619	AHH 19	AHH 32
Baseline	α [°]	0.001	0.001	0.007
	q [Pa]	1.16	0.88	0.54
	T [°C]	0.005	0.009	0.008
	p_{baro} [Pa]	0.41	0.28	0.37
	p [%]	4.25	5.71	6.54
Rough	α [°]	0.001	0.001	0.003
	q [Pa]	1.00	1.42	0.65
	T [°C]	0.006	0.005	0.005
	p_{baro} [Pa]	0.18	0.27	0.26
	p [%]	4.81	2.08	4.53

TABLE 2.8: Total uncertainty in calculated static pressure coefficients.

Configuration	Parameter	Aerofoil		
		NACA 63-619	AHH 19	AHH 32
Baseline	C_p [%]	6.83	5.71	5.13
Rough	C_p [%]	6.42	5.52	5.59

TABLE 2.9: Total uncertainty in calculated unsteady pressure coefficients.

Configuration	Parameter	Aerofoil		
		NACA 63-619	AHH 19	AHH 32
Baseline	C_p [%]	16.77	19.41	14.22
Rough	C_p [%]	22.37	23.79	19.40

On first inspection, the larger magnitude of the calculated unsteady pressure coefficient uncertainties, presented in Table 2.9, appears to suggest that the measurement system is lacking precision. However, this arises due to the random nature of the measured unsteady flow behaviour and, as discussed in Section 2.5.2, the variation in the aerofoil loading is minimised by obtaining and averaging experimental measurements over multiple motion cycles.

2.5.2   TIME & CYCLE AVERAGING

STEADY DATA SAMPLE TIME AVERAGING

To investigate the effect of the sampling time on the aerofoil static loading, data from the NACA 63-619 test section was obtained for attached, separated and post-stall flow conditions over a 20 s run. As with static runs during the test campaign, the wind tunnel flow was allowed to settle before the measurements were acquired. The percentage error of the aerofoil loads for different sampling times, with reference to the 20 s average value, are shown in Figure 2.15. The aerofoil loads and moments are processed and calculated using the method described in Section 2.4.2.

The presented data show that the selected 5 s sample time is suitable for acquiring the experimental static data to within less than 0.05 % of the longer sample time average, for all static flow conditions investigated.

UNSTEADY DATA CYCLE AVERAGING

The stochastic nature of the dynamic stall process results in an observed cycle-to-cycle aerofoil load variation (Green and Galbraith, 1995; Wernert et al., 1996), thought to arise from random features present in the separated shear layer (Liiva and Davenport, 1969). Later particle image velocimetry results (Wernert et al., 1996), showing vortical structures in the separated shear layer varying between cycles, support this understanding. Averaging of the experimental dataset will account for the variations in the aerofoil cycle loading (Corke and Thomas, 2015), with McAlister et al. (1982) obtaining 50 pitch cycles of data, at 200 samples per cycle, for suitably converged results.

Again, using the NACA 63-619 test section and the data processing method outlined in Section 2.4.2, the aerofoil load behaviour is acquired over 50 pitch cycles, at 400 samples per cycle, for the oscillatory case with the largest angle of attack and level of unsteadiness ($k = 0.1$, $\alpha = 10° \pm 6°$). The root mean square error for the averaged cycles, with reference to the cycle loading averaged over 50 cycles, were calculated and the results of averaging over different numbers of pitch cycles are shown in Figure 2.16.

Although previous investigations have required 50 pitch cycles for convergence of results, this analysis is suggesting that an equivalent level of convergence is being

(A) Normal Force Coefficient

(B) Axial Force Coefficient

(C) Pitching Moment Coefficient

(D) Pressure Drag Coefficient
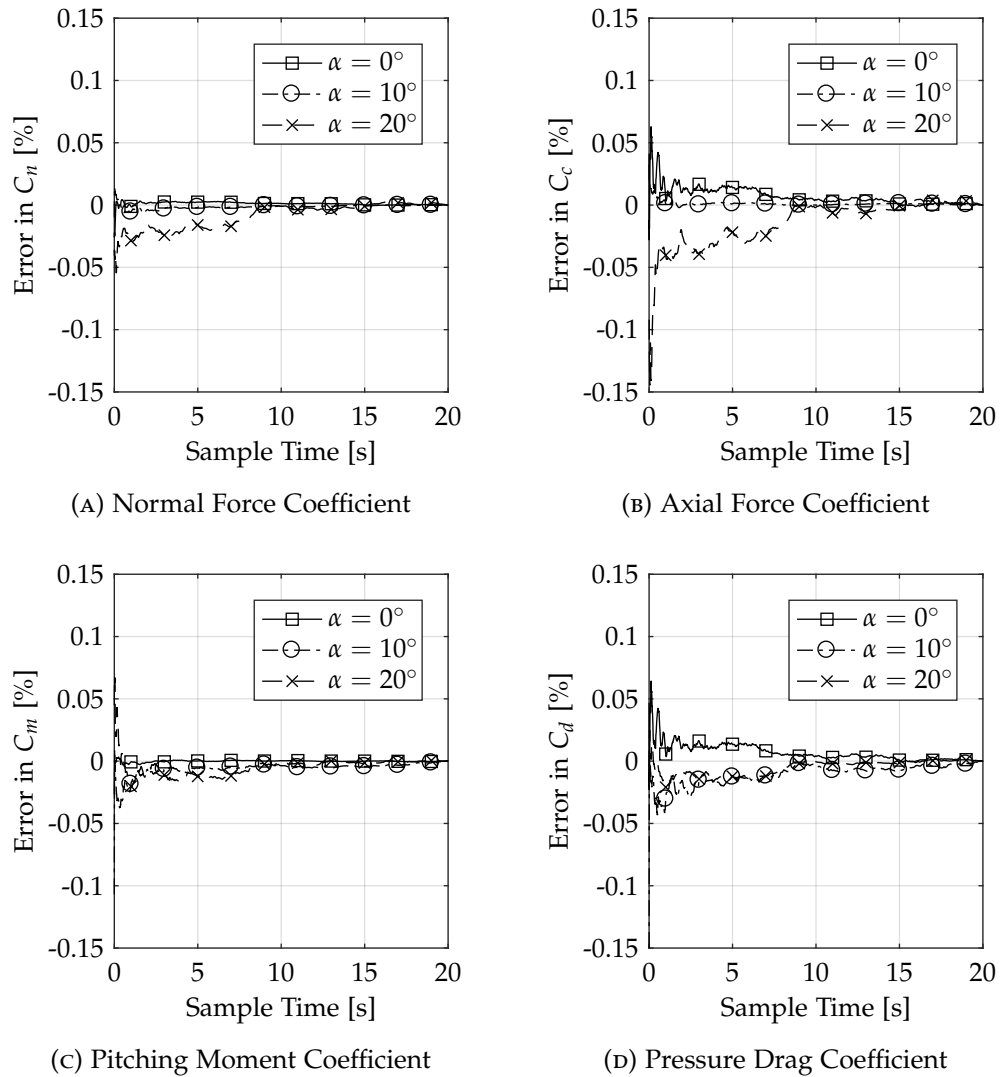
FIGURE 2.15: Effect of data acquisition sampling time on aerofoil static loading error.

achieved after only 5 cycles. Therefore, the decision to average unsteady data over 10 cycles is appropriate for obtaining the statistical trend of the aerofoil loading in the experimental datasets.

2.5.3 SURFACE PRESSURE DISCRETISATION

Using a finite number of pressure transducers in the aerofoil model results in the pressure distribution being discretised around the model chord. Although the pressure tapping locations are biased towards the leading edge, to capture the expected suction pressure peaks, an assessment has been made to quantify the discretisation error in the resultant aerofoil loading.

Pressure distributions are obtained from an XFOIL aerofoil analysis of the three aerofoil test sections for a static incidence of 5°, with Reynolds and Mach numbers matching the test conditions. The aerofoil loading cases are firstly calculated from the pressure distribution obtained from XFOIL, at 160 chordwise locations distributed
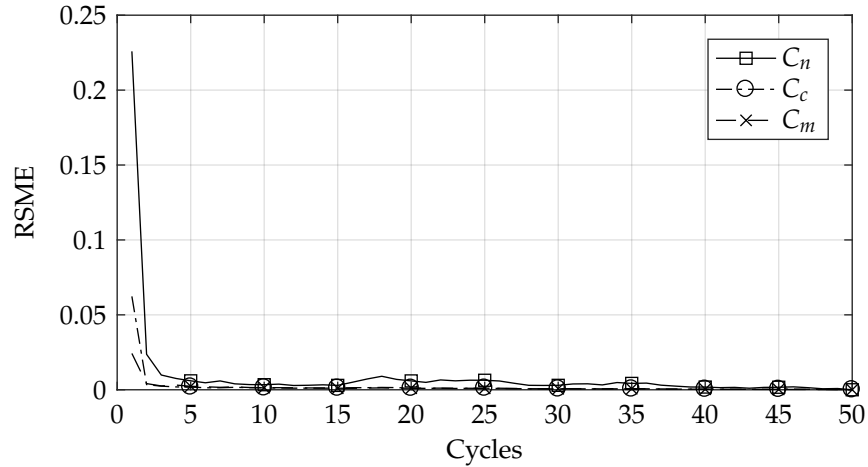
FIGURE 2.16: Oscillatory data cycle error.

TABLE 2.10: Summary of surface pressure discretisation error at 5° static incidence.

| Aerofoil | Parameter | Method | | Δ | Δ [%] |
		XFOIL	Experiment		
NACA 63-619	C_n	1.164	1.166	+0.002	+0.17
	C_c	0.094	0.101	+0.007	+7.45
	C_m	-0.133	-0.134	-0.001	-0.75
AHH 19	C_n	1.039	1.037	-0.002	-0.19
	C_c	0.082	0.090	+0.008	+9.76
	C_m	-0.127	-0.126	+0.001	+0.79
AHH 32	C_n	0.827	0.821	-0.006	-0.73
	C_c	0.060	0.066	+0.006	+10.00
	C_m	-0.092	-0.091	+0.001	+1.09

around the aerofoil surface, using the method described in Section 2.4.2 before applying linear interpolation to reduce the dataset to discrete pressure coefficient values at the model transducer locations and recalculating the loading cases. The absolute and percentage load changes attributed to discretising the aerofoil pressure distribution are summarised in Table 2.10.

The results of the analysis suggest that the selection of pressure transducer locations is capturing the variations in the pressure gradient around the aerofoil profile, particularly the normal force and pitching moment values. The variation between the continuous and discrete datasets, at a static incidence of 5° has been calculated to be less than 1 % for the normal force and pitching moment coefficients. The discretisation error in the axial force coefficient is larger, but still within 10 % of the initial calculated value. This is thought to be due to the majority of the axial force component being contributed by the pressures gradient near the aerofoil upper surface leading edge. This short analysis does not indicate that the pressure distributions obtained during testing are correct, but rather that the discretisation method used in this investigation is suitable.

2.5.4 DRAG MEASUREMENT

An aerofoil placed in a fluid flow field experiences a local stress distributed around the body – a pressure component acting normal to the surface and a tangential shear stress (Anderson, 2001). Although the pressure exerted on the aerofoil surface is approximately two orders greater than the shear stress, the tangential component contributes significantly to the total aerofoil drag, particularly at small angles of attack. As the measurement technique used in this work results in the measurement of the shear stress being neglected the impact on the calculated aerofoil characteristics will be discussed with reference to the aerofoil drag force.

The profile drag of a two-dimensional aerofoil is a combination of two constituent parts: the pressure drag (C_{d_p}); and the skin friction drag (C_{d_f}). The pressure drag, being measured by the model pressure transducers, arises from the pressure difference across the aerofoil body due to flow separation, while the skin friction drag is the force associated with maintaining the no-slip boundary condition on the aerofoil surface and acts mainly in the freestream direction. The skin friction drag does not change significantly with an increase in angle of attack and the pressure drag begins to dominate the viscous constituent and, therefore, the overall aerofoil drag profile. It is appropriate to assume that the pressure drag is a suitable approximation of the total drag at higher angles of attack (McAlister et al., 1978).

Although not being measured, the friction responsible for the generation of lift is still present on the model, but the aerofoil lift force and pitching moment are due mainly to the pressure distribution (Anderson, 2001). Therefore, the lift and moment are largely independent of the aerofoil shear stress and neglecting the tangential surface stress measurement is not detrimental to the determination of the aerofoil lift force and pitching moment.

The measurement of the full drag component of a static aerofoil is commonly measured in the wind tunnel using a downstream wake survey from a pressure rake and the drag calculated from a flow momentum balance method (Fuglsang et al., 1998a; Timmer and van Rooij, 2003). However, although the underlying theory is still valid, for separated static flows this approach has practical constraints due to the aerofoil wake not returning to parallel flow within the test section for the wake survey to be valid (Barlow et al., 1999). Although correction for this limitation is possible for static cases (Jones, 1936), for incidences beyond the attached flow region surface pressure measurements are used (Ramsay et al., 1995). For the measurement of the unsteady drag coefficient the time rate of change of the flow momentum within the control volume would need to be accounted for, alongside the flow recirculation region persisting far downstream from the aerofoil. Even when a wake rake measurement is available, the measurement of unsteady drag coefficients will revert to aerofoil surface pressure measurements (Fuglsang et al., 1998a) for the full angle of attack range. In summary, the method used in this investigation to measure the blade section drag

TABLE 2.11: Summary of defective pressure transducers and correction.

| Aerofoil | Transducer | | Interpolation Data Points |
	#	Position	
NACA 63-619	19	Upper LE	18, 20, 21, 22 and 23
	33	Lower TE	30, 31 and 32
AHH 19	4	Upper TE	2, 3, 5 and 6
	13	Upper LE	10, 11, 12 and 14
	15	Upper LE	No Correction Applied
AHH 32	29	Lower TE	27, 28, 30 and 31

coefficient will have a small deficiency at lower angles of attack, but this diminishes at higher incidences where the separated wake structure and associated pressure drag will dominate the drag profile. This is particularly true for the thicker aerofoil section with gross flow separations approaching the behaviour expected for a bluff body.

2.5.5 DEFECTIVE PRESSURE TRANSDUCERS

Although all the pressure transducers installed in the models were checked during and after installation, each model suffered from at least one defective sensor, thought to have been damaged during final assembly of the model. As the design of the model required the skins to be sealed, it was not possible to replace the unresponsive sensors. Two states have been identified on the unresponsive sensor data channels: a steady output voltage of 5 V suggests the output voltage is shorted to the PCB supply voltage; and a steady output voltage of 2.5 V suggests the silicon piezoresistive pressure sensor is damaged and not responding electrically to the applied pressure fluctuations.

The defective pressure channels were corrected using a shape-preserving piecewise cubic interpolation routine of neighbouring pressure measurements, as summarised in Table 2.11. The correction was applied in the time domain using the experimental pressure measurements before the datasets were filtered and averaged.

However, pressure transducer 15 on the AHH 19 aerofoil section was giving an inconsistent output believed to be caused by a loose or intermittent electrical connection on the sensor PCB. As it was not known when the connection was reliable, it was decided to leave this measurement uncorrected. To account for this uncertainty in the measured variable error analysis, the accuracy of this reading was set to 50 % FSS for determining the uncertainty in the calculated aerofoil forces.

As both of the faulty sensors closest to the leading edge (NACA 63-619 #19 and AHH 19 #15) are positioned ahead of the first roughness zigzag strip, for any analysis presented showing a difference between clean and rough configuration loading the error will be offset. On future models for investigations of this type it would be prudent to incorporate access to the model internal volume into the design or include

a duplexed pressure measurement array, particularly towards the leading edge of the aerofoil section, allowing replacement sensors to be installed or switched to.

2.6   EXPERIMENTAL METHOD JUSTIFICATION

Earlier in this thesis it was established that there is a requirement for obtaining datasets describing how tidal turbine blade sections behave under unsteady flow conditions, at test points representative of the deployed turbine state. Furthermore, it has also been highlighted how it is essential for the marine energy industry to be able to predict with greater confidence how this unsteady behaviour, hence the turbine performance, will be influenced by biofouling on the blade surface. To conclude this chapter, the reasoning for the key aspects of the experimental design and data handling, described in this chapter, will now be established.

Firstly, why use air as the working fluid instead of water? The testing of aerofoil sections always requires a balance of the flow parameters, model size and cost (Barlow et al., 1999), but the critical parameters influencing the unsteady aerofoil behaviour (See McCroskey, 1981) must be maintained at the scaled level. Ultimately, non-dimensional load and pitching moment coefficients obtained in the wind tunnel will recreate the expected hydrodynamic loads on the submerged tidal turbine.

It has been shown that the selected wind tunnel facility can reproduce the required test parameter range at a lower, but acceptable, Reynolds number. The limitations of a hydrodynamic towing tank for this type of testing arise when considering the combination of higher fluid viscosity, lower flow speed and a finite tank length. For a similarly sized model, testing in water would result in a marginally higher Reynolds number and an appropriate actuator could produce the required variation in angle of attack. However, due to the lower tank flow speed, at a moderate reduced frequency only a single cycle could be completed over the tank length. The unsteady aerofoil loads are highly time dependent, varying from cycle to cycle and therefore must be averaged over a number of consecutive motion cycles (Corke and Thomas, 2015). Additionally, testing in the wind tunnel removes a level of complexity involved with operating instrumentation in water and allows improved access to the test model.

The hydrodynamic loading on the turbine rotor results from a highly complex flow system. To investigate the unsteady loading at a blade section level, the system is simplified to an isolated two-dimensional aerofoil incident to a resultant flow. This method and the dynamic stall rig have played a key role over the last three decades in investigating helicopter dynamic stall (for example, Leishman, 1984; Green and Galbraith, 1995; Green et al., 2011), and latterly the dynamic stall onset of wind turbines (Sheng et al., 2006), and allows both the steady and unsteady loading in attached and separated flow regimes to be characterised. Ideally load cell or dynamic wake rake measurements would have been taken alongside the surface pressure measurements, but including the required instrumentation in the rig was not feasible.

The integration of surface pressures is a standard technique for investigating unsteady loads acting on an aerofoil (Ramsay et al., 1995; Fuglsang et al., 1998a) but also allow the pressure fluctuations and flow separation region to be identified.

Unlike wind turbines, where the distribution of leading edge roughness has been measured in the field (Ramsay et al., 1995; Corten and Veldkamp, 2001) and can therefore be replicated, no data is currently freely available describing the expected level and distribution of fouling on tidal turbines. A suitable approximation must be made using previous experimental studies (Orme et al., 2001; Walker et al., 2014) and commercial information supplied by the project industrial sponsor. The majority of biofouling investigations rely on the deployment of static sample plates in littoral waters – quite a different fouling environment to a turbine blade, with a significant surface pressure gradient, in a deeper tidal current. However, there is agreement that fouling on the tidal turbine blade exhibits as widely distributed microfouling and sparser zones of macrofouling (Miller and Macleod, 2016). Various methods are available for adding artificial roughness to a wind tunnel model (Barlow et al., 1999), but unlike a trip strip the surface fouling is required to have an adverse effect on the aerofoil performance. Investigations of wind turbine aerofoil leading edge contamination have used a range of roughness mediums including carborundum grit, and either cement or double-sided tape (Ramsay et al., 1995) as adhesive, and more recent investigations of surface roughness on tidal turbine blade sections have used bonded extruded volumes (Orme et al., 2001) or impregnated grease mixtures and contact cement (Walker et al., 2014). However, these approaches are either time intensive or removal would result in damage to the model surface – something to be avoided. Zigzag turbulator tape (van Rooij and Timmer, 2003) can be quickly and cleanly applied and removed from the model surface, remains adhered to the model throughout all the proposed test cases, and, most importantly, is a technique which provides a uniform, measurable and repeatable roughness distribution.

As has been detailed in Section 2.3, a test matrix has been constructed and is deemed to represent the operation of both the industrial project sponsors' turbine and that of a typical 1 MW turbine operating at a UK tidal site. The aerofoil pressure distribution, hence loads and moments, were obtained for three different blade sections during this research, and whilst there were limitations with the test facility, the acquired data is considered to provide a new insight into how tidal turbine blade sections will behave in an unsteady flow environment and the impact biofouling will have on this performance.

CHAPTER 3

IMPACT OF LIGHT SURFACE BIOFOULING ON BLADE SECTION LOADING

During the initial stages of marine biofouling, a widely distributed layer of moderate roughness is developed across the tidal turbine blade surface as aquatic organisms begin to colonise the available material substrate. Although the primary focus of this work is the impact of biofouling on the turbine blade section performance, a comparison can be drawn to other situations resulting in a roughened blade surface, such as: the standard of the blade surface manufacturing finish; degradation of the blade surface anti-fouling protective coating or substrate material during the turbine life cycle; or erosion of the blade material from sediment released during the seabed scouring process. This chapter will discuss the impact this level of surface roughness is likely to have on the performance of tidal turbine blade sections, using experimental aerofoil data for three different blade section geometries.

The previous chapter detailed the experimental methodology used in this investigation, including the reasoning behind the experimental approach and the determination of a suitable test matrix covering the range of parameters expected from a MW-scale tidal current turbine. A significant quantity of experimental datasets have been obtained from the wind tunnel test campaign – over 370 different combinations of test cases and configurations – resulting in the creation of a unique database describing the steady and unsteady behaviour of clean and fouled tidal turbine blade sections. However, it would not be reasonable to include all the available test data in this thesis. Therefore, specific test cases have been selected for each of the three blade sections tested to highlight the main findings and fluid mechanisms discussed.

This chapter of the thesis begins with a review of the progress made in understanding unsteady aerofoil loading, followed by the main presentation and analysis of the investigation experimental findings. Static, unsteady and transient load cases are all considered. To complete the chapter, a brief analysis of the blade section torsional pitching moments and damping is presented. The main emphasis throughout the ana-

lysis and discussion of the results are the influence of the blade motion of the loading, compared to the static case, and the influence light biofouling surface roughness has on this process.

3.1   A REVIEW OF UNSTEADY TWO-DIMENSIONAL AEROFOIL TESTS

The early work of Kramer (1932) was one of the first investigations to identify the fluid phenomena associated with unsteady aerofoil behaviour, and that aircraft wing loading in steady flow varies considerably under the influence of wind gusts or sudden aircraft manoeuvres. However, it wasn't until the late 1960s, when retreating-blade stall was found to be limiting helicopter performance in high speed forward flight and high load manoeuvres, that interest in unsteady blade section loading was renewed (McCroskey and Fisher Jr, 1972; Tarzanin Jr, 1972). Over the next two decades significant progress was made in advancing the understanding of the underlying fluid features of: the aerofoil leading edge pressure gradient (Ericsson, 1967; Carta, 1971; Beddoes, 1978); unsteady boundary layer effects (McCroskey, 1977); the role of vortex shedding (Ham, 1968); and the onset of dynamic stall for aerofoils exhibiting trailing edge stall mechanisms (McCroskey et al., 1976, 1981). McAlister et al. (1978), McCroskey et al. (1981) and Leishman (1990) present the evaluation of unsteady performance of helicopter rotor blade aerofoil families over a range of operating conditions.

With the development of wind turbines in the 1980s, it was recognised that the turbulent operating environment would increase the dynamic loads acting on the wind turbine rotor blades (Butterfield et al., 1991), which are thicker and operate at a lower Mach number compared to a helicopter rotor, but also the need to consider the effects of leading edge roughness on the blade section performance (Somers, 2005). The leading wind energy research centres (NREL, Delft and Risø) have investigated the effects of leading edge roughness on aerofoil performance, for both static and selected unsteady cases. Application of leading edge grit roughness to the S809 aerofoil (Ramsay et al., 1995), with 21 % thickness, resulted in a 16 % decrease and 41 % increase in the static maximum lift and minimum drag coefficients respectively, and an increase of between 4 % and 86 % in the unsteady maximum lift coefficient, compared to the static case. The equivalent values for the S814 aerofoil (Janiszewska et al., 1996), with 24 % thickness, were a static lift increase and drag decrease of 16 % and 67 % respectively, and an unsteady maximum lift coefficient increase of between 10 % and 55 % compared to the static case. Similar results were obtained for the effects of leading edge roughness on a selection of NACA (Hoffman et al., 1996; Fuglsang et al., 1998b), Risø (Fuglsang et al., 1998a) and Delft (van Rooij and Timmer, 2003; Timmer and Schaffarczyk, 2004) wind turbine blade sections. An analysis of aerofoil performance at a range of Reynolds numbers from 3×10^6 to 15×10^6 has shown that, for both clean and tripped aerofoils, the maximum lift coefficient increases by almost 30 % over the flow range, and the minimum drag coeffceint decreases by 22 % (Pires

et al., 2016).

A design approach for obtaining an aerofoil section with improved insensitivity to blade roughness has been described by van Rooij and Timmer (2003) and Somers (2005). Although the blade sections referenced here are designed with the intention of minimising the effects of roughness, or erosion, at the leading edge, it is evident that a loss in the overall aerofoil performance is still being obtained. This is one of many technological challenges which will have to be addressed if tidal turbines blades are going to perform to a required level throughout the life of the device.

Despite being a key area of interest to the marine energy industry, there have been no investigations identified in the available literature into the effect widely distributed marine biofouling will have on the unsteady hydrodynamic performance of thicker tidal turbine blade sections. However, Walker et al. (2014) have investigated the static performance of a NACA 63-618 tidal turbine blade section with varying levels of simulated marine biofouling roughness, albeit at a lower Reynolds number of 5×10^5, with the maximum lift coefficient decreasing by an average of 11 % for all three roughness cases ($0.008c$ leading edge only, $0.008c$ full surface and $0.0019c$ full surface) with the minimum drag coefficient increasing by 49 % for the first two cases and 153 % for the third. The results presented in the same investigation for a fouled turbine scale model test are discussed in Chapter 5. It remains that an extremely limited set of both static and unsteady performance data are available for tidal turbine blade sections, particularly in a biofouled state, and the results presented in this chapter will help to address this identified gap in knowledge.

3.2 TEST CASE DESCRIPTORS

Due to the large number of results in the experimental database it is not possible to present results from every test case in this thesis. Therefore, specific test cases of interest have been selected for analysis and presentation.

To differentiate between the two aerofoil surface finish configurations the following test case descriptors are used throughout this chapter.

- *Baseline*: Aerodynamically clean aerofoil test section.

- *Rough*: Baseline aerofoil test section, but with the addition of zigzag tape widely distributed roughness as described in Section 2.2.3.

For analysis of the steady data, all test points are included, but restricted to cover the range of the tidal turbine operational envelope. The static angle of attack range in the presentation of the test data is generally from −10° to 25°. The transient ramp data is treated similarly, but with the most appropriate pitch rate and ramp arc for the analysis being selected.

The oscillatory datasets describe the turbine behaviour during normal operation

Table 3.1: Summary of unsteady test cases selected for data analysis presentation.

Aerofoil	Unsteady Oscillatory Run Numbers	
	Typical Test Case	Limiting Test Case
NACA 63-619	$k = 0.05, \alpha = 5° \pm 4°$	$k = 0.1, \alpha = 10° \pm 6°$
	20010172 (Baseline) 20111021 (Rough)	20010303 (Baseline) 20111151 (Rough)
AHH 19	$k = 0.05, \alpha = 5° \pm 4°$	$k = 0.1, \alpha = 10° \pm 6°$
	21012782 (Baseline) 21113272 (Rough)	21012673 (Baseline) 21113402 (Rough)
AHH 32	$k = 0.1, \alpha = 8° \pm 2°$	$k = 0.2, \alpha = 12° \pm 10°$
	22011551 (Baseline) 22112151 (Rough)	22011661 (Baseline) 22112461 (Rough)

during energy production and, as such, forms the majority of the experimental database. Section 2.3.4 describes the probability variation of events occurring across the parameter space, with the blade section incidence shown in Figure 2.13 and the reduced frequency in Figure 2.14. For highlighting specific aerofoil loading cases, two statistically significant instances are of interest: a typical loading case, relating to the turbine conditions which have the highest probability of occurring; and a limiting case with the highest stall penetration and unsteadiness. The baseline and corresponding roughened cases are selected. If trends in the data results are being shown then all appropriate results from the database are used, not just from the the specific loading cases. The selected oscillatory test cases are summarised in Table 3.1.

All data presented in this results chapter, and those following, are either: time-averaged for the steady cases; ensemble-averaged over 10 cycles for the oscillatory cases; and event-averaged over 5 repeats for the transient ramp cases. In some cases the results figures have had the data density reduced to improve the clarity of the presented data, but maintaining the salient flow and loading features being discussed. Further to this, the dataset line markers in the results figure are solely to distinguish between the different test cases presented and are not indicative of the full set of points in the dataset – there will be data points between the line markers.

3.3   BLADE SECTION STATIC (STEADY STATE) LOADING

The aerodynamic performance analysis of the three test aerofoils will begin by considering the static blade section loading, in both the clean baseline and fouled rough configurations. As the NACA 63-619 and AHH 19 sections are located at a similar outboard radial position on the turbine blade, and the geometries share a likeness, they will be considered together, followed by the thicker inboard AHH 32 blade section.

Static performance data is generally readily available for non-proprietary published

aerofoil sections, including from NACA (Abbott and von Doenhoff, 1959), NREL (Tangler and Somers, 1995), Risø (Fuglsang and Bak, 2004) and Delft (Timmer and van Rooij, 2003), and is easier to obtain experimentally in a wind tunnel facility as no aerofoil pitch actuation system is required – unlike unsteady aerofoil testing. The design and performance analysis of tidal turbines relies on high quality steady aerofoil performance data employed in BEMT-based computational methods and, if required, dynamic stall models with coefficients derived predominately from the static aerofoil datasets. The static aerofoil data in this section is presented in absolute terms and the effects of surface roughness on the blade section characteristics are given as percentage changes from the baseline.

The static aerofoil loading characteristics provide an initial assessment of the blade section performance and are suitable for determining if the intent of the blade section design is met. All the presented results are for a test Reynolds number of 1.5×10^6.

3.3.1   AEROFOIL FORCES & PRESSURE DISTRIBUTION

OUTBOARD BLADE SECTIONS: NACA 63-619 & AHH 19

The results for the outboard blade section static loading cases are presented in Figures 3.1 and 3.2 in coefficient form as a function of the aerofoil incidence, for the NACA 63-619 and AHH 19 aerofoils respectively. Included in the figures are the chordwise pressure coefficient distribution at incremental angles of attack ranging from −10° to 25°. For clarity in the presented figures, the x-axis for each pressure coefficient distribution has been shifted by an arbitrary offset equal to 0.1α.

Starting with the NACA 63-619 blade section, the baseline results show a linear lift curve slope up to a clearly defined static stall at 10.2°. A peak normal force coefficient of 1.26 is being achieved. The addition of surface roughness delays the static stall by just over 2° to a value of 12.5° and reduces the maximum normal force coefficient to 1.07, a reduction of 15.6 %. The non-linear region of flow separation prior to stall begins at a slightly lower angle of attack, as the presence of the roughness decreases the suction pressure on the aerofoil upper surface. However, beyond stall there is no distinguishable differences in the loading cases. The effect of surface roughness on the blade section drag force is to increase the minimum pressure drag coefficient from 0.004 to 0.011, an increase of 175 %.

As expected, the AHH 19 blade section exhibits a similar loading behaviour to the NACA 63-619 due to having similar geometry features – both are approximately 19 % thick with a higher level of camber and larger leading edge radii. Again, the baseline stall is clearly defined at an angle of attack of 13.1° and peak normal force coefficient of 1.23. Roughness delays the stall by almost 1.5° to an incidence of 14.5° and decreases the normal force to 1.07 – a decrease of 12.6 %. The minimum drag coefficient is increased by three times from a value of 0.003 to 0.012. However, the

(A) Normal Force Coefficient

(B) Drag Force Coefficient

(C) Pressure Coefficient Distributions
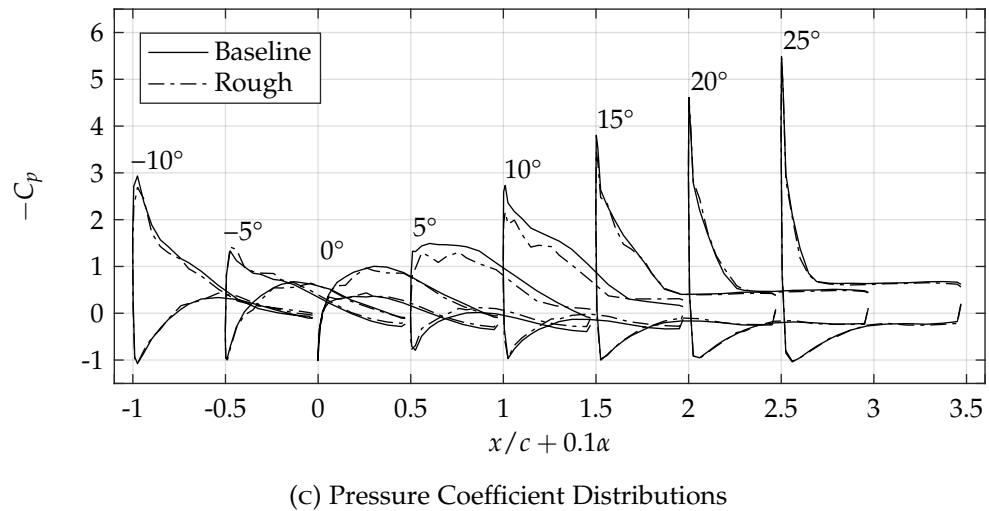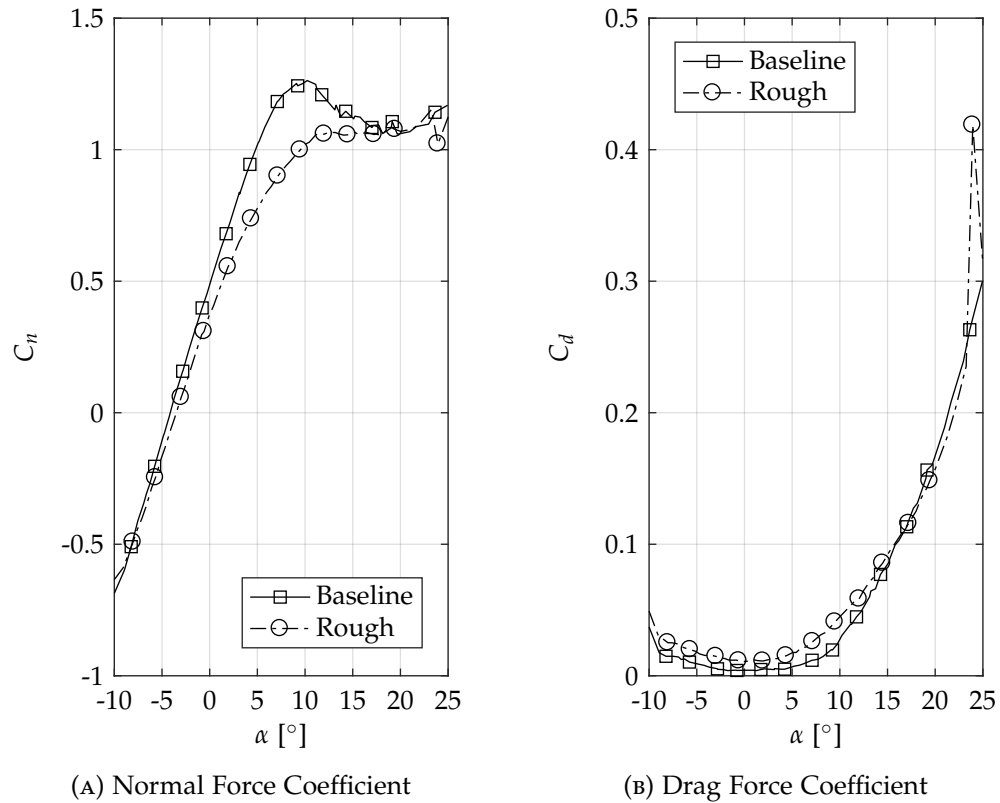
FIGURE 3.1: NACA 63-619 static force coefficients and chordwise pressure coefficient distribution for baseline and rough blade section configurations.

drag measurement for the AHH 19 blade section does have an increased uncertainty compared to the other two test sections.

The variation in the blade section loading is due to changes in the pressure around the aerofoil and is being modified by the zigzag roughness strips applied to the wind tunnel models. Any fouling on the turbine blade surface will act to accelerate the flow separation process, as it can be assumed that the flow over the blade is turbulent and the transition from laminar flow has occurred within a short distance of the blade leading edge. The effect of the roughness promoting further flow separation is most

(A) Normal Force Coefficient

(B) Drag Force Coefficient

(C) Pressure Coefficient Distributions
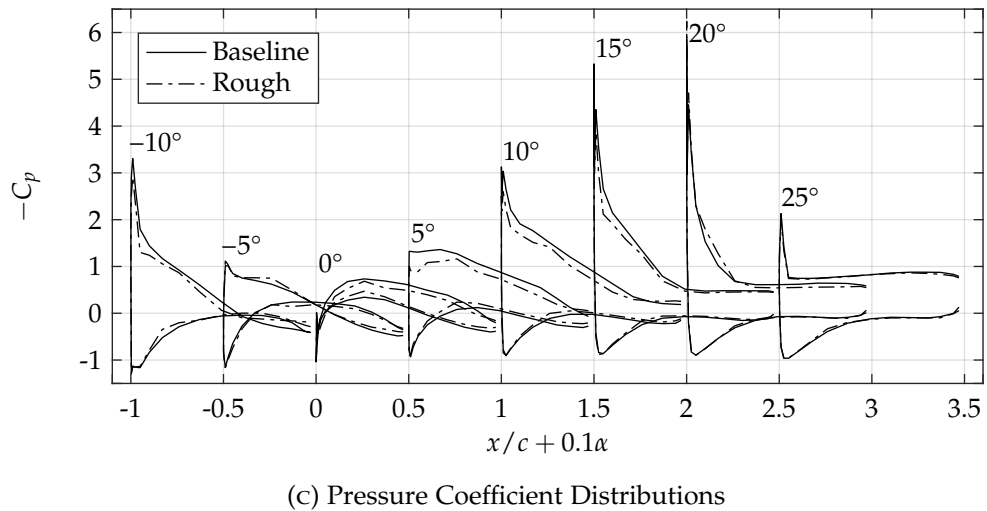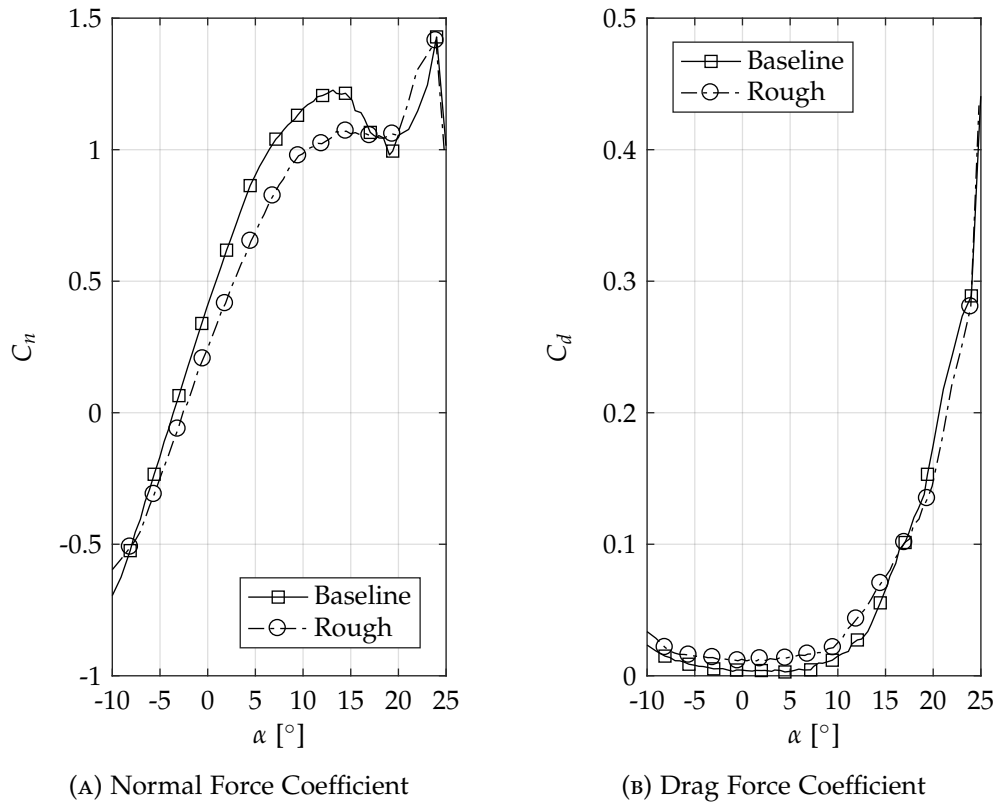
FIGURE 3.2: AHH 19 static force coefficients and chordwise pressure coefficient distribution for baseline and rough blade section configurations.

evident in the pressure distributions on the aerofoil suction side for attached flow, where the local pressure is reduced. Differences between the baseline and rough pressure distributions decrease towards the trailing edge and with increasing angle of attack. The decrease in aerofoil loading due to roughness is dependent on the the angle of attack, hence has a dependency on the chordwise location of the flow separation point. As the flow becomes fully separated, starting from the trailing edge, the influence of the surface roughness is diminished, but the leading edge pressure peak is maintained at higher angles of attack. This is likely to be due to having no

roughness applied to the front 5 % of the aerofoil model. Local pressure variations for the rough configuration, particular evident in Figure 3.1c over the attached flow region, are due to the proximity of the zigzag tape edge to the pressure transducer measurement tapping.

INBOARD BLADE SECTION: AHH 32

The results for the inboard blade section static loading cases are shown in Figure 3.3, in the same format as those for the two outboard blade sections.

For the baseline configuration the point of static stall is identified at 11.6°, where a peak normal force coefficient of 0.99 is achieved. The addition of surface roughness changes the profile of the normal loading significantly and introduces a large kink to the curve and it becomes difficult to detect the rough configuration stall from the load curves. From inspection of the static pressure distribution, to identify the point where the separation point remains fixed for increasing incidence, the roughness is delaying stall by almost 10° to 21.1°. The corresponding peak normal force coefficient reduces to 0.84 – a decrease of 15.1 %. A small deviation in the pitching moment behaviour can also be identified at this incidence. The surface roughness results in the minimum pressure drag coefficient almost doubling from 0.007 to 0.015, an increase of just over 115 %.

In the rough configuration the force and pressure results are indicating that the flow on both the upper and lower aerofoil surfaces is becoming grossly separated. The first roughness strip is positioned at $x/c = 0.05$ so is forcing early transition. As described in more detail by van Rooij and Timmer (2003), the surface roughness is promoting early turbulent flow separation which effectively reduces the aerofoil camber, hence the gross loss of lift, and the observed behaviour is approaching that expected from an aerodynamically bluff body – a state where the drag force is dominated by pressure losses in the wake and the lift and drag forces are on a comparable order (Flay, 2013). The influence of the loading kink under fouled conditions can be reduced by removing aft loading on the aerofoil, but would significantly reduce the lift in the clean baseline configuration (van Rooij and Timmer, 2003).

STATIC STALL MECHANISM

All three test sections are exhibiting behaviour to suggest the flow separation is of the trailing edge stall class, as identified from the gradual transition into stall and a rounded peak in the normal force coefficient curve (McCullough and Gault, 1951). Inspection of the pressure distributions in the trailing edge region supports this reasoning by displaying a change in suction pressure over the incidence range around the static stall angle.

(A) Normal Force Coefficient

(B) Drag Force Coefficient

(C) Pressure Coefficient Distributions
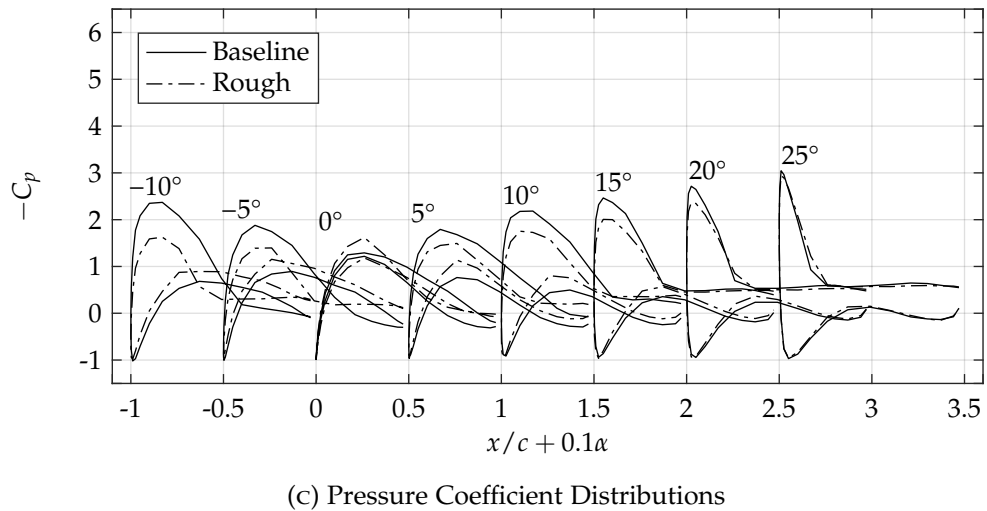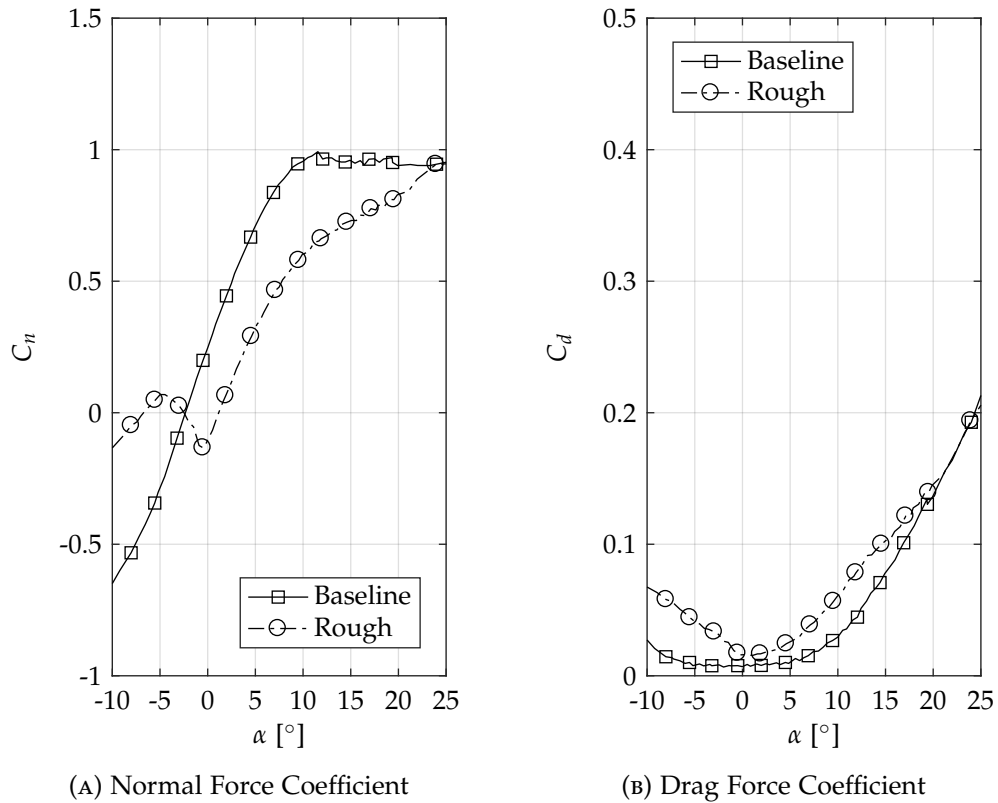
FIGURE 3.3: AHH 32 static force coefficients and chordwise pressure coefficient distribution for baseline and rough blade section configurations.

The NACA 63-619, in the rough configuration, and the AHH 19, in both configurations, are displaying signs of leading edge separation at higher angles of attack, as seen in Figures 3.1 and 3.2. Approaching an incidence of 25° a sudden drop in normal force coefficient and corresponding increase in drag coefficient indicates a collapse of the negative pressure peak the aerofoil leading edge, indicating that complete flow separation over the aerofoil chord has occurred. This is confirmed by inspection of the measured pressure distributions at these incidences. Although beyond the typical operating envelope of the turbine, leading edge separation has been linked to multiple
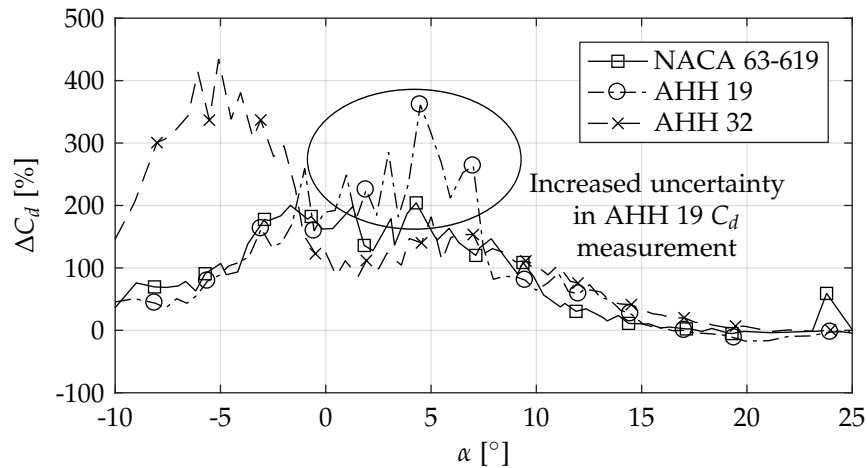
FIGURE 3.4: Percentage change of static drag coefficient due to light surface biofouling for each of the three tidal turbine blade sections.

stall levels on wind turbine rotors (Corten and Veldkamp, 2001) with the aerofoil angle of attack at the point of leading edge separation correlating with the aerofoil nose thickness (Timmer and van Rooij, 2003).

3.3.2 DRAG COEFFICIENT INCREASE

The increase in the blade section static pressure drag coefficient due to surface fouling is shown in Figure 3.4. Results for each of the three test sections are presented over the expected angle of attack range of the turbine during normal operation. The variation is given in terms of a percentage change, at each incidence, from the clean baseline case. The uncertainty in the AHH 19 drag measurement between 0° and 10° is highlighted. As the tested blade sections are thick and highly cambered, the measured drag coefficients are not symmetrical.

For all three blade sections a large increase in the drag coefficient is identified with a strong dependency on the local blade section angle of attack. The largest increases for the outboard sections are observed over the attached flow region for angles of attack, between −5° and 10°, while the largest increase for the inboard blade section is seen at negative incidences, where a region of massively separated flow has been previously identified.

Taking each blade section in turn, a peak drag increase of approximately 180 % is seen for the NACA 63-619 aerofoil, at around 3° angle of attack, increasing to just over 200 % at approximately the same incidence for the AHH 19 aerofoil. This value takes the underprediction of drag in this blade section dataset into account. A peak drag increase of 400 % is identified at an incidence of −5° for the AHH 32 blade section. Across the attached flow region, an average estimate of the drag increase would be 150 %. A similar trend beyond this region is observed for all three blade sections, with the measured drag increase converging to within 20 % of the baseline values by 13°,
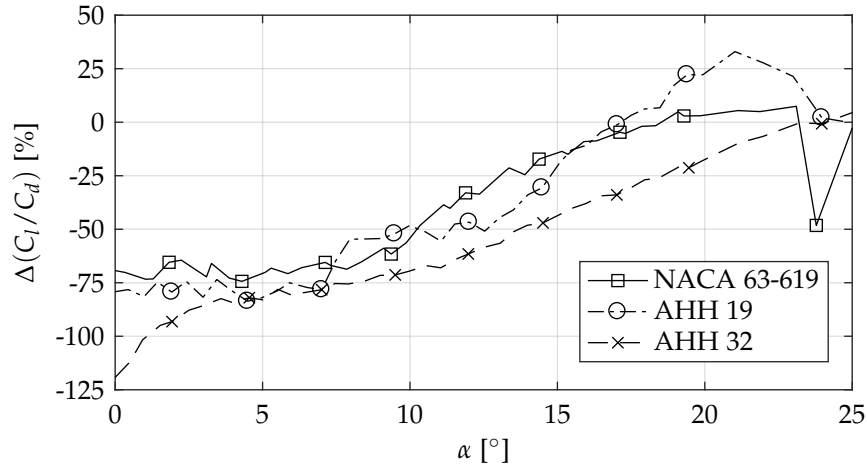
FIGURE 3.5: Percentage change of static lift-to-drag ratio due to light surface biofouling for each of the three tidal turbine blade sections.

15° and 17° angle of attack, for the three blade sections respectively. These findings agree with the aerofoil sensitivity to roughness decreasing as the region of separated flow develops on the aerofoil surface.

3.3.3 LIFT-TO-DRAG RATIO

The calculated change in the static blade section lift-to-drag ratio, for the three blade sections, is shown in Figure 3.5. Again, the ratio increment is given as a percentage change from the corresponding baseline aerofoil configuration, as a function of the aerofoil static angle of attack from 0° to 25°. For reference, Figure 3.6 presents the aerofoil drag polars (C_l vs. C_d) in the left hand figure column, and the aerofoil absolute lift-to-drag ratios (C_l/C_d) with respect to angle of attack in the right hand figure column.

The variation in the lift-to-drag ratio due to the surface roughness can be approximated by a first-order relationship across the majority of the turbine angle of attack operating range. This applies to all three blade sections, with the largest changes occurring at aerofoil incidences below 10°. The tidal turbine performance and efficiency is obtained from achieving a high lift-to-drag ratio from the turbine rotor. This set of results is suggesting that surface roughness on the turbine blade is reducing the lift-to-drag ratio of the blade sections to the order of 50 % to 75 %, at the most likely operating conditions, which would be expected to result in significant turbine performance losses. This is investigated further in Chapter 5.

3.3.4 SUMMARY OF STATIC BLADE SECTION LOADING PARAMETERS

An overview of the static aerodynamic parameters, for both the baseline and rough configuration, are presented in Table 3.2 for the NACA 63-619 and AHH 19 aerofoils,
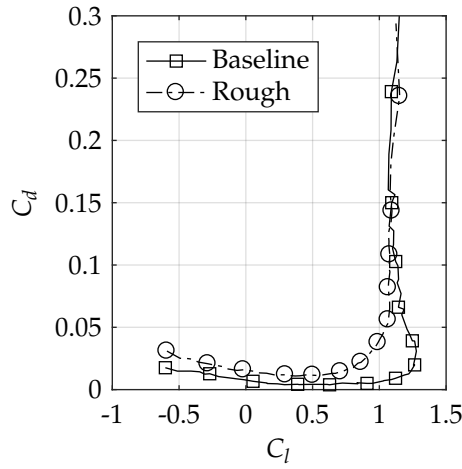
(A) NACA 63-619 Drag Polar
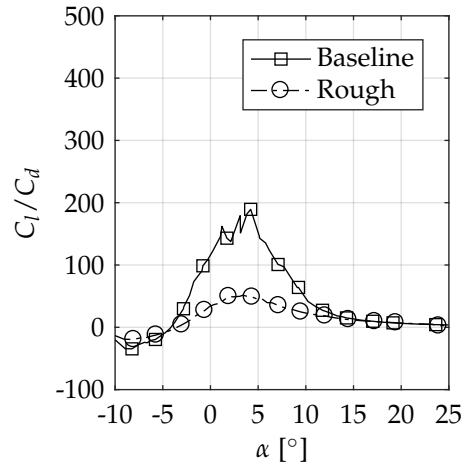
(B) NACA 63-619 Lift-to-Drag Ratio
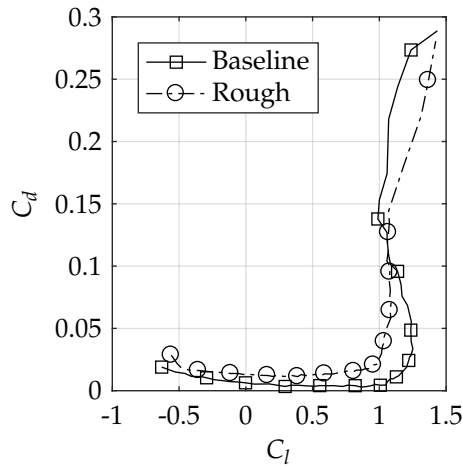
(C) AHH 19 Drag Polar
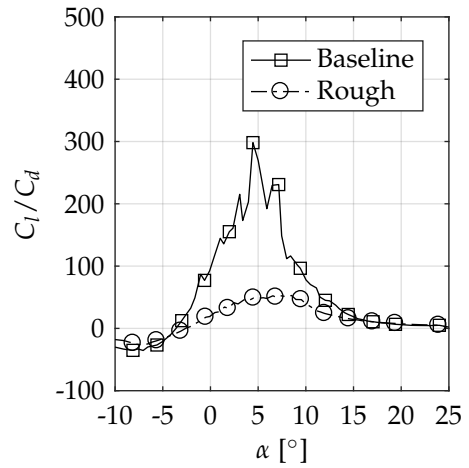
(D) AHH 19 Lift-to-Drag Ratio
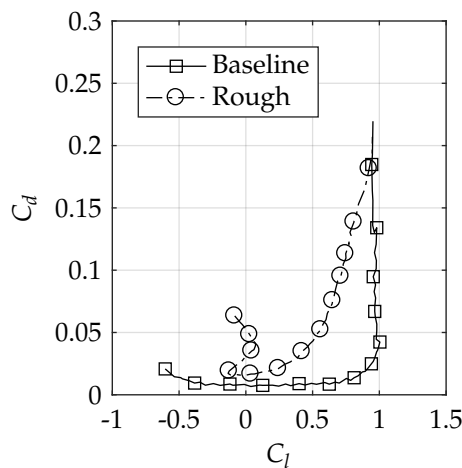
(E) AHH 32 Drag Polar
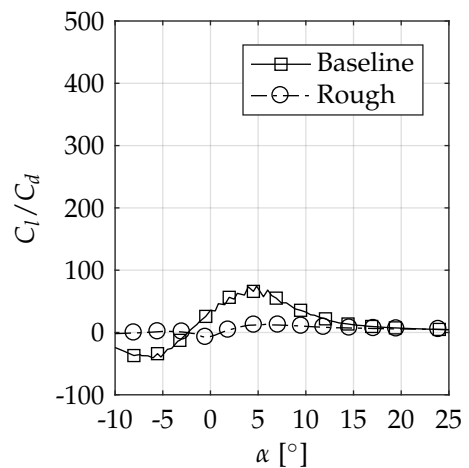
(F) AHH 32 Lift-to-Drag Ratio

FIGURE 3.6: Static lift and drag coefficient relationships for baseline and rough aerofoil datasets.

TABLE 3.2: Summary of outboard static blade section loading parameters.

Parameter	NACA 63-619			AHH 19		
	Baseline	Rough	Δ	Baseline	Rough	Δ
$C_{n_{\max}}$ [–]	1.26	1.07	-0.19	1.23	1.07	-0.16
α_{ss} [°]	10.2	12.5	+2.3	13.1	14.5	+1.4
C_{n_α} [1/rad]	6.540	5.607	-0.933	6.122	5.354	-0.768
$\alpha_{C_n=0}$ [°]	-4.1	-3.5	+0.6	-3.6	-2.6	+1.0
$C_{n_{\alpha=0}}$ [–]	0.49	0.36	-0.13	0.40	0.24	-0.16
C_{d_0} [–]	0.004	0.011	+0.007	0.003	0.011	+0.008
$\alpha_{C_d=0}$ [°]	0.3	0.4	+0.1	3.3	0.5	-2.8
$(C_l/C_d)_{\max}$ [–]	170	50	-120	245	52	-193

TABLE 3.3: Summary of inboard static blade section loading parameters.

Parameter	AHH 32		
	Baseline	Rough	Δ
$C_{n_{\max}}$ [–]	0.99	0.84	-0.15
α_{ss} [°]	11.6	21.1	+9.5
C_{n_α} [1/rad]	5.899	5.232	-0.667
$\alpha_{C_n=0}$ [°]	-2.3	1.2	+3.5
$C_{n_{\alpha=0}}$ [–]	0.24	-0.10	-0.34
C_{d_0} [–]	0.007	0.015	+0.008
$\alpha_{C_d=0}$ [°]	-1.2	0.5	+1.7
$(C_l/C_d)_{\max}$ [–]	68	13	-55

and Table 3.3 for the AHH 32 aerofoil. The reported values have taken the local variation of the parameters into account and, in some cases, a point which best describes the data has been selected. The sensitivity of the tested blade sections to light surface biofouling has also been quantified under static flow conditions.

It is expected that with an increase in the surface roughness level the peak normal force will decrease and the minimum drag coefficient will increase with a further, but smaller, delay to the static stall angle, as demonstrated in the results of Walker et al. (2014) for a NACA 63-618 aerofoil.

COMMENT ON AEROFOIL DESIGN APPROACH

The results presented in this section comparing the baseline and rough aerofoil loading and aerodynamic parameters raise an interesting question concerning the blade section design approach. The process to design a tidal turbine blade section is a compromise between producing a high performance aerofoil and ensuring an improved insensitivity to surface roughness arising from marine biofouling. However, ensuring improved performance in a roughened state is generally at the expense of

performance at the clean baseline design condition (van Rooij and Timmer, 2003). If it is accepted that the deployed tidal turbine blades will become fouled during their life cycle, perhaps it would be beneficial to move the blade design point to a lightly fouled state. This would optimise the turbine performance for a blade condition expected over a larger portion of the life cycle and may reduce the performance loss which might otherwise be experienced during operation from the current design point to a fouled state. Consideration should be made to the marine conditions the turbine is most likely to encounter and not necessarily design for the optimal clean blade configuration. However, a thorough understanding of the expected level and distribution of the blade fouling throughout the turbine life cycle would be required for this design process.

Although it is beyond the scope of this thesis to critique the design of the propriet-ary AHH aerofoils, the available datasets for the two outboard blade sections allow the potential performance benefits of using a blade section designed for optimised tidal turbine applications over a general aerospace aerofoil to be briefly highlighted. In the baseline configuration, the AHH 19 aerofoil maintains attached flow for a wider range of the turbine operating envelope, compared to the NACA 63-619, and demonstrates a more gradual stall behaviour. This leads to an increased static stall angle, but with only a minimal penalty in the peak normal blade section loading. In addition, the peak performance point ($(C_l/C_d)_{\mathrm{max}}$) is centred in the middle of the blade section angle of attack range (See Figure 2.12) instead of at a lower aerofoil incidence, suggesting a more optimal performance is achieved over a wider range of the turbine operating envelope. By designing for improved roughness sensitivity, the performance advantage remains by achieving an equivalent normal aerofoil loading, but at a higher angle of attack, and maintaining the peak lift-to-drag distribution around the expected mean blade section incidence.

3.3.5 COMPARISON WITH SIMILAR AEROFOIL SECTIONS

To complete this section the static experimental data is compared to published data for NACA aerofoils and wind turbine blade sections at an appropriate Reynolds number, in both clean and roughened configurations. The comparison data is also obtained from wind tunnel testing, not from CFD analysis. An overview of the selected investigations are summarised in Table 3.4 and the lift coefficient is presented in Figures 3.7 and 3.8 for the outboard and inboard blade sections respectively.

Validation of the test aerofoil static aerodynamic parameters are presented in Appendix D, using published NACA data (Abbott and von Doenhoff, 1959) for the NACA 63-619 blade section and AHH supplied CFD datasets for the the two AHH blade sections.

TABLE 3.4: Details of steady wind tunnel investigations on thicker aerofoil sections with surface roughness (SS: Suction Side, PS: Pressure Side, ZZ: Zigzag).

Aerofoil	*Re*	Roughness	Source
NACA 63-618	1×10^6	0.2 mm Cement Full Aerofoil	Walker et al. (2014)
NREL S809	1.5×10^6	0.8 mm Grit Leading Edge	Ramsay et al. (1995)
Risø-A1-18	1.6×10^6	0.35 mm ZZ Tape 5 % SS, 10 % PS	Fuglsang et al. (2004)
NACA 63-430	1.6×10^6	0.35 mm ZZ Tape 5 % SS, 10 % PS	Fuglsang et al. (1998b)
FFA-W3-301	1.6×10^6	0.5 mm ZZ Tape 5 % SS, 10 % PS	Fuglsang et al. (1998b)
DU 97-W-300	3×10^6	0.35 mm ZZ Tape 5 % SS, 20 % PS	Timmer et al. (2004)
DU 00-W-350	3×10^6	0.5 mm Bump Tape 2 % SS, 10 % PS	van Rooij et al. (2003)

(A) Baseline Configuration

(B) Rough Configuration
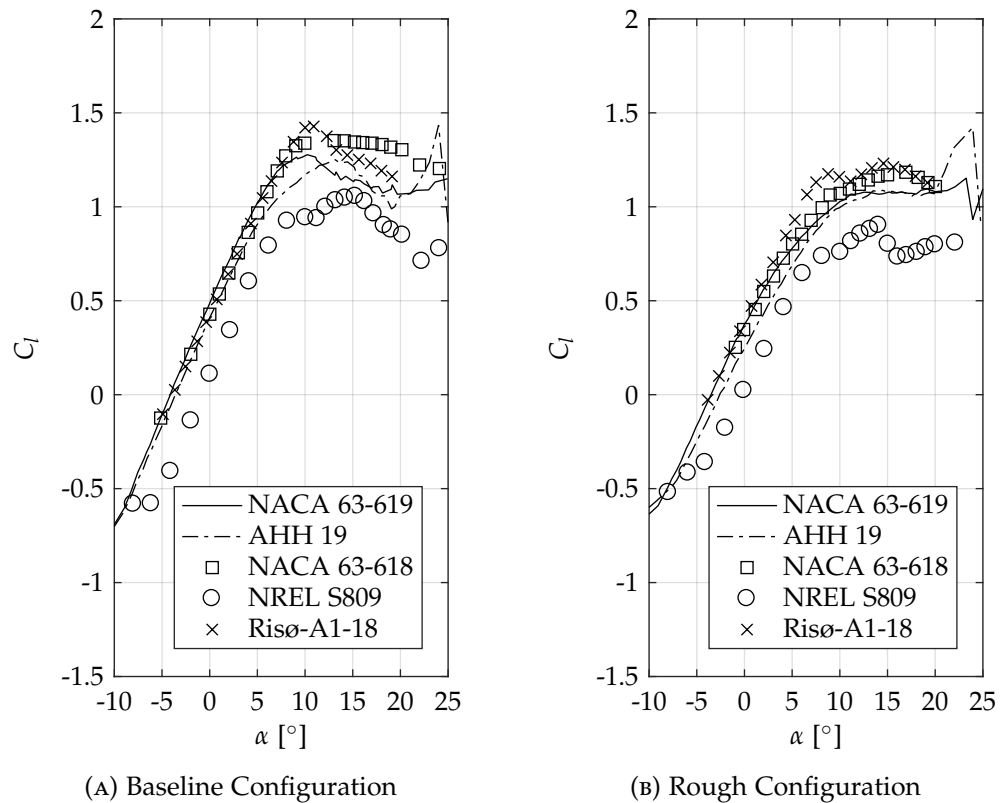
FIGURE 3.7: Comparison of inboard blade section static lift coefficients with published data for clean and rough configurations. Test details for the published data are provided in Table 3.4.

(A) Baseline Configuration   (B) Rough Configuration
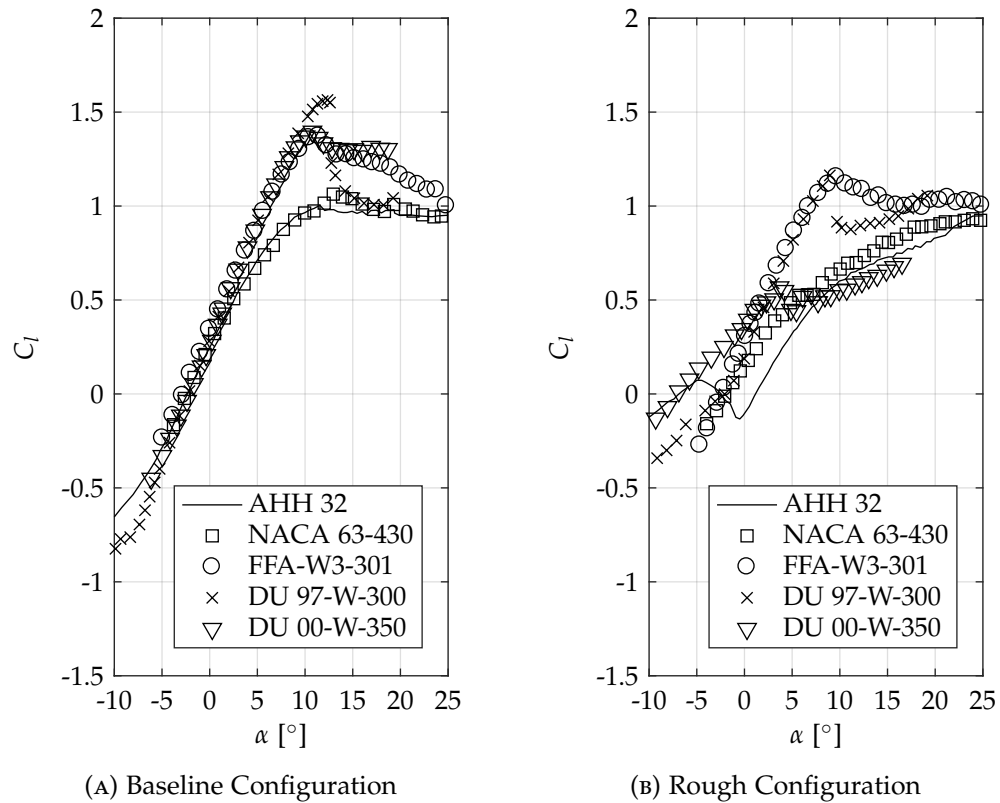
FIGURE 3.8: Comparison of outboard blade section static lift coefficients with published data for clean and rough configurations. Test details for the published data are provided in Table 3.4.

3.4 BLADE SECTION DYNAMIC (UNSTEADY) LOADING

Having described the static behaviour of the three tidal turbine blade sections, the unsteady blade loading will now be discussed. The results presented in this section demonstrate the blade section response to the unsteady flow field the turbine blades will encounter during operation. It is known that the magnitude and cycle variation of the blade section unsteady loading will depend on the blade section reduced frequency, determined from the turbine rotational speed, and the level of stall penetration, which is dependent on the unsteadiness of the flow field. For each aerofoil comprising the turbine blade, it is imperative to be able to evaluate the load overshoot, with reference to the equivalent static loading, but also be able to estimate the equivalent cycle loading when the blade is in a fouled state. In addition, the unsteady database created from the described test campaign will be particularly useful for evaluating whether numerical models are capturing the unsteady flow effects appropriately, although this task is beyond the scope of the present work. As before, both the clean baseline and rough aerofoil configurations are considered for a test Reynolds number of 1.5×10^6.

3.4.1 Unsteady Blade Section Loading for Selected Test Cases

This section discusses the unsteady normal force and drag coefficients for the selected statistically significant oscillatory test cases, as described in Section 3.2. The unsteady results are presented in Figures 3.9 and 3.10 for the NACA 63-619 blade section, Figures 3.11 and 3.12 for the AHH 19 blade section and Figures 3.13 and 3.14 for the AHH 32 blade section. The corresponding static values are included for reference.

Considering the unsteady normal force results (Figures 3.9, 3.11 and 3.13) first, the unsteady load behaviour exhibited in the results is characteristic of classical dynamic loading and stall loading cycles – a lift overshoot on the pitch cycle motion upstroke and the peak lift occurring at a delayed blade section incidence. At higher reduced frequencies and aerofoil incidences the size of the hysteresis loop increases as the unsteady flow effects begin to dominate the aerofoil behaviour. For lower reduced frequency blade motions in the attached flow region, the unsteady effects are minimised and the static loading curve acts as a suitable indicator of the blade section unsteady loading.

As also shown in the static blade section results, the largest loading change brought on by the introduction of fouling to the blade section is the reduction of the unsteady load magnitudes. Inspection of the results has also shown that fouling on the blade results in a minimal change in the aerofoil incidence for peak normal loading. This suggests that the moment break is occurring at the same position during the pitch cycle. The width of the hysteresis loop at the mid-pitch position is reduced and the blade section loading change in the fully stalled region is suggesting a less abrupt stall mechanism. In addition, the process of the flow reattaching, as the incidence decreases on the pitch cycle downstroke, is initiated sooner in the cycle, perhaps due to a smaller pressure gradient over the blade section surface and the roughness damping some of the unsteady effects.

The overall unsteady behaviour of the normal force coefficient can be suitably approximated by the static loading plus an additional second-order dynamic effect to account for the boundary layer flow separation delay and non-circulatory loading terms. This second-order effect is identified as a function of the blade section reduced frequency and stall penetration. In terms of the turbine operation, this second order effect will be related to the rotor speed and the radial position on the blade. The magnitudes of the peak cycle loading are discussed further in Section 3.4.3, with reference to the equivalent static normal force, and the effect that the blade fouling will have on these magnitudes. Similarly, the effects of varying reduced frequency and maximum incidence are discussed further in Sections 3.4.4 and 3.4.5 respectively.

In terms of the unsteady drag coefficients results (Figures 3.10, 3.12 and 3.14), the variation through the pitch cycle is an order of magnitude smaller than that for the unsteady normal force and is predominantly indicated by the static drag coefficient, particularly during the flow reattachment phase.

(A) $k = 0.05$, $\alpha = 5° \pm 4°$ (B) $k = 0.1$, $\alpha = 10° \pm 6°$
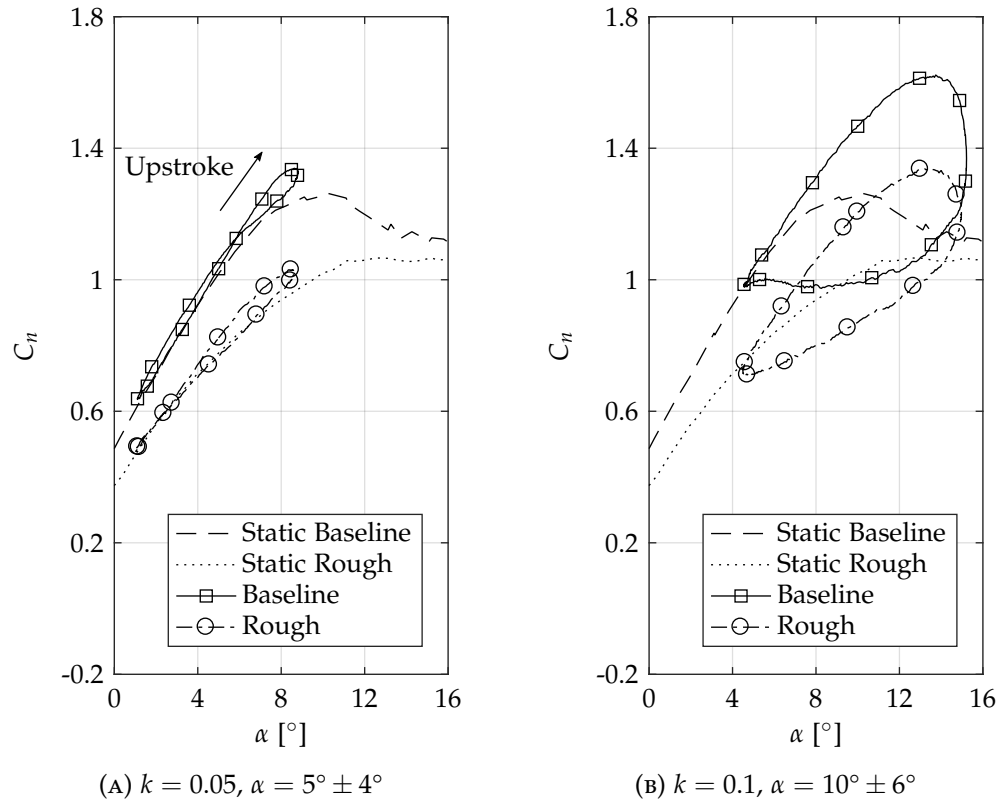
FIGURE 3.9: Unsteady normal force coefficient for selected baseline and rough NACA 63-619 datasets.

(A) $k = 0.05$, $\alpha = 5° \pm 4°$ (B) $k = 0.1$, $\alpha = 10° \pm 6°$
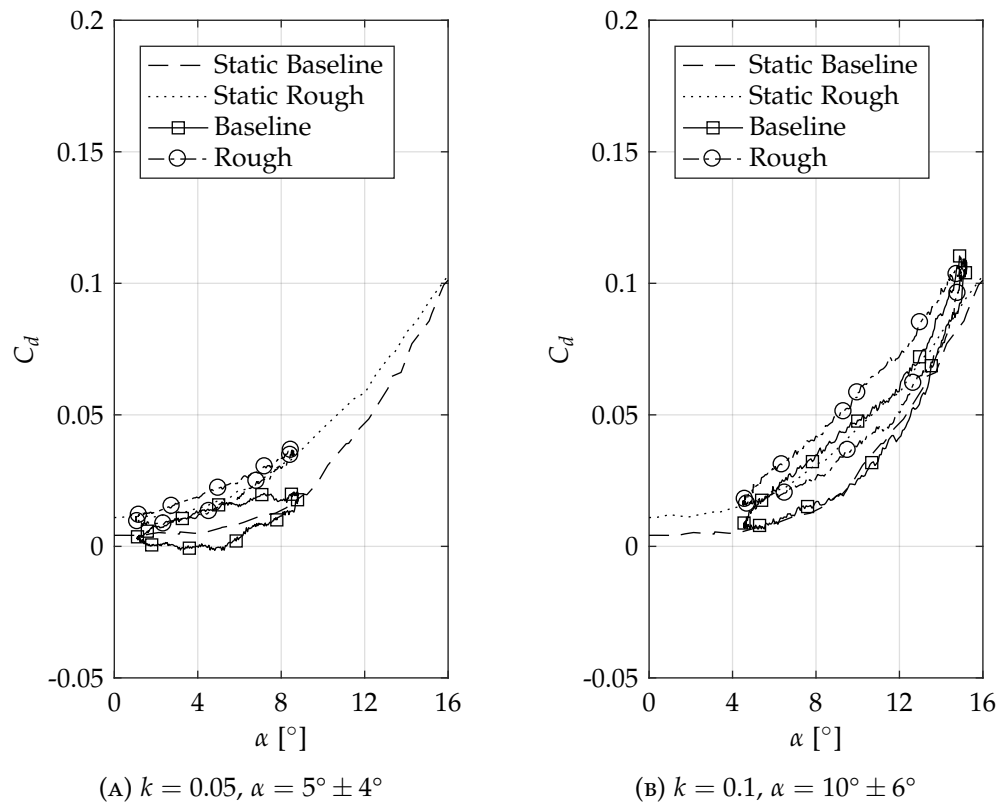
FIGURE 3.10: Unsteady pressure drag coefficient for selected baseline and rough NACA 63-619 datasets.

(A) $k = 0.05$, $\alpha = 5° \pm 4°$ (B) $k = 0.1$, $\alpha = 10° \pm 6°$
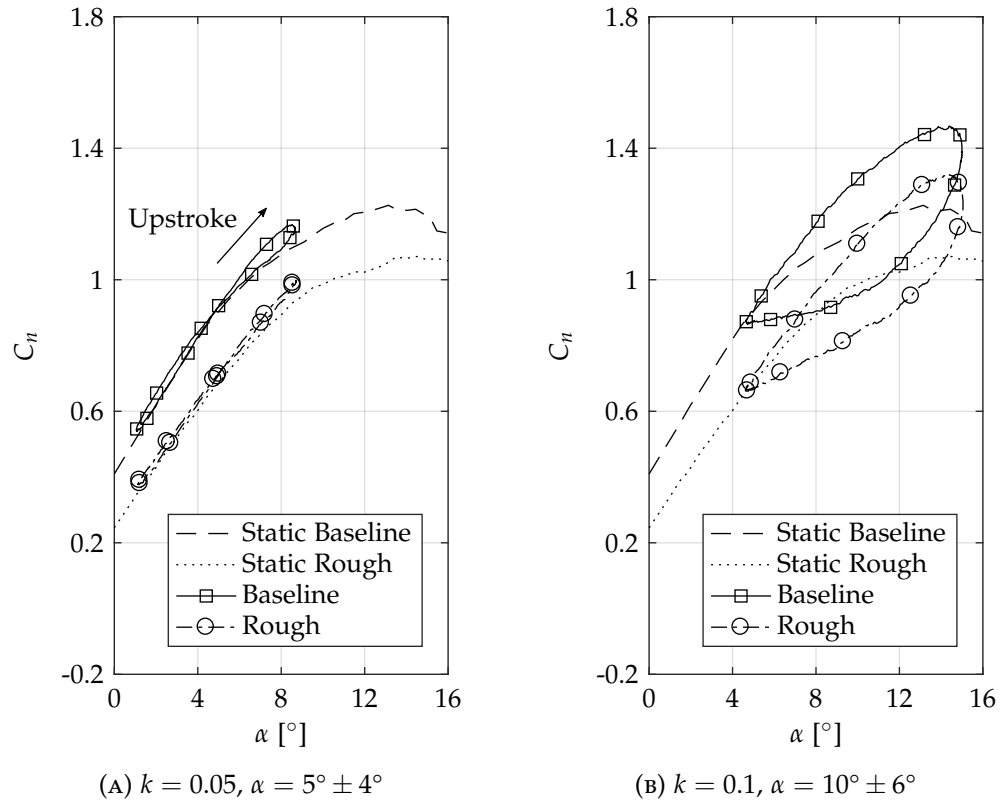
FIGURE 3.11: Unsteady normal force coefficient for selected baseline and rough AHH 19 datasets.

(A) $k = 0.05$, $\alpha = 5° \pm 4°$ (B) $k = 0.1$, $\alpha = 10° \pm 6°$
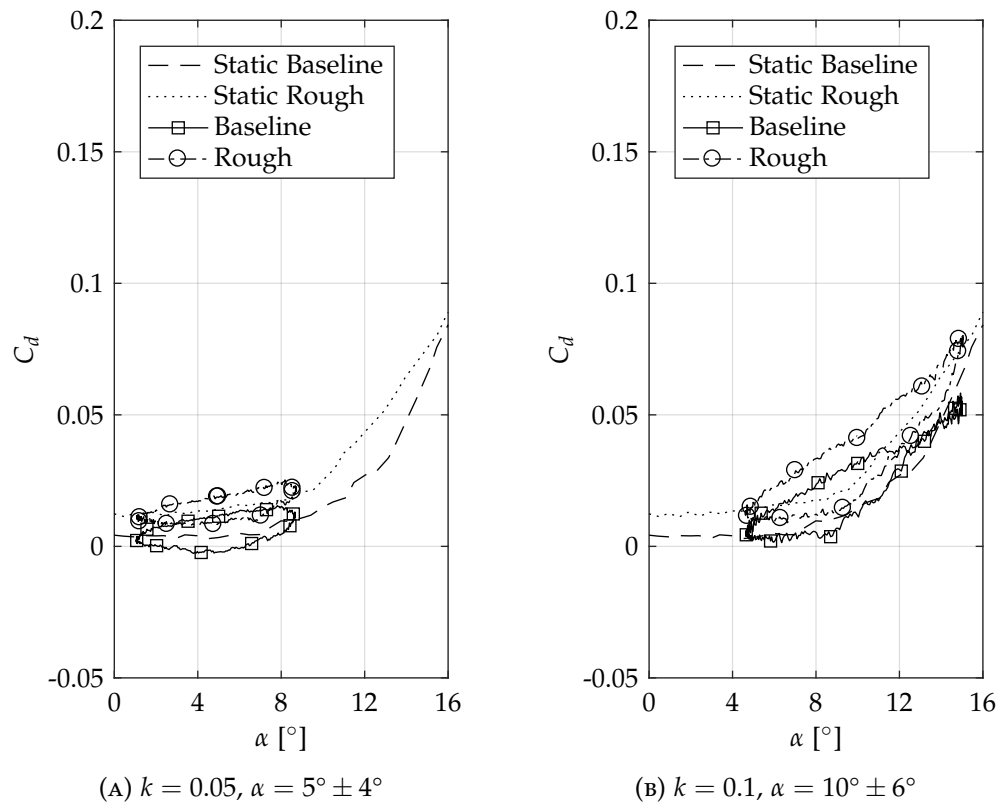
FIGURE 3.12: Unsteady pressure drag coefficient for selected baseline and rough AHH 19 datasets.

(A) $k = 0.1$, $\alpha = 8° \pm 2°$

(B) $k = 0.2$, $\alpha = 12° \pm 10°$
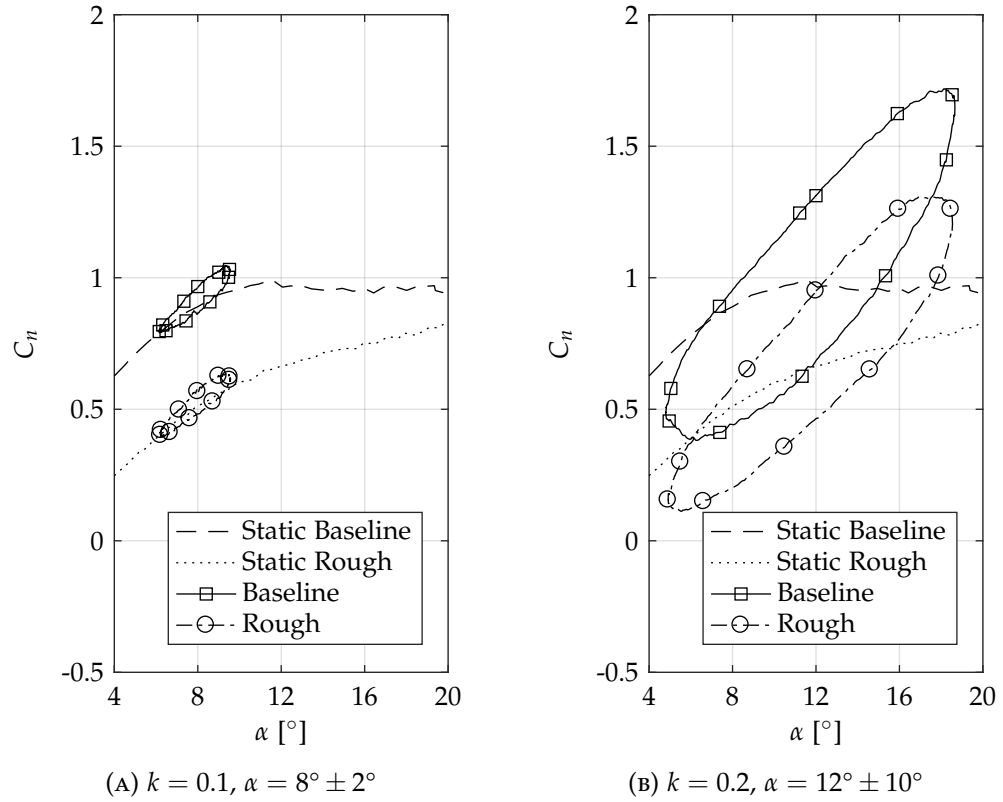
FIGURE 3.13: Unsteady normal force coefficient for selected baseline and rough AHH 32 datasets.

(A) $k = 0.1$, $\alpha = 8° \pm 2°$

(B) $k = 0.2$, $\alpha = 12° \pm 10°$
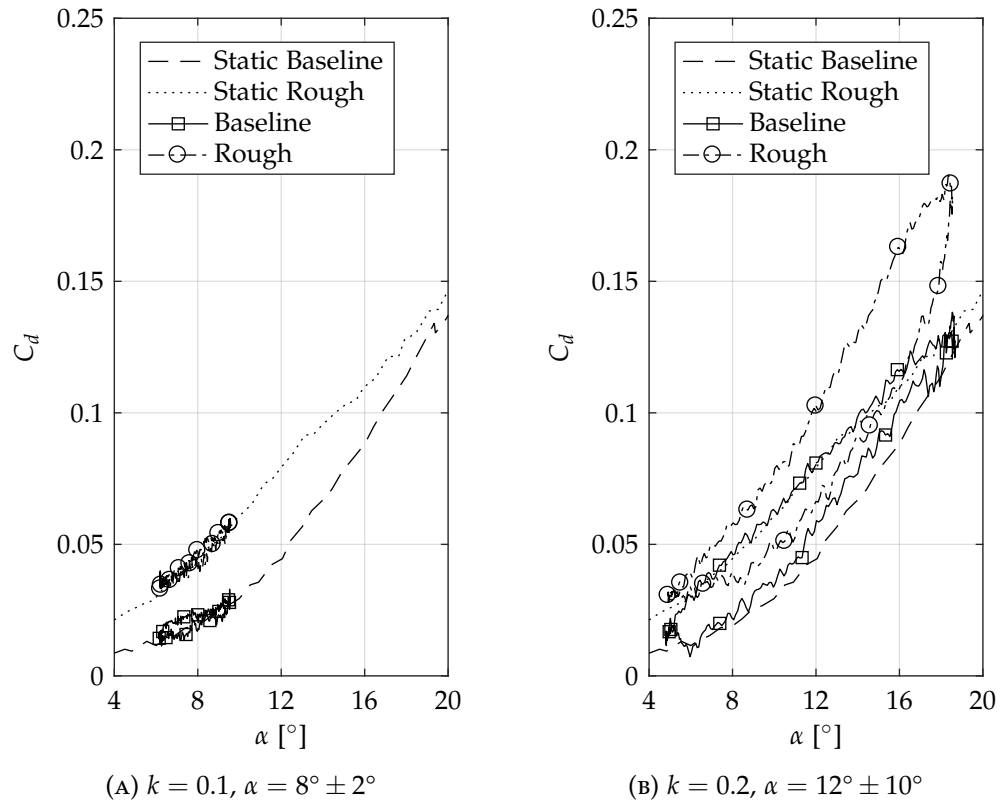
FIGURE 3.14: Unsteady pressure drag coefficient for selected baseline and rough AHH 32 datasets.

TABLE 3.5: Summary of selected outboard blade section unsteady normal force results for baseline and rough configurations.

Parameter	NACA 63-619			AHH 19		
	Baseline	Rough	Δ	Baseline	Rough	Δ
Typical Test Case: $k = 0.05$, $\alpha = 5° \pm 4°$						
$C_{n_{max}}$ [−]	1.34	1.03	-0.31	1.17	0.99	-0.18
α_{ds} [°]	8.7	8.6	-0.1	8.5	8.6	+0.1
$C_{d_{max}}$ [−]	0.021	0.037	+0.016	0.015	0.025	+0.010
$\alpha(C_{d_{max}})$ [°]	8.7	8.5	-0.2	7.9	8.2	+0.3
Limiting Test Case: $k = 0.1$, $\alpha = 10° \pm 6°$						
$C_{n_{max}}$ [−]	1.62	1.34	-0.28	1.47	1.32	-0.15
α_{ds} [°]	13.7	13.6	-0.1	14.5	14.5	0.0
$C_{d_{max}}$ [−]	0.109	0.105	-0.004	0.057	0.079	+0.022
$\alpha(C_{d_{max}})$ [°]	15.0	14.9	-0.1	14.9	15.0	+0.1

TABLE 3.6: Summary of selected inboard blade section unsteady normal force results for baseline and rough configurations.

Parameter	AHH 19		
	Baseline	Rough	Δ
Typical Test Case: $k = 0.1$, $\alpha = 8° \pm 2°$			
$C_{n_{max}}$ [−]	1.05	0.63	-0.42
α_{ds} [°]	9.4	9.4	0.0
$C_{d_{max}}$ [−]	0.029	0.059	+0.030
$\alpha(C_{d_{max}})$ [°]	9.3	9.5	+0.2
Limiting Test Case: $k = 0.2$, $\alpha = 12° \pm 10°$			
$C_{n_{max}}$ [−]	1.72	1.30	-0.42
α_{ds} [°]	18.1	18.0	-0.1
$C_{d_{max}}$ [−]	0.138	0.189	+0.051
$\alpha(C_{d_{max}})$ [°]	18.5	18.4	-0.1

SUMMARY OF UNSTEADY RESULTS

An overview of the effect a light level of biofouling is having on the blade section normal force coefficient parameters is given in Tables 3.5 and 3.6, for the outboard and inboard blade sections respectively.

3.4.2 UNSTEADY PRESSURE COEFFICIENT DISTRIBUTIONS

The unsteady pressure distributions are shown in Figures 3.15 to 3.18 for the NACA 63-619 and AHH 32 test cases presented in Section 3.4.1. Due to the unreliable leading edge transducer measurement on the AHH 19 blade section, these datasets are not
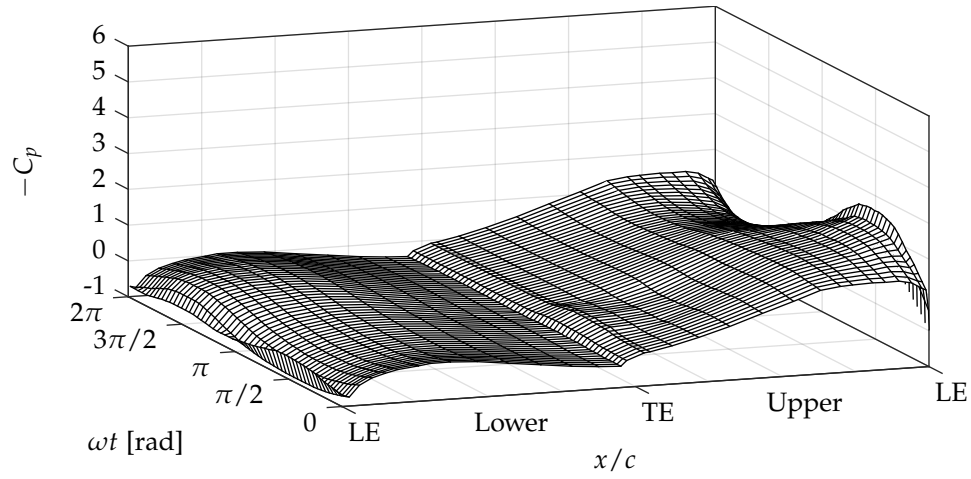
(A) Baseline Configuration
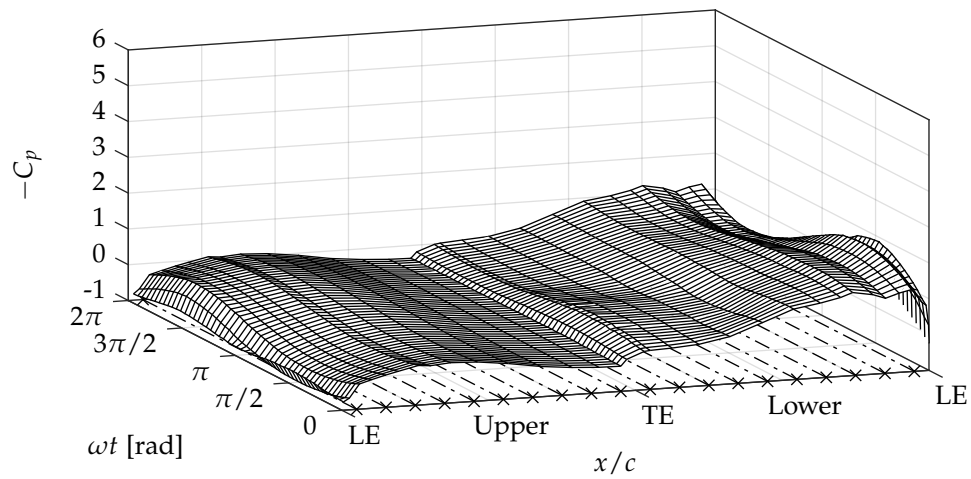
(B) Rough Configuration

Figure 3.15: NACA 63-619 unsteady pressure distribution: $k = 0.05$, $\alpha = 5° \pm 4°$.

presented in this section. For clarity in the figures, the pressure distributions have been unwrapped around the trailing edge and reduced to approximately fifty samples over the pitch cycle. Figure 3.15b includes the positions of the the roughness strips on the aerofoil models for reference.

The presentation of these results highlights the pressure fluctuation on the blade section surface during a pitch cycle, particularly in the leading edge region of the aerofoil upper surface. The main features are the leading edge suction peak which increases with increased flow unsteadiness, but is reduced by the surface roughness as the flow is forced to separate earlier than for the baseline case, and the area of separated flow towards the blade section trailing edge centred around the maximum angle of attack. There is no dominant dynamic stall vortex identified in the two limiting cases presented (Figures 3.16 and 3.18). This compares to the case of a thinner aerofoil rapidly pitching into a light dynamic stall regime where the convection of the dynamic stall vortex over the aerofoil upper surface can be clearly identified in the unsteady pressure distribution and, in some cases, also the secondary vortex system
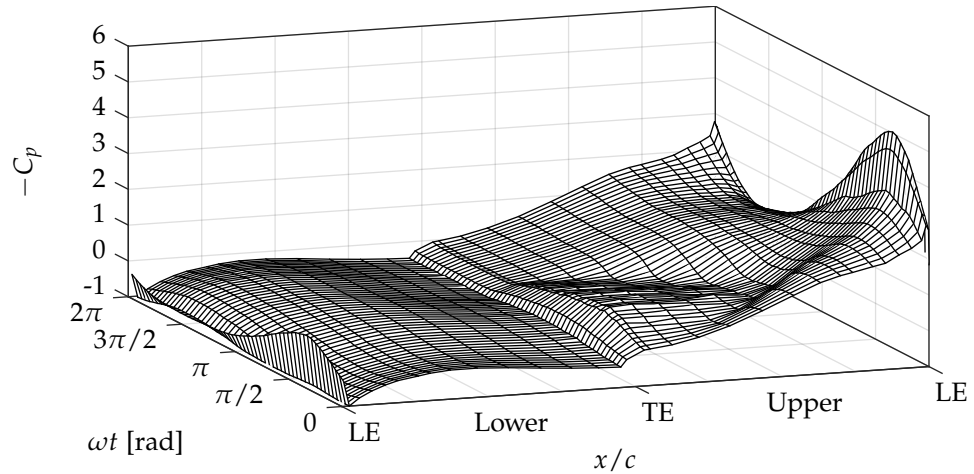
(A) Baseline Configuration
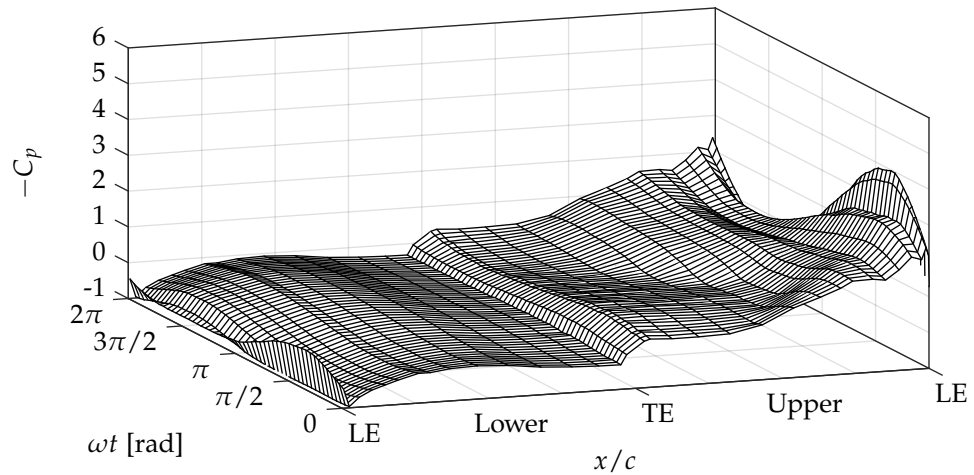
(B) Rough Configuration

FIGURE 3.16: NACA 63-619 unsteady pressure distribution: $k = 0.1$, $\alpha = 10° \pm 6°$.

(See Leishman (1990)). This suggests that for thicker, cambered blade sections, such as those investigated in the present work, the vortex formed is weaker and the unsteady effects are highly damped. In addition, the non-circulatory loading components are dominated by the added-mass terms from accelerating the fluid surrounding the blade section, and not from the presence of the vortex system convecting over the blade section upper surface. A flow separation front and plateau can clearly be seen in the limiting cases for both blade sections.

3.4.3 MAXIMUM BLADE SECTION NORMAL FORCE COEFFICIENT

The previous parts of this section have focussed on the unsteady loading for selected test cases, but this section will present trends in the peak blade section normal loading using the full database of available results. The peak blade section unsteady normal load with respect to the static data and change in the peak unsteady values when roughness is introduced to the blade surface are both considered.
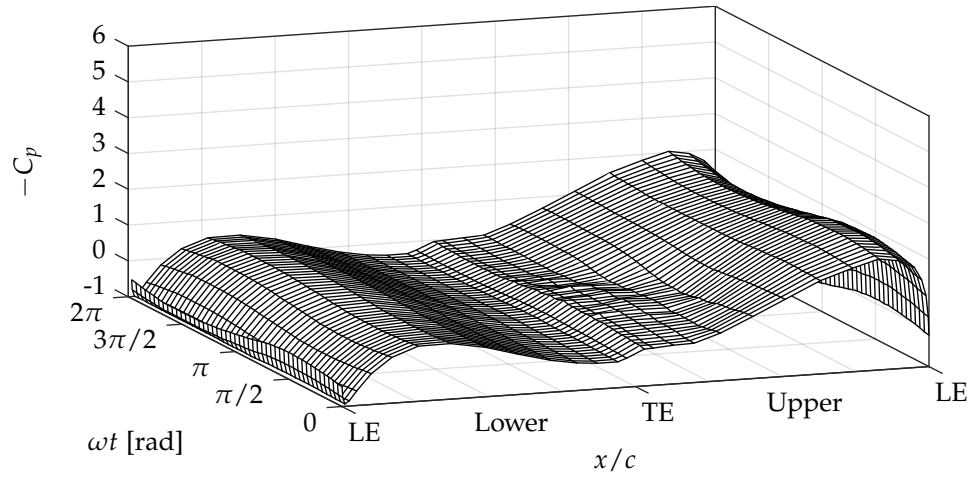
(A) Baseline Configuration
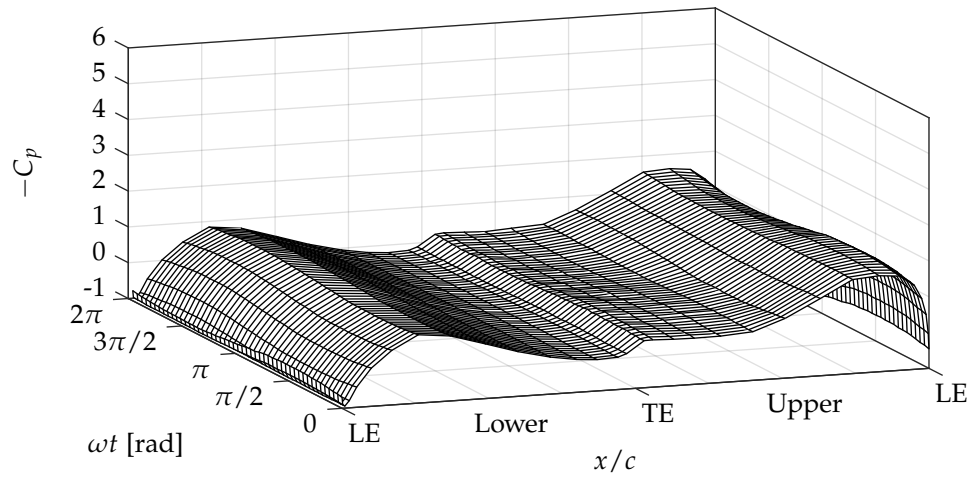
(B) Rough Configuration

Figure 3.17: AHH 32 unsteady pressure distribution: $k = 0.1$, $\alpha = 8° \pm 2°$.

Comparison with Equivalent Static Loading

Figure 3.19 presents the percentage increase of the peak unsteady normal force with reference to the static value at the corresponding incidence. The peak normal force does not normally occur at the maximum pitch cycle incidence, but at a slightly lower incidence – moment break occurs before the aerofoil fully stalls. However, the results in this section are presented as a function of maximum pitch cycle incidence because, from a turbine design point of view, the maximum incidence will be known, but not necessarily the incidence at which the peak normal force will occur. Each point in the figure represents the peak normal force value for an individual test case.

It can be seen in the presented trends that the peak unsteady normal force is significantly higher than the equivalent static value. As expected, the largest differences are for the motion with the higher reduced frequencies and larger pitch cycle incidence. For the NACA 63-619 blade section, the maximum increase attributed to the unsteadiness is approximately 40 % of the static value, and approximately 10 % at the
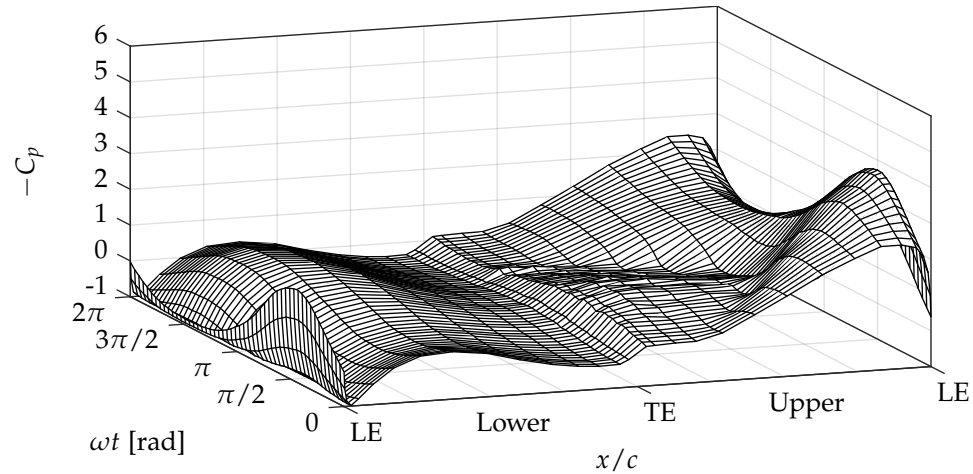
(A) Baseline Configuration
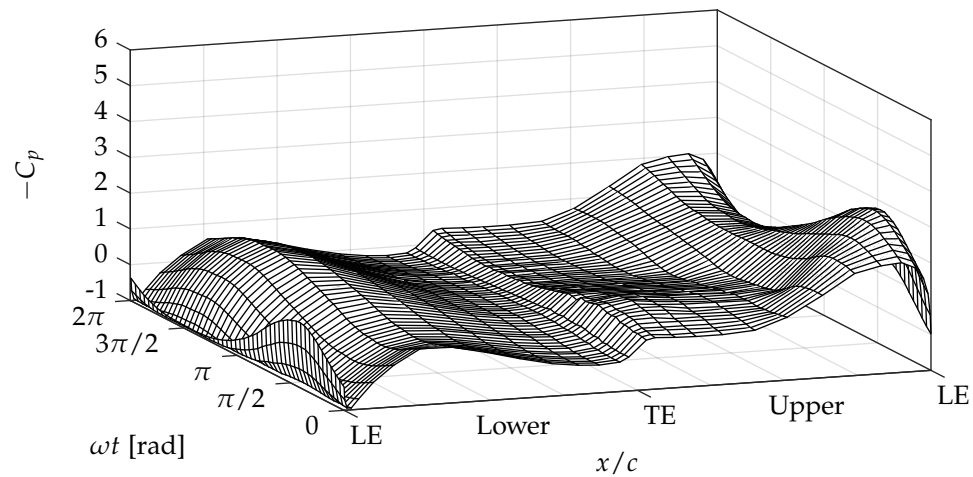
(B) Rough Configuration

FIGURE 3.18: AHH 32 unsteady pressure distribution: $k = 0.2$, $\alpha = 12° \pm 10°$.

typical turbine operating point. The effect of roughness on the peak force difference is a reduction to approximately 25 %. The unsteady peak normal force increase for the AHH 19 blade section shows a negligible change when roughness is included and a maximum increase of approximately 20 % is identified. The unsteady normal force increase for typical operation is the same as that for the NACA 63-619 blade section. The largest increases are observed for the thicker inboard AHH 32 blade section, but compared to the outboard blade positions will be experiencing a considerably higher reduced frequency and incidence range. At the extreme operating conditions, the peak unsteady normal force is approximately 80 % greater than the static case, and only reduces to 70 % when surface roughness is added. For typical turbine operating conditions, an increase of approximately 20 % is likely at the inboard blade position.

(A) NACA 63-619 (Baseline)

(B) NACA 63-619 (Rough)

(C) AHH 19 (Baseline)

(D) AHH 19 (Rough)

(E) AHH 32 (Baseline)

(F) AHH 32 (Rough)
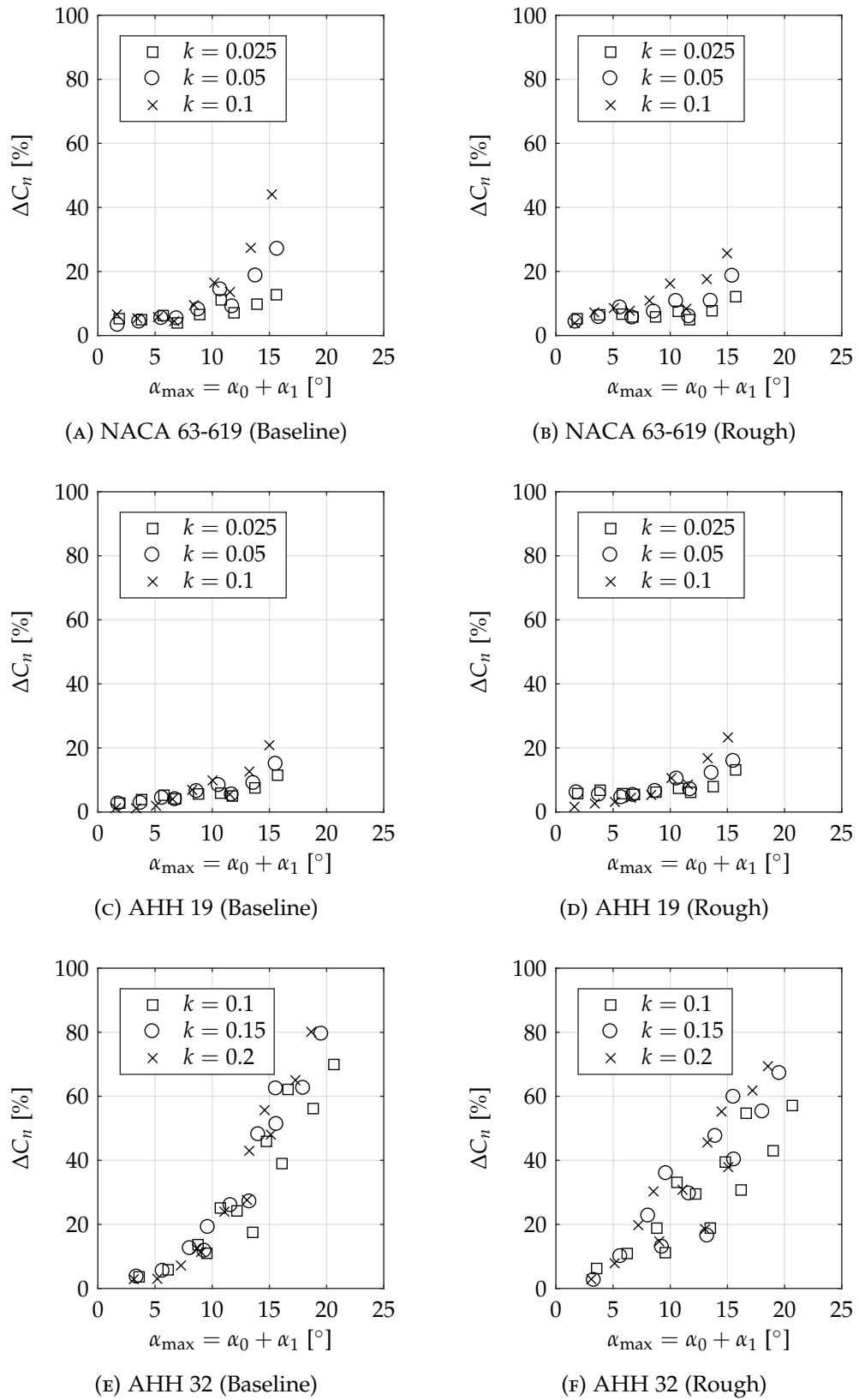
FIGURE 3.19: Percentage change in peak unsteady normal loading from static normal loading at equivalent incidences, with reference to the static case.

COMPARISON OF EQUIVALENT UNSTEADY RESULTS

Figures 3.20, 3.21 and 3.22 presents the change in the peak unsteady normal force between the baseline and rough unsteady cases. The absolute values for each test case are shown in the left hand column and the percentage change due to fouling for the corresponding test conditions in the right hand column. The percentage change is the difference between the baseline and rough peak normal load with reference to the baseline value, for each oscillatory test case. A negative change indicates a force decrease.

The most striking feature of this set of results is that the percentage decrease of the peak normal loading when the blade section becomes fouled is independent of the reduced frequency, hence turbine rotational speed, and only dependent on the blade section incidence. In other words, no matter what speed the turbine is operating at, the change in the blade section peak unsteady normal force is known for a light level of biofouling on the blade surface. Therefore, the decrease in peak load when the blade becomes fouled can be estimated across the full turbine operating range. This is the case for all three blade sections.

3.4.4 EFFECT OF REDUCED FREQUENCY ON UNSTEADY NORMAL FORCE

The effects of varying the reduced frequency on the blade section unsteady normal force coefficients are highlighted by showing the change in normal force due to surface roughness at the three aerofoil test frequencies. These results are shown in Figure 3.23, 3.24 and 3.25, for the NACA 63-619, AHH 19 and AHH 32 blade sections respectively. To account for the small time variation in the pitch cycle incidences, the datasets are interpolated over an interval of 0 to 2π and then reverted to blade section incidence in the time domain.

For the thinner blade sections under attached flow conditions, the change in normal force through the pitch cycle is independent of reduced frequency during the upstroke motion of the cycle, and the static reference is a suitable indicator of the blade loading change. However, the unsteady blade loading on reattachment during the downstroke motion is showing a dependency on the reduced frequency. Once the flow is separated and approaching stall, the effects of roughness influence the blade loading for both increasing and decreasing changes in incidence, and this is shown to be dependent on reduced frequency hence turbine rotational speed. The overall trend observed in the thinner blade section results is that reduced frequency increases the thickness of the unsteady load loop. Comparing the results for the NACA 63-619 and AHH 19 blade sections, the variation in the blade loading change when roughened are suggesting that the AHH 19 aerofoil loading is less susceptible to unsteady cycle effects in the rough configuration. For the thicker blade section at lower incidences, the change in the unsteady normal force is found to be independent of reduced frequency, but highly unsteady and not correlated at higher incidences.

(A) $C_{n_{max}}$

(B) Unsteady $\Delta C_{n_{max}}$
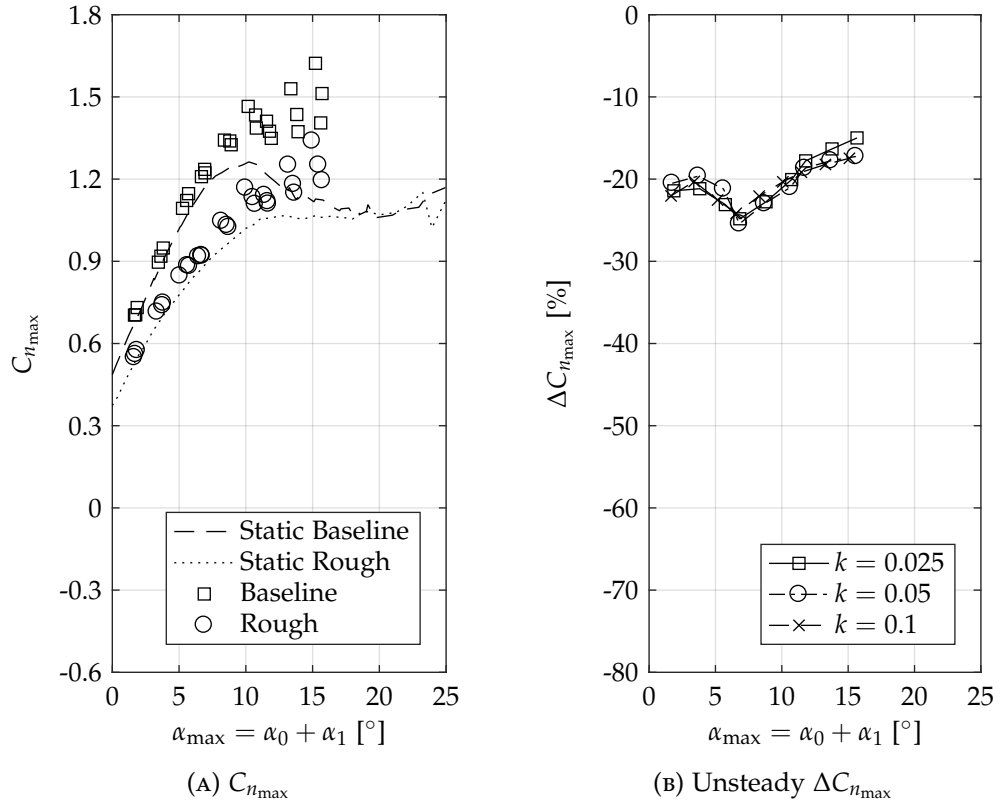
FIGURE 3.20: Peak unsteady loading for baseline and rough NACA 63-619 datasets and change in peak unsteady loading for addition of roughness.

(A) $C_{n_{max}}$

(B) Unsteady $\Delta C_{n_{max}}$
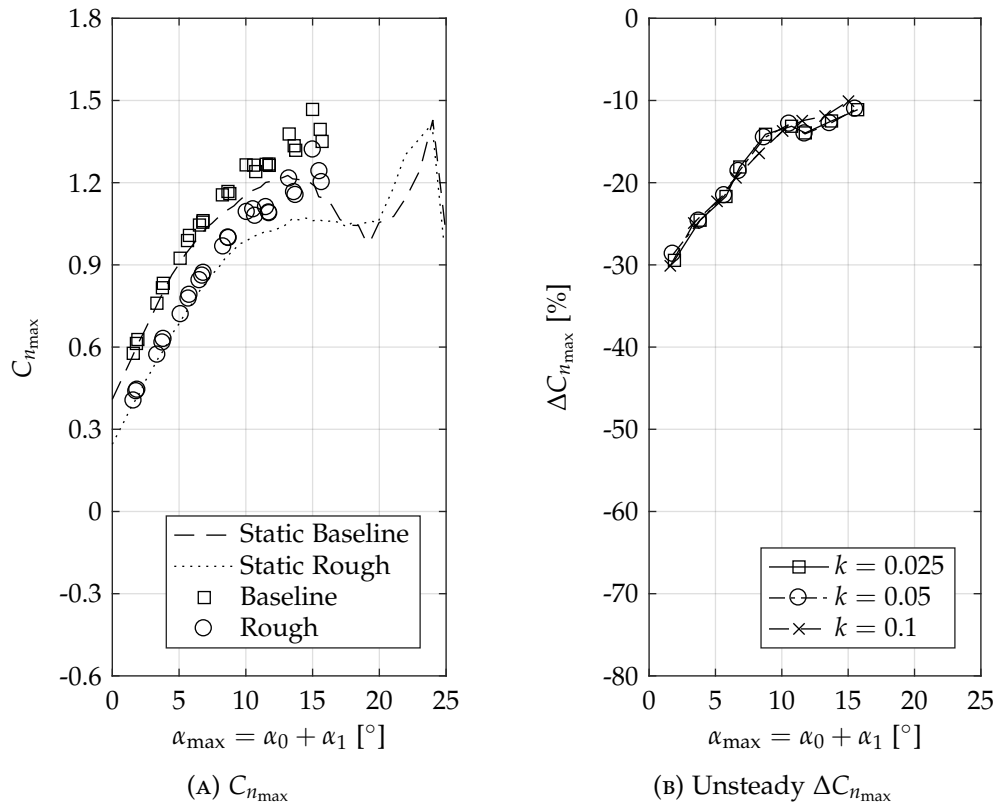
FIGURE 3.21: Peak unsteady loading for baseline and rough AHH 19 datasets and change in peak unsteady loading for addition of roughness.

(A) $C_{n_{\max}}$
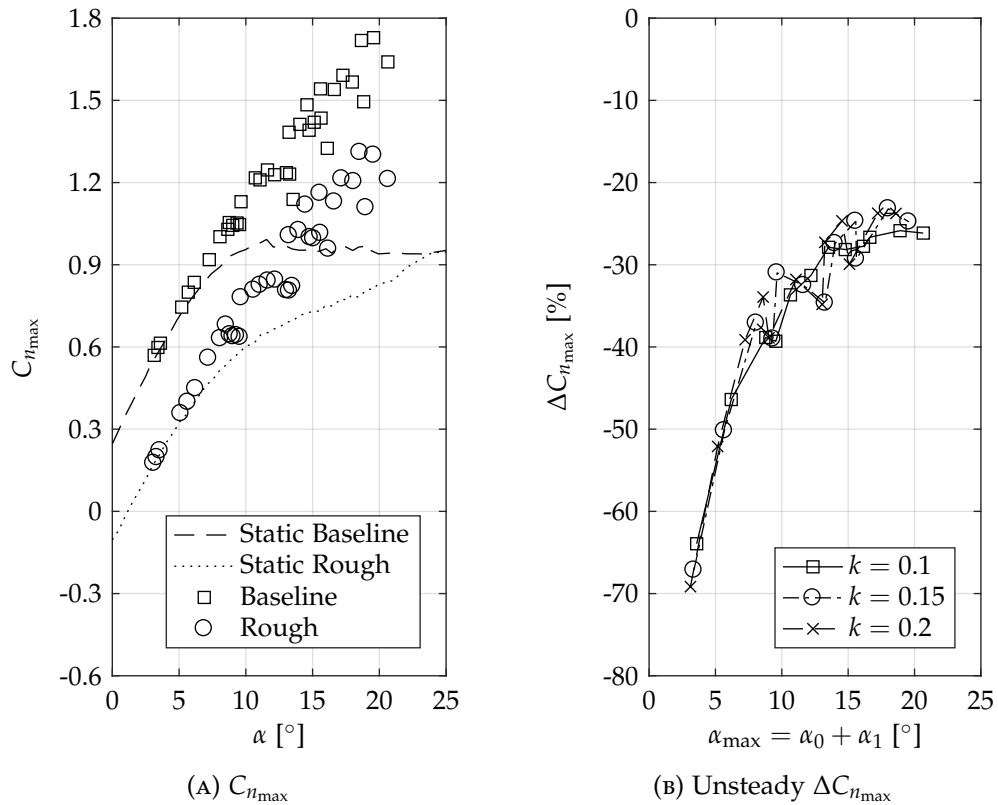
(B) Unsteady $\Delta C_{n_{\max}}$

FIGURE 3.22: Peak unsteady loading for baseline and rough AHH 32 datasets and change in peak unsteady loading for addition of roughness.

3.4.5   EFFECT OF MAXIMUM INCIDENCE ON UNSTEADY NORMAL FORCE

The effect of varying the maximum angle of attack on the blade section unsteady normal force coefficient is investigated using a similar approach. The maximum angle of attack achieved during the pitch cycle is varied by maintaining the mean incidence for the selected test cases and using the three available cyclic angles. The results of this analysis are presented in Figures 3.26 to 3.28.

The change in normal force through the pitch cycle is shown to be independent of incidence under attached flow conditions for all three blade sections. Further to this, the change in the static normal force is once again a suitable indicator for the change in the steady blade section loading due to biofouling, particularly on the pitch cycle upstroke. Only beyond the static stall incidence does the variation in the blade section normal load become dependent on incidence. As the amplitude of the pitch cycle increases, so does the level of stall penetration, and with increasing amplitude the variation in the measured normal load increases at an equivalent blade section incidence. This is particularly evident for the thicker AHH 32 blade section which is operating in a deeper dynamic stall regime.

(A) $\alpha = 5° \pm 4°$

(B) $\alpha = 10° \pm 6°$
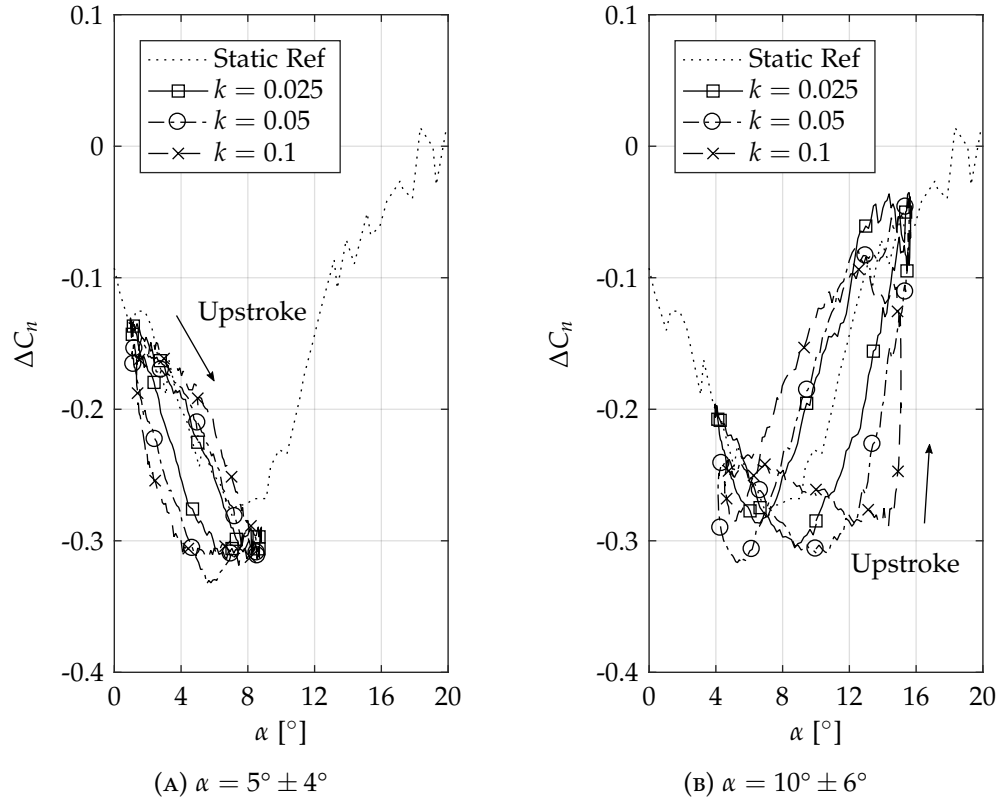
Figure 3.23: Effect of surface roughness and varying reduced frequency on unsteady normal force coefficient for the NACA 63-619 blade section.

(A) $\alpha = 5° \pm 4°$

(B) $\alpha = 10° \pm 6°$
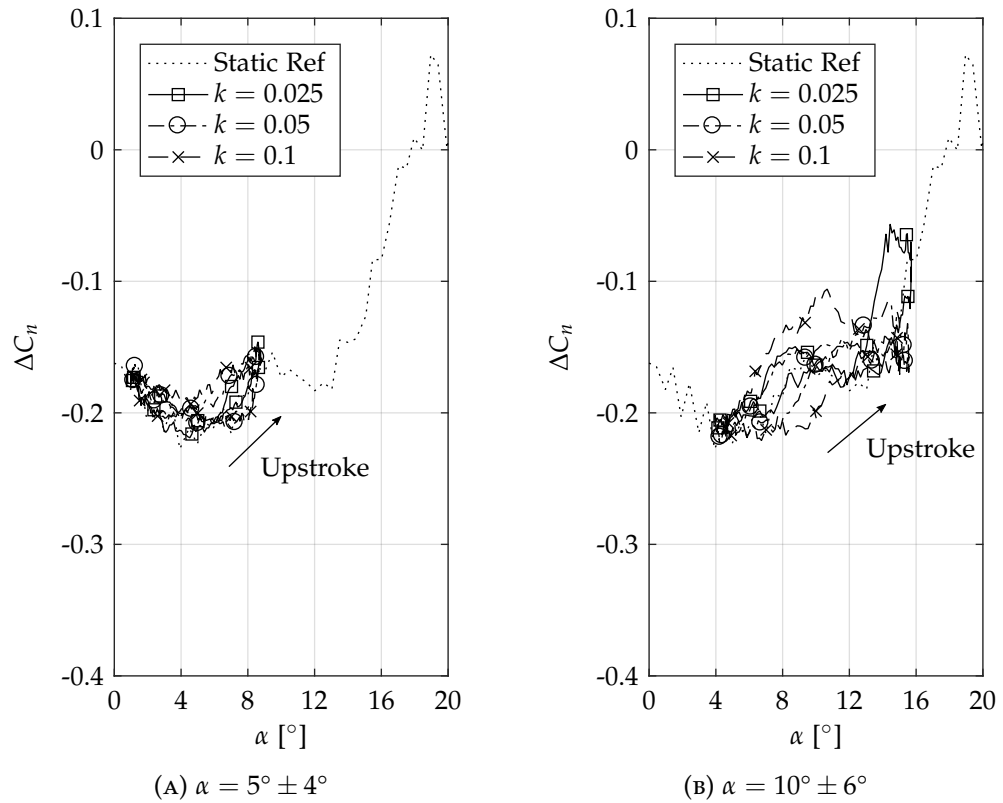
Figure 3.24: Effect of surface roughness and varying reduced frequency on unsteady normal force coefficient for the AHH 19 blade section.

(A) $\alpha = 8° \pm 2°$

(B) $\alpha = 12° \pm 10°$
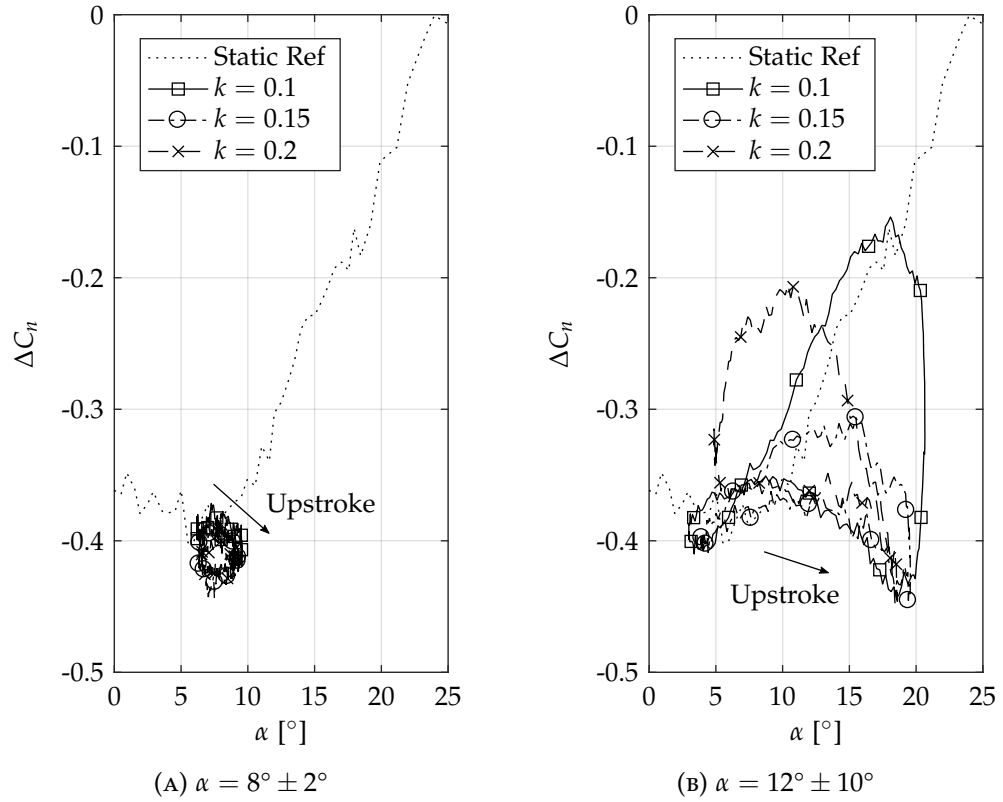
FIGURE 3.25: Effect of surface roughness and varying reduced frequency on unsteady normal force coefficient for the AHH 32 blade section.

(A) $k = 0.05$, $\alpha_0 = 5°$

(B) $k = 0.1$, $\alpha_0 = 10°$
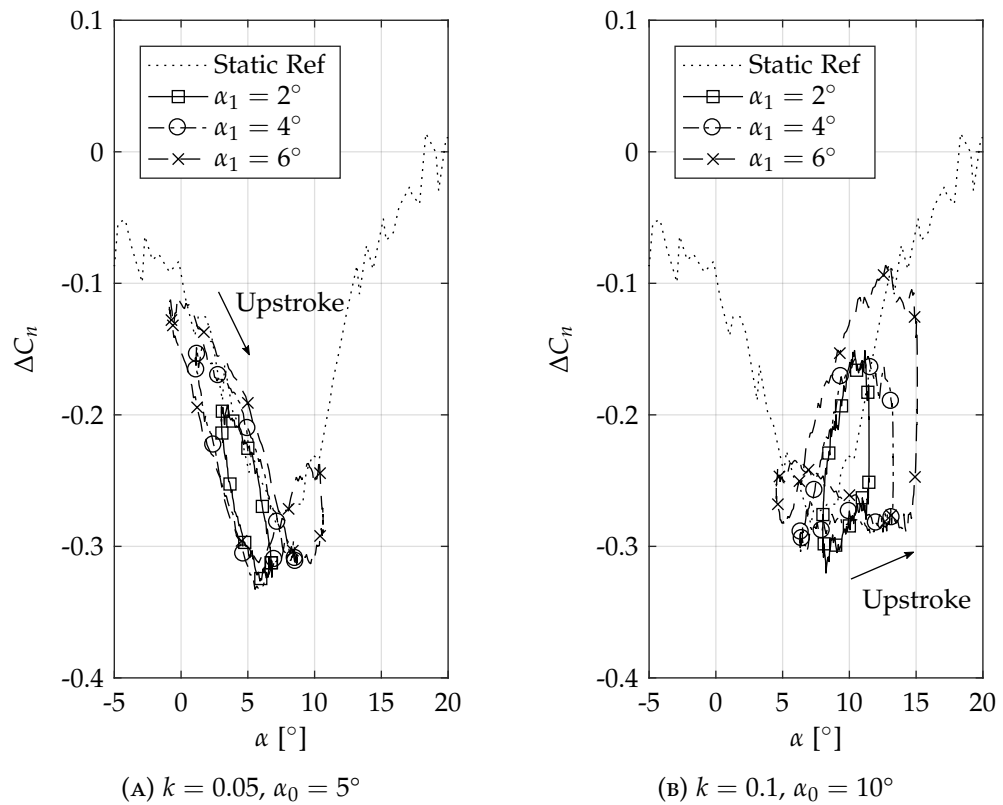
FIGURE 3.26: Effect of surface roughness and varying pitch cycle amplitude on unsteady normal force coefficient for the NACA 63-619 blade section.

(A) $k = 0.05$, $\alpha_0 = 5°$ (B) $k = 0.1$, $\alpha_0 = 10°$
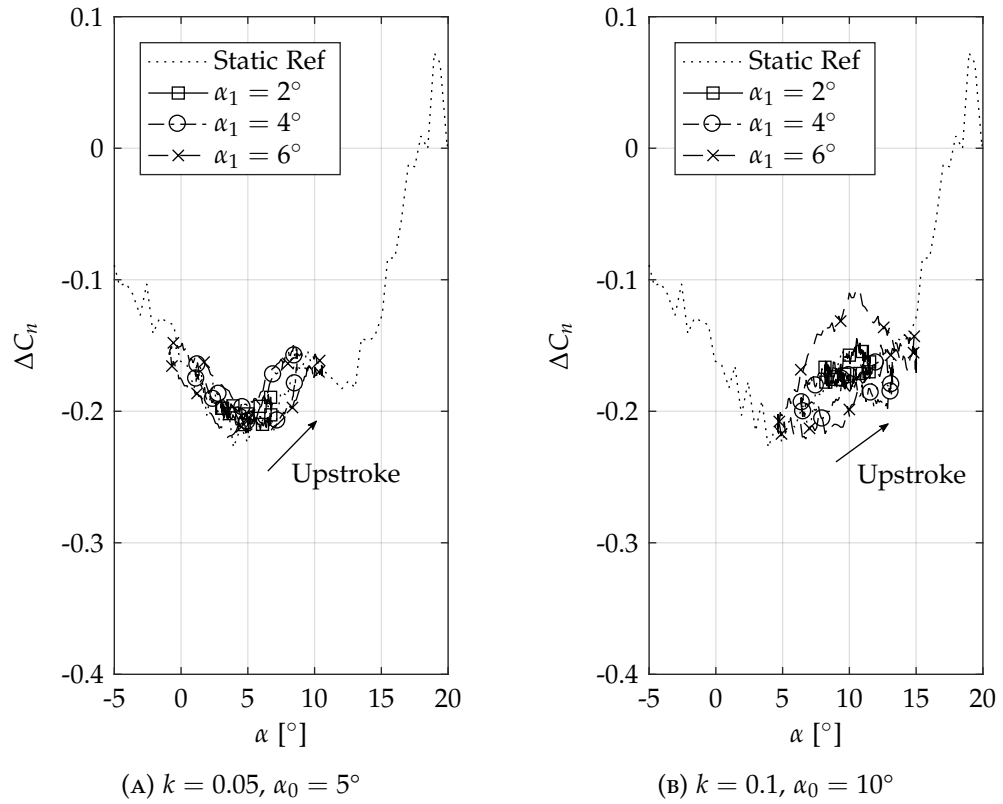
FIGURE 3.27: Effect of surface roughness and varying pitch cycle amplitude on unsteady normal force coefficient for the AHH 19 blade section.

(A) $k = 0.1$, $\alpha_0 = 8°$ (B) $k = 0.2$, $\alpha_0 = 12°$
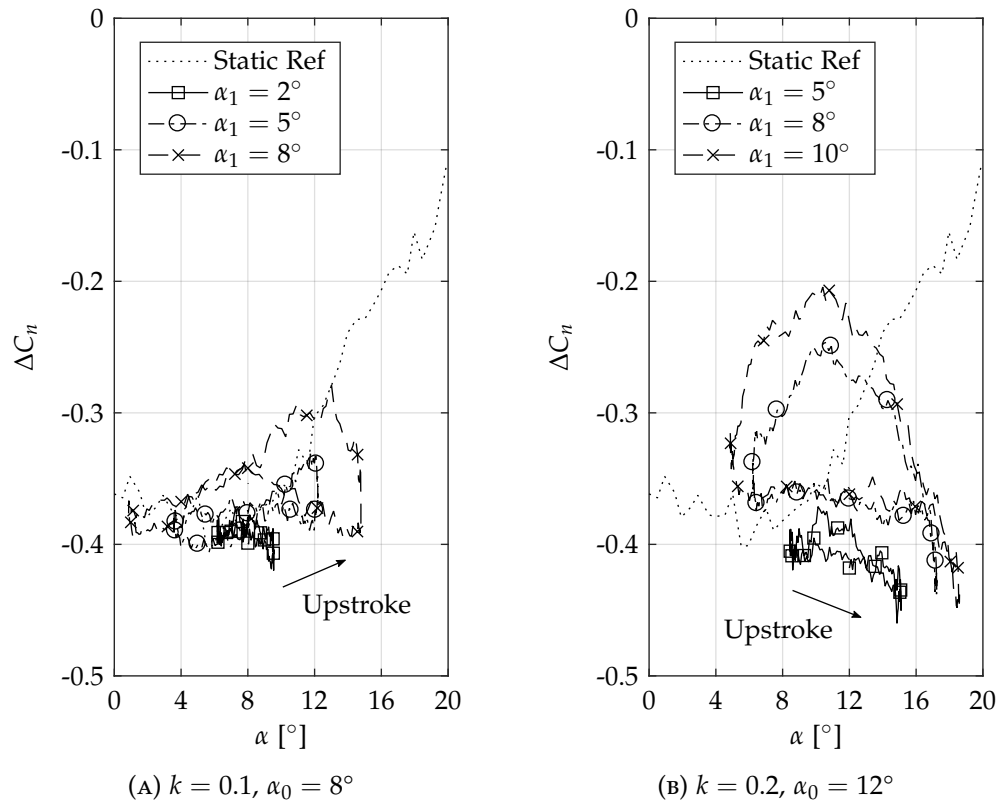
FIGURE 3.28: Effect of surface roughness and varying pitch cycle amplitude on unsteady normal force coefficient for the AHH 32 blade section.

3.5 BLADE SECTION TRANSIENT LOADING

The largest extreme loads acting on the tidal turbine do not necessarily arise during normal energy production, but often occur during transient turbine events. Two such circumstances are a large wave encountering a parked or idle turbine and an emergency stop of the system, which also produces the highest stresses in the turbine support structure (DNV GL, 2015b). Using load results from the ramp and hold test cases, for the two AHH blade sections, the load cases for the two highlighted transient events will be explored, starting with the turbine emergency stop.

The transient pitching motion input is modelled during the wind tunnel tests as a step change in angle of attack over a time interval calculated to achieve the correct reduced pitch rate for the wind tunnel flow conditions. Even though the model positioning system controller is critically damped to prevent an overshoot beyond the dynamic stall rig range, a similar response would be expected from the tidal turbine pitch control system. In addition, a maximum aerofoil angle of attack of 25° could be achieved safely within the displacement limitations of the wind tunnel rig.

Investigating the aerofoil aerodynamic response to a constant rate ramp motion is beneficial as the dependence on the model acceleration term ($\ddot{\alpha}$) in the input forcing is removed. Although the exact transient blade motions from the operating turbine are not reproduced in the idealised test cases, an appropriate set of results have been presented to allow the blade loading magnitudes during specific transient events to be estimated as required.

3.5.1 OPERATING TURBINE: EMERGENCY STOP

During an emergency event, usually due to a fault case being identified in the turbine system, the shaft mounted braking system decelerates the turbine rotation while each blade is simultaneously pitched to the feathered parked position. This results in a highly time-dependent variation in the blade reduced pitch rate and angle of attack as the resultant flow on the blade section decreases from being a function of the tidal current freestream and a rotational component to zero rotation and only the freestream component. The change in resultant velocity and incidence are demonstrated in Figure 3.29. To estimate the reduced pitch rates during this class of event, as defined in Equation 1.6, it is assumed that a 20 m diameter turbine is operating at 10 rpm in a 2.5 m/s tidal current. The two blade sections of interest located at radial positions of 0.45R and 0.75R, with chord lengths of 1.4 m and 0.8 m respectively. The emergency pitch rate ($\dot{\alpha}$) of the AHH HS1000 turbine is stated as 10 °/s (C Phillips, Personal Communication, 8$^{\text{th}}$ Sep 2016). For an emergency event under these conditions, idealised ramp up reduced pitch rates ranging from 0.010 to 0.028, for the 19 % thick outboard blade section, and 0.012 to 0.049, for the 32 % thick inboard section, are obtained.

(A) Turbine in Operation   (B) Stationary Parked Turbine
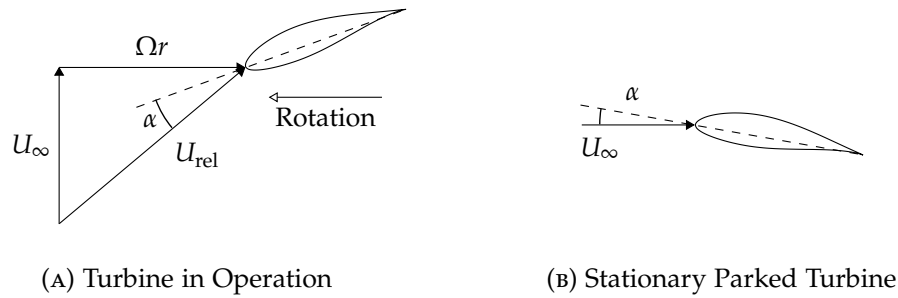
FIGURE 3.29: Summary of incident velocity and angle of attack for turbine blade section in parked and operating blade pitch positions.

Figures 3.30 and 3.31 present transient blade loading measurements, for the outboard and inboard blade sections respectively, which approximate the loads expected during an emergency stop event. The idealised motion starts at an aerofoil incidence of 0° and ramps to a final incidence of 25° – from attached flow through flow separation and into the deep stall condition – at three different reduced pitch rates. Only the blade section normal loading is considered and the equivalent static loading is provided for reference.

The main characteristic of this transient aerofoil loading is the large lift overshoot occurring significantly beyond the aerofoil static stall angles, but recovering to the equivalent static loading case, where the lift augmentation is slightly greater compared to the oscillating test cases. Interestingly, at both radial positions on the turbine blade, in both clean and rough configurations, a limit to the transient normal aerofoil loading is reached for the two higher reduced pitch rates. This is despite the reduced pitch rate almost doubling from a value of 0.025 to 0.04. This is in contrast to the transient response approaching the quasi-static state with decreasing reduced pitch rate. It is believed that this is due to the stall vortex convection speed falling for increasing pitch rate, but reaching a condition where the convection speed becomes constant, as reported by Green et al. (1992) for NACA 0015 and NACA 0018 aerofoils.

For the AHH 19 blade section in the clean configuration, the aerofoil stall is delayed for all three pitch rates by approximately 11° to an angle of attack just beyond 21°. In terms of the blade section normal force, the coefficient increases by close to 40 % for $\dot{\alpha}_{\mathrm{red}} = 0.010$, the lowest reduced pitch rate presented, and by 60 % for the two higher pitch rates, when compared to the static aerofoil loading at stall. Compared to the baseline case, the effect on the fouled blade is to decrease the absolute peak normal loads on aerofoil and reduce the incidence the peak load occurs at by approximately 1°. Again, the load increase compared to the reference static case is close to 40 %, but increases to around 70 % for the higher pitch rates.

A similar response is seen in the transient load results for the AHH 32 blade section. However, the peak transient load increases, compared to the baseline static, are significantly increased. For the lowest pitch rate an increase of almost 60 % is observed, increasing to over 90 % for the higher pitch rates. The introduction of roughness to

(A) Baseline Configuration (B) Rough Configuration
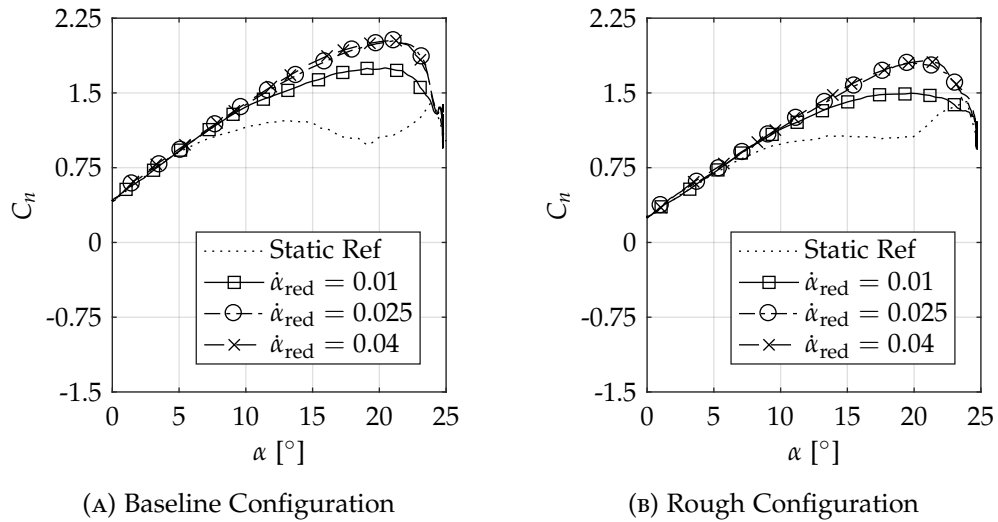
FIGURE 3.30: Outboard AHH 19 blade section normal loading estimates for a transient turbine emergency stop event: Ramp up motion from 0° to 25° at selected reduced pitch rates.

(A) Baseline Configuration (B) Rough Configuration
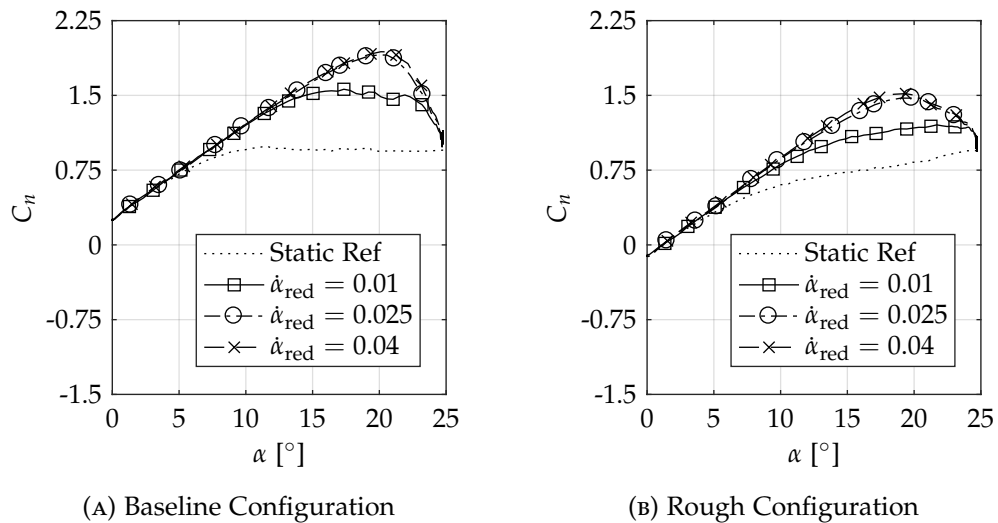
FIGURE 3.31: Inboard AHH 32 blade section normal loading estimates for a transient turbine emergency stop event: Ramp up motion from 0° to 25° at selected reduced pitch rates.

the aerofoil surface results in the peak transient loads decreasing by approximately 20 %, with reference to the peak transient loads in the clean configuration, for all three reduced pitch rate cases. This compares to a peak load decrease of between 10 % to 15 % for the thinner AHH 19 blade section associated with the surface becoming fouled.

3.5.2 STATIONARY PARKED TURBINE

When the turbine is not generating energy the blades are feathered to the parked position. This reduces the torque transferred to the turbine gearbox to a minimum

(Manwell et al., 2002). As the blade is a solid structure, the parked position considers the net effect of the entire blade load and not individual local blade sections, and therefore is highly dependent on the turbine geometry, particularly the blade spanwise twist. Test performance data supplied by the project industrial sponsor for the turbine deployed at AHH Site 3 gives the turbine parked position as approximately 75° from the operating pitch angle (C Phillips, Personal Communication, 24th February 2017). Typical blade twist angles, at the two turbine radial positions of interest, are between 10° and 15° for the inboard section and 2° and 8° for the outboard position. Using approximations for the operating conditions, and assuming a steady uniform flow when parked, the incidence of the inboard section is approximately 8° greater than the outboard location, where the local blade section incidence when parked is likely to be around 2°. If, for example, the turbine is struck by a large wave when in the parked position, especially if yawed, the blade sections will see a short duration of increased or decreased incidence as the wave passes.

As the previous section has already described the loading increase of a transient increase in angle of attack, Figures 3.32 and 3.33 show the equivalent pitch rate cases, but for a ramp down motion through an arc of 20° starting in the stalled flow regime at 20° and reattaching a lower angle of attack. The selected reduced pitch rates correspond to transient events at pitch rates between 0.89 °/s and 3.58 °/s for the outboard blade section, and 0.51 °/s and 2.05 °/s for the inboard blade section. This again assumes a tidal freestream current of 2.5 m/s at the turbine hub height. For transient events occurring between tides on a parked turbine the equivalent pitch rates would be significantly lower. Again, only the blade section normal loading is presented and the static case is included for reference.

The loading response for the parked turbine, for a decreasing positive aerofoil incidence, is similar to the downstroke component of the oscillatory loading with measured normal loads equal or less than the steady loading at the same aerofoil incidence. For all the presented cases, the flow has reattached at an angle of attack of 2°, just prior to reaching the final transient position, and the load magnitudes have recovered to those of the static aerofoil state. With increasing pitch rate, hence unsteadiness, the deficiency between the static reference and unsteady case increases. When comparing to the steady loading, the dynamic response for the rough configuration is very similar to that for the clean configuration, albeit at a decreased load magnitude.

3.5.3 INFLUENCE OF TEST PARAMETERS ON TRANSIENT LOADING

Two specific sets of transient motion loading have been been presented in the previous sections – ramp up motions from 0° to 25° and ramp down motions from 20° to 0°, for a range of reduced pitch rates with the AHH 19 and AHH 32 blade sections. However, these motions only cover a range of positive aerofoil incidences over ramp arcs which are perhaps larger than those that may be experienced by the tidal turbine.

(A) Baseline Configuration (B) Rough Configuration
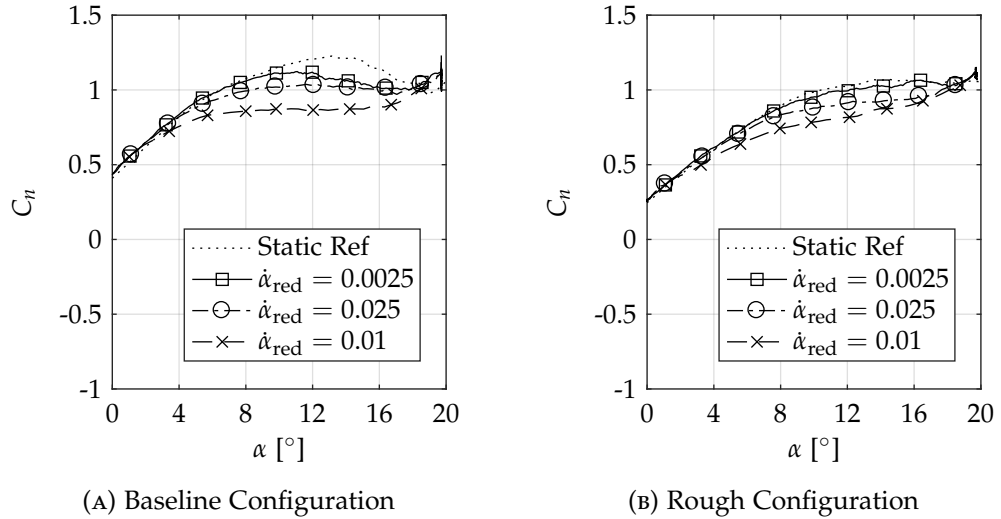
FIGURE 3.32: Outboard AHH 19 blade section normal loading estimates for a transient event on a parked turbine: Ramp down motion from 20° to 0° at selected reduced pitch rates.

(A) Baseline Configuration (B) Rough Configuration
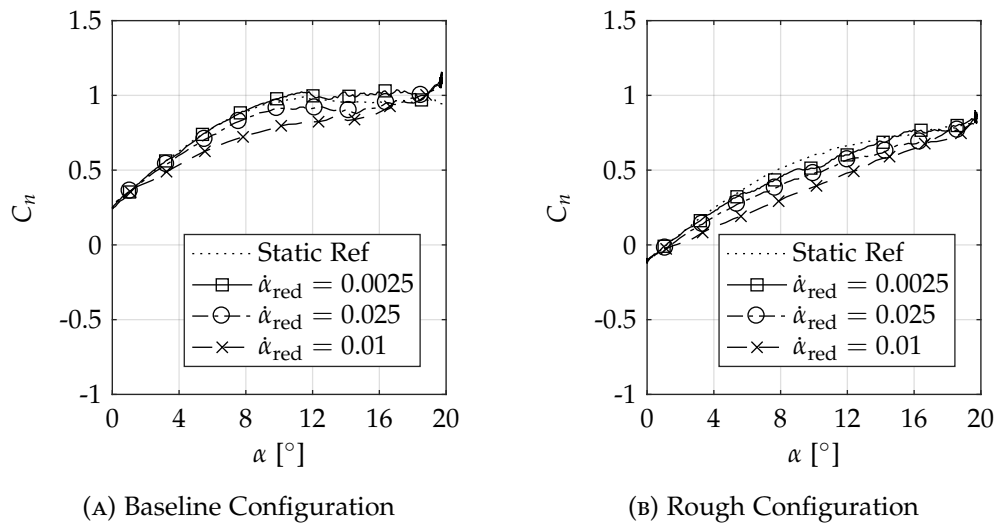
FIGURE 3.33: Inboard AHH 32 blade section normal loading estimates for a transient event on a parked turbine: Ramp down motion from 20° to 0° at selected reduced pitch rates.

Firstly, for transient motions to or from separated negative aerofoil incidences it can be assumed that a ramp down to a negative incidence has a behaviour close to that for a ramp up to a positive incidence, including the large load overshoot and delayed stall in the negative stall region, and similarly, the transient loading for a ramp up from a negative angle of attack can be approximated from the loading for a ramp down motion from a positive incidence. This approach is summarised in Figure 3.34. Over the attached flow regions of the loading curve it would be sufficient to use the static reference loading results.

Secondly, test data is available for an additional subset of wind tunnel tests carried out on the NACA 63-619 aerofoil (See Table 2.4) to highlight the expected load
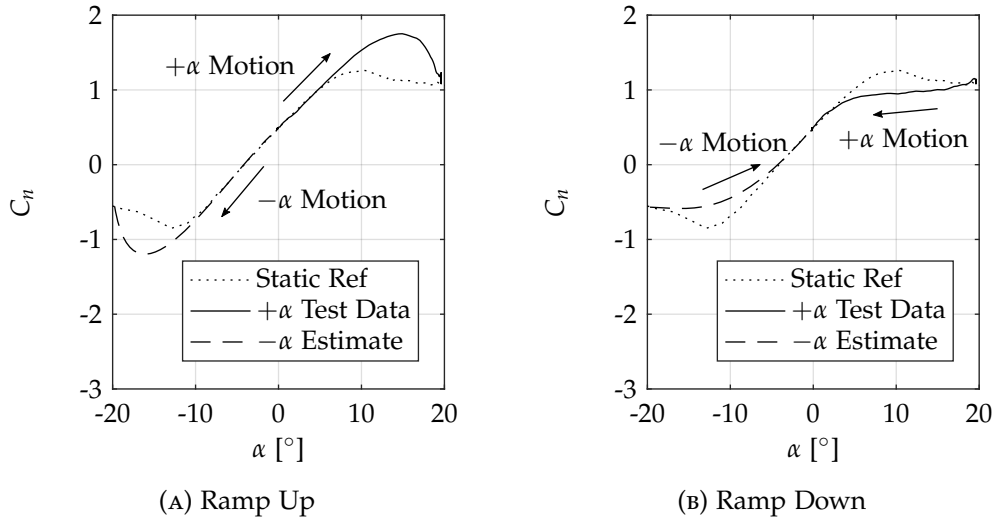
(A) Ramp Up

(B) Ramp Down

FIGURE 3.34: Indication of aerofoil transient normal loading for negative aerofoil incidences, for ramp up motions starting at 0° angle of attack and ramp down motions ending at 0° angle of attack.

(A) $\dot{\alpha}_{\mathrm{red}} = 0.0025$

(B) $\dot{\alpha}_{\mathrm{red}} = 0.01$
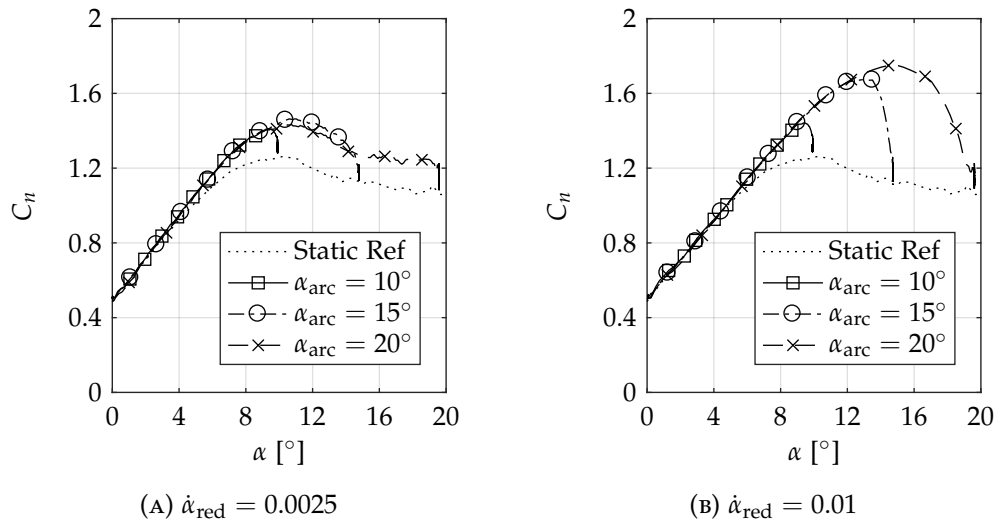
FIGURE 3.35: Differences in NACA 63-619 blade section normal loading in the baseline configuration for two reduced pitch rates and varying ramp arc incidences.

variations for different reduced pitch rates and ramp arcs. Results are shown in Figure 3.35 for ramp up motions at reduced pitch rates of 0.0025 and 0.01, starting at 0° and pitching though 10°, 15° and 20°.

From inspection of the normal loading curves, the loading dependency on the two parameters can be obtained. For the case where the maximum aerofoil incidence does not exceed the stall static angle, $\alpha_{\mathrm{arc}} = 10°$, a minimal difference is seen between the two pitch rates. However, for greater ramp arcs the peak normal loading behaviour begins to become more dependent on the pitch rate.

For the slower pitch rate ($\dot{\alpha}_{\mathrm{red}} = 0.0025$) the dynamic stall angles are all within 1° of the static stall angle, and the peak normal loading ranges from 1.41 to 1.46, compared to the static value of 1.26 – a percentage increase of between 11.6 % and

15.8 %. The overall behaviour is very similar to the static reference, although with an almost constant offset though the separated flow region.

With increased pitch rate a significant peak load increase becomes apparent for the two larger aerofoil movements. The dynamic stall angles are delayed to 13.5° and 14.9°, with the peak aerofoil loads reaching 1.67 and 1.75 – a percentage increase of 32.3 % and 38.7 % respectively. In summary, as the aerofoil movement and reduced pitch rate are both increased, the aerofoil peak normal loads ($C_{n_{max}}$) will increase, but only up until the limit linked to the stall vortex convection speed is reached.

3.6 BLADE SECTION PITCHING MOMENT AND TORSIONAL EFFECTS

The primary design aim for a tidal turbine blade is to produce a blade which generates an optimal power output over the turbine operating range. This is achieved by defining an optimal lift-to-drag ratio across the span of blade sections, alongside minimising the sensitivity of the final design loading parameters to surface roughness due to biofouling.

Although this thesis is primarily focussed on the turbine blade section loading, it is also of interest to consider the chordwise torsional components affecting the blade during turbine operation. The aerofoil pitching moment coefficient provides information on the blade section torsional behaviour. As only blade sections have been tested, not a full three-dimensional blade, no conclusions regarding the spanwise torsional effects, such as root bending moment, will be drawn from the available datasets. During the turbine design and development phase, the local blade section pitch axis, which varies along the blade span, is selected to minimise any potentially undesirable blade loading from the blade section pitching moments. The inboard blade section has a pitch axis at a chordwise location of approximately $x/c = 0.35$ and an approximate chordwise location of $x/c = 0.3$ for the outboard blade section pitch axis. These values are used when determining the pitching moment coefficients.

This section of the chapter will present a short analysis of chordwise torsional effects on the blade section, based on the pitching moment coefficient. As with the previous analysis in this work, both the baseline and rough configurations, for both unsteady and dynamic test cases, are presented.

3.6.1 STATIC PITCHING MOMENTS

The static blade section pitching moment coefficients, around the defined blade section pitch axes, are presented in Figure 3.36 as a function of the aerofoil incidence. For each of the tested sections, the absolute pitching moment coefficient values, for both the baseline and rough configuration, are shown in the left hand column. The change in pitching moment coefficient from the clean baseline to the fouled state is shown

in the right hand column. The aerofoil nose-up direction is denoted by a positive pitching moment.

As discussed previously in Chapter 2, the blade section pitching moment is largely independent of the aerofoil chordwise shear stress distribution. Therefore, it can be assumed that, even with the roughness included on the wind tunnel models, a reliable measurement of the pitching moment can be obtained from the aerofoil normal pressure distribution alone. The overall trend displayed in the pitching moment results over the turbine operating range is for the surface roughness to decrease the blade section nose-down pitching moment.

First, the pitching behaviour of the two thinner outboard blade sections is considered. As would be expected for two aerofoils with a similar geometry, the moment behaviour of the NACA 63-619 and AHH 19 sections are alike, with the largest variations over the attached flow region, but diminishing beyond stall. Over the blade section operating incidences, the effect of biofouling on the blade surface will be to decrease the pitching moment coefficient, hence the blade will become slightly less stable as the nose-down restoring moment is consequently decreased. The role of roughness on the blade section moment behaviour can be explained from inspection of the static loading results shown in Figures 3.1 and 3.2. For the attached flow region incidences, the effect of the surface roughness is to reduce the peak suction pressure at the blade leading edge and reduce the magnitude of the nose-down moment acting on the blade section. Beyond stall, the suction pressure peak moves rapidly towards the leading edge and the roughness elements will be predominantly in separated flow, hence a negligible post stall change in the blade section static pitching moment.

For the thicker inboard AHH 32 blade section, the static loading and pressure distributions in Figure 3.3 show roughness on the aerofoil lower surface is contributing to a modification in the aerofoil pitching moment, to an extent greater than that observed on the two thinner aerofoils. In the attached and pre-stall region, the reduction in the upper surface suction pressure peak and increased mid-chord loading on the aerofoil lower surface, albeit with a shorter moment arm, are combining to reduce the nose-down moment acting around the blade section pitch axis. Stall for the roughened configuration is being significantly delayed and this is reflected in the pitching moment coefficient curve at the higher blade section incidences.

An overview of the pitching moment coefficient parameters are presented in Table 3.7, for the outboard blade sections, and Table 3.8, for the inboard blade section.

The effect of biofouling on the blade surface will be to decrease the nose-down moments acting on the individual blade sections by up to 50 %. This will need to be taken into account when determining the required drive torque of the blade pitch control system. The presented results suggest that as the fouling level on the blade surface increases as increase pitch control torque may be required for decreasing blade incidence and, conversely, a decreased torque for increasing incidence.
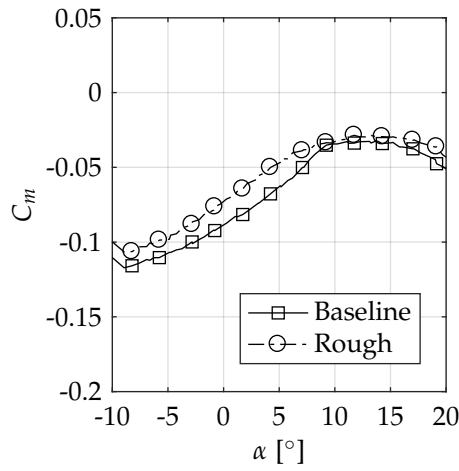
(A) NACA 63-619 C_m
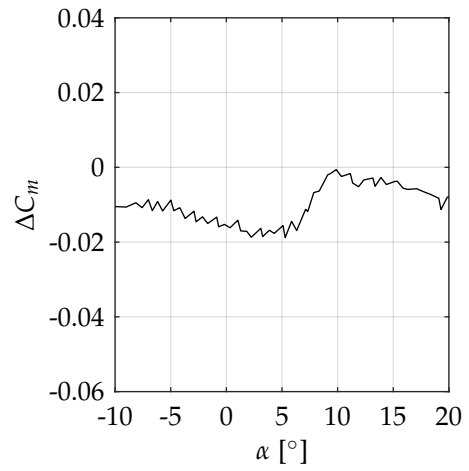
(B) NACA 63-619 ΔC_m
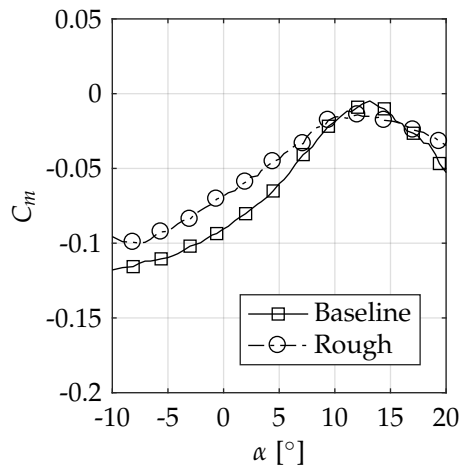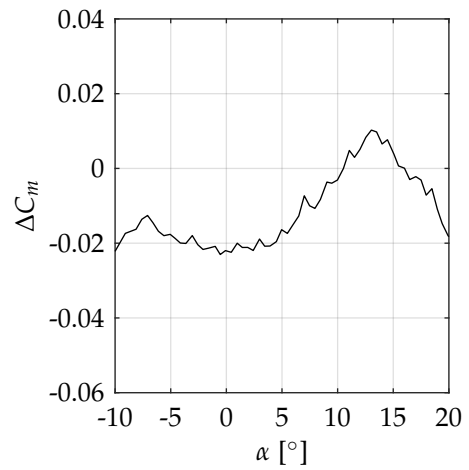
(C) AHH 19 C_m

(D) AHH 19 ΔC_m
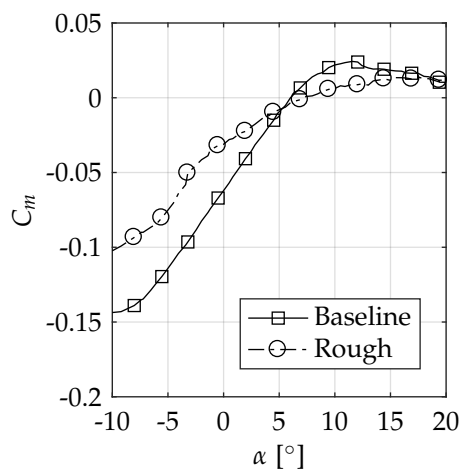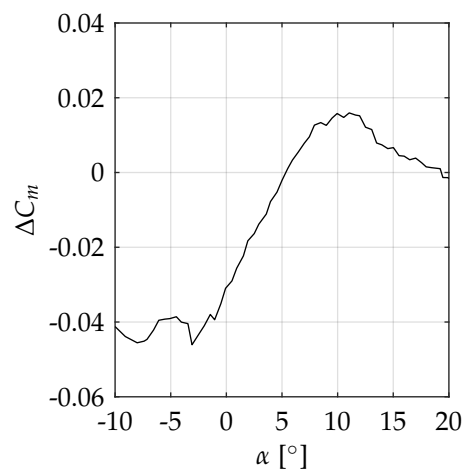
(E) AHH 32 C_m

(F) AHH 32 ΔC_m

FIGURE 3.36: Static pitching moment coefficients for the baseline and rough configurations and the change in pitching moment coefficient.

TABLE 3.7: Summary of outboard static aerofoil pitching moment coefficients.

Parameter	NACA 63-619			AHH 19		
	Baseline	Rough	Δ	Baseline	Rough	Δ
$C_{m_{\max}}$ [–]	-0.033	-0.029	+0.004	-0.005	-0.014	-0.009
C_{m_0} [–]	-0.089	-0.073	+0.016	-0.091	-0.069	+0.022

TABLE 3.8: Summary of outboard static aerofoil pitching moment coefficients.

Parameter	AHH 32		
	Baseline	Rough	Δ
$C_{m_{\max}}$ [–]	0.024	0.013	-0.011
C_{m_0} [–]	-0.062	-0.031	+0.031

3.6.2 DYNAMIC PITCHING MOMENTS & PITCH CYCLE DAMPING

Chordwise torsional effects on the local blade section are investigated by determining the response of the unsteady aerofoil pitching moment over a pitch cycle. The blade section torsional stability is widely studied (Green et al., 2011; Bowles et al., 2014) by considering the two-dimensional cycle-integrated aerodynamic pitch damping coefficient associated to the work cycle or, in other words, the net aerodynamic work per cycle of oscillation (McCroskey, 1981). The measure of work done over the pitch cycle (W) is given in Equation 3.1 in terms of the aerofoil pitching moment (M) and incidence, and expressed in coefficient form in Equation 3.2.

$$W \equiv \oint M \, \mathrm{d}\alpha \tag{3.1}$$

$$C_w = \oint C_m \, \mathrm{d}\alpha \tag{3.2}$$

This leads to the two-dimensional aerodynamic cycle pitch damping coefficient (Ξ) given in Equation 3.3 as a function of the pitch cycle work and amplitude. Traditionally the nomenclature used for this aerodynamic damping term is Ξ_{a_2} or simply a_2.

$$\Xi_{a_2} = \Xi = \frac{-C_w}{\pi \alpha_1^2} \tag{3.3}$$

However, a disadvantage of this approach is that no information on the instantaneous damping is obtained. A pitch cycle with a positive aerodynamic cycle damping value can still present with loops of a negative contribution (Green et al., 2011; Bowles et al., 2014). Inspection of the relationship between the aerofoil pitching moment, around the pitch axis and with positive nose-up, and incidence indicates the behaviour of the aerodynamic damping, which manifests itself in the pitching moment plots as a

counter-clockwise loop for positive damping and a clockwise loop indicating negative damping (Carta, 1967). In terms of work done, during loops of positive damping work is being done by the blade on the flow and, conversely, work being done by the flow on the blade results in negative damping. It is usual for the unstalled portion of the blade cycle to be stable.

The unsteady pitching moment coefficients for the selected test cases are shown in Figures 3.37, 3.38 and 3.39 as a function of the aerofoil angle of attack, for the NACA 63-619, AHH 19 and AHH 32 blade sections respectively. The static pitching moment coefficient curves are included for reference.

The individual aerodynamic pitch cycle damping parameters are shown in Figure 3.40 for all oscillatory test cases available from the experimental database. The left hand column presents the damping parameter calculated for the baseline configuration and the change in aerodynamic damping once roughness is added to the blade section is presented in the right hand column. A positive change in the cycle damping indicates that the pitch cycle is becoming more stable.

Considering the pitching moment coefficients for the outboard blade sections first, the difference between the typical and limiting baseline test cases highlights the effects of increasing stall penetration and reduced frequency. For the limiting cases, the point of moment break close to the static stall angle is more pronounced and the magnitude of the moment loop is significantly increased compared to that for the typical case. It also appears that the AHH 19 section is entering a small, but negatively damped, loop at the highest pitch cycle incidences. McCroskey (1981) has previously identified the light stall regime as having the greatest tendency towards negative aerodynamic damping. From inspection of the results, it can be seen that the effect of surface roughness on the blade outboard sections is to improve the stability of the limiting case pitch cycle and decrease the moment amplitude during the pitch cycle for both cases.

The limiting case for the inboard blade section is approaching the deep stall regime, where vortex-shedding dominates and loading is less sensitive to the aerofoil motion and geometry (McCroskey, 1981). From inspection, a significant loop of negative damping can be seen for the baseline configuration, but again the effect of the blade surface roughness is to stabilise the pitch cycle, and in this case the negative damping loop is removed.

The effects of the blade section geometry and motion can be observed in the aerodynamic cycle damping parameter, shown in the left hand column of Figure 3.40. On thicker blade sections from a tidal turbine blade, which exhibit a trailing edge stall mechanism (McCullough and Gault, 1951), the onset of stall is a more gradual process and unsteady effects tend to suppress the separation process more than an aerofoil exhibiting a leading edge stall mechanism. The more gradual the progression of the trailing edge separation, the less likely negative aerodynamic damping will

(A) $k = 0.05$, $\alpha = 5° \pm 4°$

(B) $k = 0.1$, $\alpha = 10° \pm 6°$
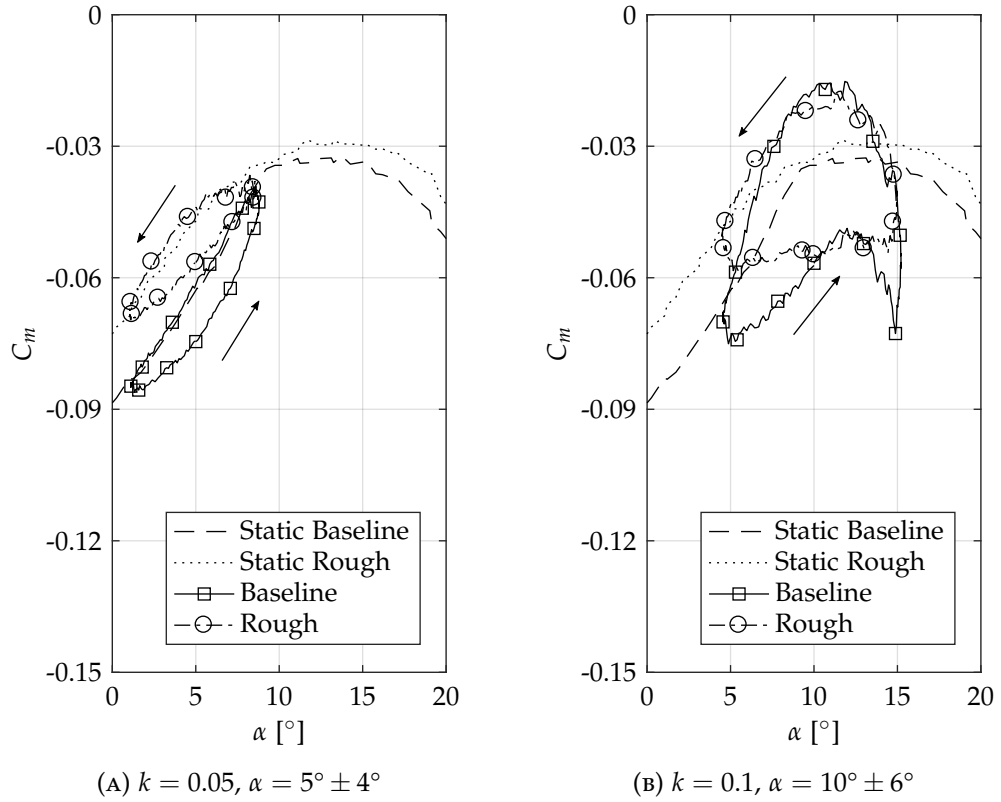
FIGURE 3.37: Unsteady pitching moment coefficient for selected baseline and rough NACA 63-619 datasets.

(A) $k = 0.05$, $\alpha = 5° \pm 4°$

(B) $k = 0.1$, $\alpha = 10° \pm 6°$
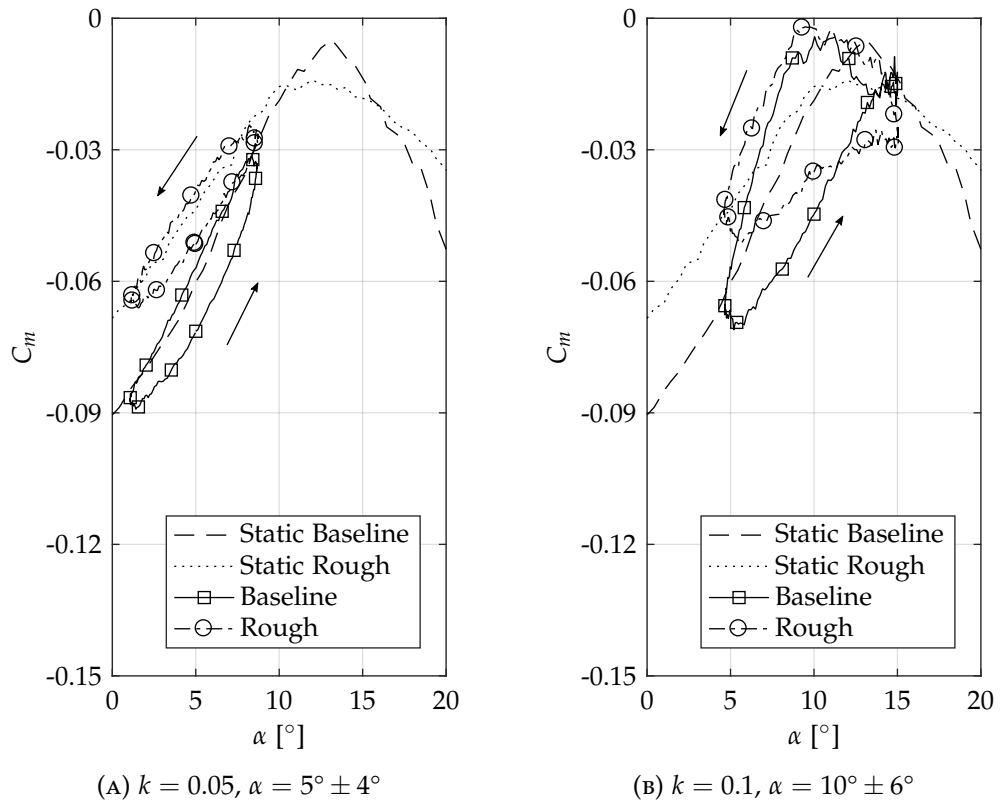
FIGURE 3.38: Unsteady pitching moment coefficient for selected baseline and rough AHH 19 datasets.

(A) $k = 0.1$, $\alpha = 8° \pm 2°$ (B) $k = 0.2$, $\alpha = 12° \pm 10°$
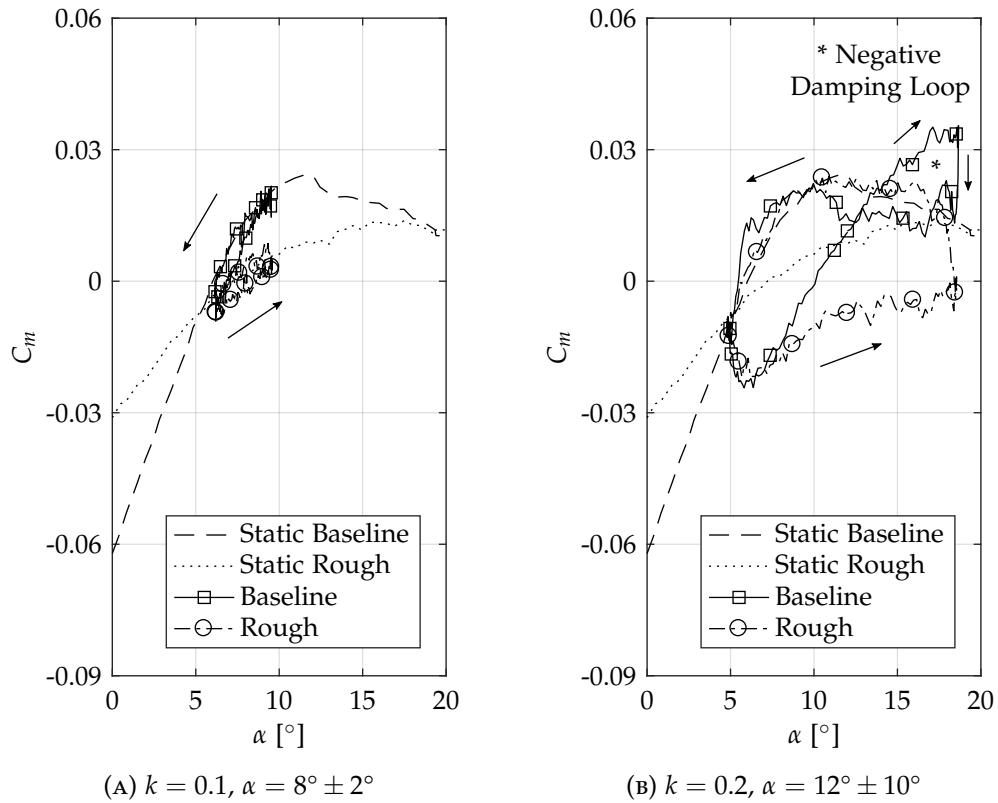
FIGURE 3.39: Unsteady pitching moment coefficient for selected baseline and rough AHH 32 datasets.

occur during the pitch cycle (McCroskey, 1981). Therefore, compared to a thinner aerofoil, a thicker blade section would be expected to exhibit increased aerodynamic damping (Leishman, 2000). Furthermore, it has been reported for helicopter aerofoil sections the pitch cycles in the light stall regime have a greater tendency to produce an unstable damping response, while the deep stall regime is more aerodynamically stable (McCroskey et al., 1981), but not enough data from this investigation is available to confirm this for the tested blade sections as the deep stall regime is largely beyond the normal turbine operating range.

A strong dependency on both the motion reduced frequency and mean pitch cycle incidence is seen for the damping parameter. For an equivalent pitching motion, a higher reduced frequency will produce a more positive value for the aerodynamic cycle damping. In terms of the effect of surface roughness on the damping behaviour, a contrasting result is observed between the inboard and outboard blade sections. The cycle damping of the outboard blade sections reduces with increasing incidence and are largely independent of the reduced frequency, hence rotor speed, but remain positive for all investigated test cases, while the inboard section damping is significantly improved at higher levels of stall penetration and, as highlighted previously, is resulting in a significantly more stable pitch cycle at incidences above stall.

(A) NACA 63-619 Ξ

(B) NACA 63-619 $\Delta\Xi$

(C) AHH 19 Ξ

(D) AHH 19 $\Delta\Xi$

(E) AHH 32 Ξ

(F) AHH 32 $\Delta\Xi$
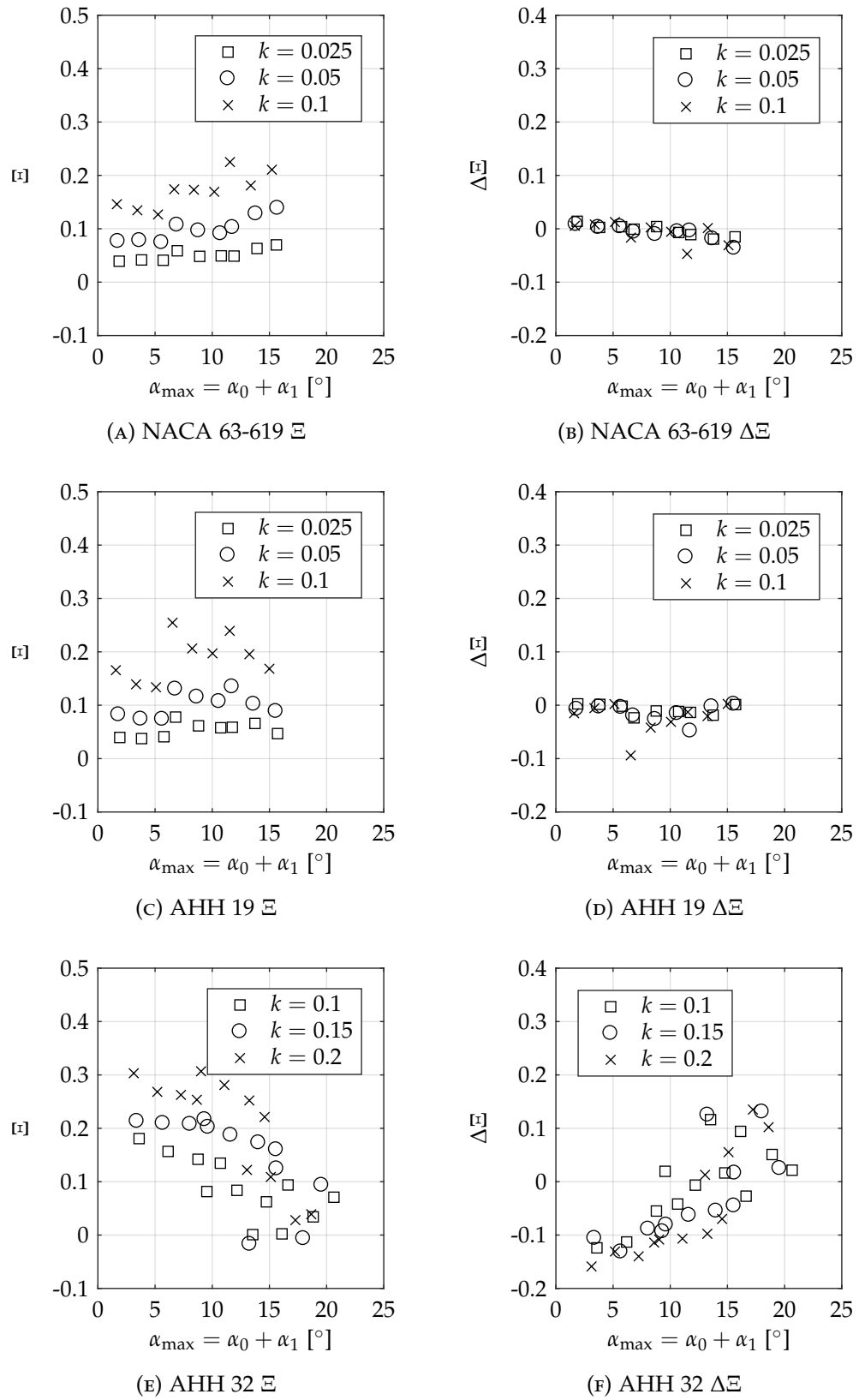
FIGURE 3.40: Aerodynamic cycle damping for the baseline blade configuration and the effect of roughness on the parameter.

3.7 CHAPTER SUMMARY

This chapter has investigated and presented the impact of marine biofouling on both steady and dynamic loading parameters for three tidal turbine blade sections. Comparisons have been drawn between the calculated loads for a baseline configuration, which is aerodynamically smooth, and a rough configuration, which is representative of the widely distributed microfouling layer which will form on the submerged turbine blades. The main findings from this chapter are now summarised.

- The static force coefficients and pressure distributions for each blade section, in both the baseline and fouled configurations have been presented. For the two thinner aerofoils, fouling has delayed the static stall angle by 2.3° and 1.4°, and reduced the maximum normal force coefficient at stall by 0.20 and 0.16, for the NACA 63-619 and AHH 19 blade sections respectively. Roughness on the AHH 32 aerofoil is significantly delaying static stall by 9.5° and a reduction of 0.15 is observed for the peal normal force coefficient at stall.

- The lift curve slope is being reduced to a greater extent than that seen in previous studies for leading edge roughness on wind turbine blade sections.

- A light level of surface fouling increases the minimum pressure drag coefficient by 0.007, 0.009 and 0.008, for the NACA 63-619, AHH 19 and AHH 32 blade sections respectively. A corresponding decrease is identified in the maximum lift-to-drag ratio for each blade section.

- From the results of the static blade section loading presented, it can be confirmed that the tidal turbine blade section investigated are demonstrating a sensitivity to a light level of marine biofouling.

- A discussion on the blade section design objective suggests that as the geometry is sensitive to biofouling, then the aerofoil design point should be moved towards the fouled state to reduce the cumulative performance loses over the turbine life cycle.

- The turbine blade will enter into a light dynamic stall regime, but only at the limits of the turbine operating envelope. The unsteady blade section load cycle can be described with the static loading at the equivalent incidence plus a second-order dynamic effect, dependent on the turbine rotational speed and level of stall penetration.

- Compared to the equivalent static blade section loading, the baseline peak unsteady normal loads are approximately 10 % and 20 % greater at the typical turbine operating conditions, for the outboard and inboard blade sections respectively. These magnitudes increase to approximately 20 % and 80 % at the limiting operating conditions. There is no significant change identified for the corresponding values when the blade section becomes fouled.

- Roughness reduces the magnitude of the normal loading hysteresis loop, as well as dampening the unsteady flow effects. The position of the moment break in the pitch cycle does not change significantly, but the onset of fully stalled flow is less abrupt and the flow reattaches sooner on the pitch cycle downstroke.

- No dominant dynamic stall vortex is observed convecting over the blade upper surface in the unsteady pressure distributions for the investigated cases presented. It is suggested that the added-mass terms associated with accelerating the fluid surrounding the aerofoil are dominating the non-circulatory loading component.

- The decrease in the peak unsteady normal force coefficient due to blade surface fouling is shown to be independent of the turbine rotational speed. This suggests that the decrease in the peak normal blade loading can be evaluated at all points in the turbine operating envelope.

- Surface biofouling on the blade with reduce the restorative nose-down pitching moment acting around the local blade pitch axis and improve the pitch cycle damping, particularly for the inboard blade section towards the limits of the turbine operating envelope.

CHAPTER 4

IMPACT OF A SINGLE BARNACLE ON BLADE SECTION LOADING & FLOW

It has been shown in the previous chapter what the impact of a light level of surface roughness, or microfouling, is on the performance of three tidal turbine blade sections. However, this is only part of the potential problem when considering biofouling on the performance of the turbine. Once an initial fouling layer is established, or the blade surface degrades, then the blade surface becomes susceptible to larger scale macrofouling, mainly from encrusters, such as barnacles and molluscs, colonising the developing surface. This chapter of the thesis is going to extend the analysis presented so far by considering the case of when a barnacle attaches to the upper surface of the blade section. The objective is to evaluate how the presence of the barnacle alters the pressure distribution on the aerofoil surface, hence the blade section loading.

To recap, unlike the analysis presented in the previous chapter where three blade sections were tested, only the AHH 19 section has been considered in this part of the investigation. The barnacle model was positioned on the aerofoil upper surface, at 60 % chord and 25 % span, in both the clean and rough configurations described previously. Due to a limitation in the number of available channels on the pressure scanner, only a single barnacle could be included on the model. However, this will still provide a useful insight into the detrimental impact of the specific fouling cases investigated in this chapter.

This chapter begins with a review of the role of roughness on the flow over a body, followed by the presentation and discussion of the experimental investigation findings. Both the chordwise pressure distributions, and resulting blade section loading, and the surface pressure distributions around and over the barnacle body are considered.

4.1   A REVIEW OF THREE-DIMENSIONAL ROUGHNESS ELEMENTS

Surface roughness on an aerofoil, or flat plate, is known to result in premature boundary layer transition (Kerho and Bragg, 1997). In the case of isolated three-dimensional roughness elements, transition in the element wake can be predicted by correlations using the roughness-based critical Reynolds number (Tani, 1969). For roughness-based Reynolds numbers greater than the critical value, transition would be expected just downstream of the element, and the unsteady disturbance growth rate increases with increasing roughness-based Reynolds number (Ergin and White, 2006). Two approaches to the research are usually followed: investigations into the role of the roughness size and location on the transition location and performance (Roberts and Yaras, 2005); and investigations into the underlying fluid mechanisms which result in premature transition (Klebanoff et al., 1992). The majority of research into the fluid mechanisms has been limited to flat plates with zero pressure gradient and roughness heights smaller than the laminar boundary layer thickness.

Jacobs (1934) investigated larger scale protuberances, up to $0.0125c$ height, at different chordwise locations on a NACA 0012 aerofoil, with minimal change in lift for lower surface protuberances, but large drag increases, particularly for roughness height greater than $0.005c$ in the forward portion of the upper surface. Other work on aerofoil performance has included: leading edge ice accretion (Bragg et al., 2005; Cummings and Bragg, 1996); surface imperfections on gas turbine blades (Roberts and Yaras, 2005); and bio-inspired leading edge designs (Johari et al., 2007).

Barnacle fouling is not limited to the leading edge region of the blade, has a considerably larger roughness height of approximately $0.02c$, and will be in a turbulent, not laminar, boundary layer on the tidal turbine blade. Although the roughness-based Reynolds number will be approximately two orders greater than the critical value, in this work the barnacle is, for the most part, downstream of the aerofoil transition, therefore would not be expected to play a role in the transition process and quantifying the loading performance is the main objective.

Despite significantly influencing the hydrodynamic loading of submerged offshore support structures (Theophanatos and Wolfram, 1989) and the efficiency and cost of maritime operations (Schultz et al., 2011), and now the performance of tidal turbines (Orme et al., 2001), the effect of barnacle fouling has not been widely reported in the available literature. Furthermore, the published data have focussed on static loading and not the dynamic loading a tidal turbine blade experiences, yet understanding biofouling, from both an engineering and ecological perspective, has been identified as a key operability challenge to advance the tidal power technology currently available (Mueller and Wallace, 2008; Ng et al., 2013).

Investigations have primarily been concerned with quantifying the barnacle fouling effect based on lift and drag measurements, including that of Theophanatos and Wolfram (1989) which suggests that even the lightest of marine fouling may cause a

substantial increase in drag. However, they conclude that an increase in hydrodynamic drag with surface cover is non-linear and depends primarily on the distribution of the roughness elements.

In terms of a tidal turbine, Orme et al. (2001) studied the effects of barnacle fouling on a NACA 4424 aerofoil in a wind tunnel experiment, at a Reynolds number of 4×10^5. Arrays of conical extrusions, of different size and density, were applied to the model to represent the fouling, which was informed by a sample collection at a local marine site. The values for roughness element height ranged from $0.0035c$ to $0.0285c$. As expected, the performance of the aerofoil decreased as fouling variables increased, with a reduction in efficiency of 25 % for low level fouling increasing to 70 % at higher levels. The trend in drag increase was not seen in the lift coefficient which initially decreased with the introduction of fouling, but showed little variation with increasing fouling severity. In addition, the stall angle was observed to be delayed by approximately 10°. This paper remains the major reference on the subject over fifteen years on from its publication, but does not provide any understanding of the flow behaviour.

More recently, CFD has been utilised to investigate the systematic changes in the flow structure and underlying flow mechanisms – not just the effect on the aerofoil loading. Khor and Xiao (2011) used the work of Orme et al. (2001) as the basis for a numerical simulation, using a standard κ-ϵ turbulence model, of the fouling effects on the NACA 4424 aerofoil, and were generally in good agreement with the previous work. Alongside a lift-to-drag ratio reduction of up to 80 %, it was identified that with an increase in fouling, the stagnation point moves forwards towards the leading edge and the area towards the trailing edge experiences significant separation, while areas of favourable pressure gradients decrease resulting in earlier separation, lower lift and stalled flow. However, both these investigations only considered widely distributed barnacle fouling and did not include the likely blade microfouling. Therefore, behaviour attributed to the barnacle may not be strictly correct.

It has been identified that there is a gap in the knowledge concerning both the static and dynamic performance of an aerofoil in a macrofouled state. The aerofoil loading results in this chapter are computed by the method outlined in Section 2.4.2, but with pressure distributions modified to include the barnacle measurements. Barnacles appear in the latter stages of the fouling process and this chapter will discuss and quantify what effect the addition of a barnacle to the surface has on the blade section loading compared to the equivalent cases with no barnacle. The chapter begins by presenting the influence of the barnacle on the chordwise pressure distribution. As with the previous chapter, both static and oscillatory cases are considered in both the clean and rough configurations, showing the change in aerofoil section performance which can be attributed solely to the presence of the barnacle on the aerofoil surface. The chapter continues with a discussion of the three-dimensional aspects of the flow

(A) AHH HS1000 Turbine at EMEC

(B) Identified Barnacle Fouling Locations
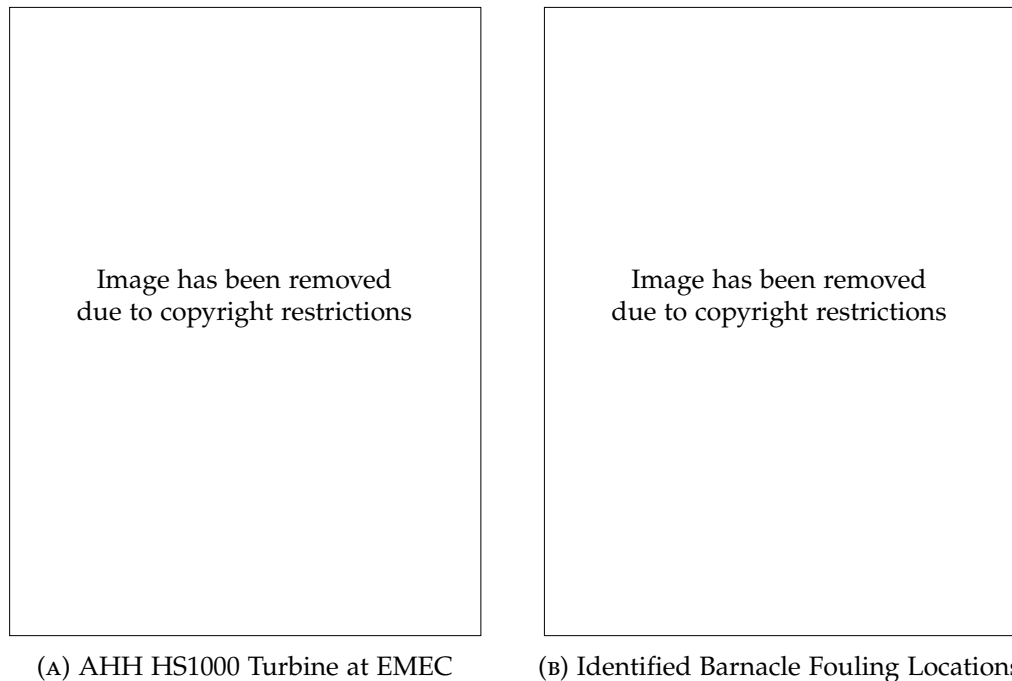
Figure 4.1: Barnacle biofouling on a deployed tidal turbine blade. Image supplied by AHH.

around the barnacle and concludes with a summary of the main findings.

4.2 BARNACLE LOCATION ON THE AEROFOIL

Previous investigations (Orme et al., 2001; Khor and Xiao, 2011) into barnacle fouling have assumed evenly distributed fouling over both aerofoil surfaces, including the upper surface leading edge. However, this is in contrast to evidence available in this project. Although difficult to measure experimentally, it is thought that the shear forces acting on the blade surface are preventing barnacles from attaching on the upper surface of the blade towards the leading edge. It is only at chordwise locations aft of the adverse pressure gradient, where the local shear stress at the wall decreases, and in separated flow where the shear stress is low enough for the barnacle to attach. This is supported by evidence of barnacle fouling distribution on a deployed tidal turbine blade, as shown in Figure 4.1, with the upper surface barnacle fouling falling into two distinct zones where no fouling is identified over the forward portion of the blade, but is located over the aft 40 % of the blade.

The image on the left of Figure 4.1 was taken during the recovery of the AHH HS1000 demonstrator device from its test berth at EMEC, and the drawing on the right highlights the location and distribution of barnacle fouling on the blade, and includes identified barnacles and calcareous membranes, where the barnacle has been dislodged. The assumption of the 60 % chord barnacle fouling limit is clearly identified and marked on the diagram. The device was deployed at EMEC during 2011 and recovered in early 2015 on completion of the test programme (EMEC, 2017).

4.3   TEST CASE DESCRIPTORS

Continuing with the convention from the previous chapter, the following test case descriptors are used to differentiate between the various sets of presented data, where the *clean* and *rough* configurations keep their prior meaning, as described in Section 2.2.3.

- *Baseline*: Aerofoil with no contribution from the barnacle, in both clean and rough configurations, as presented in Chapter 3.

- *Barnacle*: Aerofoil including the influence of the barnacle, in both clean and rough configurations.

To isolate the role of the barnacle in the four test configurations above, the following comparison cases were investigated, and summarised in Table 4.1.

- *Case 1*: *Baseline* vs. *Barnacle* in the clean configuration.

- *Case 2*: *Baseline* vs. *Barnacle* in the rough configuration.

In addition, a third case was included which is illustrative of the blade section hydrodynamic performance decrease from the blade section design specification to the worst fouling case investigated.

- *Case 3*: *Baseline* in the clean configuration vs. *Barnacle* in the rough configuration.

Table 4.1: Static comparison test cases for barnacle.

Case	Configuration A	Configuration B
1	Baseline Clean	Barnacle Clean
2	Baseline Rough	Barnacle Rough
3	Baseline Clean	Barnacle Rough

Of the three cases, Case 1 is least likely to occur on the turbine blade, but is included here for completeness. The time frame of the fouling process suggests that the blade surface will be roughened and degraded to a certain extent by the time a barnacle has attached to the surface and matured to a larger size (Vance et al., 2014; Miller and Macleod, 2016). Therefore, it seems less likely that barnacles would colonise a clean blade.

In terms of understanding the change of tidal turbine operational performance, results from Case 3 will be the most beneficial. Blade design and turbine modelling relies on high quality aerofoil data and generally clean aerofoil performance polars are used for this purpose. The comparisons from Case 3 will highlight the expected aerofoil performance degradation at a future point in the turbine life cycle, compared to the initial design input. However, a caveat of this dataset is that the time taken for a turbine blade to reach a certain level of fouling is dependent on multiple external factors and it is unknown how long it will take a blade to reach the level of fouling

as tested in this series of experiments (Miller and Macleod, 2016). Additionally, the potential level and distribution of biofouling covers a large parameter space and it has only been possible to investigate a limited set of configurations.

For considering the influence of the barnacle on dynamic blade loading and stall behaviour, the same two test cases as those selected for the AHH 19 blade section in the previous chapter (See Section 3.2) are presented.

- $k = 0.05$, $\alpha = 5° \pm 4°$. Run Numbers: 21012782 (Clean) and 21113272 (Rough).

- $k = 0.1$, $\alpha = 10° \pm 6°$. Run Numbers: 21012573 (Clean) and 21113402 (Rough).

To recap, the first corresponds to the typical blade motion determined to have the highest probability of occurring during turbine operation at a moderate reduced frequency, and the second is a limiting case corresponding to the test case with highest stall penetration and level of unsteadiness.

4.4   CHORDWISE PRESSURE DISTRIBUTIONS

This section presents a description and discussion based on the two-dimensional pressure distribution around the aerofoil section and barnacle model. Pressure measurements from the barnacle are combined with the principal aerofoil pressure measurements to determine the impact of the barnacle on the integrated aerofoil loads.

It is prudent at this point to briefly describe the reasoning for the analysis method outlined in the following pages. The flow field measured around the barnacle is three-dimensional and two main options are appropriate for combining this data into the two-dimensional flow around a blade section. The first approach would represent the two-dimensional pressure field over a discrete barnacle protuberance and requires the three-dimensional pressure field around the barnacle to be interpolated onto the two-dimensional aerofoil pressure distribution. The second approach, and the one followed in this work, inserts the chordwise pressure distribution over the barnacle into the blade section pressure distribution and is representative of a continuous spanwise extrusion of the barnacle cross-section across the blade, similar to a quasi two-dimensional strake. This is therefore not representative of a single barnacle, but has the advantage of simulating an engineering worst design case.

The focus of the discussion will primarily be on the aerodynamic loading and quantifying the changes due to the barnacle, but will also consider the salient features of the flow structure. Following the presentation of the steady and unsteady blade section loading, the limitations of the pressure measurement method are analysed and discussed.
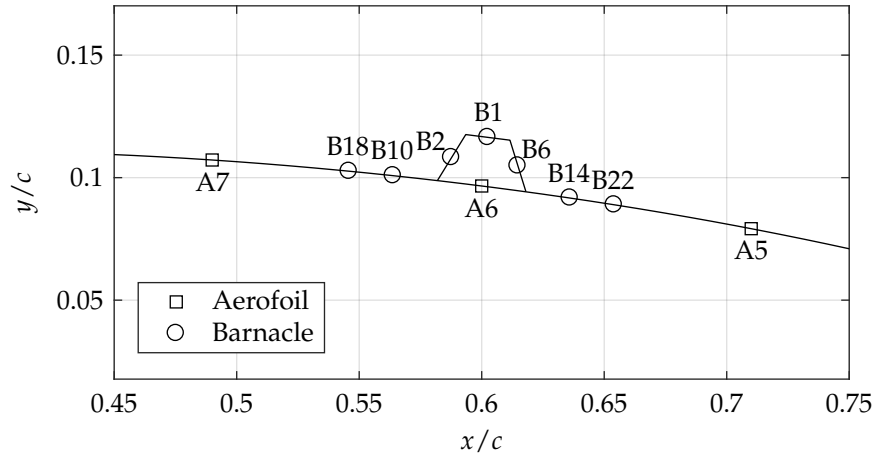
FIGURE 4.2: Location and numbering of barnacle pressure tappings relative to aerofoil surface, where A and B denote the aerofoil and barnacle respectively.

4.4.1 COMBINING AEROFOIL & BARNACLE PRESSURE MEASUREMENTS

The spanwise location of the barnacle is offset from the model midspan, where the principal experimental measurement array is positioned. To include the effects of the pressure measurements around the barnacle on the aerofoil two-dimensional pressure distribution, the seven chordwise barnacle pressures (Locations B18, B10, B2, B1, B6, B14 and B22, from the forward position aft respectively) are inserted into the aerofoil pressure distribution, as shown in Figure 4.2.

To achieve this the aerofoil pressure measurement from Transducer 6 is discarded and the panel lengths for Transducers 5 and 7 are reduced, allowing the pressure distribution over the chordwise range $0.537 \leqslant x/c \leqslant 0.663$ to be replaced by the measurements taken from the barnacle. The barnacle panel lengths and gradients are determined and the two-dimensional pressure distribution around the aerofoil, but including the barnacle, is now described by the updated geometry parameters and 38, instead of the original 32, pressure transducer measurements. The locations are renumbered 1 through 38 using the numbering convention in Figure A.4. As the data from both measurement systems were obtained simultaneously, it is appropriate to assume the model and flow parameters (i.e. α and q) are comparable.

Even though a pressure transducer (#15) at the leading edge of the aerofoil was generating an unreliable output signal, and will predominately influence the aerofoil drag measurement, this approach is still valid as the aim is to quantify the role of barnacle fouling on the blade. The assumption in the methodology is that the barnacle will not influence the portion of the pressure distribution towards the leading edge. Therefore, any changes in the aerofoil loading can be attributed as a direct consequence of the pressure variations over the barnacle surface.

4.4.2   RESULTS & DISCUSSION: STATIC (STEADY STATE) DATA

AEROFOIL LOADING

The results for the static loading cases are presented in Figures 4.3 and 4.4, as a function of the aerofoil incidence. The angle of attack range has been reduced to concentrate on the main operating envelope of the turbine blade and only the normal force and pressure drag coefficients are presented. The corresponding pressure distributions, at angles of attack 5°, 10° and 15°, are shown in Figure 4.5, where the x-axis has been limited to the chordwise area of interest around the barnacle and only the upper surface pressure distribution is shown. In the three figures, the left hand column is the clean aerofoil configuration and the right column is the rough aerofoil configuration.

From the results presented, the effect of the barnacle of the static aerofoil loading can now be described in more detail, starting with the normal force. Compared to the baseline case, there is a negligible effect on the aerofoil static normal loading, suggesting that for the test conditions the addition of a barnacle has a minimal effect. The maximum percentage change is less than 2 % of the baseline measurement. This is seen for both the clean and rough configurations, and in particular there is no observed change in the stall process and the post-stall behaviour is indistinguishable from the baseline.

As discussed in the previous chapter, the introduction of surface roughness to the baseline case resulted in a stall delay and a decreased maximum normal force at the static stall angle. However, increasing the roughness level further with the introduction of the barnacle, in both the clean and rough configurations, results in no further deterioration of the blade section normal force characteristics. Therefore, in terms of the aerofoil normal force, the data suggests that for these test variables, the blade section is insensitive to larger scale roughness towards the trailing edge on the blade upper surface. This is particularly evident in the clean configuration where the barnacle is the only roughness element present on the aerofoil surface.

Conversely, the barnacle is having a significant impact on the section drag coefficient due to pressure, but diminishes with increasing angle of attack. A large pressure gradient is seen to be induced, at moderate blade section incidences, across the barnacle body and is leading to downstream flow separation. It is thought that this is a product of the flow mixing due to the barnacle acting as an excrescence. Upstream of the barnacle, the front face of the body is dominated by an area of high pressure, approaching the stagnation pressure ($C_p = 1$) at lower angles of attack, while above and downstream sits an area of lower pressure as the wake behind the barnacle develops.

As the angle of attack is increased, the prominence of the pressure gradient reduces as the flow separation point on the aerofoil surface moves upstream towards the leading edge and the barnacle is increasingly immersed in turbulent separated

(A) Clean Configuration

(B) Rough Configuration
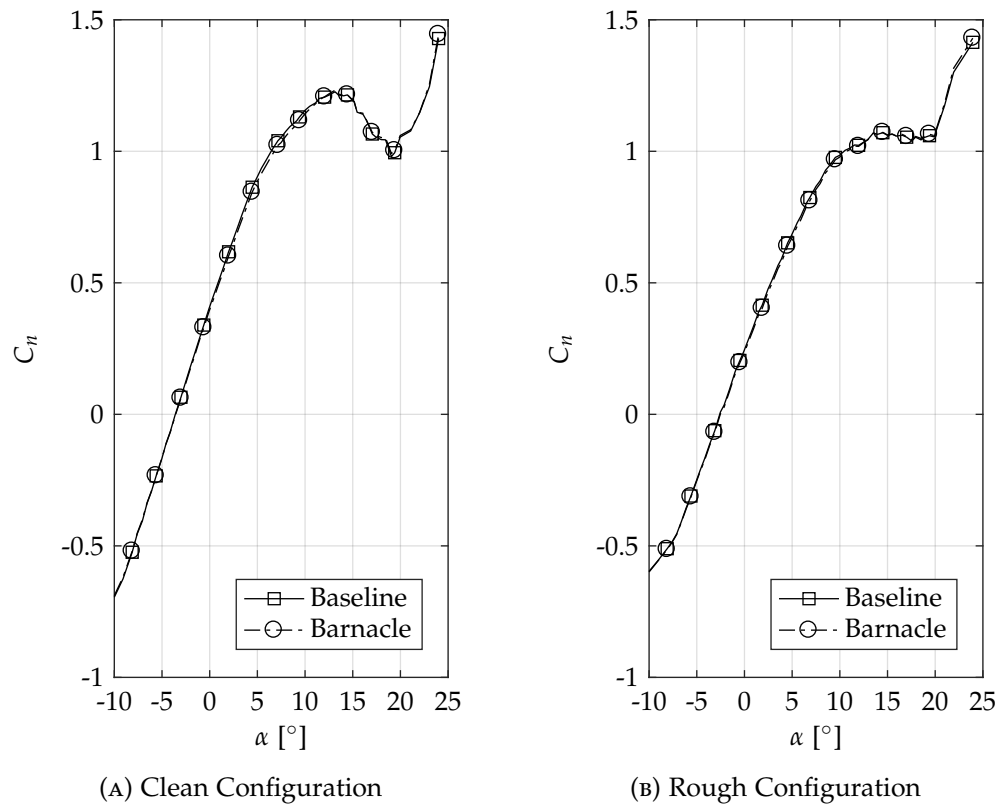
Figure 4.3: Static normal force coefficient for baseline and barnacle datasets.

(A) Clean Configuration

(B) Rough Configuration
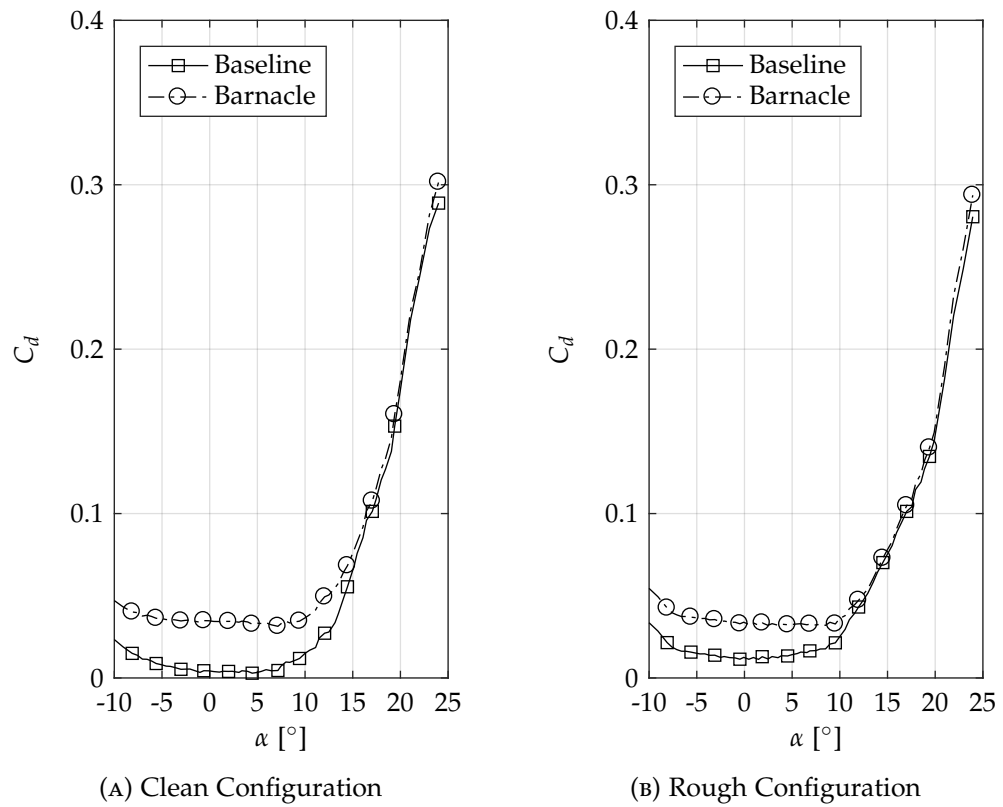
Figure 4.4: Static pressure drag coefficient for baseline and barnacle datasets.
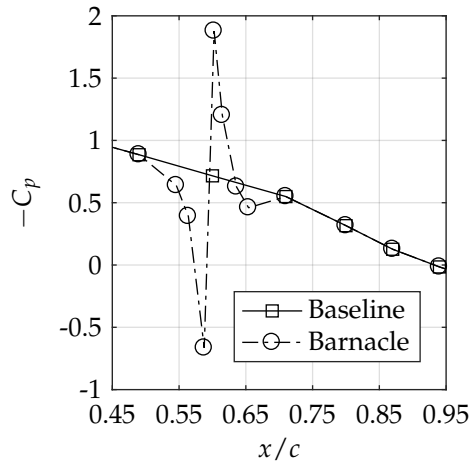
(A) Clean Configuration: $\alpha = 5°$
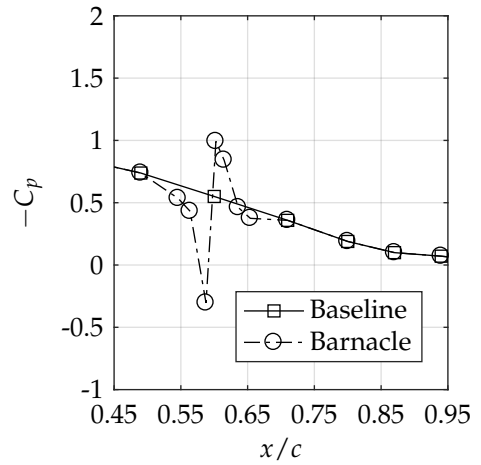
(B) Rough Configuration: $\alpha = 5°$
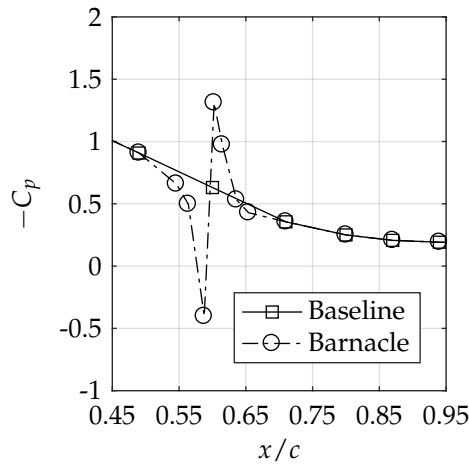
(C) Clean Configuration: $\alpha = 10°$
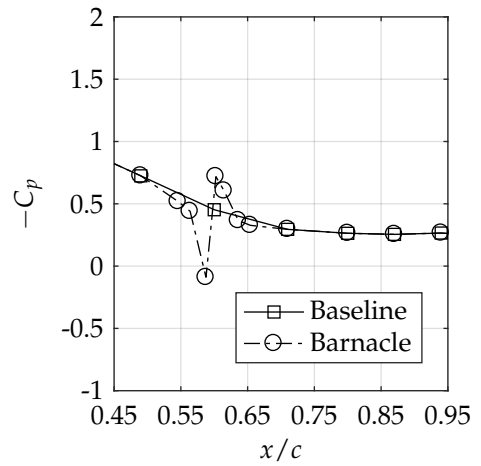
(D) Rough Configuration: $\alpha = 10°$
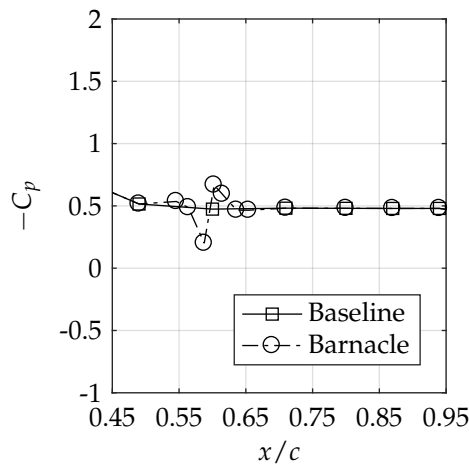
(E) Clean Configuration: $\alpha = 15°$
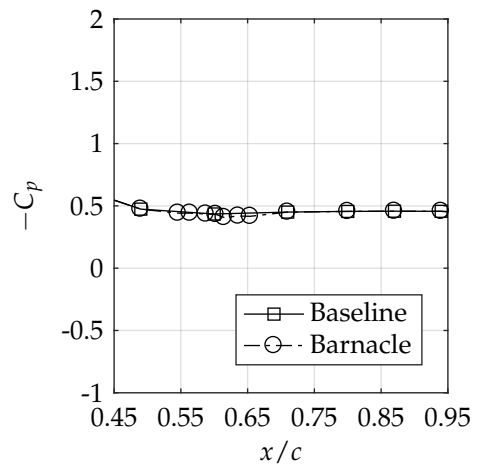
(F) Rough Configuration: $\alpha = 15°$

FIGURE 4.5: Static chordwise pressure coefficients across the barnacle location for selected angles of attack in both clean and rough configurations.
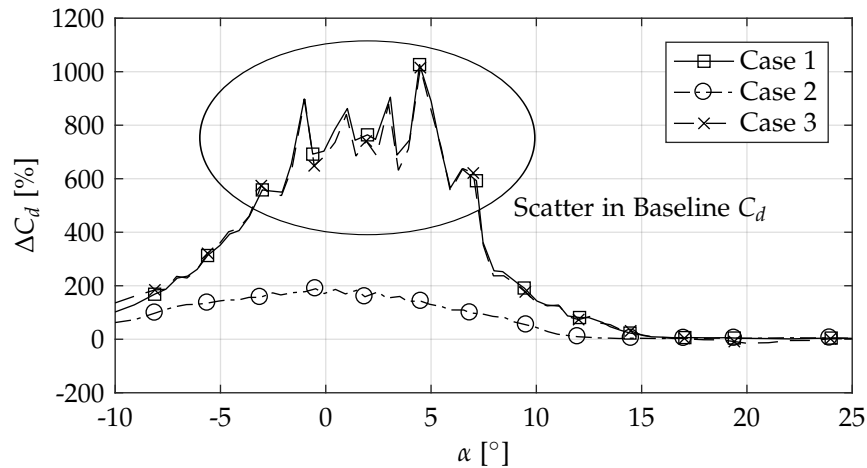
FIGURE 4.6: Percentage increase of static drag coefficient due to barnacle. The three presented comparison cases are detailed in Table 4.1.

flow. In Figure 4.4 it can be seen that the two sets of drag coefficient results from the rough configuration converge approximately 5° earlier than those for the clean configuration. As a consequence of introducing roughness to the aerofoil surface, an increase in the momentum thickness of the turbulent boundary layer is expected, as demonstrated in Figure 4.5 when comparing the clean and rough configurations for the same angle of attack. However, the horseshoe vortex structure generated around the barnacle body will continue to have an impact on the surrounding flow.

The impact of the changes in the section drag coefficient on the aerofoil static performance will now be investigated in more details, specifically quantifying the drag increase and change in lift-to-drag ratio.

DRAG COEFFICIENT INCREASE

Figure 4.6 shows the increase in the section static pressure drag coefficient due to the barnacle. The variation is presented in terms of the percentage increase from the baseline, for each of the three comparison cases, as a function of the aerofoil static angle of attack covering the turbine blade operating range.

For each of the three cases a large increase in drag coefficient is observed, with the biggest variation occurring in the attached flow region, between 0° and 5° for the clean configuration baseline (Cases 1 and 3) and between −5° and 5° for the rough configuration baseline (Case 2). This confirms that, for all cases tested, the drag increase due to the barnacle is highly dependent on the section angle of attack and the evolution of the separated flow on the aerofoil upper surface.

A peak drag increase of 10 times the baseline, at an incidence of approximately 4°, is seen for the two cases referenced to the clean configuration baseline. However, the scatter highlighted in the data across the attached flow region is thought to be due to small variations in the baseline drag measurement being amplified when calculating

the change in the drag coefficient. Therefore, taking this into account, a peak drag increase for these cases of approximately 7.5 times the baseline, at an incidence of 2°, could be expected. Similarly, for the case with the rough configuration baseline, a peak drag increase of 180 % at 0° could be expected. Beyond stall, the variation in drag diminishes rapidly and generally is within 5 % of both the baseline cases. The similarity between Cases 1 and 3 is showing that the drag increment created by the barnacle body has a greater influence on the aerofoil performance than that caused by the zigzag tape. The drag coefficient is constructed from the resolved components of the aerofoil normal and axial (thrust) force coefficients. As the normal force is not changing, the change in drag will be predominantly due to an increase in the aerofoil axial loading.

As with the previous analysis in this thesis, the baseline drag measurement does not include the skin friction component of the drag force. Therefore, the presented drag increases due to the barnacle will be larger than those reference to the total section drag. The chordwise extent of the barnacle influence is not going to significantly change the aerofoil shear force component, therefore it can be assumed that the absolute change in drag coefficient is suitably captured. In terms of the total section drag, the peak drag increase would be expected to be approximately 400 % for the cases referenced to the clean baseline configurations, and unchanged at incidences above the attached flow regime. For the case referenced to the rough baseline configuration, the pressure drag is increased due to the roughness and it is thought that the drag increase, in terms of the total section drag, will be of approximately the same order.

LIFT-TO-DRAG RATIO

The calculated change in the blade section lift-to-drag ratio, for the three cases, is shown in Figure 4.7. Again, the ratio increment is presented as a percentage of the appropriate baseline condition as a function of the aerofoil static angle of attack. For reference, the aerofoil drag polar (C_l vs. C_d) is shown in Figure 4.8.

The results of the changes in the lift-to-drag ratio for the three presented cases are in agreement with the results for the change in normal force and drag coefficients. It has been shown that the barnacle is having a negligible impact on the blade section of the normal force coefficient, and therefore the lift coefficient, so this suggests that the changes in the lift-to-drag ratio can be attributed to the barnacle increasing only the section drag coefficient. This applies for all three cases.

The cases referenced to the clean baseline configuration (Cases 1 & 3) are experiencing a larger increase in drag coefficient, hence the larger decrease in lift-to-drag ratio. A maximum decrease of between 80 % and 90 % over the region of attached flow is identified in these datasets, and similarly, the case referenced to the rough baseline configuration (Case 2), a reduction of up to 60 % could be expected. Due to the changes in the lift-to-drag ratio predominately being a function of the drag
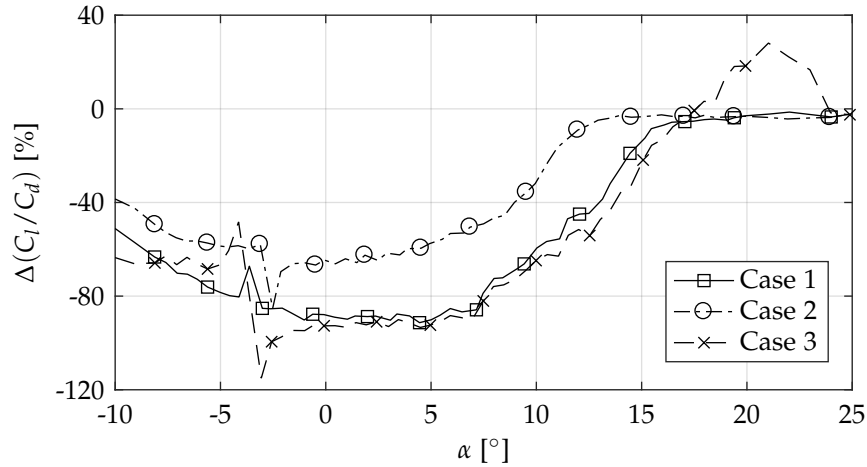
Figure 4.7: Percentage change of static lift-to-drag ratio due to barnacle fouling. The three presented comparison cases are detailed in Table 4.1.

(A) Clean Configuration

(B) Rough Configuration
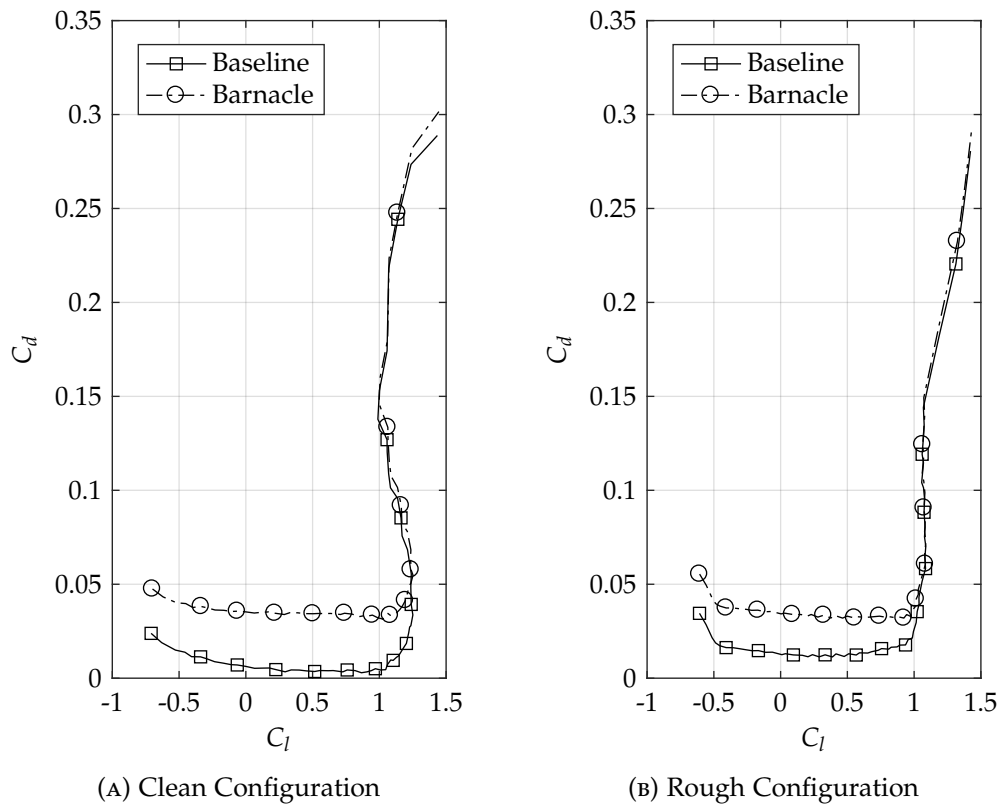
Figure 4.8: Static drag polar for baseline and barnacle datasets.

coefficient, the changes in lift-to-drag ratio also diminish with increased angle of attack.

The results in Figure 4.7 include two interesting features which are now discussed. Firstly, a significant variation in all three cases can be seen between −5° and −2° can be explained as an artefact of the data processing routine. The zero-lift angle of attack occurs at around −3°, and as with the drag coefficient analysis above, the ratio of variations in a small measurement are being amplified. Otherwise the overall scatter

in the presented data is reduced from those in Figure 4.6 as the lift measurement is generally an order of magnitude larger than the drag coefficient at a fixed incidence, particularly over the attached flow region. Secondly, a hump in the results for Case 3 can be seen at higher angles of attack, but is occurring at incidences beyond the typical turbine operating range, for a blade section of this thickness, so will not provide a performance benefit during normal turbine operation and performance.

SUMMARY OF STATIC (STEADY STATE) RESULTS

An overview of the effect the barnacle has on the static aerodynamic parameters describing the AHH 19 blade section performance is given in Table 4.2. Data provided covers the baseline and barnacle cases and for both clean and rough configurations.

TABLE 4.2: Summary of static aerofoil results with barnacle.

Parameter	Clean Configuration			Rough Configuration		
	Baseline	Barnacle	Δ	Baseline	Barnacle	Δ
$C_{n_{\max}}$ [–]	1.23	1.23	0.0	1.07	1.07	0.0
α_{ss} [°]	13.1	13.1	0.0	14.5	14.5	0.0
C_{n_α} [1/rad]	6.122	6.019	-0.103	5.354	5.314	-0.040
$\alpha_{C_n=0}$ [°]	-3.6	-3.6	0.0	-2.6	-2.6	0.0
$C_{n_{\alpha=0}}$ [–]	0.40	0.39	-0.01	0.24	0.24	0.0
C_{d_0} [–]	0.003	0.034	+0.031	0.011	0.033	+0.022

4.4.3 RESULTS & DISCUSSION: DYNAMIC (UNSTEADY) DATA

Following on from the presentation of the results described the influence a single barnacle has on the static aerofoil loading, the changes in the unsteady oscillatory loading cases will now be considered. As previously, both clean and rough aerofoil configurations are presented.

UNSTEADY AEROFOIL LOADING FOR SELECTED OSCILLATORY TEST CASES

This section discusses the unsteady normal force and drag coefficients for the two selected oscillatory test cases, as described at the start of this chapter. Results for the first selected test case ($k = 0.05$, $\alpha = 5° \pm 4°$) are shown in Figures 4.9 and 4.10, for the normal force and pressure drag coefficients respectively, and in Figures 4.11 and 4.12 for the second selected test case ($k = 0.1$, $\alpha = 10° \pm 6°$). The figures include the corresponding static reference values and it must be remembered that the experimental approach used cannot capture the viscous effects due to the boundary layer displacement and friction introduced by vortices generated by the barnacle extrusion.

(A) Clean Configuration

(B) Rough Configuration
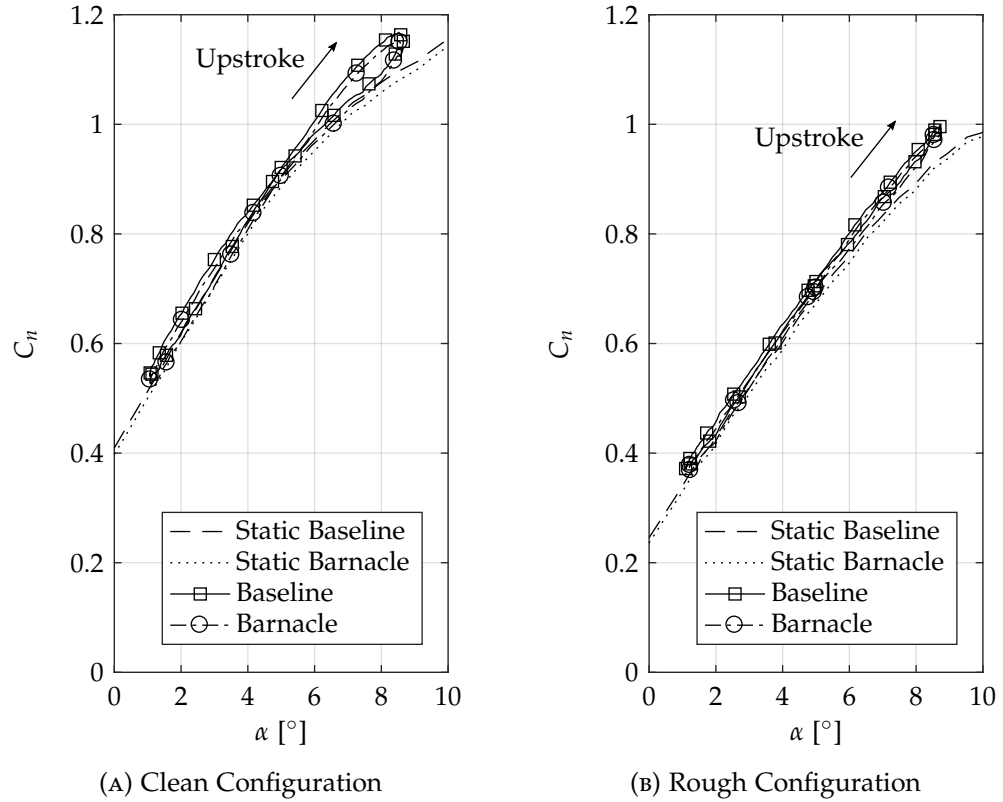
FIGURE 4.9: Unsteady normal force coefficient for baseline and barnacle datasets: $k = 0.05$, $\alpha = 5° \pm 4°$.

(A) Clean Configuration

(B) Rough Configuration
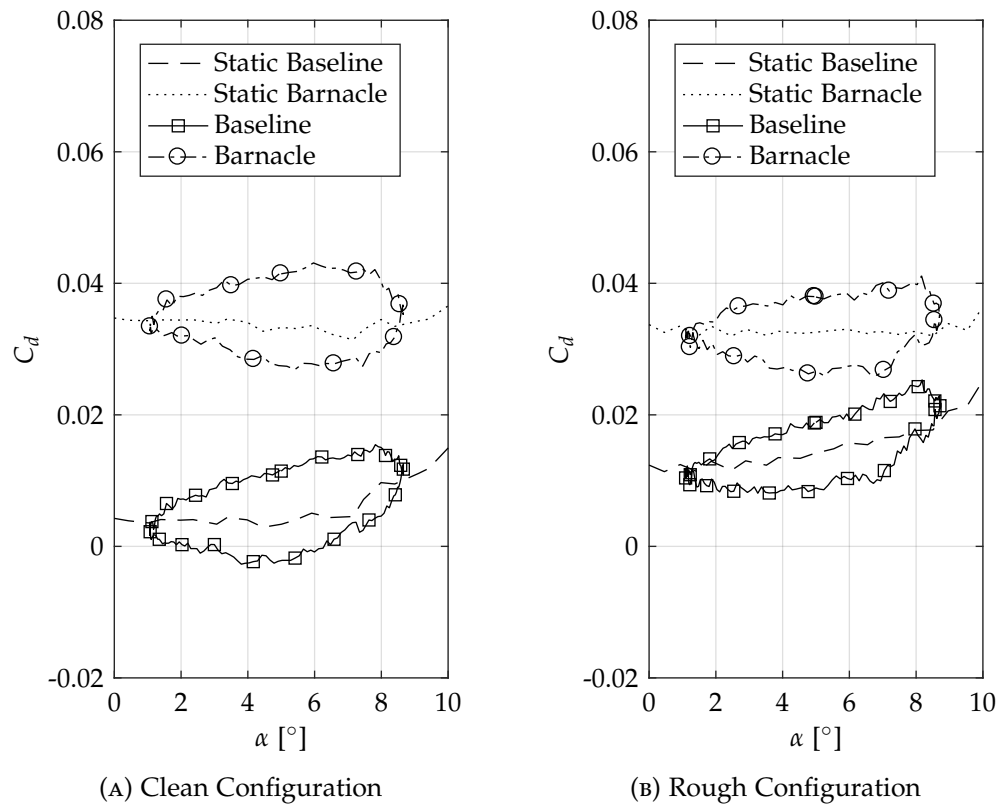
FIGURE 4.10: Unsteady pressure drag coefficient for baseline and barnacle datasets: $k = 0.05$, $\alpha = 5° \pm 4°$.

(A) Clean Configuration

(B) Rough Configuration
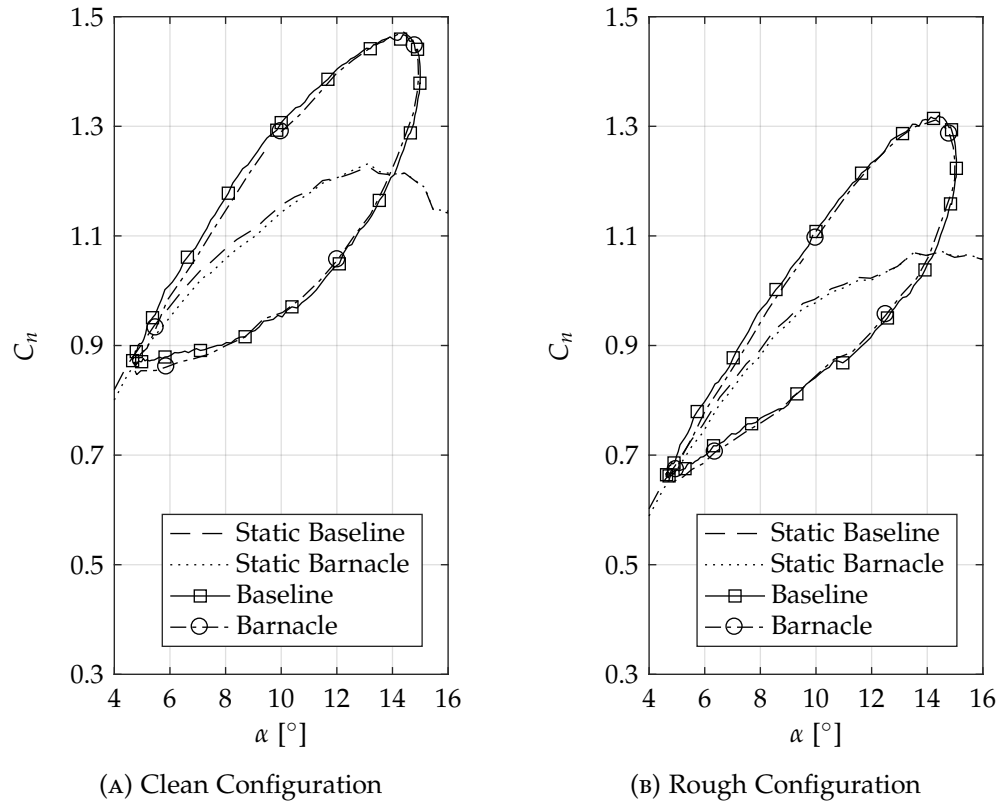
FIGURE 4.11: Unsteady normal force coefficient for baseline and barnacle datasets: $k = 0.1$, $\alpha = 10° \pm 6°$.

(A) Clean Configuration

(B) Rough Configuration
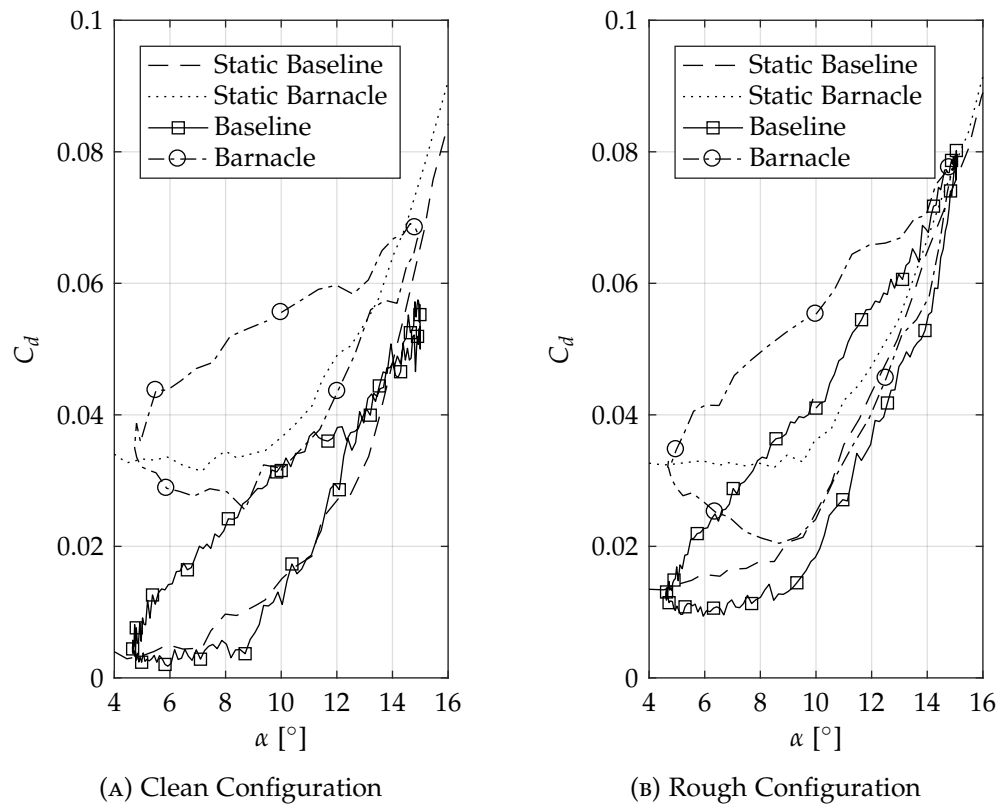
FIGURE 4.12: Unsteady pressure drag coefficient for baseline and barnacle datasets: $k = 0.1$, $\alpha = 10° \pm 6°$.

For the cases selected, the plots of the aerofoil normal force (Figures 4.9 and 4.11) show that the addition of the barnacle does not significantly change the dynamic behaviour of the aerofoil normal force, in either clean or rough configuration – as with the static results. Both selected test cases are demonstrating a typical dynamic stall response, with a lift overshoot attributed to the vortex passage over the aerofoil upper surface, and reattachment on the motion downstroke returning to the static values. The small load variations, on the upstroke and at reattachment between the baseline and barnacle cases, have been determined to be within 2 % of the measured values. This is an insignificant quantity with regards to the confidence bounds of the measurement and follow the trend of difference in the corresponding static cases. This variation has been attributed to the measurement system, as discussed in Section 4.4.4 at the end of this section.

In terms of the pressure drag coefficient (Figures 4.10 and 4.12), the unsteady data is generally following the trends of the static results, with the static drag coefficient being a good indicator of expected unsteady loading at the maximum and minimum aerofoil incidences. The addition of the barnacle to the model results in a widening of the dynamic drag loop, particularly the difference between the upstroke and downstroke loads at the collective angle of attack. Again, the influence of the barnacle on the drag coefficient is reduced with increased angle of attack.

Using the two defined test cases as a starting point, the effects of the reduced frequency and motion amplitude – the main model parameters describing the different oscillatory motions – will now be investigated. Looking at the change in the aerofoil peak normal loads ($C_{n_{\max}}$) for all oscillatory test cases, and shown in Figure 4.13 as a function of the blade section incidence, the presented results confirm that for all model motion parameters tested – not just the static and oscillatory cases already discussed – the peak oscillatory normal loads across the turbine operating range are not being impacted by the presence of a barnacle on the blade section.

The boundary of the augmented pressure drag coefficient during the aerofoil motion cannot easily be reduced to a suitable single indicator of the unsteady behaviour, such as the peak normal force, therefore the effects on the drag coefficient are presented over the full motion cycle for a set of model parameters.

EFFECT OF REDUCED FREQUENCY ON UNSTEADY PRESSURE DRAG COEFFICIENT

The effects of varying reduced frequency on the unsteady drag coefficient increment are illustrated by comparing results at reduced frequency values of 0.025, 0.05 and 0.1, as depicted in Figures 4.14 and 4.15. The static drag coefficient increment is included in the figures for reference.

The reduced frequency is often the most significant parameter in unsteady aerofoil investigations, and is most closely related to the tidal turbine rotational speed. However, the presented datasets are suggesting that the measured drag increase due to

(A) Clean Configuration   (B) Rough Configuration
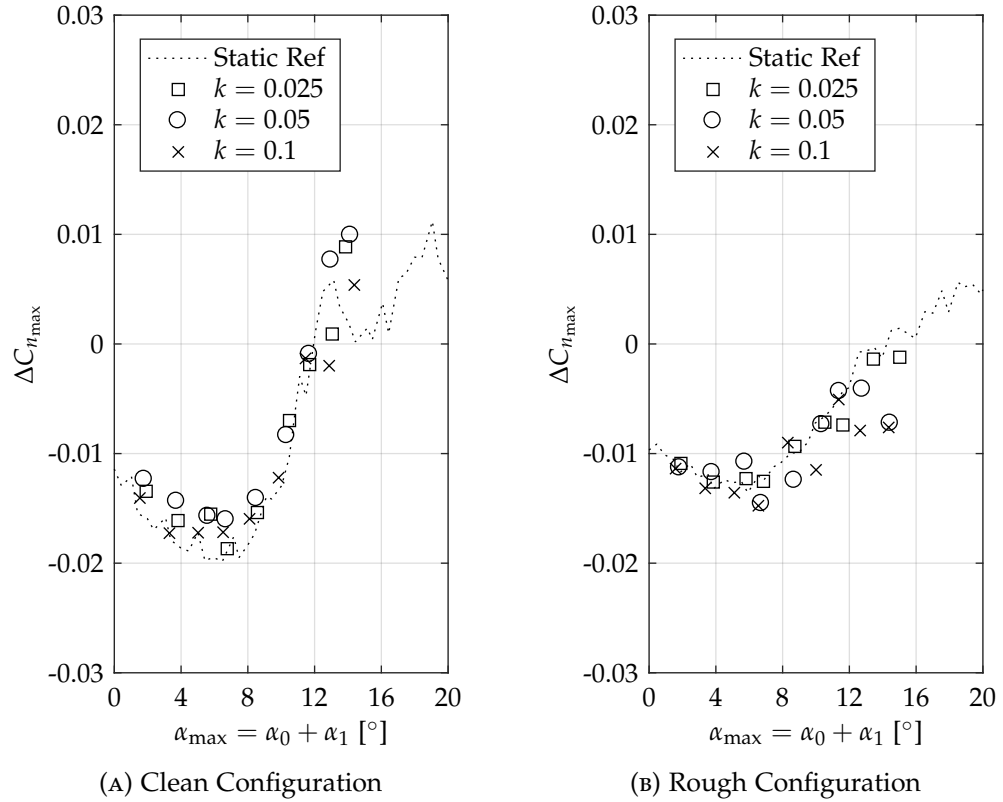
FIGURE 4.13: Change in unsteady peak normal force coefficient for all oscillatory datasets at different reduced frequency.

the barnacle is not being strongly influenced by the blade section reduced frequency, despite spanning a parameter range from the quasi-steady ($k = 0.025$) to the unsteady ($k = 0.1$). The overall trend of the data is for the drag increment to decrease with increasing angle of attack.

For the first motion case ($\alpha = 5° \pm 4°$) the aerofoil incidence is largely confined to the static attached flow region, while the second case ($\alpha = 10° \pm 6°$) is penetrating beyond the static stall angle and experiencing light dynamic stall. In both cases, and configurations, no significant variation which could be correlated to the reduced frequency is observed on the motion upstroke. A larger variation in the drag change increment is identified on the motion downstroke, particularly during reattachment from the higher angle of attack, but again does not show any trend with respect to reduced frequency. The presented sets of dynamic data are showing that the drag increase from the barnacle is not a function of reduced frequency and that the results from the static drag coefficient analysis are a suitable indicator of the drag increase from the barnacle expected under unsteady aerofoil conditions.

EFFECT OF STALL PENETRATION ON UNSTEADY PRESSURE DRAG COEFFICIENT

The effect of varying the maximum angle of attack on the drag coefficient increment is investigated using a similar approach. The maximum angle of attack varied by

(A) Clean Configuration

(B) Rough Configuration
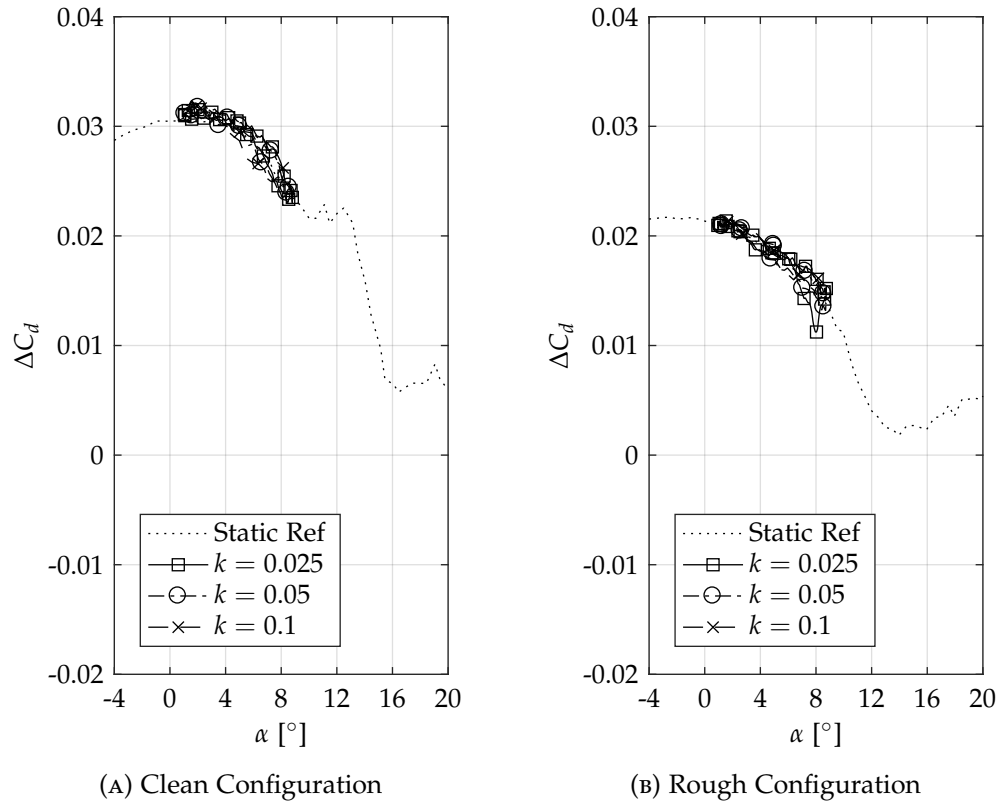
Figure 4.14: Effect of varying reduced frequency on the pressure drag coefficient increment due to barnacle: $\alpha = 5° \pm 4°$.

(A) Clean Configuration

(B) Rough Configuration
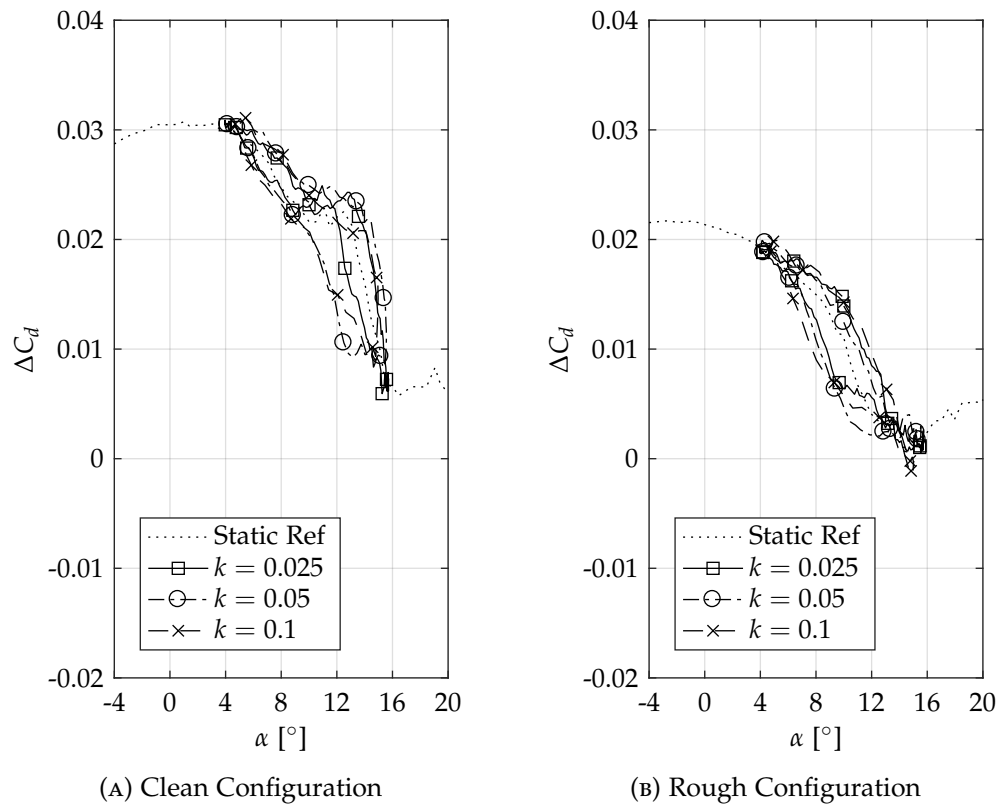
Figure 4.15: Effect of varying reduced frequency on the pressure drag coefficient increment due to barnacle: $\alpha = 10° \pm 6°$.

(A) Clean Configuration

(B) Rough Configuration
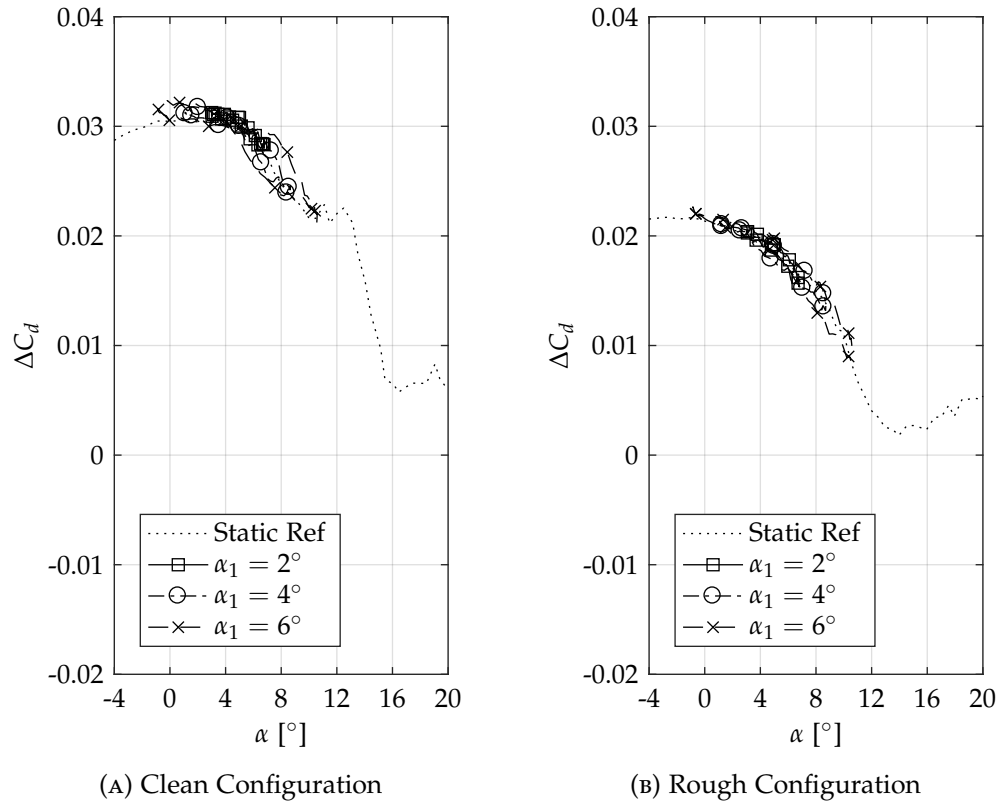
FIGURE 4.16: Effect of varying pitch cycle amplitude on the pressure drag coefficient increment due to barnacle: $k = 0.05$, $\alpha_0 = 5°$.

(A) Clean Configuration

(B) Rough Configuration
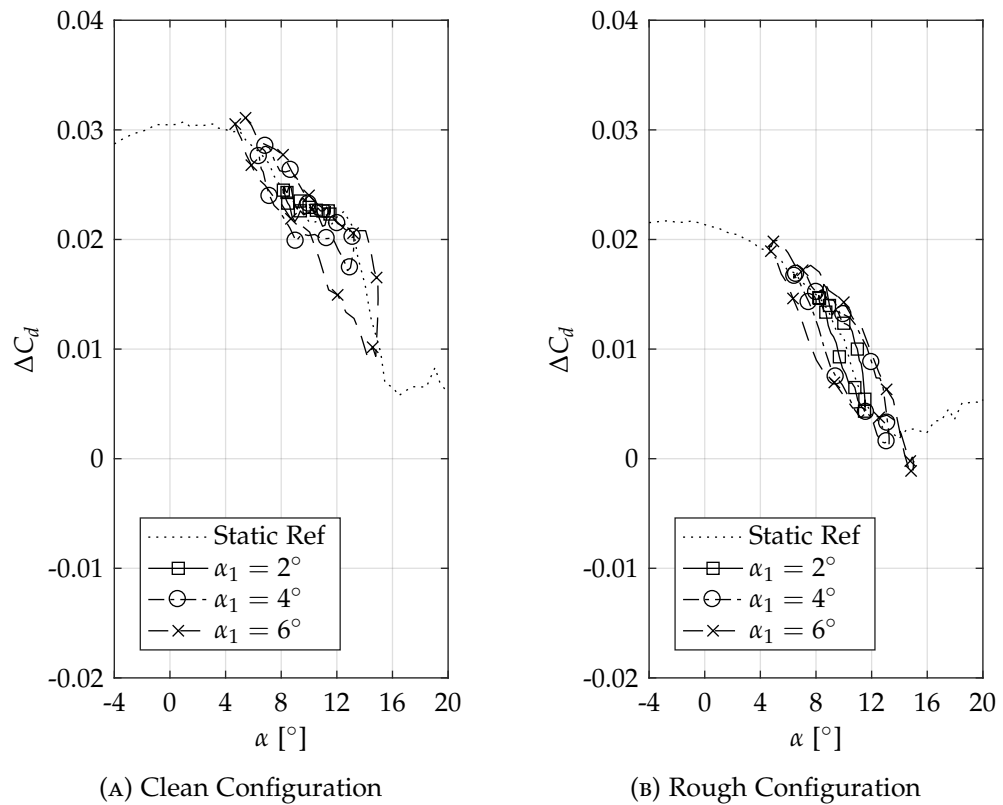
FIGURE 4.17: Effect of varying pitch cycle amplitude on the pressure drag coefficient increment due to barnacle: $k = 0.1$, $\alpha_0 = 10°$.

TABLE 4.3: Summary of oscillatory aerofoil results with barnacle.

Parameter	Clean Configuration			Rough Configuration		
	Baseline	Barnacle	Δ	Baseline	Barnacle	Δ
Typical Test Case: $k = 0.05$, $\alpha = 5° \pm 4°$						
$C_{n_{\max}}$ [–]	1.17	1.15	-0.02	0.99	0.99	0.0
α_{ds} [°]	8.5	8.5	0.0	8.6	8.7	+0.1
$C_{d_{\max}}$ [–]	0.015	0.043	+0.028	0.025	0.041	+0.016
$\alpha(C_{d_{\max}})$ [°]	7.8	6.0	-1.8	8.2	8.2	0.0
Limiting Test Case: $k = 0.1$, $\alpha = 10° \pm 6°$						
$C_{n_{\max}}$	1.47	1.47	0.0	1.32	1.31	-0.01
α_{ds} [°]	14.5	14.4	-0.1	14.5	14.3	-0.2
$C_{d_{\max}}$	0.057	0.069	+0.012	0.080	0.079	-0.001
$\alpha(C_{d_{\max}})$ [°]	14.9	14.6	-0.3	15.1	15.0	-0.1

maintaining the collective angle of attack (5° and 10°) and using the three available cyclic angles (2°, 4° and 6°) from the test dataset. The results of this analysis are presented in Figures 4.16 and 4.17.

For a fixed collective angle of attack, the variation of the motion amplitude controls the degree of penetration beyond the static stall angle and hence the aerofoil load response. For the case where the motion amplitude is varied around a mean angle of 5°, with increasing the amplitude from 2° to 6° the aerofoil is operating within the attached and separated flow regimes, but does not enter dynamic stall, beyond 13.1° and 14.5° for the clean and rough configuration respectively. The variation in drag coefficient on the initiation of the motion downstroke, in separated flow, is greater than at the lower angles of attack, but continues to follow the trend of the static reference. The dynamic response is reduced for the rough configuration.

The same effects can be observed for the increased collective angle case, but the blade section is now entering the dynamic stall regime. Although a relationship between the pressure drag coefficient change and maximum angle of attack has been identified in the data, the static drag coefficient increment remains a suitable estimate of the aerofoil drag coefficient increase for unsteady conditions.

SUMMARY OF DYNAMIC (UNSTEADY STATE) RESULTS

An overview of the effect the barnacle has on the dynamic aerodynamic parameters describing the AHH 19 blade section performance is given in Table 4.3. Data provided covers the baseline and barnacle cases and for both clean and rough configurations.

4.4.4 Pressure Downstream of the Barnacle

The previous sections of this chapter have discussed the steady and unsteady loading cases of the blade section with a single barnacle. However, as the barnacle measurement system did not account for the pressures downstream of the barnacle, beyond the outer tapping ring, an additional investigation was completed to quantify the loading deficiency which may arise. Only the downstream locations were considered since the upstream pressure behaviour is being adequately captured, as shown in Figure 4.5.

A removable non-instrumented barnacle model of the same dimensions was attached at 60 % chord, on the upper surface, in the principal pressure measurement array at the midspan, but on the NACA 63-619 test section which has a similar trailing edge geometry to the AHH 19. This allowed the pressures directly downstream, between the barnacle body and trailing edge, to be measured. A reduced subset of the test matrix covering the major static angles of attack and the two selected oscillatory cases was explored for the clean aerofoil configuration. To quantify any variance between the described measurement systems, the contribution from the pressure measurements downstream of the barnacle to the normal and drag force coefficients are calculated and termed $C_{n_{\mathrm{TE}}}$ and $C_{d_{\mathrm{TE}}}$ respectively. The subscript TE signifies that only the contribution of the downstream pressure measurements, in the vicinity of the trailing edge, are considered as this approach assumes that the pressure distribution at all other aerofoil locations is equal and that only the measurements downstream of the barnacle will be affected.

The difference between the approximated and actual contribution to the aerofoil loading are presented in Figure 4.18 for the static cases. The absolute loading values over a full motion cycle, for the two selected unsteady cases, are presented in Figure 4.19, where *Array A* is the measurement system as described in Section 4.4.1 and *Array B* include the five actual pressure measurements downstream from the barnacle.

The results for the static comparison suggest that, by not including the pressure measurements from immediately downstream from the barnacle, the aerofoil loads will be overpredicted over the attached flow region, but reduces through the stalling process to an approximately equal value. A negative percentage change indicates a load reduction when including the pressures immediately downstream from the barnacle and are referenced to the aerofoil peak normal load and drag coefficients in the clean configuration, for the normal and drag force respectively. However, an overprediction error of less than 1 % in the normal force is within the confidence bounds of the calculated variable error. Similarly, the overprediction of the drag coefficient is of the same order as the measurement error and suggests the outlined processing method is suitable for this work.

Following the trend of the static overprediction, the variation of the unsteady $C_{n_{\mathrm{TE}}}$ values is also less than 1 % of the peak normal force coefficient over the full cycle, for

(A) Normal Force Coefficient

(B) Drag Coefficient
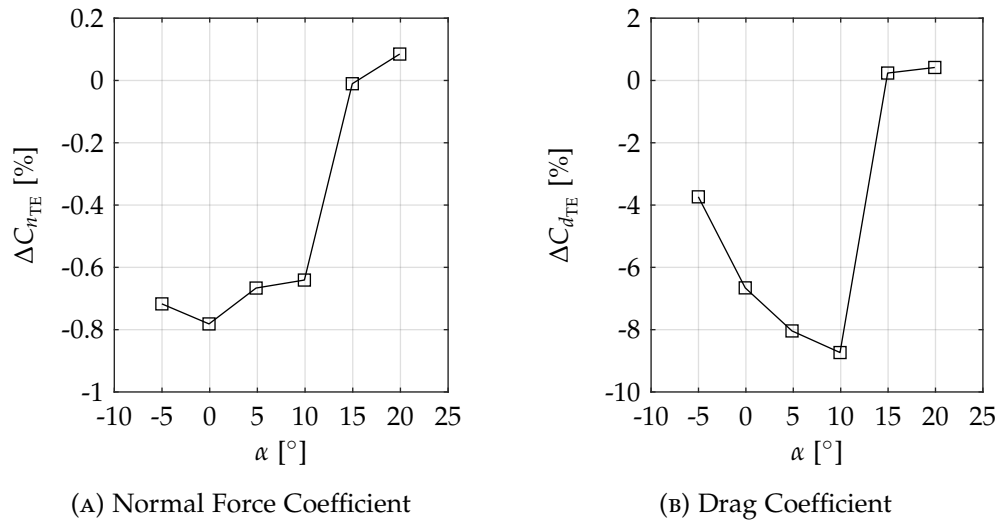
FIGURE 4.18: Error in static aerofoil loads from downstream pressure measurement.

(A) C_n: $k = 0.05$, $\alpha = 5° \pm 4°$

(B) C_n: $k = 0.1$, $\alpha = 10° \pm 6°$

(C) C_d: $k = 0.05$, $\alpha = 5° \pm 4°$

(D) C_d: $k = 0.1$, $\alpha = 10° \pm 6°$
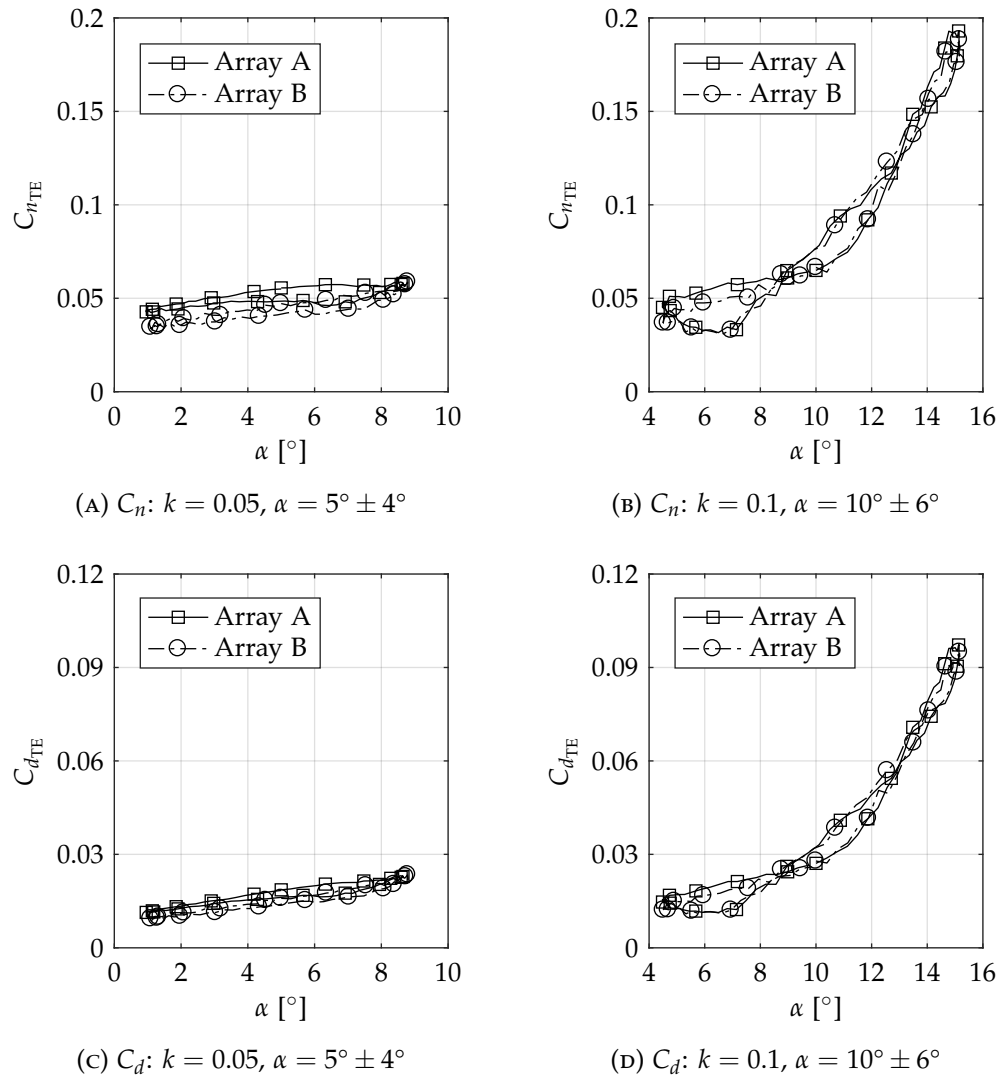
FIGURE 4.19: Error in oscillatory aerofoil loads from downstream pressure measurement.

both presented cases. Likewise, the difference in the unsteady $C_{d_{\mathrm{TE}}}$ is also in close agreement with the static values, with the largest overpredictions occurring at the bottom of the downstroke and start of the upstroke ($-5.9\,\%$ at $1.0°$ and $-8.1\,\%$ at $4.5°$ for the two cases).

These results are what might be expected when comparing the two sets of measurements behind the barnacle – with increasing angle of attack, the flow over the aerofoil begins to separate and the wake behind the barnacle will be immersed in the aerofoil wake. Taking this into account, and from inspection of the pressure data in Figure 4.5, the overprediction of the aerofoil loading should be reduced in the rough configuration. A final point to consider is that these datasets are ultimately of use in design loading cases which will include a safety factor (Liu and Veitch, 2012; Zeiner-Gundersen, 2015) which will likely be an order greater than the overprediction highlighted in this section.

4.5 SURFACE PRESSURE DISTRIBUTIONS AROUND THE BARNACLE

4.5.1 INTERPOLATION OF PRESSURE CONTOURS

The pressure distribution on the barnacle and the surrounding aerofoil surface is constructed from the discrete tappings in the barnacle measurement array and presented as surface contour maps of pressure coefficient. The individual pressures are cubically interpolated, both radially and angularly, and projected onto the *xz*-plane neglecting the local curvature of the aerofoil surface. The surface pressure coefficients are plotted in terms of the barnacle chordwise and spanwise position on the test section and centred on the barnacle rotational axis. The presented test cases are the same as those described in Section 4.3 for the chordwise investigation.

A common scale is provided with all the results in this section to allow a direct comparison between the set of presented cases and the pressure contours have a resolution of $\Delta C_p = 0.2$. The slight asymmetry in the pressure surface contours is a consequence of a pressure tapping (#9) on the barnacle upstream side being slightly recessed into the barnacle body.

4.5.2 RESULTS & DISCUSSION: STATIC (STEADY STATE) DATA

Figure 4.20 presents the pressure contours around the barnacle at the three static aerofoil angles of attack ($5°$, $10°$ and $15°$), with the clean configuration results in the left hand column and the rough configuration on the right. For reference and comparison, the corresponding aerofoil pressure distributions from the principal measurement array are those provided previously in Figure 4.5.

The main features of the static surface pressure distributions are: a distinct upstream region of low pressure, as previously identified in the chordwise pressure

(A) Clean Configuration: $\alpha = 5°$

(B) Rough Configuration: $\alpha = 5°$

(C) Clean Configuration: $\alpha = 10°$

(D) Rough Configuration: $\alpha = 10°$

(E) Clean Configuration: $\alpha = 15°$

(F) Rough Configuration: $\alpha = 15°$

FIGURE 4.20: Pressure coefficient contours around barnacle at selected static angles of attack for clean and rough configurations.

distributions; a zone of higher pressure over the barnacle upper side and lateral surfaces; and a plane of symmetry in the chordwise direction. These features are observed in all the surface pressure results, with their prominence being dependent on the aerofoil angle of attack and inclusion of roughness.

The chordwise static pressure distribution variations attributed to the aerofoil incidence and roughness observed in Figure 4.20 have already been described previously in Section 4.4.2. In summary, with increasing angle of attack the barnacle is gradually immersed in the aerofoil separated flow and impact of the barnacle on the flow is reduced. The boundary layer thickness increases, for equivalent incidences, with the inclusion of surface roughness hence reducing the pressure gradient across the barnacle compared to the baseline case. However, the surface distribution allows for the spanwise (z/c) pressure variation to be examined.

Inspection of the measured pressure coefficients confirm that the pressure at the lateral extent of the barnacle measurement array, i.e. the outer tapping ring at a chordwise position of $x/c = 0.6$, has recovered to the corresponding baseline pressure in the principal measurement array at the aerofoil midspan. This suggests that the lateral radial extent of the barnacle influence on the flow can be considered to be no greater than three times the base radius of the barnacle from the barnacle central axis. The barnacle upstream influence on the flow will be of approximately the same length, but the wake downstream of the barnacle will persist, at moderate angles of attack, significantly further. With increasing angle of attack, and also the addition of surface roughness, the barnacle region of influence is decreased.

Only surface pressure measurements around the barnacle were obtained and will not include the three-dimensional horseshoe vortex system produced by the barnacle. This has the effect of increasing the boundary layer displacement and the viscous friction drag contribution and, therefore, the drag results presented in this chapter which are attributed to the barnacle are expected to be lower than if the full three-dimensional flow effects were considered.

4.5.3 Results & Discussion: Dynamic (Unsteady) Data

Contours of the pressure coefficient around the barnacle body are shown in Figures 4.21 and 4.22 for the first oscillatory motion case, in clean and rough configurations respectively. The equivalent results for the second motion case are given in Figures 4.23 and 4.24. Four aerofoil incidences of interest in the motion cycle were chosen: the collective angle of attack on the upstroke; the maximum angle of attack; the collective angle of attack on the downstroke; and the minimum angle of attack. For reference, each figure includes the midspan aerofoil pressure distribution from the principal measurement array (i.e. the pressure distribution with no barnacle present), covering the same chordwise range of the pressure coefficient surface contours.

The overall trends observed in the unsteady pressure distributions around the

(A) Upstroke Motion: 5.0° (α_0)

(B) Maximum Angle of Attack: 8.7°

(C) Downstroke Motion: 4.9° ($\approx \alpha_0$)

(D) Minimum Angle of Attack: 1.1°

(E) Aerofoil Pressure Distribution (No Barnacle) for Subfigures A to D
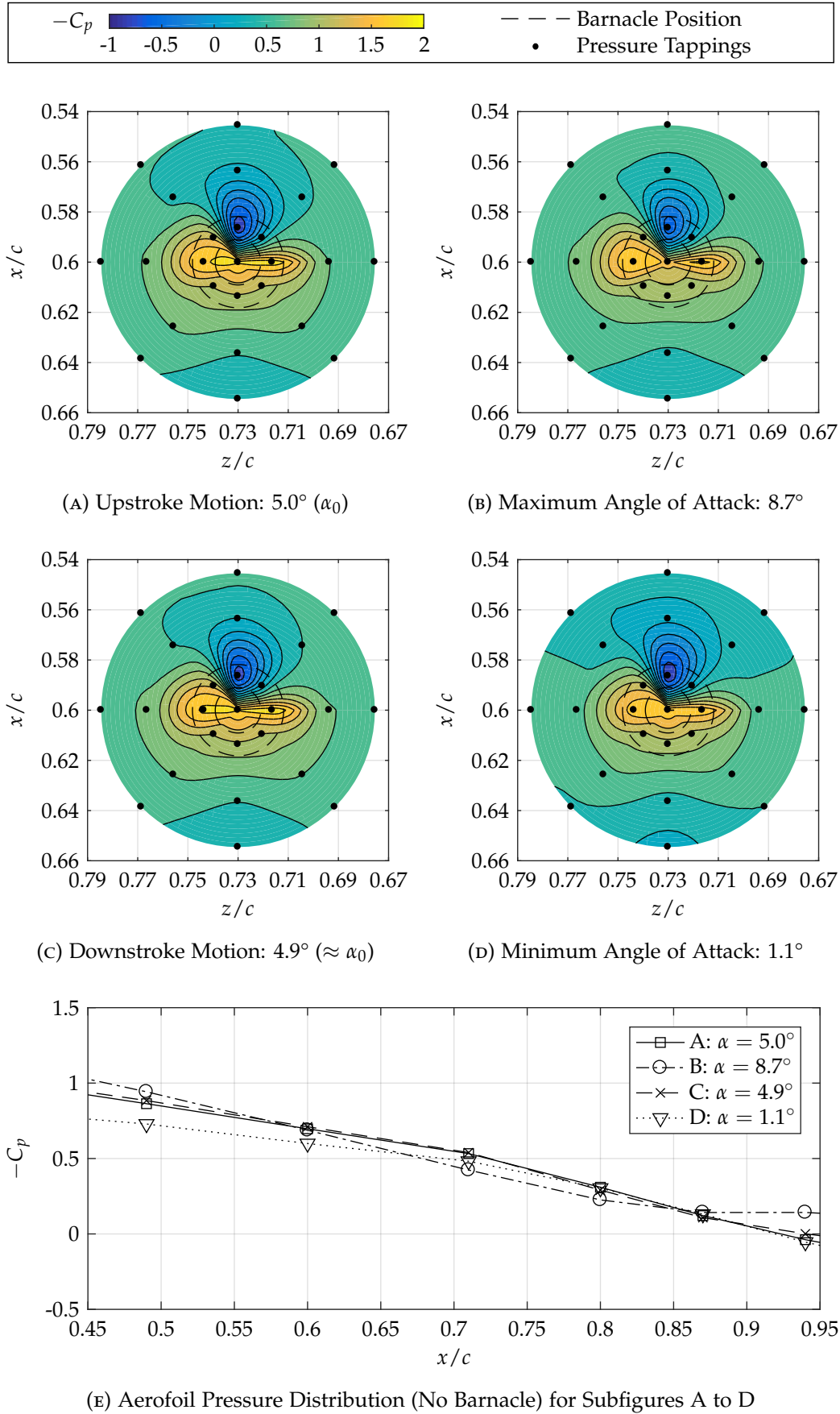
FIGURE 4.21: Pressure coefficient contours around barnacle for oscillatory test in the clean configuration at selected angles of attack and reference chordwise pressure distribution: $k = 0.05$, $\alpha = 5° \pm 4°$.

(A) Upstroke Motion: 5.0° (α_0)

(B) Maximum Angle of Attack: 8.7°

(C) Downstroke Motion: 5.0° (α_0)

(D) Minimum Angle of Attack: 1.1°

(E) Aerofoil Pressure Distribution (No Barnacle) for Subfigures A to D
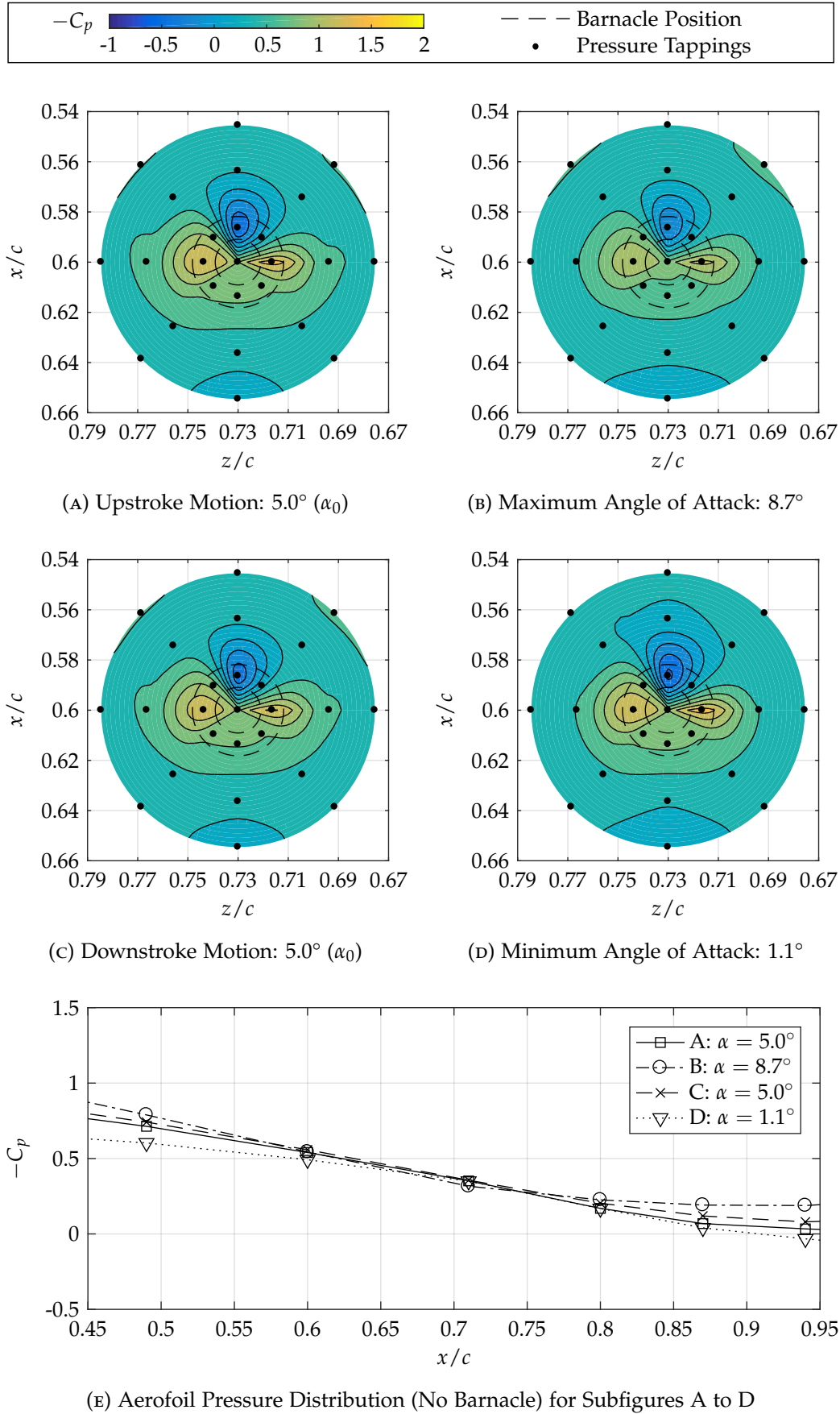
FIGURE 4.22: Pressure coefficient contours around barnacle for oscillatory test in the rough configuration at selected angles of attack and reference chordwise pressure distribution: $k = 0.05$, $\alpha = 5° \pm 4°$.

(A) Upstroke Motion: 10.0° (α_0)

(B) Maximum Angle of Attack: 14.9°

(C) Downstroke Motion: 10.1° ($\approx \alpha_0$)

(D) Minimum Angle of Attack: 4.7°

(E) Aerofoil Pressure Distribution (No Barnacle) for Subfigures A to D
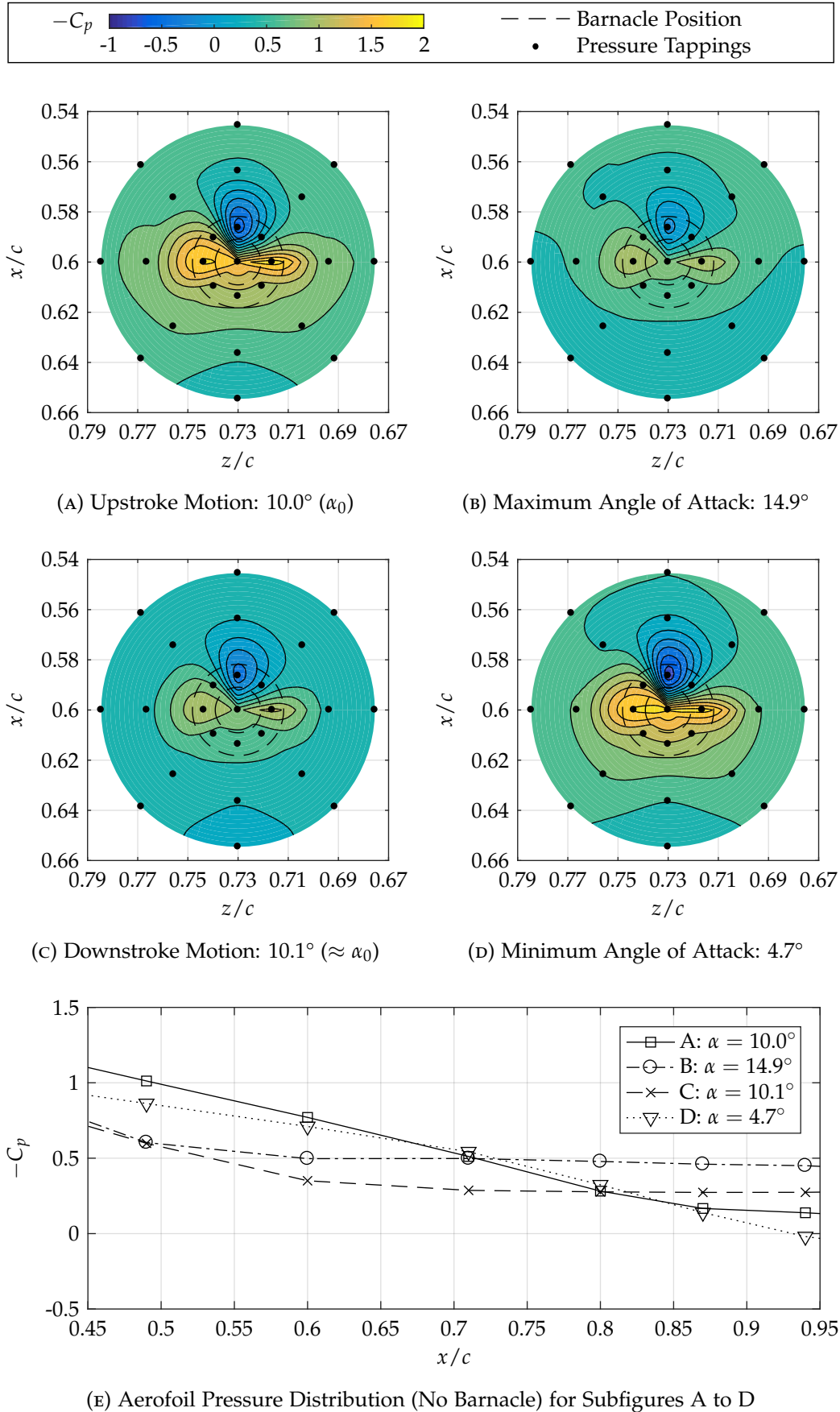
FIGURE 4.23: Pressure coefficient contours around barnacle for oscillatory test in the clean configuration at selected angles of attack and reference chordwise pressure distribution: $k = 0.1$, $\alpha = 10° \pm 6°$.

(A) Upstroke Motion: 10.0° (α_0)

(B) Maximum Angle of Attack: 15.0°

(C) Downstroke Motion: 10.0° (α_0)

(D) Minimum Angle of Attack: 4.7°

(E) Aerofoil Pressure Distribution (No Barnacle) for Subfigures A to D
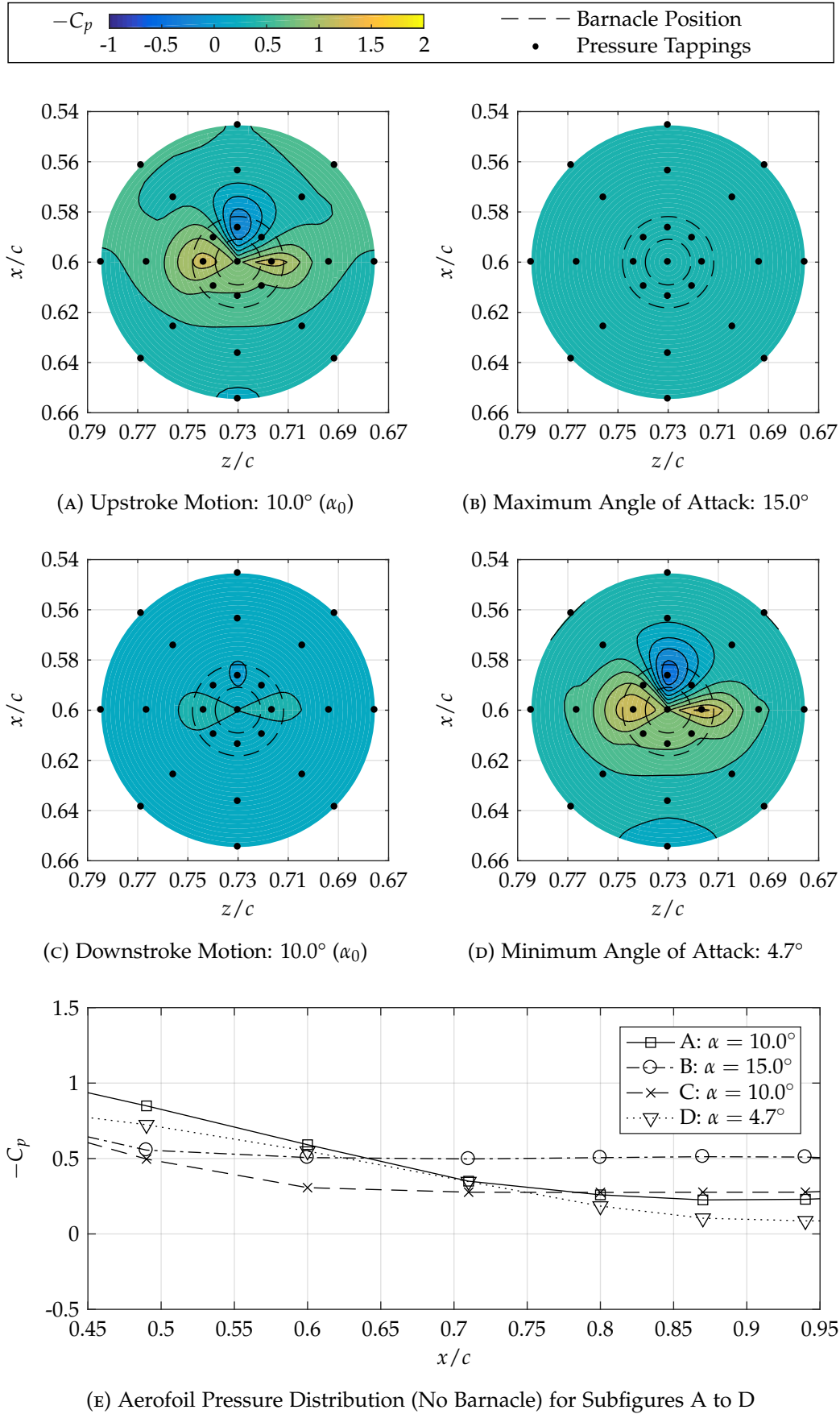
FIGURE 4.24: Pressure coefficient contours around barnacle for oscillatory test in the rough configuration at selected angles of attack and reference chordwise pressure distribution: $k = 0.1$, $\alpha = 10° \pm 6°$.

barnacle, at the discrete aerofoil incidences, are broadly in line with those identified for the static cases, as summarised previously in Section 4.5.3. As with the static surface pressure distributions, the influence of the barnacle on the flow diminishes with increasing angle of attack and surface roughness, hence reduced pressure gradients across the barnacle body.

Of particular interest are the comparisons between the pressure contours in subfigures A and C, where the difference between the flow structure on the upstroke and downstroke portions of the motion cycle, but at the same aerofoil incidence (α_0), is highlighted. For the higher probability test case ($k = 0.05$, $\alpha = 5° \pm 4°$) the aerofoil angle of attack is predominately in the attached flow region of the aerofoil loading and, as such, no significant variation is seen between the upstroke and downstroke parts of the cycle. This applies for both the clean and rough configurations. However, for the limiting test case ($k = 0.1$, $\alpha = 10° \pm 6°$), where the aerofoil is entering the dynamic stall regime, a marked difference is observed. During the aerofoil motion upstroke a region of lower pressure is formed around the barnacle, as the aerofoil flow separates and the dynamic stall vortex convects along the upper surface from the leading edge. As the flow reattaches on the motion downstroke, a region of comparably higher pressure is formed as expected. This corresponds to the loading variations seen in the dynamic load cycle results. As for previous results, with an increase in flow unsteadiness and stall angle penetration the increased variation in the pressure field around the barnacle body.

Finally, a comparison between the oscillatory results and equivalent static angle of attack is made for both the clean and rough configurations. For the first test case, in both configurations, there is no pronounced distinction between the static and oscillatory pressure contours, at the respective angles of attack. For the limiting test case, compared to the corresponding static case, the pressure is lower on the upstroke and at the maximum aerofoil incidence, higher on the downstroke, and equivalent to the static at the minimum incidence as the flow is reattached to the aerofoil surface. Again, this is seen for both the clean and rough configuration.

4.6   CHAPTER SUMMARY

This chapter has examined the effect the addition of a single barnacle to the aerofoil upper surface has on the aerodynamic performance of the AHH 19 tidal turbine blade section. The distribution of macrofouling on a tidal turbine blade is a largely unknown quantity, particularly due to the lack of operational experience with such devices, and is dependent on a myriad of external environmental factors. Although the results presented only consider a very specific fouling case, they are believed to give an illustrative example of the blade section performance losses which could occur on a deployed tidal turbine.

The approach taken in this part of the work was to measure the pressure distribu-

tion around the roughness element and substitute the chordwise pressure measurements into the principal aerofoil two-dimensional pressure distribution, assuming that the barnacle is only influencing the flow in the immediate vicinity of the roughness element. It has been shown that this assumption is suitable for determining the role of the barnacle in modifying the blade section loading.

The motivation for this approach is so that the effect of the barnacle can be isolated from the other aerofoil factors – any changes in the blade section performance can be directly attributed to the measured pressure distribution around the barnacle body, hence its presence – and changes in the aerofoil loading can be compared fairly. The presented results should be taken with this in mind. The main findings from this chapter are now summarised.

- A single barnacle, positioned in an aft upper surface position on the AHH 19 blade section, is shown to cause a significant performance loss and have a significant impact on the blade loading. The performance loss of the blade section is being driven by a large increase in the aerofoil drag coefficient.

- Over the turbine operating range static aerofoil incidences there is no discernible change in the blade section normal force coefficient. A small variation between flow separation and stall is identified and can be attributed to the presence of the barnacle, but is negligible quantity with regards to the aerofoil loading. This applies for both the clean design and rough blade configurations. However, at moderate angles of attack there is a large increase in the pressure drag coefficient, but beyond stall the drag converges with the baseline measurement as the aerofoil wake dominates the drag measurement. As the rough aerofoil flow separates earlier, the drag increment from the barnacle diminishes at a lower aerofoil incidence.

- The drag coefficient increase is being driven by a large pressure gradient over the small distance across the barnacle. A zone of high pressure is forming on the upstream barnacle face, approaching the stagnation pressure for attached flows, and a suction peak on the top and downstream barnacle faces. With increasing angle of attack and flow separation the magnitude of this pressure gradient decreases. The impact is reduced further with the introduction of surface roughness as the boundary layer momentum thickness is increased and the effective barnacle height is decreased.

- For the clean design case, the peak pressure drag coefficient is expected to be almost eight times greater than the baseline measurement and reduces to twice the baseline for the rough configuration. Similarly, the lift-to-drag ratio would be expected to decrease by up to 90 % and 60 %, for the clean and rough configurations respectively. As a negligible change in the normal force coefficient has been identified, the changes in blade loading can be attributed solely to the increase in the blade section drag coefficient.

- A similar trend in the oscillatory results is also observed. The barnacle does not significantly influence the dynamic aerofoil normal force loading, including during reattachment of the motion downstroke. The peak normal force coefficient, an important indicator of the unsteady aerofoil loading, remains unchanged across the test parameter space. The observed difference in the measurements at lower angles of attack has been attributed to the measurement system, as described earlier in this chapter, and follow the variation between the static baseline and barnacle cases.

- The dynamic aerofoil drag coefficient increment (ΔC_d) is showing a weak relationship with reduced frequency, but a stronger trend with maximum angle of attack for the cycle. The trend with angle of attack is as expected – with increasing angle of attack the aerofoil approaches and penetrates the static stall angle, resulting in an increased influence of the dynamic fluid mechanisms. However, the overall trend of the drag coefficient increment is being adequately described by the static drag coefficient increment.

- The blade section loading results presented in this chapter suggest that, for these test conditions and the tidal turbine operating range, a static aerofoil test would be sufficient for estimating the blade section drag increase due to a barnacle on the aerofoil upper surface.

- It is also believed that the influence of the barnacle on the aerofoil loading will reduce as the barnacle body moves aft towards the aerofoil trailing edge and, unlike previous investigations, that barnacle fouling on the aerofoil upper surface leading edge will not arise. It is proposed that the forward limit of barnacle fouling on the aerofoil upper surface is a chordwise location of approximately 60 %. However, the full extent of the blade lower surface of a deployed tidal turbine is highly likely to experience barnacle fouling.

- Inspection of the surface pressure distribution around the barnacle body highlights the strong pressure gradients acting on the barnacle, particularly a strong upstream region of low pressure and a wake structure immediately downstream of the barnacle. In addition, the chordwise plane of symmetry identified in the pressure contours suggest that two-dimensional flow is being achieved on the test models.

- For the oscillatory motion test cases, for pitch cycles which do not penetrate the static stall angle of attack, and remain predominately in the attached flow region, the static results accurately describe the surface pressure distribution. For pitch cycles exceeding the static stall incidence a variation between the upstroke and downstroke portions of the motion is seen, with a region of lower pressure formed on the upstroke and higher pressure on the downstroke.

- At the chordwise location of the barnacle the pressures measurement at the barnacle measurement array extent have recovered to the equivalent pressures

measured on the principal measurement array at the aerofoil midspan. This indicates the the spanwise influence of the barnacle extents to no greater than three times the base diameter of the barnacle body.

CHAPTER 5

CONSEQUENCES ON THE TIDAL TURBINE

The previous two chapters of this thesis have investigated the performance of three different aerofoil sections as used in the design of tidal turbine blades. Both a clean baseline configuration and two different levels of marine biofouling – light surface microfouling and barnacle macrofouling – have been considered. This chapter will build on the work presented so far by applying the experimental aerofoil data to full-scale turbine operations through the use of established numerical approaches, namely blade element momentum theory and cavitation inception criteria, to provide estimates of the tidal turbine performance in both the baseline and fouled states. The principal aim of this chapter is to quantify the turbine output power decrease for a MW-scale turbine with a representative level of marine biofouling. The impact of marine biofouling on the turbine thrust loading and changes to cavitation inception on the turbine blade will also be discussed.

This chapter begins with a review of both experimental and numerical investigations on the hydrodynamic loading and performance of horizontal-axis tidal turbines, followed by the presentation and discussion of the numerical analyses. The following consequences of marine biofouling on the turbine performance are considered: the change in the turbine power output and rotor thrust; determining the total blade drag increase from barnacle macrofouling; and the influence of surface microfouling on the occurrence of cavitation on the blade.

5.1   A REVIEW OF TIDAL TURBINE HYDRODYNAMIC LOADING

Both numerical and experimental approaches have been followed to assess the hydrodynamic loading of tidal turbines. However, numerical approaches still require blade section performance data as an input, and this is usually obtained from experimental testing of two-dimensional blade sections, and experimental data for validation. The unsteady rotor loading is ultimately driven by the turbulence in the tidal flow

upstream of the turbine.

Firstly, the numerical validation approaches are reviewed. Batten et al. (2007) validated a BEMT method, which includes a model for the rotor wake pressure increase and extrapolation of stall data, with experimental data from cavitation tunnel testing of a 1/20th scale, 0.8 m diameter turbine. Good agreement was shown at the optimal rotor tip speed ratio, but overpredicts both the turbine power and thrust at higher rotor tip speed ratios. This numerical work was extended to evaluate the performance of a 20 m diameter turbine (Batten et al., 2008), including the fluctuations of turbine power and thrust over a single revolution. The hub pitch angle is shown to significantly alter the optimal turbine power coefficient – a decrease of approximately 50 % for a pitch angle increase of 12° – and the effects of blade fouling are included as a fixed increase to the blade elements drag coefficient, as discussed later in this chapter. A similar set of numerical validation investigations are presented in (Bahaj et al., 2007a) and (Bahaj et al., 2007b). More recently, Masters et al. (2015) compared results from basic BEMT with tip and hub losses and CFD methods with experimental data, with the BEMT method showing good agreement at the optimum turbine power coefficient. This is deemed to be a suitable approach for predicting the turbine performance with degraded blade elements and highlights the sensitivity of the rotor thrust to decreases in the blade element lift term, while the rotor power is more sensitive to increases in the blade element drag force.

As part of the ETI ReDAPT project, Tidal Bladed (DNV GL, 2016), the turbine design and simulation software used widely in the marine energy industry, has been fully validated by comparing unsteady time domain blade loading with performance data obtained from the 1 MW Alstom DeepGen tidal turbine deployed at EMEC (Parkinson and Collier, 2016). Good predictions of the turbine power performance and hydrodynamic blade bending are obtained using a BEMT method with the onset flow turbulence modelled by a von Kármán spectra, allowing accurate estimations of the turbine blade fatigue loads due to turbulence in the tidal flow.

Numerous experimental investigations have been reported for turbine scale models, in both circulation tunnels and towing tanks, with an aim of determining the influence of various parameters on the turbine performance. Steady and unsteady flows have been considered, but more work is required to understand the effect of turbulence on unsteady turbine loading for both single devices (Bahaj, 2011) and devices in tidal arrays (Bahaj and Myers, 2013). A downside of turbine scale model testing is the reduced blade Reynolds number which has required additional wind tunnel testing to quantify the effects of the lower Reynolds number of the blade loading and flow behaviour (Milne, 2014), and the blade shape and thickness is generally idealised and thinner than the turbine blades considered in the present work.

Barltrop et al. (2007) report performance results for a three-bladed 0.4 m diameter turbine, with a fixed blade thickness of 24 %, tested in a towing tank with surface waves. Surface waves are found to increase the turbine torque at lower flow speeds,

but have a negligible effect on the turbine thrust loading. The impact of a fixed turbine being misaligned to the freestream flow has been investigated by Maganga et al. (2010) on a $1/30^{th}$ scale, 0.6 m diameter turbine model, with a 15 % decrease in the optimal turbine power and thrust coefficients for a 10° misalignment. It is also estimated that the turbine power coefficient is reduced by between 5 % and 10 % as the flow turbulence intensity is increased from 3 % to 15 %. Mycek et al. (2014) describe the wake behaviour of a turbine in a wave and current flume tank at the same turbulence intensities. At the lower turbulence level the rotor wake persists at ten rotor diameters downstream from the turbine, but dissipates faster at the higher turbulence level and is almost fully recovered at a distance of six rotor diameter downstream from the turbine.

Only one experimental investigation of simulating marine biofouling on a scaled turbine model has been identified in the available literature (Walker et al., 2014). For the case with widely distributed $0.014c$ roughness on the $1/25^{th}$ scale 0.8 m diameter turbine, the peak turbine power coefficient was reduced by 19 % and an overall downward shift in the turbine power curve is seen. However, for the case with a coating of slime of the turbine blades, no discernible change in the turbine performance is identified.

Studies for turbines experiencing uniform oscillatory flow in a towing tank have found that the out-of-plane blade root bending moments are increased by approximately 15 %, compared to the steady case (Milne et al., 2015), with the blade loading increase being attributed to flow separation on the blade (Milne et al., 2013). Unsteady fluctuations of the rotor loading have been directly linked to the unsteady fluctuations in the turbine blade loading, suggesting that tidal turbine blade fatigue loads can be estimated through the real time monitoring of the turbine power output (Blackmore et al., 2016).

The effects of unsteady flow and turbulence on the loading and performance of wind turbines has also been investigated. Hansen and Butterfield (1993) report that dynamic stall and inflow effects can increase some turbine operating loads by between 50 % and 100 %, and the average torque over a cycle of a vertical-axis offshore wind turbine decreases by 33 % at a flow turbulence intensity of 15 %, compared to the zero-turbulence flow case (Siddiqui et al., 2015). This will be of particular interest for tidal turbine arrays where the devices will be operated in the turbulent wake of upstream turbines. A method to assess power output of wind turbines from a zero-turbulence power curve and an equivalent turbulence factor is described by Hedevang (2014). This method could potentially be adapted for tidal turbine applications which experience a broad range of turbulent length and time scales during operation.

5.2   ESTIMATES OF TURBINE ROTOR THRUST, TORQUE AND POWER

Both momentum and blade element theories have been widely utilised and validated for the analysis of wind turbine performance (Manwell et al., 2002), and also that of horizontal-axis tidal stream turbines (Batten et al., 2007). This approach allows the turbine blade geometry parameters to be defined for a required performance under known flow conditions, or conversely, the turbine performance for known blade geometry and flow conditions. A brief overview of the theory is now presented, with full details of the method available from Manwell et al. (2002). Additional model implementations relevant to tidal turbines are discussed in Masters et al. (2011).

5.2.1   BLADE ELEMENT MOMENTUM THEORY METHOD

Blade element momentum theory combines components of both momentum theory and blade element theory to allow the forces acting on the turbine blade to be calculated for a specific flow condition, usually defined by the non-dimensional turbine blade tip speed ratio, which is expressed in Equation 5.1.

$$\lambda = \frac{\Omega R}{U_\infty} \tag{5.1}$$

An overview of the flow angles, velocities and resultant forces acting on a blade element at a local radial position is shown in Figure 5.1.

(A) Flow Angles & Velocities   (B) Blade Element Forces
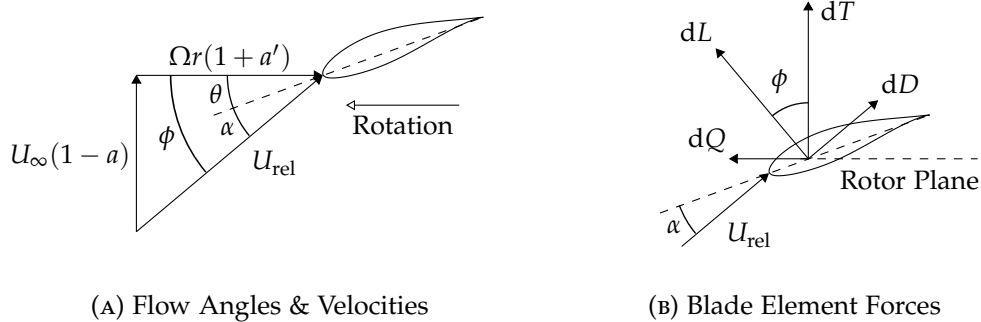
FIGURE 5.1: Definition of blade element parameters in the BEMT model.

The basis of momentum theory is in a control volume analysis where the linear and angular momentum on the rotor disc are conserved. As the forces acting on the rotor are derived from the rate of change of momentum across the rotor, expressions for the turbine thrust and torque are obtained for an annular ring of the rotor disc, as described in Equations 5.2 and 5.3. The local flow conditions are accounted for through the axial and tangential induction factors, a and a', which are assumed to be a function of the annulus local radius.

$$\mathrm{d}T = \rho U^2 4a(1-a)\pi r \, \mathrm{d}r \tag{5.2}$$

$$\mathrm{d}Q = 4a'(1-a)\rho U \pi r^3 \Omega \, \mathrm{d}r \tag{5.3}$$

Blade element theory describes the process in which the turbine blade is subdivided along the length of the blade span into discrete elements, usually of equal width. The resultant forces acting on each discrete blade element are obtained as a function of the local angle of attack, hence local lift and drag forces, and the total blade loading is the summation of the individual forces acting on the blade elements. It is assumed that there is no aerodynamic interaction between the blade elements and local forces are determined solely from reference static lift and drag tables. Equivalent expressions for the turbine thrust and torque can be derived from blade element theory and are given in Equations 5.4 and 5.5, where B is the number of blades in the turbine rotor.

$$\mathrm{d}F_N = \mathrm{d}T = Bq(C_l \cos\phi + C_d \sin\phi)c \, \mathrm{d}r \tag{5.4}$$

$$\mathrm{d}Q = Bq(C_l \sin\phi - C_d \cos\phi)cr \, \mathrm{d}r \tag{5.5}$$

The axial and tangential induction factors are obtained by equating the differential thrust (Equations 5.2 and 5.4) and torque (Equations 5.3 and 5.5) expressions from both the momentum and blade element derivations. The procedure is simplified by setting the drag coefficient terms to zero (Wilson and Lissaman, 1974), and results in the expressions for the axial and tangential induction factors described in Equations 5.6 and 5.7 respectively.

$$a = \left(1 + \frac{4F \sin^2\phi}{\sigma' C_l \cos\phi}\right)^{-1} \tag{5.6}$$

$$a' = \left(\frac{4F \cos\phi}{\sigma' C_l} - 1\right)^{-1} \tag{5.7}$$

The local flow inflow angle, ϕ, and solidity, σ', at each blade element are defined in Equations 5.8 and 5.9, where λ_r is the local speed ratio at the blade element radius.

$$\tan\phi = \frac{U(1-a)}{\Omega r(1+a')} = \frac{1-a}{(1+a')\lambda_r} \tag{5.8}$$

$$\sigma' = \frac{Bc}{2\pi r} \tag{5.9}$$

The standard BEMT method does not account for the spanwise flow present on the turbine blade, particularly in the region at the blade tip. As with any viscous flow around a finite wing a helical vortex will be shed from the blade tip as the turbine

(A) Chord   (B) Thickness   (C) Pre-Twist Angle
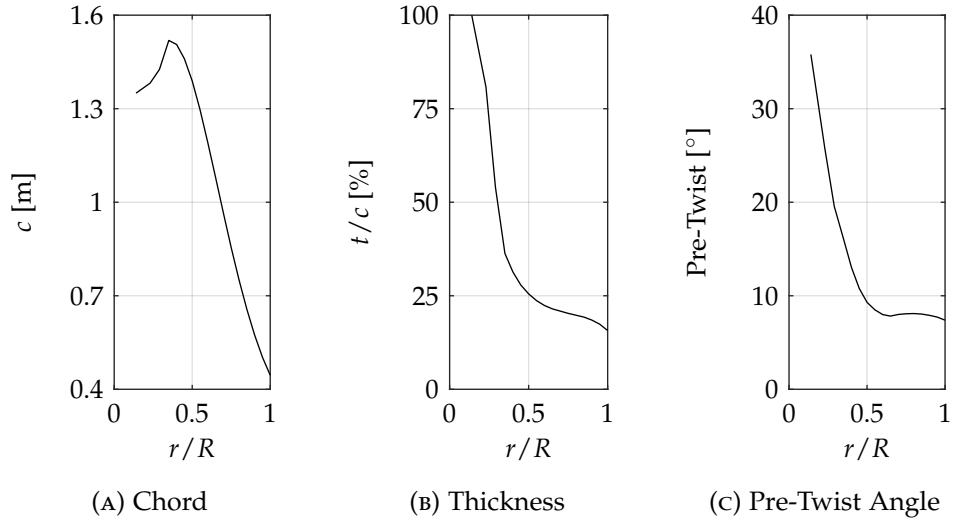
FIGURE 5.2: Turbine geometry parameters for BEMT model input.

rotates. This has the effect of reducing the lift and efficiency of the blade sections in the blade tip region and to increase the local axial induction factor. Comparing tidal and wind turbines, a consequence of a tidal turbine having a relatively shorter blade length is that the tip losses will have a more significant influence on the turbine spanwise loading distribution and efficiency (Masters et al., 2011). To account for the blade tip losses, and also for the losses due to the vortex shed in the turbine hub region, a correction factor, F, has been included in the preceding expressions for the axial and tangential induction factors, but only applied to the terms derived from momentum theory. The total losses across the blade span are determined from the product of both the tip and hub losses, where $F = F_{\text{tip}} \times F_{\text{hub}}$, based on the original work by Prandtl and developed by Glauert (1935). The correction factor, combining both the tip and hub losses, is expressed in Equation 5.10.

$$F = \frac{2}{\pi} \left[\cos^{-1} \left\{ \exp \left(\frac{B(r/R) - B}{2(r/R) \sin \phi} \right) \right\} \times \cos^{-1} \left\{ \exp \left(\frac{B(R_{\text{hub}} - r)}{2r \sin \phi} \right) \right\} \right] \qquad (5.10)$$

To determine the induction factors and flow conditions for each turbine tip speed ratio an iterative process is followed until the induction factors converge to within a set tolerance. Starting with an initial guess for the induction factors, in this case fixed values of $a = 0.3$ and $a' = 0.05$ across the blade span, the inflow angle is calculated from Equation 5.8. Knowledge of the blade geometry is required to determine the local angle of attack, hence the lift coefficient, and the axial and tangential induction factors can be updated from Equations 5.6 and 5.7.

For this analysis the blade geometry from the AHH turbine for Site 3 (See Section 2.3) has been used and a blade setting angle of 0° is inferred. The blade chord, thickness and twist distributions for this selected turbine geometry are shown in Figure 5.2.

Unlike previously published performance investigations for biofouled tidal turbines (Walker et al., 2014), this work has used an actual blade geometry from a deployed 1 MW turbine. However, the blade element performance is only known at limited radial positions. The experimental data obtained for the NACA 63-619 or AHH 19 aerofoil is used at a radial position of approximately $0.85R$, and the AHH 32 data at approximately $0.4R$. Drag coefficient values for the cylindrical section at the blade root were taken from Achenbach and Heinecke (1981) for a Reynolds number of 1.5×10^6, giving values of 0.671 and 1.235 for the baseline and rough blade configurations respectively. It is assumed that zero lift is produced by the cylindrical root section at all angles of attack. The tip blade section is approximately 15 % thick and as the calculated local angle of attack is in the aerofoil attached flow region the lift coefficient at the blade tip can be obtained from the lift curve slope of the 19 % thick blade section, assuming the blade sections belong to the same aerofoil family. The spanwise lift and drag distribution can then be obtained by linear interpolation of the four known loads as a function of the blade thickness at each discrete radial position.

Once the flow induction factors and force distributions are determined at each blade element, the differential turbine parameters can be combined to obtain the turbine power and thrust coefficients, using Equations 5.11 and 5.12 respectively, over a range of tip speed ratios. The expressions for the power and thrust coefficient are related to the turbine upstream tidal flow freestream conditions, where the power coefficient is in indication of the power in the tidal current flow extracted by the turbine rotor.

$$C_P = \frac{2P}{\rho U^3 A} = \frac{8}{\lambda^2} \int_{\lambda_{\text{hub}}}^{\lambda} F \lambda_r^3 a'(1-a) \left[1 - \left(\frac{C_d}{C_l} \right) \cot \phi \right] \, \mathrm{d}\lambda_r \qquad (5.11)$$

$$C_T = \frac{2T}{\rho U^2 A} = \frac{2}{R^2} \int_{R_{\text{hub}}}^{R} \sigma' r (1-a)^2 \frac{(C_l \cos \phi + C_d \sin \phi)}{\sin^2 \phi} \, \mathrm{d}r \qquad (5.12)$$

The relationship between the turbine power, rotational speed and torque is described in Equation 5.13.

$$P = \int_{R_{\text{hub}}}^{R} \mathrm{d}P = \int_{R_{\text{hub}}}^{R} \Omega \, \mathrm{d}Q \qquad (5.13)$$

This analysis only includes fixed blade pitch and twist terms and does not account for any blade pitch control inputs. However, as the turbine pitch controller only operates above rated power conditions, to maintain the rated power output at higher tidal flow speeds, the turbine pitch controller would only be operating at tip speed ratios lower than the optimal value.

The addition of roughness on the blade surface will modify the blade performance resulting in a reduced torque being generated by the turbine. Therefore, even for the same tidal flow conditions, the blade element inflow angles and induction factors

must be determined for each blade configuration and performance point, even for equivalent tip speed ratios.

5.2.2   TURBINE PERFORMANCE CURVES

The results of the turbine performance analysis are presented as a function of the turbine tip speed ratio for both the baseline and rough blade configurations. The turbine power coefficients are presented in Figure 5.3 and the turbine thrust coefficients in Figure 5.4. Separate performance curves are shown for the turbine blade with the NACA 63-619 blade section and that with the alternative AHH 19 outboard blade section.

Starting with the turbine power coefficient for the baseline configuration, optimal tip speed ratios of $\lambda = 6$ and $\lambda = 6.2$ are observed for the turbine using the NACA 63-619 and AHH 19 aerofoils respectively, corresponding to peak power coefficients of 0.399 and 0.403 on both analysed turbines. For the rough blade configuration the respective optimal tip speed ratios decrease to $\lambda = 5.8$ and $\lambda = 5.4$, with a significant change seen in the peak power coefficient – decreases of 19.1 % and 27.6 % from the baseline cases. The impact of light biofouling on the blade is seen to have an increasing effect on the degraded turbine power coefficient as the tip speed ratio increases. Decreases of 27.6 % and 47.7 % for the two investigated turbine geometries are observed at a higher tip speed ratio of $\lambda = 8$.

Similar trends are seen for the turbine thrust coefficient. For the baseline configuration the peak thrust loads are occurring at tip speed ratios of $\lambda = 6.4$ for both turbine geometries – marginally higher than the optimal tip speed ratios identified from the turbine power curves. This tip speed ratio corresponds to thrust coefficients of 0.589 and 0.560, for the NACA 63-619 and AHH 19 based turbines respectively. The introduction of roughness on the blade reduces the respective thrust coefficients by 22.0 % to 0.460 at a tip speed ratio of $\lambda = 5.8$, and by 26.9 % to 0.409 at a tip speed ratio of $\lambda = 5.4$. At a tip speed ratio of $\lambda = 8$ the decreases in the turbine thrust coefficient increase to 25.4 % and 37.8 %, for the two turbine geometries respectively.

The inclusion of the two turbine geometries in the performance analysis – based on the NACA 63-619 and AHH 19 aerofoil datasets – highlights the sensitivity of the turbine power and thrust coefficients calculation to the blade element lift and drag coefficient inputs. The NACA 63-619 and AHH 19 blade sections are of a comparable thickness and similar class of aerofoil, yet variations in the turbine performance between the two geometries are evident, particularly in the baseline thrust coefficient and all rough configuration results. This in turn confirms that the prediction of the performance degradation throughout the turbine life cycle is highly dependent on the level of biofouling distributed across the blade surface, hence the changes to the blade element lift and drag coefficients. Further investigation is required to understand the biofouling variation throughout the turbine life cycle. This will allow improvements
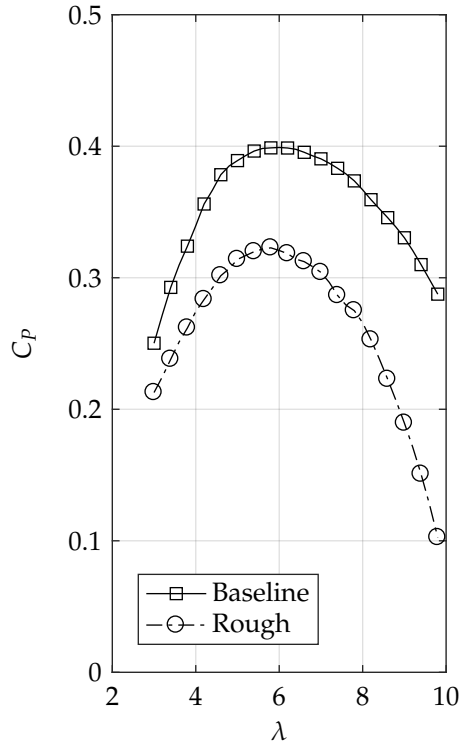
(A) NACA 63-619 and AHH 32
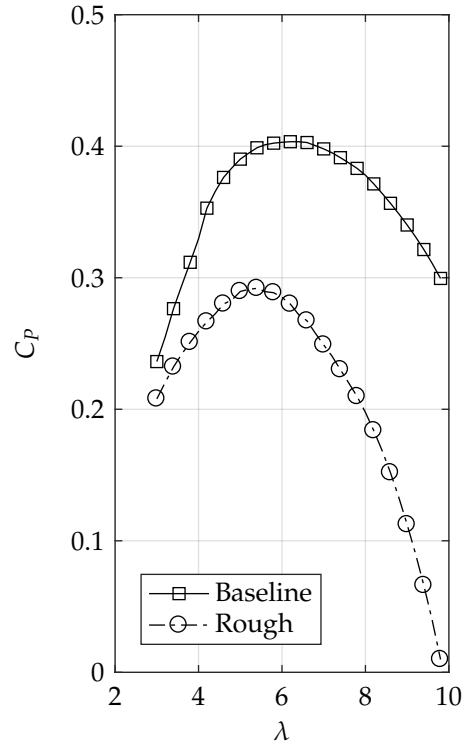
(B) AHH 19 and AHH 32

FIGURE 5.3: Power coefficient, C_P, performance curves for a representative 1 MW tidal turbine for both the baseline and rough blade configurations.
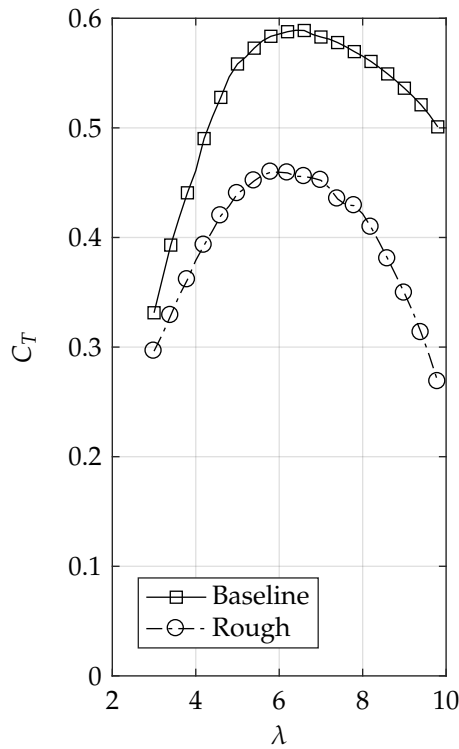
(A) NACA 63-619 and AHH 32
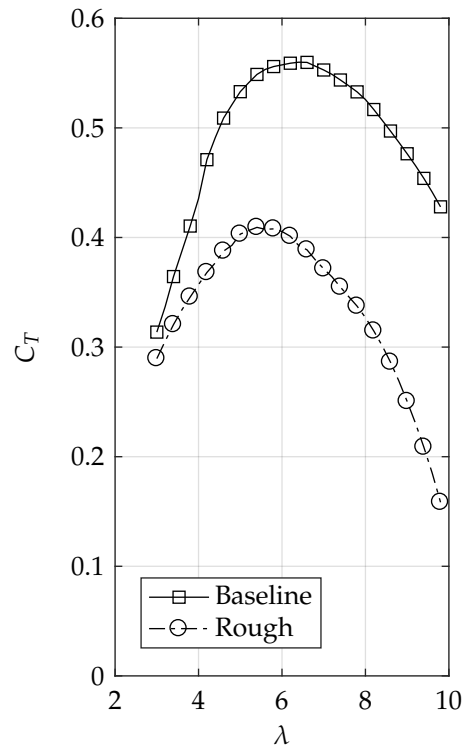
(B) AHH 19 and AHH 32

FIGURE 5.4: Thrust coefficient, C_T, performance curves for a representative 1 MW tidal turbine for both the baseline and rough blade configurations.
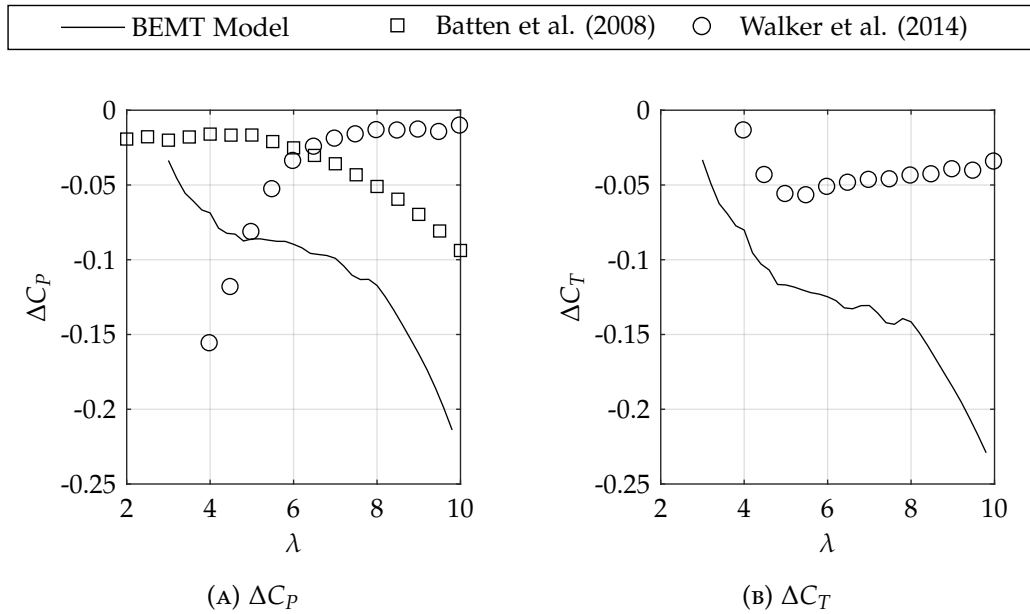
FIGURE 5.5: Comparison of changes in turbine power and thrust coefficients due to blade surface roughness between the described BEMT model and published datasets.

to future turbine performance estimates at various fouling levels and not just for a single representative fouling point as presented here.

Previously published investigations are available which estimate the turbine performance using a BEMT approach with experimental aerofoil data in both a clean and fouled state (Batten et al., 2008; Walker et al., 2014). Comparison of the BEMT model results with experimental data obtained from turbine scale model testing in a water tank showed good agreement for the turbine power and thrust coefficients over the turbine operating range, but the BEMT method was overpredicting the power coefficient and underpredicting the thrust coefficient at higher tip speed ratios. However, the level of performance degradation identified in this current work is significantly higher than that presented in the referenced work. These differences are now discussed.

5.2.3   COMPARISON WITH PUBLISHED FOULING INVESTIGATIONS

A comparison of the changes in the turbine performance attributed to fouling on the turbine blade is shown in Figure 5.5 as a function of the turbine tip speed ratio. No thrust coefficient data is available in Batten et al. (2008) for the blade in a fouled state and results from the BEMT model using the NACA 63-619 and AHH 32 blade sections, at the outboard and inboard blade radial positions, are presented.

Both reference turbines have a 20 m rotor diameter, but are only rated for a power output of 500 kW. Rated power is achieved at a rated flow speed of 2 m/s and have an optimal tip speed ratio of $\lambda = 6$. No previous performance investigations on a 1 MW turbine with blade fouling have been identified in the literature. The most notable variation between the three turbine models is the blade geometry and the method

used to account for blade fouling. Batten et al. (2008) models a 3 blade turbine with a thickness of 24 % close to the blade root varying to 12.6 % at the blade tip, with a 15° blade twist. The effects of blade roughness are included by increasing the blade section drag coefficient by 50 % across all operating conditions, but with no variation to the lift coefficient – an assumption not supported by the findings in this current work. The 2 blade turbine modelled in Walker et al. (2014) is based on the NREL turbine design (Bir et al., 2011) and uses a constant NACA 63-618 blade section over the outer 60 % blade span, increasing to 25.4 % at the blade root with a 13° blade twist. The roughness level is 0.00084c across the entire blade surface, marginally lower than for the BEMT model presented here, and force coefficients are obtained from both clean and fouled static wind tunnel testing. The blade geometry of these two reference turbines are noticeably thinner than those of the MW-scale turbines investigated in this work.

It is believed that the current work provides a representative description of both the blade geometry of a 1 MW tidal turbine, including a cylinder blade root section and blade tip thickness of 15 %, and an applicable level of marine biofouling operating in flow conditions representative of those experienced by a deployed turbine. The blade thickness distributions for the two reference cases described are considerably thinner from that of larger scale turbines currently undergoing development and commercialisation. This is particularly evident in the blade root region where a large drag contribution from the thicker blade sections will be expected. The described BEMT model includes not only the effects of blade tip losses, but also those at the rotor hub, and the variation in lift and drag due to fouling varies with the blade element angle of attack – not a fixed drag increase as assumed by Batten et al. (2008).

Comparing the datasets at the optimal tip speed ratio of $\lambda = 6$, the peak turbine power coefficient for the two reference cases is decreased by 0.025 and 0.034 when the blade is fouled, in contrast to a decrease of 0.090 calculated in this work. This suggests that the power output loss due to biofouling could be up to three times greater than previously determined. A similar tendency is seen for the thrust coefficient where a decrease of 0.125 is observed, compared to 0.051 in the previous study. Again, the results suggest the turbine thrust decrease due to biofouling is larger than previously estimated.

5.2.4 ESTIMATE OF TURBINE PERFORMANCE DEGRADATION

As part of the turbine commissioning process, the turbine must be able to demonstrate a defined performance specification (DNV GL, 2015a), but it is apparent that over time biofouling is going to reduce the power output of the turbine. However, no performance data for fouled deployed turbines is freely available and methods such as that outlined here must be used to predict the likely performance degradation. Further to this, only prototype and demonstration full-scale tidal devices have been deployed

over relatively short periods of time and not for the five year periods expected for fully commercialised turbines. Therefore, any fouling data collected to date may not be capturing the potential levels of blade fouling. The results for the turbine using the NACA 63-619 blade section will now be used to highlight the potential power output decrease due to marine biofouling for the turbine with reference to the baseline blade configuration.

A tidal turbine implementing pitch to feather control, such as those considered in this work, will operate at the optimal tip speed ratio for flow speeds between the rotor cut-in and cut-out conditions, or until the turbine rated power is achieved. Starting with the baseline turbine configuration, with an optimal tip speed ratio of $\lambda = 6$, the turbine rated power of 1 MW is achieved at a freestream tidal current of 2.42 m/s, giving a turbine rotational speed of 13.21 rpm at these flow conditions. The baseline turbine operating parameters at rated power are summarised in Table 5.1.

TABLE 5.1: Turbine performance parameters for the baseline blade configuration at the turbine rated power and optimal tip speed ratio.

Configuration	λ [–]	U_∞ [m/s]	Ω [rpm]	P [kW]	Q [kN m]	T [kN]
Rated P (Baseline)	6.0	2.42	13.21	1003.0	872.5	563.9

Secondly, as the biofouled turbine will operate at the roughened optimal tip speed ratio, from the cut-in flow speed to the rated power, the equivalent set of performance parameters for the rough configuration have been determined and are summarised in Table 5.2.

TABLE 5.2: Turbine performance parameters for the rough blade configuration at the turbine rated power and optimal tip speed ratio.

Configuration	λ [–]	U_∞ [m/s]	Ω [rpm]	P [kW]	Q [kN m]	T [kN]
Rated P (Rough)	5.8	2.68	14.12	998.7	873.9	505.9

Thirdly, the performance difference between the baseline turbine configuration and the rough configuration, but both at the baseline rated flow speed can be assessed. The baseline rated flow speed of 2.42 m/s is less than that at which the fouled turbine achieves rated power. At this flow speed the fouled turbine will be operating in the turbine variable speed range, but still at the rough optimal speed ratio. Therefore, the turbine rotational speed and performance parameters can be established and are detailed in Table 5.3.

TABLE 5.3: Turbine performance parameters for the rough blade configuration at the optimal tip speed ratio and flow speed for rated power in the baseline configuration.

Configuration	λ [–]	U_∞ [m/s]	Ω [rpm]	P [kW]	Q [kN m]	T [kN]
Rated U (Rough)	5.8	2.42	12.77	735.3	712.6	412.5

The three investigated turbine performance points of interest, presented in Tables 5.1 to 5.3 – baseline and rough turbine configurations at rated power, and the rough configuration at the baseline rated power flow speed – are summarised in Figure 5.6.
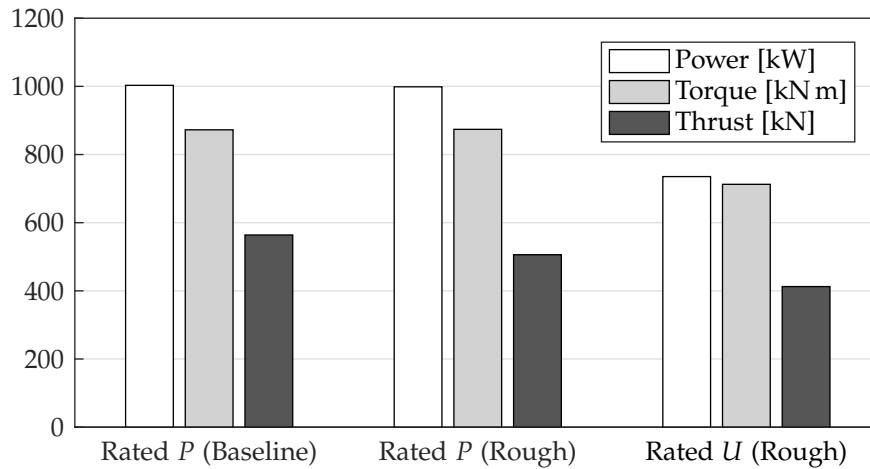
FIGURE 5.6: Turbine power, torque and thrust estimates at rated power and optimal tip speed ratio for baseline ans rough blade configurations.

Comparing the two rated power cases, at a power output of 1 MW there is a negligible increase of 1.4 kN m between the turbine driving torque values, which is to be expected as the power output varies directly as a function of the turbine rotational speed, and there is a small thrust decrease of 58.0 kN identified in the data. However, a higher tidal flow is required to achieve rated power for the fouled blade and would be expected to increase further as the roughness level increases. Comparing the baseline and rough turbine configurations again, but at the baseline rated flow speed, reveals a more significant change in the turbine performance. For the same tidal current flow the power generated by the fouled turbine is decreasing by 26.7 % to 735.3 kW, with 18.3 % and 26.8 % decreases for the turbine torque and thrust respectively – a dramatic decrease in power output.

The tidal turbine design is optimised for a specified flow distribution at each tidal power project site to maximise energy production for the prevalent flow conditions, including the flow speed for which rated power is achieved. However, the estimated results are indicating that if no action is taken to address the impact of biofouling on the turbine performance then there will be longer term consequences for the device operator, particularly with regards to the device economics due to the negative impact on the device annual energy production. Further investigation to assess the decrease of the turbine annual energy production will be required. The changes in the turbine performance are highlighted in Figure 5.7. The turbine power and thrust estimates are presented as a function of the tidal current flow speed, from an approximate value of the cut-in flow speed to the turbine rated power flow conditions. Although not included in this numerical model, the turbine pitch control system will maintain the rated power output at higher flow speeds and the turbine thrust is expected to decrease as the blade pitch angle is increased.

(A) Turbine Power
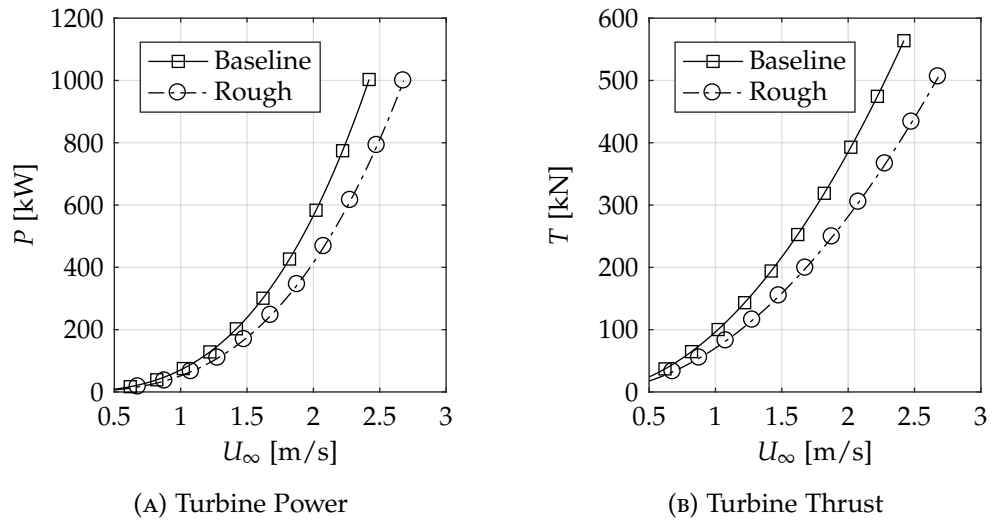
(B) Turbine Thrust

FIGURE 5.7: Estimates of the tidal turbine power output and thrust over the turbine variable speed operating range for both baseline and rough blade configurations.

5.2.5   ACCOUNTING FOR TIDAL TURBINE POWER DEGRADATION

The principal purpose of the tidal turbine is to generate power to supply to the National Grid – converting kinetic energy in the tidal stream to shaft power at the turbine gearbox and ultimately electrical energy output from the converter, either offshore or onshore. It has been shown in the current analysis that even a light level of marine biofouling on the tidal turbine blades is having a consequential impact on the performance parameters defining the turbine capacity and operation. This is most noticeable, and problematic, for the impact on the turbine power coefficient at equivalent flow conditions.

The turbine is designed to achieve rated power at a defined flow speed, unique to each tidal project site, and the annual energy production can be evaluated from the site flow probability distribution. As the roughness level of the blade fouling increases, the turbine will still achieve the rated power, but at a higher tidal flow speed. This results in the power output of the fouled turbine decreasing for a specified flow speed, until rated power is met, and a corresponding decrease in the annual energy production.

The turbine specification, including power output, forms part of the commercial guarantee provided to energy generators by the device developers. Compliance with the specification is demonstrated during the turbine commissioning phase, when the turbine is initially deployed in the sea. If the impact of marine biofouling on the turbine performance has not been accounted for at this stage then there is a risk that the turbine will not be performing within agreed bounds at a later date during the device life cycle. There are further commercial implications for energy generators and suppliers dependent on supplying a target level of energy to the Grid, including the Levelised Energy Cost (BEIS, 2016) and accreditation schemes such as Renewables

Obligation (Ofgem, 2016). As no commercially deployed turbine has been generating for a significant length of time – less than a year at time of writing – it remains to be seen what the future repercussions of this uncertainty may be. Experience can be drawn from the experience of the wind energy sector where: leading edge erosion on the blade has become an issue sooner than expected (Keegan et al., 2013); and a moderate drag increase of 80 %, compared to drag increases of up to 200 % for wind turbine leading edge erosion investigations, has been shown to reduce the annual energy production by 7 % (Sareen et al., 2014).

From the results presented in this work, it is recommended that tidal turbines could be commissioned in a two-stage process requiring initial compliance with the baseline design specification at deployment, as currently completed, and an additional evaluation at a predetermined point, after a certain number of operating hours or maintenance procedures, to demonstrate compliance with age-performance curves. These would account for any potential decline in turbine performance, based on the turbine load factor, and as well as marine biofouling could be extended to include anticipated levels of mechanical wear and availability of the device. However, this will only be possible with more experience of offshore operations and sharing of information within the marine energy industry.

A potential control strategy could exploit future versions of systems already installed on the turbine. Currently the turbine pitch controller is used for maintaining the power output at flow speeds above the rated power condition and feathering the blade during times the turbine is parked. An area of interest would be whether the pitch controller could be utilised to account for fouling on the blade so that rated power is achieved for the same flow conditions no matter the surface state of the blade. This could take the form of a periodic adjustment to account for the anticipated fouling level, perhaps through a remote access connection to the device, or an active control mechanism which could be integrated with future developments of turbine health monitoring systems.

5.3 TURBINE BLADE DRAG INCREASE FROM BARNACLE FOULING

The previous chapter of this work presented and discussed the impact of a single barnacle on the loading of a blade section, particularly the drag increase on the investigated AHH 19 aerofoil. However, although the presence of a barnacle is significantly increasing the blade section drag, how does this translate to a barnacle on a full-scale turbine blade and, further to this, how many barnacles would be expected to increase the total blade drag to a significant level?

To present the problem in terms of a comparison between the barnacle and turbine blade geometries: a barnacle of 25 mm base diameter has a contact surface area of approximately $490 \, \text{mm}^2$, compared to the blade suction side surface area of approximately $12 \, \text{m}^2$. For these parameters, the ratio of the areas is 0.0041 % indicating

that approximately 26000 barnacles would be required to completely colonise the available blade surface. Therefore, a particular level of barnacle fouling will have to be reached before a consequential increase in the total blade drag is realised.

This section provides a solution to this question by using a blade element theory approach to relate the blade section findings from Chapter 4 to the full turbine case. From the previous analysis, a negligible change in the both the static and unsteady blade section normal loading, hence also the blade lift, was identified. As the change in the unsteady drag coefficient was shown to be described by the equivalent static case, an analysis based on the static experimental data is suitable for this current investigation.

5.3.1 TURBINE BLADE DRAG FROM BLADE SECTION FORCES

As summarised in Section 5.2.1, blade element theory is a process in which a three-dimensional blade is subdivided along the length of the blade span into discrete elements, usually of equal width, and the total force acting on blade is the summation of the individual forces acting on the blade elements. It is assumed that there is no aerodynamic interaction between the elements and forces are determined solely from static lift and drag tables. The drag force (D) acting on a single turbine blade is expressed in Equation 5.14, where N is the total number of blade elements, in this case 101, and dr is the fixed blade element width.

$$D = \sum_{i=1}^{N} C_{d_i} q_i c_i \, dr \qquad (5.14)$$

In Chapter 2 a generic tidal turbine was created for the purpose of confirming a representative operating envelope, and is summarised in Appendix B. This design will be used as the basis for the blade element model and the variation in the blade angle of attack and chord are shown in Figure 5.8 and full details of the turbine design are provided in Appendix B.

Using the static drag tables from Chapter 3, the reference (i.e. no barnacle fouling) spanwise drag distribution is defined for each element as a function of the element angle of attack, for both the baseline and roughened blade configurations. As for the previous analysis, the drag profile is not known for each unique blade element thickness. The drag distribution is interpolated as a function of element thickness from fixing test data at three known radial points – a cylinder at the root, AHH 32 at $0.35R$ and NACA 63-619 at $0.85R$. The drag values for the baseline and roughened cylinder are given in Section 5.2.1. The dynamic pressure along the blade span is calculated at the turbine design rated power for a uniform 2.4 m/s tidal current and a turbine rotational speed of 11.12 rpm.

To include the effects of the barnacle, the percentage drag coefficient increase

(A) Angle of Attack
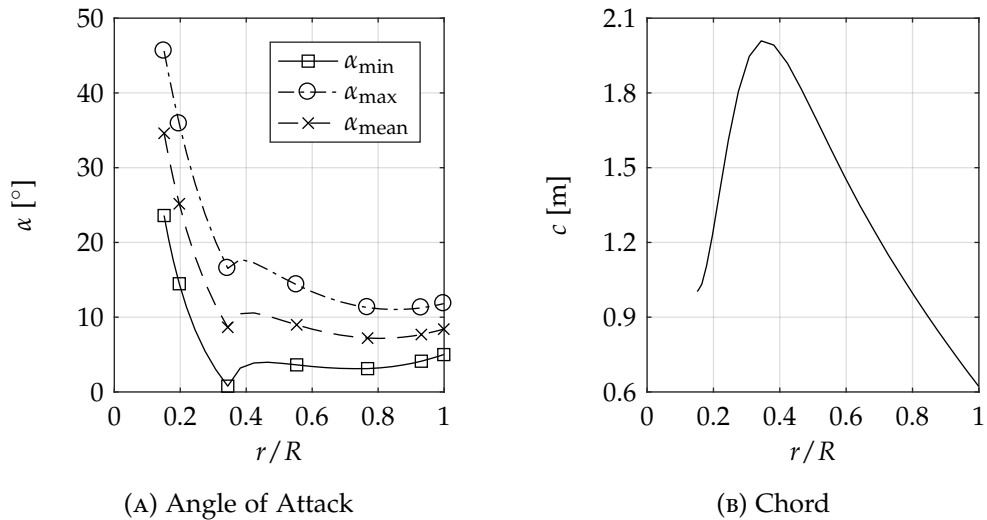
(B) Chord

FIGURE 5.8: Spanwise variation of turbine blade angle of attack and chord for blade element theory model parameter inputs.

results presented in Figure 4.6 are applied in the model by adjusting the blade element drag force as a function of the local angle of attack. It is assumed that only one barnacle can be located on each of the blade elements and does not account for the barnacle chordwise position. For this illustrative example four different idealised distribution patterns are investigated, as described in Table 5.4 and shown diagrammatically in Figure 5.9, where an increasing number of barnacles will be applied, starting with one, until the upper limit defined by the number of blade elements is reached.

TABLE 5.4: Overview of the investigated barnacle distributions on the turbine blade.

Distribution	Description
A	Root: Located starting from the first blade element at the blade root and added out towards the blade tip.
B	Tip: Located starting from the last blade element at the blade tip and added in towards the blade root.
C	Mid: Distributed around the blade midpoint and added in pairs to the adjacent elements towards both the blade root and tip.
D	Even: Evenly distributed across the 8.5 m length of the blade between the root and tip.

With reference to Figure 4.6, at the thicker blade elements towards the blade root the barnacle is expected to have a smaller influence on the drag increase, particularly at higher angles of attack. This is accounted for in this method by adjusting the percentage drag increase for the blade element incidence and as the angles of attack are higher on the inboard sections the percentage drag increase applied to the element will be significantly reduced. Further to this, where the blade element incidence is beyond the range of the experimental datasets, for incidences greater than 25°, the drag increase is set to zero, but maintains the trend observed in the data. The variation

(A) Distribution A

(B) Distribution B

(C) Distribution C
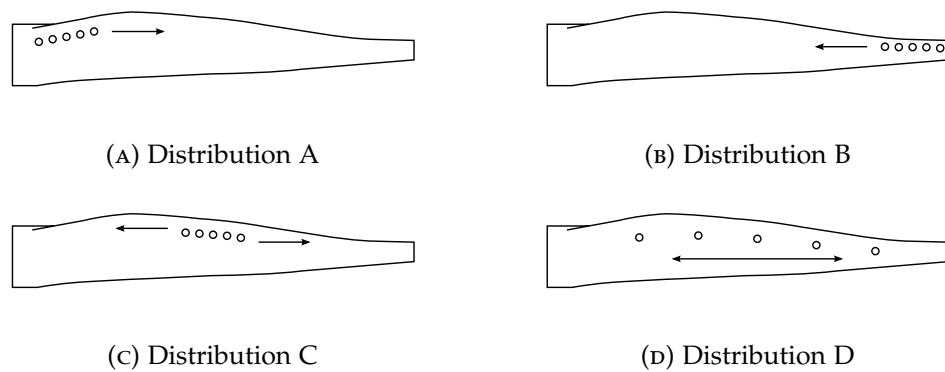
(D) Distribution D

FIGURE 5.9: Overview of illustrative barnacle distributions along the turbine blade span for determining the drag coefficient increase for the entire turbine blade.

in the percentage drag coefficient increase highlighted in the discussion of the results in Section 4.4.2, due to scatter in the baseline drag coefficient measurement, has been modified for this analysis using anticipated values for incidences between −5° to 10°. This modification has only been applied to the clean baseline percentage drag increase.

Two cases are considered for this analysis – the addition of distributed barnacles to both the clean baseline and fouled rough blade configurations – which correspond to Cases 1 and 3 in Table 4.1 for the blade section. As Case 2 was previously shown to give similar results to Case 1 it has not been included here. As no data is available for the drag increase from barnacles on the blade pressure side, the method only considers fouling at a single chordwise position of $x/c = 0.6$ on the blade upper surface.

The results are presented as a drag ratio at a range of barnacle coverage levels on the blade upper surface. The drag ratio is a measure of the blade drag including barnacle fouling to the reference blade drag measurement and the blade barnacle coverage is a measure of the proportion of the blade elements modelled to include barnacle fouling. This parameter ranges from 0, which indicates no barnacle fouling, to 1, which indicates barnacle fouling on all blade elements. To convert this parameter to a physical number of barnacles present on the blade the coverage value is simply multiplied by the number of individual blade elements in the model, which allows the results to be shown independently of the number of blade elements.

The minimum and maximum variations in angle of attack are included for reference, but it is thought that the mean values will provide a good indicator of the total turbine drag increase over a full rotation. Through a full rotation each blade element will experience an oscillatory variation in angle of attack. The total drag acting on the turbine rotor can be estimated as three times the mean drag experienced by a single blade – as the incidence variation is approximated by a sinusoidal function, the instantaneous average blade incidence over three equally spaced rotor blades is equal to the mean angle of attack during a full rotation. To clarify, the rough blade configuration is the microfouled state artificially simulated in the experimental work

by the widely distributed zigzag tape roughness.

5.3.2   BASELINE BLADE CONFIGURATION

The results for the drag analysis on the baseline blade configuration are shown in Figure 5.10, for all three angle of attack spanwise distributions and the four barnacle distribution patterns, and Figure 5.11, which presents a comparison of a subset of these results showing the drag increase for only the mean angle of attack distribution and all four barnacle distribution patterns.

The largest values for the drag ratio are being obtained for the minimum angle of attack distribution along the blade span, with a threefold drag increase for a blade fully covered in barnacles. This decreases to only just under a 50 % increase for the maximum angle of attack distribution. Comparison of the four different barnacle distributions highlights the variation in the blade drag loading which could be expected and is highly dependent on where barnacles colonise the blade surface – a process complicated by a myriad of environmental parameters – particularly for instances where around half of the blade elements are fouled.

As expected, the results are suggesting that the outboard blade elements are more sensitive to barnacle fouling due to having a thinner blade section and lower incidence, hence a larger blade drag coefficient increase. This is most apparent when comparing the drag ratio for distributions A and B. For the mean angle of attack dataset and barnacles distributed from the blade root outwards the drag ratio only begins to appreciably increase once 20 % of the blade elements are fouled and this increases to 55 % of the blade elements for a drag increase of 50 %. This compares to just under 30 % blade coverage for a 50 % drag increase for the barnacle distribution from the blade tip inwards.

From inspection of Figure 4.1 showing a AHH turbine being recovered from a tidal site, the barnacle distribution and blade coverage are closest to the evenly distributed case (Distribution D) with 50 % of the blade elements fouled. This ignores barnacles at multiple chordwise locations present on the same blade element. For this distribution and level of barnacle fouling a drag increase of approximately 75 % could be expected for a single turbine blade. Sareen et al. (2014) have shown this level of drag increase on a wind turbine blade leads to an annual energy production loss of 7 %.

To summarise, in terms of a physical number of barnacles on the upper blade surface, the potential drag increase from the blade design point to a blade state with barnacle fouling could be approximately 50 % for 35 barnacles and increases to twofold for 70 barnacles. Further to this, the results presented are suggesting that the relationship between the number of barnacle on the blade surface and drag increase can be approximated by a linear correlation, but with up to a 50 % variation in the drag ratio dependent upon the barnacle fouling distribution.

(A) Distribution A (Root)

(B) Distribution B (Tip)

(C) Distribution C (Mid)

(D) Distribution D (Even)
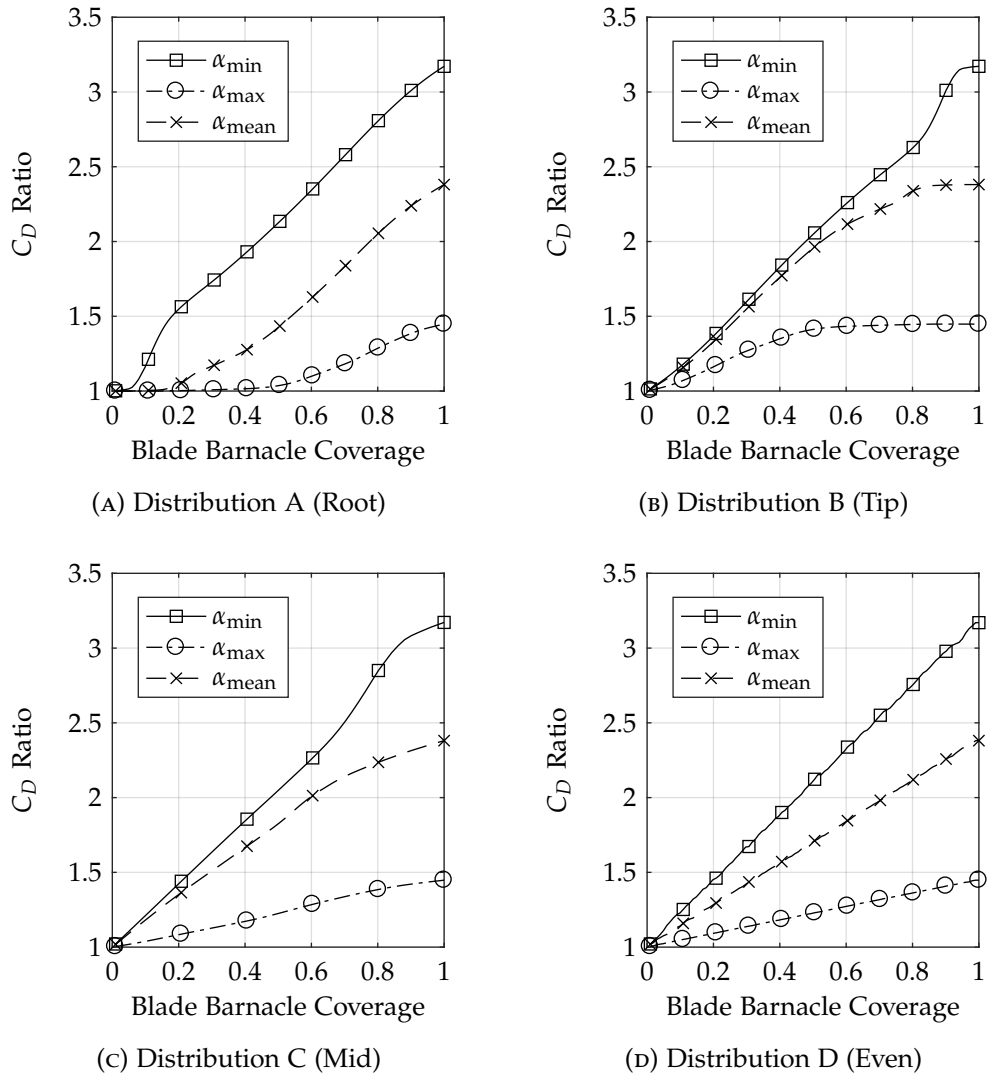
FIGURE 5.10: Drag ratio due to variations in barnacle fouling level and distribution for the baseline blade configuration at three different operating angle of attack spanwise distributions. Details of the distributions can be found in Table 5.4 and Figure 5.9.
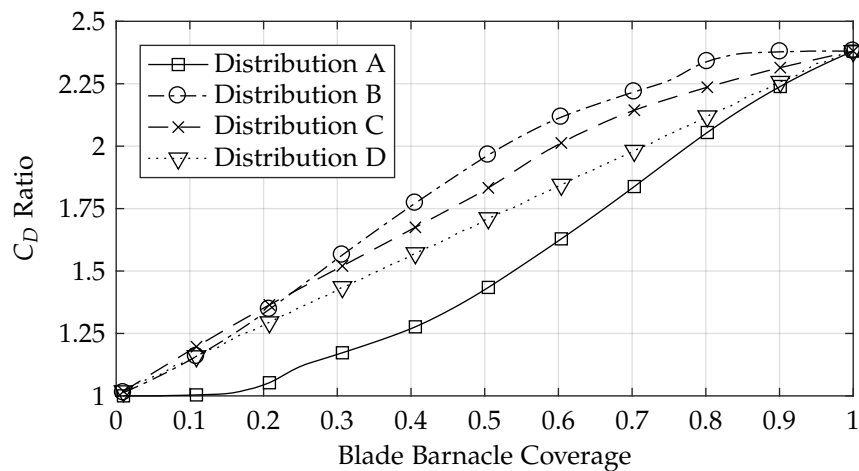
FIGURE 5.11: Drag ratio due to variations in barnacle fouling level and distribution on the baseline blade configuration at the operating envelope mean angle of attack. Details of the distributions can be found in Table 5.4 and Figure 5.9.

5.3.3 ROUGH BLADE CONFIGURATION

For completeness the equivalent results for the rough blade configuration are shown in Figures 5.12 and 5.12.

As the blade section becomes roughened with microfouling the influence of the barnacle on the section drag increase has been shown to decrease. The drag ratio results for the full blade agree with this previous finding and display a similar trend in drag ratio as the number of barnacles on the blade elements increases, albeit with a reduced magnitude. It is more likely that a turbine blade will have a certain level of macrofouling present on the blade surface before the process of barnacle attachment begins, but the difference from the design point to the expected blade state is required for predicting life cycle turbine loading. The drag increase from the baseline configuration to a fully fouled state, with both macrofouling and microfouling present, has been shown to be the same as that for the baseline configuration with microfouling alone.

The peak blade drag increase, when all blade elements are modelled to have a barnacle present, for the rough blade configuration is just under 85 % for the minimum angle of attack distribution and decreases to only 7 % for the maximum incidence distribution. The mean angle of attack distribution shows a peak drag increases of just under half, while the most probable barnacle distribution and level results in a blade drag increase of just under 25 %. Even with a light level of surface microfouling, the drag ratio for a specified number of barnacles across the blade span remains approximated by a linear relationship, but with a reduced variation between the four different barnacle distributions.

5.3.4 BARNACLE INFLUENCE ON TURBINE POWER & THRUST

As a final consideration in the role barnacles may play in the degradation of the turbine performance, the impact of barnacle fouling on the turbine power and thrust can be determined from the presented blade section loading results. Using the BEMT method outlined in Section 5.2.1 and the blade element drag increase procedure summarised in Section 5.3.1, the total turbine power and thrust are determined from the summation of the differential thrust and torque parameters. As the drag coefficient is set to zero for determining the axial and tangential inductions and blade elements drag coefficient is only used in Equations 5.11 and 5.12 to calculate the final power and thrust coefficients at each turbine tip speed ratio. Therefore the flow conditions determined from the induction factors at each turbine tip speed ratio will not change when the barnacle is included on the reference blade. The assumption of evenly distributed barnacle fouling (Distribution D) over 50 % of the blade elements is maintained for this analysis and the drag increase due to the barnacle is again applied as a function of the local angle of attack. As before, the presence of the barnacle will only increase the drag
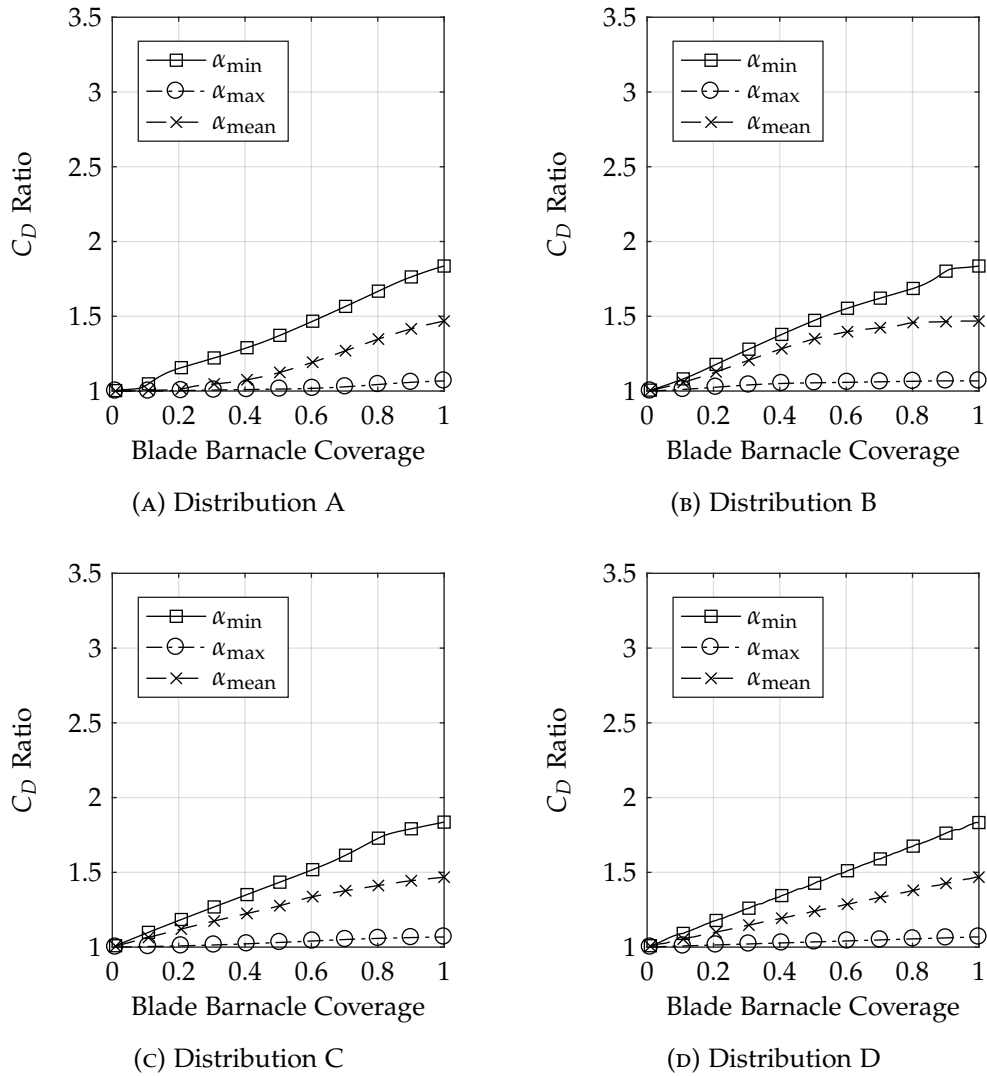
FIGURE 5.12: Drag ratio due to variations in barnacle fouling level and distribution for the rough blade configuration at three different operating angle of attack spanwise distributions. Details of the distributions can be found in Table 5.4 and Figure 5.9.
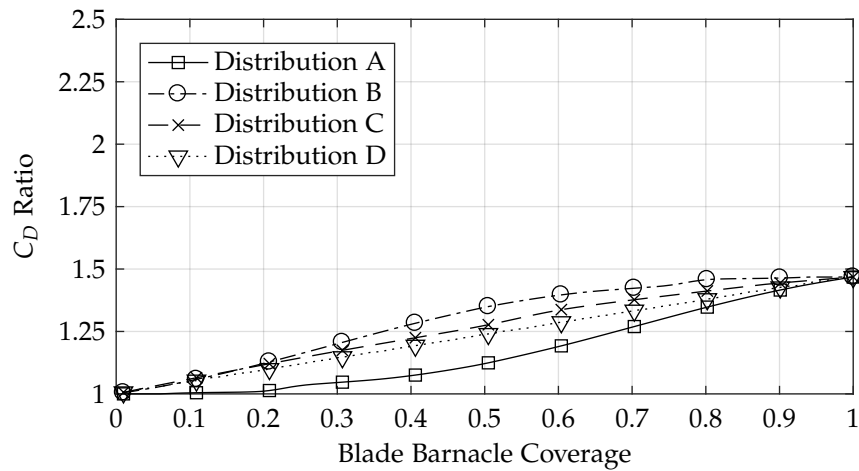
FIGURE 5.13: Drag ratio due to variations in barnacle fouling level and distribution on the roughened blade configuration at the operating envelope mean angle of attack. Details of the distributions can be found in Table 5.4 and Figure 5.9.

coefficient of the blade section and the lift coefficient terms in Equations 5.11 and 5.12 will remain unchanged.

To allow a direct comparison to the performance curves presented in Figures 5.3 and 5.4, the generic HARP_Opt designed turbine geometry used in Section 5.3 is replaced with the turbine geometry from AHH Site 3 (See Section 2.3), as used for the BEMT analysis in Section 5.2. The results of the turbine performance analysis with barnacle fouling present on the turbine blade are shown in Figure 5.14, for the turbine power coefficient, and Figure 5.15, for the turbine thrust coefficient.

The NACA 63-619 and AHH 19 blade sections are located at a comparable radial position on the turbine blade and therefore will be considered separately, but with the AHH 32 aerofoil at its equivalent inboard blade location, and although similar, are both included in the results for completeness. The turbine performance curves presented in Section 5.2 are included here for reference, where the dataset descriptors *Baseline* and *Rough* take their usual meaning and *Fully Fouled* is the blade configuration with both a light level of surface microfouling and the barnacle macrofouling distributed as described. The inclusion of all three datasets in the results allows the performance evolution of a representative tidal turbine, from the baseline design case through an initial fouling state through to the final fully fouled state which can be regarded as a representative fouled state on a deployed turbine blade.

From inspection of the presented performance curves it is apparent that barnacle fouling is only influencing the turbine performance at higher tip speed ratios. The turbine rated power will be achieved close to, or ideally at, the optimal tip speed ratio. Therefore, the results suggest that barnacle fouling will have a minimal influence on the turbine power output and thrust loading when the turbine is operating at rated power. This region of turbine operation is identified at tip speed ratios less than the optimal value and corresponds to the left hand side of the curves. Conversely, at higher tip speed ratios, corresponding to the turbine cut-in flow velocity and variable speed range, barnacle fouling will result in a further decrease in the turbine power coefficient and an increase in the turbine thrust loading as the blade element drag contribution is also increased. At a tip speed ratio of $\lambda = 8$ the power coefficient is decreasing by 0.044 for both turbine geometries – a percentage decrease of 15.1 % and 19.7 % for the NACA 63-619 and AHH 19 based turbines respectively, with reference to the performance of the rough blade configuration. The thrust coefficient is increasing by 0.028 at the equivalent conditions – increases of 6.6 % and 8.6 % respectively.

Although suitable for a simple engineering model, the analysis presented here is showing that estimates of the changes in the turbine power and thrust due to marine biofouling cannot be solely determined by applying fixed percentage increases to the BEMT lift and drag terms in Equations 5.2 to 5.5 and that consideration must be made to the changes arising in the turbine inflow conditions due to the decreased rotor rotational speed for the same upstream tidal flow conditions.
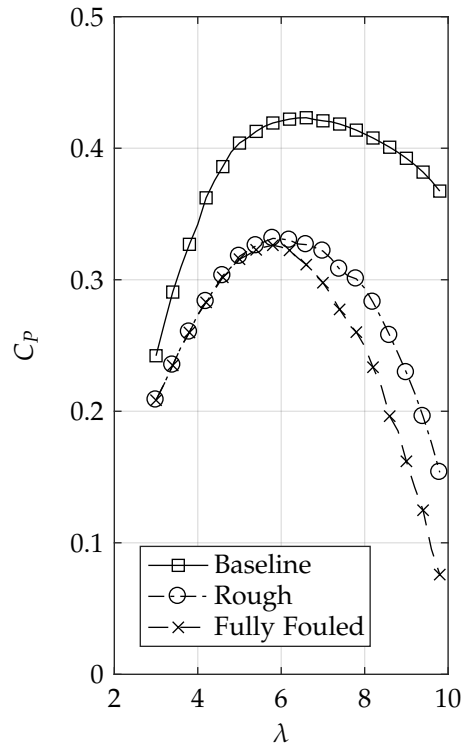
(A) NACA 63-619 and AHH 32
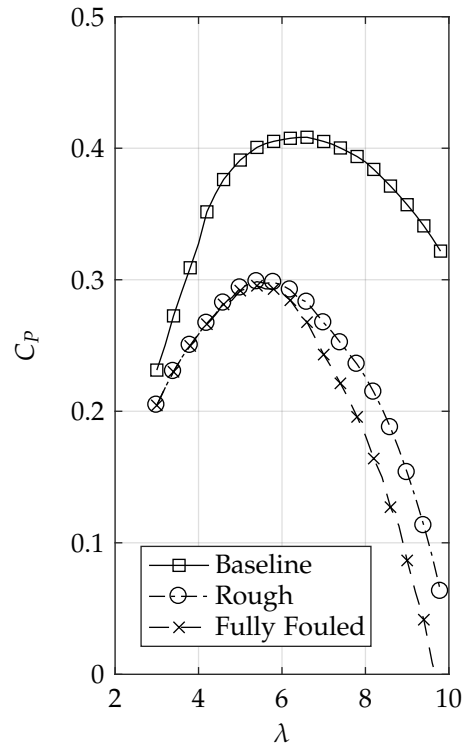
(B) AHH 19 and AHH 32

Figure 5.14: Power coefficient, C_P, performance curves for a 1 MW tidal turbine with varying levels of roughness arising from marine biofouling.
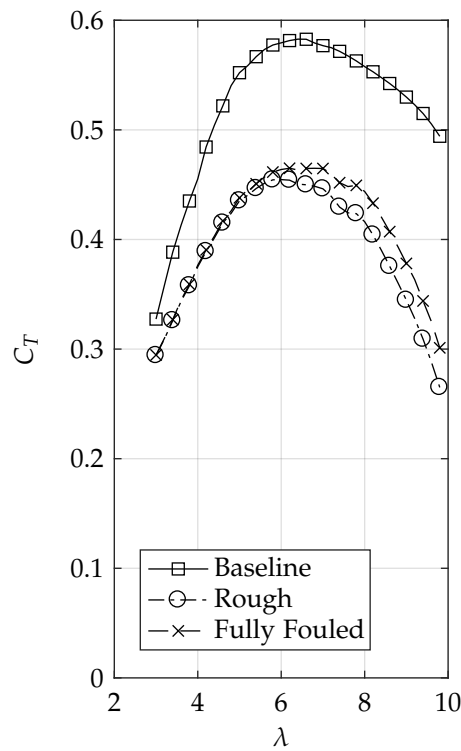
(A) NACA 63-619 and AHH 32
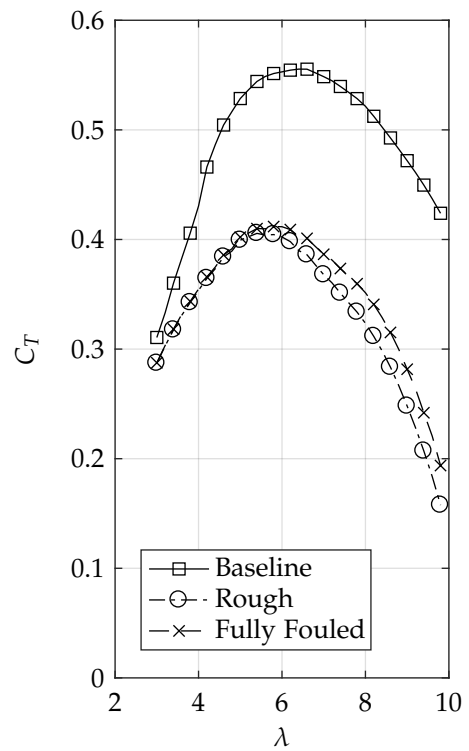
(B) AHH 19 and AHH 32

Figure 5.15: Thrust coefficient, C_T, performance curves for a 1 MW tidal turbine with varying levels of roughness arising from marine biofouling.

5.3.5   Barnacle Influence on Estimates of Turbine Degradation

Section 5.2.4 presented estimates of the turbine performance in the baseline and rough blade configurations. This section presents the same turbine performance parameters, but for the fully fouled blade configuration – light surface microfouling roughness and barnacle fouling evenly distributed across the blade span applied over half the blade surface. The turbine performance results for the baseline reference configuration are shown in Table 5.1.

In the fully fouled state, the turbine operates at an optimal tip speed ratio of $\lambda = 5.8$ and achieves rated power of 1 MW at a freestream tidal current of 2.6 m/s, giving a turbine rotational speed of 13.71 rpm. Table 5.5 presents the turbine performance parameters for these flow conditions.

Table 5.5: Turbine performance parameters for the fully fouled blade configuration at the turbine rated power and optimal tip speed ratio.

Configuration	λ [–]	U_∞ [m/s]	Ω [rpm]	P [kW]	Q [kN m]	T [kN]
Rated P (F. Fouled)	5.8	2.60	13.71	998.4	908.0	543.3

The performance parameters for the fully fouled turbine, but at the flow speed at which the baseline configuration achieves rated power are given in Table 5.6.

Table 5.6: Turbine performance parameters for the fully fouled blade configuration at the optimal tip speed ratio and flow speed for rated power in the baseline configuration.

Configuration	λ [–]	U_∞ [m/s]	Ω [rpm]	P [kW]	Q [kN m]	T [kN]
Rated U (F. Fouled)	5.8	2.42	12.77	805.1	786.6	470.6

A comparison of the fully fouled turbine performance parameters to those in the baseline and rough blade configurations are shown in Figure 5.16, for the rated power condition, and in Figure 5.17, for the flow speed at which rated power is achieved in the baseline configuration.

Comparing the performance of the three configurations at rated power, there is little variation in the estimated values for the turbine torque and thrust. The fully fouled configuration achieves rated power at a flow speed of 2.6 m/s, marginally lower than 2.68 m/s for the rough case, but both higher than the rated flow speed of 2.42 m/s. With the addition of barnacle fouling, the turbine torque increases by 34.1 kN m, with reference to the rough configuration, and the thrust increases by 37.4 kN, as would be expected. In the previous section the significant reductions in the turbine power output, of over 25 %, at the rated flow speed was highlighted. The addition of barnacle fouling to the rough configuration shows an improvement to the power output. The fully fouled turbine is estimated to generate 805.1 kW compared to 735.3 kW in the rough configuration. However, this still results in a dramatic power
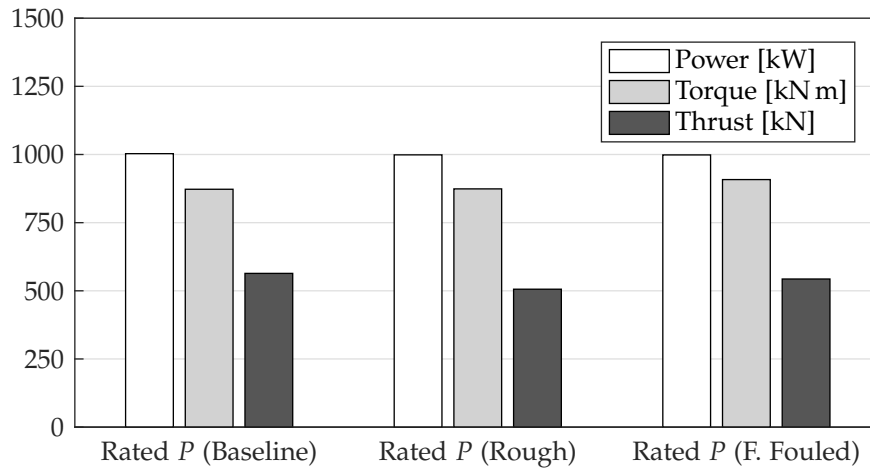
FIGURE 5.16: Turbine power, torque and thrust estimates at rated power and optimal tip speed ratio for baseline, rough and fully fouled blade configurations.
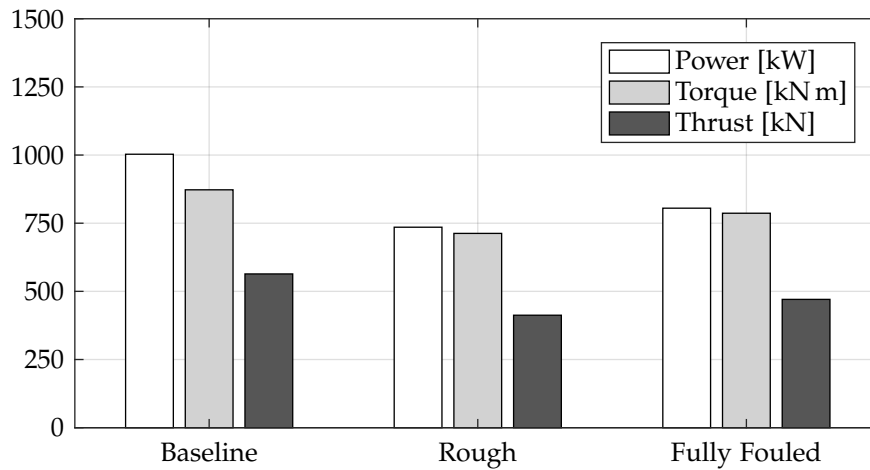
FIGURE 5.17: Turbine power, torque and thrust estimates at flow speed for baseline rated power and optimal tip speed ratio for baseline, rough and fully fouled blade configurations.

output reduction of 19.7 % from the 1 MW rated power.

The turbine power and thrust, at the optimal tip speed ratio, across the turbine variable speed range is presented in Figure 5.18, which highlights that the baseline turbine configuration will generate a higher power output at lower tidal flow speeds, but always with a higher thrust force. It would perhaps be expected that any level of fouling would increase the turbine thrust, due to the increased drag component of the force acting on the blade, but the fouling is also reducing the lift component. From inspection of these results it can be seen that the addition of barnacle to the rough configuration increases the rotor thrust, as macrofouling is not thought to significantly change the lift force, but also marginally improves the turbine power output at a given flow speed. This result is counter-intuitive and should be treated with caution, but can be explained by the fact that the viscous boundary layer effects have not been accounted for in the drag measurement and have therefore not been considered in the

(A) Turbine Power   (B) Turbine Thrust
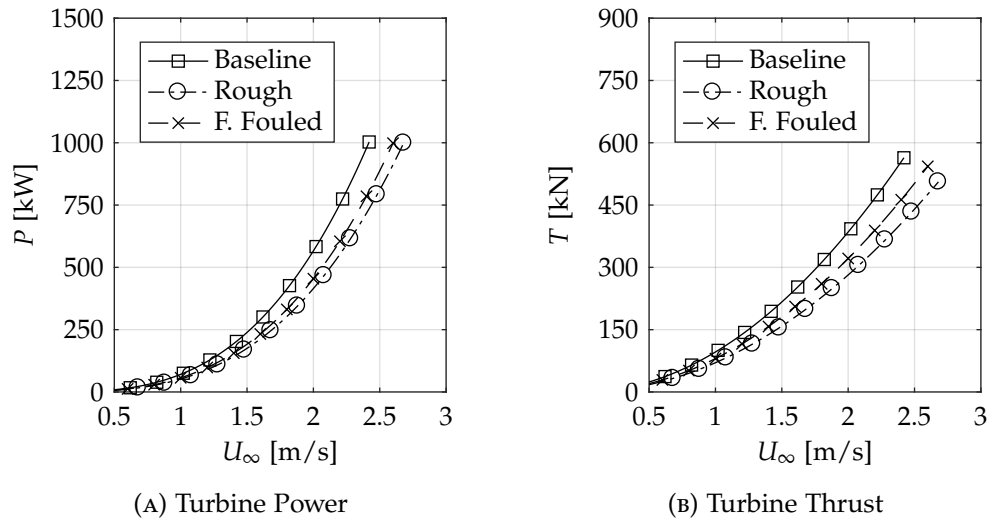
FIGURE 5.18: Estimates of the tidal turbine power output and thrust over the turbine variable speed operating range for both baseline, rough and fully fouled blade configurations.

analysis presented.

5.4   TURBINE BLADE CAVITATION CONSIDERATIONS

When rotational machines are operating in a liquid working fluid, local pressure and velocity variations can result in the formation of vapour cavities in the fluid during a fluid phenomenon called cavitation (Carlton, 2012). For a tidal turbine operating in seawater, blade cavitation has been confirmed from experimental investigations to be an issue which needs to be considered during the design of the turbine blades (Wang et al., 2007; Bahaj et al., 2007a). Alongside hydrodynamic performance implications, the blade cavitation process can have significant consequences on both the structural integrity of the blade (Uzawa et al., 2008) and increased environmental noise (Wang et al., 2007; Shi et al., 2016). Cavitation has been widely investigated on maritime propellers (Carlton, 2012) and the ability to predict cavitation inception on the turbine blade, which is most likely to occur on outboard blade sections, is of particular benefit at the preliminary design stage of the tidal turbine (Molland et al., 2004). It is desirable to delay cavitation inception on the tidal turbine blade, but this needs to be balanced with the design requirements for a blade which exhibits delayed stall and an optimal lift-to-drag ratio over a wide range of turbine operating conditions. Further to this, marine propellers can operate with no significant loss of performance despite high levels of cavitation, but no equivalent acceptance criteria have been proposed for tidal turbines (Batten et al., 2006). A major challenge remains to understand the erosion effects of cavitation on the composite materials widely used in the construction of the turbine blades (Uzawa et al., 2008). The NACA 63-619 aerofoil has been selected for highlighting cavitation considerations in this section of the chapter.

5.4.1 CAVITATION INCEPTION

Cavitation will occur on the blade if the local blade pressure, p_L, falls below or equal to the vapour pressure, p_v, of the working fluid. Using the convention described by Buckland et al. (2013), the local blade pressure can be expressed using the cavitation number, σ, given in Equation 5.15. This non-dimensional parameter is the ratio of the static and dynamic pressure heads acting at the position of the blade section of interest.

$$\sigma = \frac{p_{\text{baro}} + \rho g h - p_L}{q} = -C_p \tag{5.15}$$

The static pressure head includes the influence of the water column, atmosphere and local blade pressure on the blade element and the dynamic pressure head is based on the local resultant velocity at a blade section at the appropriate turbine radial position. Similarly, the critical cavitation number, σ_{crit}, is defined in Equation 5.16.

$$\sigma_{\text{crit}} = \frac{p_{\text{baro}} + \rho g h - p_v}{q} \tag{5.16}$$

If the condition $\sigma \geqslant \sigma_{\text{crit}}$ is satisfied then cavitation will occur, otherwise $\sigma < \sigma_{\text{crit}}$ and no cavitation occurs on the blade section.

This approach, using two-dimensional pressure distributions in conjunction with cavitation criteria, has been experimentally validated for tidal turbine blades (Molland et al., 2004; Batten et al., 2008). However, the analysis does not take the smaller scale physics into account, such as the growth and decline of the cavitation nuclei, but is a good engineering model for understanding the turbine operational limitations (Carlton, 2012). As this method uses two-dimensional pressure data, it is most suitable to assume sheet cavitation would occur on the aerofoil and no conclusions with regard to tip vortex cavitation can be made.

The cavitation inception envelope for the NACA 63-619 aerofoil is shown in Figure 5.19 for the baseline and rough blade configurations. The section cavitation number is estimated at each aerofoil incidence to be equal to $-(C_{p_{\text{min}}})$ from the steady experimental aerofoil chordwise pressure dataset. The four primary cavitation zones are identified.

The width of the bucket indicates the blade incidences which can be expected to be cavitation free. For a tidal turbine which has a wide range of operating conditions a wider bucket is beneficial as a narrow bucket limits cavitation-free operation to the operational line and does not allow for off-design conditions. The effect of light biofouling roughness on the blade is to increase the incidence range in which cavitation is not likely to occur, particularly at positive angles of attack beyond flow separation. As these envelopes are based on two-dimensional aerofoil results they are not strictly
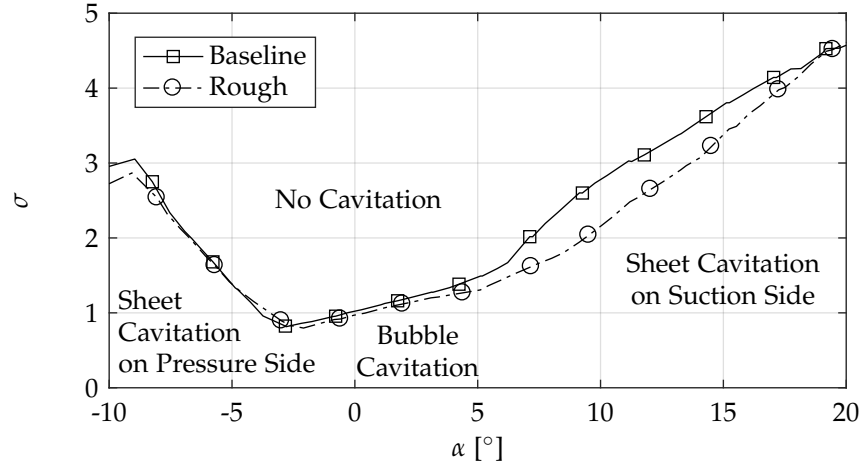
FIGURE 5.19: Cavitation inception envelope as a function of angle of attack for the NACA 63-619 aerofoil in baseline and rough configurations.

TABLE 5.7: Turbine parameters for blade cavitation investigation.

Parameter	30 m Water Depth		50 m Water Depth	
	0.7R	0.85R	0.7R	0.85R
h [m]		30		50
z_{hub} [m]		15		20
U_{hub} [m/s]		3.0		2.2
D [m]		18		26
Ω [rpm]		14.3		7.6
c [m]	1.20	0.85	0.90	0.65
U_{rel} [m/s]	9.91	11.86	7.61	9.11
k_{turbine} [–]	0.091	0.054	0.047	0.029
k_{model} [–]	0.1	0.05	0.05	0.025

correct for highly three-dimensional flows at the blade tip and root regions, but this investigated blade section is located inboard from the tip where the flow will be closer to the two-dimensional case.

5.4.2 TURBINE CASE STUDIES

As the blade cavitation number is a function of both the blade position in the water column and the local blade flow conditions, the cavitation number will vary through a complete revolution of the turbine. To investigate this variation and the potential for cavitation to occur on the turbine blade, the experimental data for the NACA 63-619 blade section is applied to two typical 1 MW turbine sites of different depths and mean hub height flow speeds, as summarised in Table 5.7. As previously, the 19 % thick blade sections are taken to be at radial positions between 70 % and 85 % of the rotor span.

The first case is for an 18 m diameter turbine sited at a water depth of 30 m with a

mean hub height flow speed of 3 m/s. At rated power a rotational speed of 14.3 rpm is achieved. The second case considered is a deeper, slower flow tidal site with a 50 m water depth and a mean hub height flow speed of 2.2 m/s, resulting in an increased turbine diameter of 26 m and reduced rotational speed of 7.6 rpm. The larger diameter turbine has a more slender blade, hence a shorter blade section chord at the equivalent radial positions. The turbine reduced frequency is calculated for the selected turbine parameters, using the mean hub height flow velocity, and matched to the closest entries in the experimental database. The values obtained are in agreement with the previously determined reduced frequency spanwise distributions shown in Figure 2.12.

The vapour pressure of seawater is dependent on both temperature and salinity. The sea surface temperature in northern UK waters, including the areas around the EMEC tidal test site and the Pentland Firth, ranges between 7 °C and 13 °C over the course of the year (World Sea Temperatures, 2017). Using an average sea temperature of 10 °C and a standard seawater salinity of 35 g/kg gives a seawater vapour pressure of 1200 Pa. For the depth of water the turbines are deployed in, the sea temperature can be assumed to be constant through the water column. A value of 2000 Pa is widely used for the seawater vapour pressure, particularly for laboratory investigations (Batten et al., 2006), however, this corresponds to a fluid temperature of 20 °C.

The oscillatory experimental aerofoil data is transposed to the turbine rotational frame of reference, where one pitch cycle corresponds to one complete turbine revolution, and the maximum angle of attack will coincide with a turbine azimuth angle of 180° at the bottom position of the rotation. The velocity shear profile is modelled with the one-seventh power-law and the resultant velocity of the blade section is calculated assuming a constant rotational speed. For this analysis the axial and tangential induction factors are neglected and the height of surface waves is ignored with an assumed average mean free surface height equal to the water depth.

By equating the cavitation number to the minimum aerofoil pressure coefficient, this approach only considers if cavitation will occur on the blade section at the radial position of interest and not the chordwise extent of the blade section where cavitation is occurring. Cavitation is most likely to occur at the leading edge region of blade sections towards the blade tip (Buckland et al., 2013) and even though the results presented here are for a blade section slightly further inboard on the blade the results are still suitable to investigate cavitation inception, particularly with regards to how surface roughness and water depth representative of real actual tidal sites influence cavitation inception. Cavitation results from cavitation tunnel testing of a clean tip blade section, a NACA 63-615 aerofoil from a radial position of $0.95R$, can be found in Batten et al. (2008). Although the turbine rated power case has been selected, the turbine reduced frequencies at the other turbine speed ratings are of approximately the same magnitude to the rated power case once the slower tidal current speed and turbine rotational speed have been accounted for. Furthermore, this method does

not account for the fact that roughness of the blade surface will modify the turbine loading. Blade fouling will decrease both the turbine torque, hence power output, and thrust, as shown in Section 5.2. Therefore, a decrease in the rotational speed of a turbine with roughened blades at equivalent flow conditions for the baseline turbine would be expected. However, small changes in the turbine speed for the same flow conditions in the outlined method will not lead to significant changes in the local blade incidence or reduced frequency.

CASE 1 RESULTS: 30 M WATER DEPTH

Cavitation analyses for the shallower 30 m deep tidal site are shown in Figures 5.20 and 5.21, for the $0.7R$ and $0.85R$ radial blade positions respectively. The results are presented in terms of a cavitation inception margin ($\sigma_{\text{crit}} - \sigma$) as a function of the turbine azimuth angle for both the typical ($\alpha = 5° \pm 4°$) and limiting ($\alpha = 10° \pm 6°$) incidence cases. A negative cavitation margin – identified from a loop in the results – indicates that cavitation will occur on the blade section. Both the baseline and rough blade configurations are included.

Examination of the cavitation inception margins reveal that, for all presented cases, the rough blade configuration is reducing the occurrence of flow cavitation compared to the equivalent case in the baseline blade configuration. This is due to the blade surface roughness reducing the peak suction pressure on the blade upper surface, hence reducing the cavitation number of the blade section under those flow conditions.

The variation in the cavitation inception margin introduced by the blade roughness is seen to be dependent on the turbine operating condition. The largest difference for the typical loading cases coincides with the deepest blade immersion, occurring at an azimuth angle of approximately 180°, and the largest variation is identified at an approximate azimuth angle of 150° for the limiting loading cases. This agrees with the cyclic position the peak suction pressure occurs at during a pitch cycle, which is identified as the incidence at which moment break occurs. As the level of unsteadiness and stall penetration increases, the moment break incidence moves to an incidence marginally lower than the maximum angle of attack achieved during an oscillatory cycle.

The turbine reduced frequency has been related to the blade radial position and turbine rotational speed for this analysis, allowing the spanwise variation of cavitation inception to be assessed. For the typical oscillatory incidence variation no cavitation occurs at, or between, either of the investigated blade radial positions. The smallest cavitation margin is occurring at a turbine azimuth angle of 0°, which coincides with the minimum blade section immersion depth. However, moving outboard along the blade, from a radial position of $0.7R$ to $0.85R$, the cavitation margin decreases as the blade section tangential flow speed, hence dynamic pressure, increases, although the level of flow unsteadiness as indicated by the reduced frequency decreases. These

(A) $k = 0.1$, $\alpha = 5° \pm 4°$ (B) $k = 0.1$, $\alpha = 10° \pm 6°$
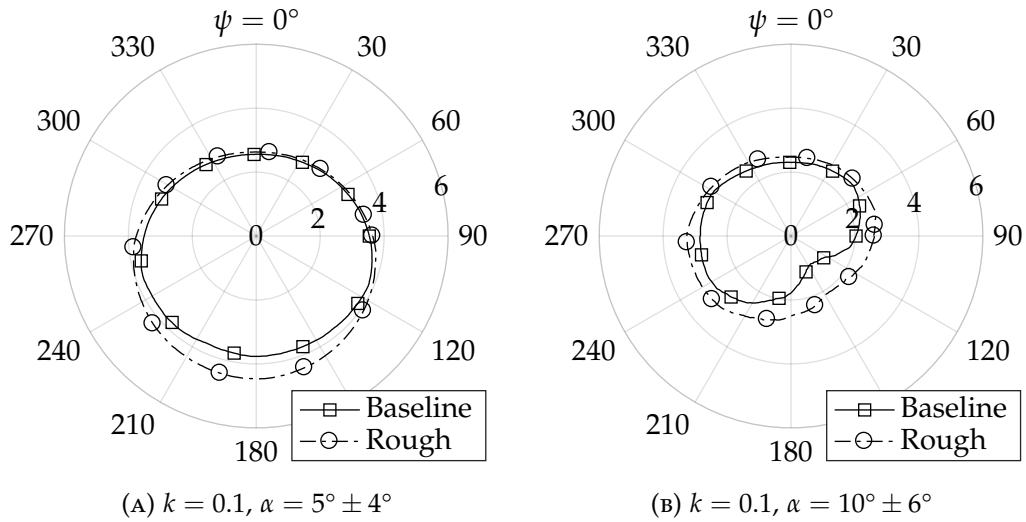
FIGURE 5.20: Cavitation inception margin as a function of the turbine blade azimuth angle at a radial position of $0.7R$ and 30 m water depth in both clean and rough blade configurations for typical and limiting blade section incidences.

(A) $k = 0.05$, $\alpha = 5° \pm 4°$ (B) $k = 0.05$, $\alpha = 10° \pm 6°$
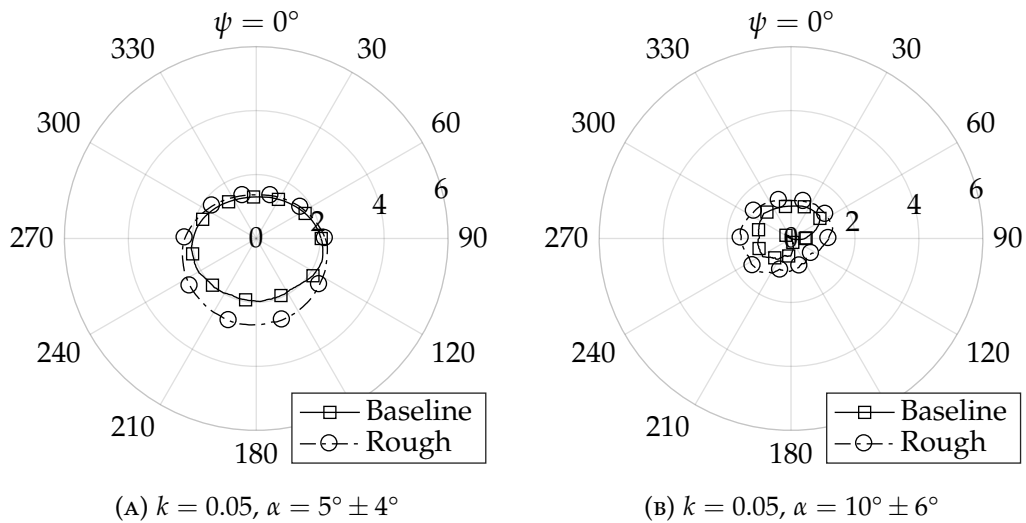
FIGURE 5.21: Cavitation inception margin as a function of the turbine blade azimuth angle at a radial position of $0.85R$ and 30 m water depth in both clean and rough blade configurations for typical and limiting blade section incidences.

results suggest that the likelihood of blade cavitation occurring towards the blade tip region is increased and agrees with previously published investigations (Buckland et al., 2013; Shi et al., 2016). For the limiting loading case a comparable behaviour is seen, but for these flow conditions cavitation is now expected to occur on the blade. However, this is only for the one investigated case in the baseline configuration.

Comparing the influence of blade loading at the same radial position with the same level of flow unsteadiness, but different levels of stall penetration, the largest changes in the cavitation inception margin are seen for turbine azimuth angles between 60° and 240°, where the blade is travelling through the deepest portion of the water column. This can be highlighted by comparing the two baseline cases presented in Figure

5.20. At a turbine azimuth angle of 0° the cavitation inception margins are 2.63 and 2.31, for the typical and limiting cases respectively, compared to 3.76 and 1.10 at 150°, confirming that the cavitation inception variation across the blade is a function of the local flow unsteadiness and level of blade section stall penetration. It is also apparent that the position of the minimum cavitation inception margin will move move around the rotor azimuth as the flow unsteadiness and blade loading increase from close to the top dead centre 0° azimuth position moving to a position at appropriately 150°.

CASE 2 RESULTS: 50 M WATER DEPTH

The results for the cavitation analyses at the deeper 50 m tidal site are shown in Figures 5.22 and 5.23. They are presented in the same format as those for the 30 m water depth case and include the same blade section incidence variations around the turbine azimuth. It should be noted that the results for the 50 m water depth are presented on a different scale to the previous set of results for a water depth of 30 m.

As with the results for the shallower tidal site, a distinct pattern in the cavitation behaviour is observed, particularly with blade roughness increasing the cavitation inception margin through the turbine rotation. However, the magnitude of the cavitation inception margin is significantly larger for the turbine deployed in a deeper tidal site, indicating that cavitation is less likely to occur on the turbine blade with increasing immersion depth. For the selected test cases and radial position range of interest, no cavitation is identified or would be expected to occur on the turbine blade over the extent of the typical turbine operating conditions.

Again, the cavitation inception margin is smallest at the top of the turbine rotation, at 0° azimuth angle, but coincides with the position where the blade roughness has a minimal effect. The roughness is having its biggest impact on the inception margin at an azimuth angle of approximately 180°, but moving closer to 120° as the static stall penetration increases to the maximum values investigated. This set of results suggests that when considering the occurrence of cavitation at the blade design stage, not only does the local pressure distribution around the blade need to be considered, but also the local flow conditions and depth for the selected tidal site.

VARIATION OF TURBINE PARAMETERS

Results for the two water depths have presented the cavitation inception margin as a function of the turbine azimuth angle over one complete rotation of the turbine blade, for two selected turbine blade section loading cases. Determining the minimum inception margin over a single rotation ($(\sigma_{\mathrm{crit}} - \sigma)_{\mathrm{min}}$) reduces the parameter to a single value for each rotational cycle, independent of the turbine azimuth angle. This allows the minimum cavitation inception margin to be presented as a function of the maximum blade section incidence over a complete revolution for the full turbine

(A) $k = 0.05$, $\alpha = 5° \pm 4°$ (B) $k = 0.05$, $\alpha = 10° \pm 6°$
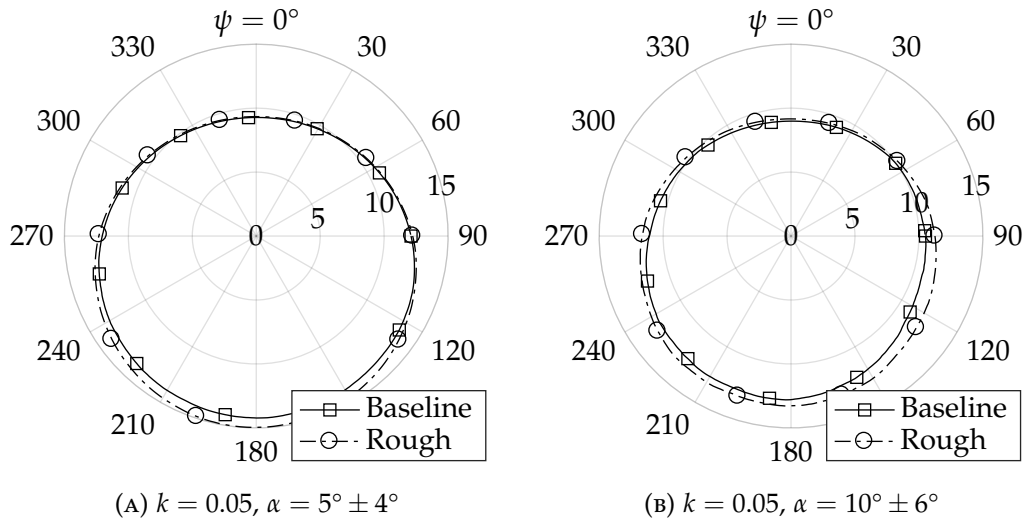
FIGURE 5.22: Cavitation inception margin as a function of the turbine blade azimuth angle at a radial position of $0.7R$ and 50 m water depth in both clean and rough blade configurations for typical and limiting blade section incidences.

(A) $k = 0.025$, $\alpha = 5° \pm 4°$ (B) $k = 0.025$, $\alpha = 10° \pm 6°$
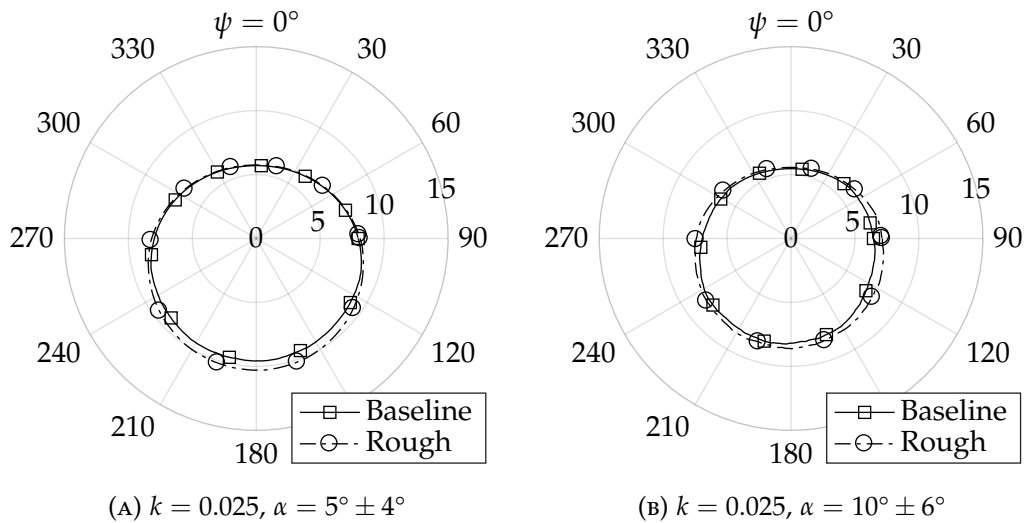
FIGURE 5.23: Cavitation inception margin as a function of the turbine blade azimuth angle at a radial position of $0.85R$ and 50 m water depth in both clean and rough blade configurations for typical and limiting blade section incidences.

operating range, as shown in Figure 5.24. The left hand figure column corresponds to data for a water depth of 50 m, and 30 m water depth for the right hand figure column.

Firstly, the effect of blade surface roughness on the minimum cavitation inception margin is discussed. Previously it was shown that surface roughness will increase the cavitation inception margin, particularly at the bottom of the water column. However, when considering the minimum margin as a function of the maximum blade section incidence during a rotation, it can be seen for each of the four datasets that the roughness is having a negligible influence for cases in the attached flow regime. The NACA 63-619 aerofoil used in this cavitation study has a static stall angle in the
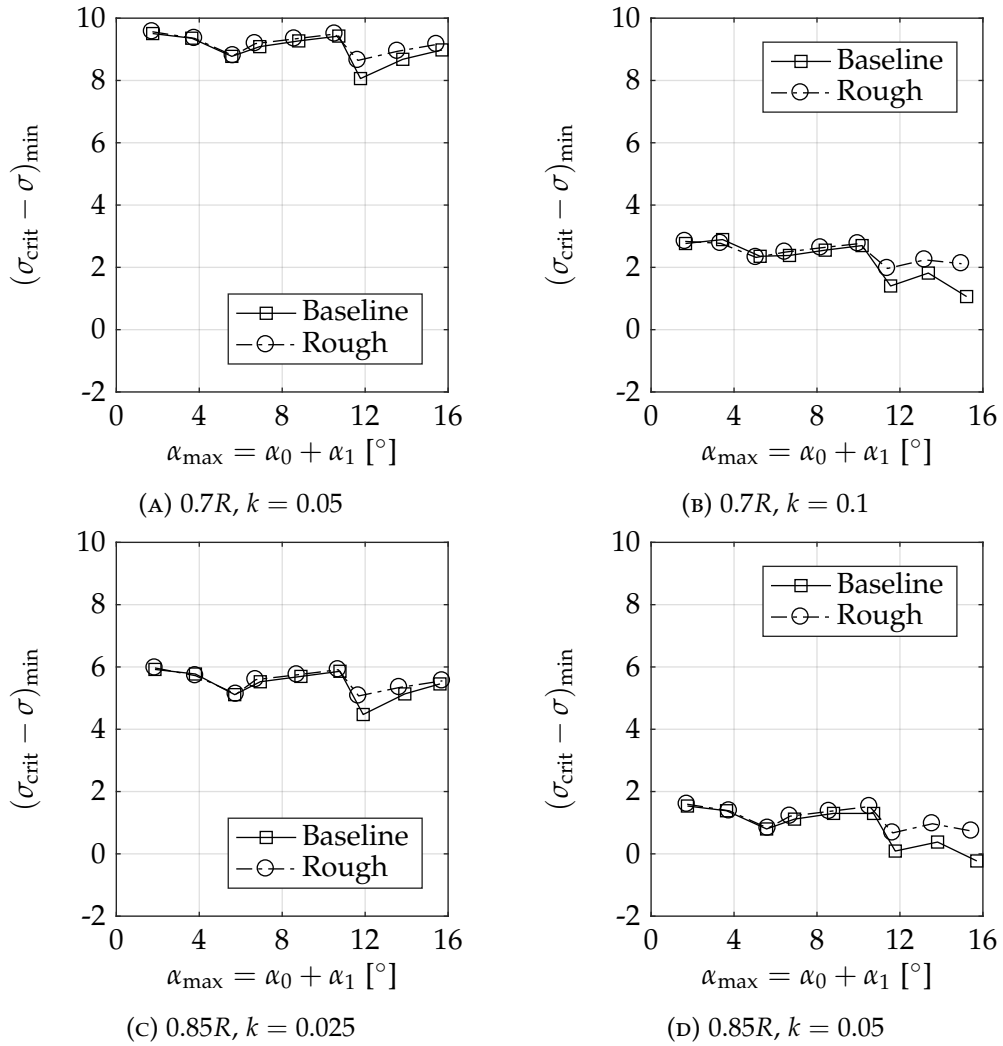
FIGURE 5.24: Variation in minimum cavitation inception margin as a function of maximum blade section angle of attack.

baseline configuration of 10.2°, and only beyond this incidence is roughness improving cavitation inception. In other words, even though the roughness is improving the overall inception margin throughout a blade rotation, the point where the inception margin is smallest is only improved is the maximum blade incidence in a rotation exceed the static stall angle of the local blade section. This effect is being driven by the difference in the peak suction pressures, and where it occurs in the pitch cycle, compared to the roughened case.

As the results are presented in terms of the reduced frequency it is appropriate to compare the two cases with $k = 0.05$ in Figure 5.24 to interpret the change in water depth. This shows the cavitation inception margin increasing for increased water depth. However, as cavitation is most likely to occur at an azimuth angle of 0° for the majority of the turbine operating conditions, it is not just the water depth which has to be considered, but the minimum blade immersion at the top of the turbine rotation and the blade section incidence variation during the rotation. This suggests that cavitation will be more of an issue at shallower tidal sites towards the blade tip

and for unsteady flows penetrating beyond stall.

In all but the most extreme operating conditions, it is thought that flow cavitation will be restricted to the tip region of the blade. This analysis does not account for the local pressure distribution due to the tip vortex system on the blade, but using the same cavitation theory approach the possible behaviour at the blade tip can be suggested. Compared to the results presented here, the tip blade section will have a shorted chord and higher tangential flow speed, hence a lower reduced frequency. The maximum blade incidence during a rotation will also be smaller. It is known that the cavitation inception margin will be reduced and that flow cavitation is likely to occur, but it is thought that due to the lower blade operating incidences any surface roughness will improve the cavitation behaviour.

Cavitation on a tidal turbine blade is driven by the peak suction pressure on the blade upper surface towards the leading edge. As it has been suggested that barnacle fouling is unlikely to occur on this region of the blade surface then it is thought that barnacle fouling will not change the behaviour of cavitation inception on the blade.

5.5   CHAPTER SUMMARY

This chapter has investigated and estimated the consequences of marine biofouling on the performance of a full-scale 1 MW tidal turbine. Using the blade section loading results presented in Chapters 3 and 4, for the baseline and fouled blade configurations, numerical models based on blade element momentum theory and cavitation criteria have been developed. The main performance parameters investigated are the turbine power coefficient, thrust coefficient and cavitation inception margin. The main findings from this chapter are now summarised.

Findings for the effect light surface biofouling has on the turbine performance are as follows:

- Performance curves for both the turbine power and thrust coefficients have been presented for an authentic full-scale turbine geometry with a representative level of blade microfouling. Two different outboard blade section geometries are considered which highlight the sensitivity of the BEMT method to the lift and drag coefficients used as model inputs.

- The results confirm that a light level of surface fouling on the turbine blades will have a dramatic impact on the performance of the turbine rotor.

- For the baseline turbine configuration based on the NACA 63-619 aerofoil, a peak power coefficient of 0.399, and thrust coefficient of 0.589, at an optimal tip speed ratio of 6 are identified. With the inclusion of biofouling these key performance indicators are modified to a peak power coefficient of 0.323 and thrust coefficient of 0.460 at a tip speed ratio of 5.8 – both decreases of approximately 20 %.

- In both blade configurations the turbine will achieve rated power, at tidal flow speeds of 2.4 m/s and 2.68 m/s, for the baseline and fouled cases respectively. The fouled turbine will experience a lower thrust loading at the rated power conditions. Although a small variation in the rated flow speeds is calculated this will have longer term consequences on the turbine energy production. At the baseline rated flow speed of 2.4 m/s the fouled turbine is estimated to be producing 25 % less power.

- A recommendation to the industry has been proposed which would require deployed tidal turbines to undergo a two-stage commissioning process to demonstrate initial compliance with the design specifications and a later demonstration of compliance with a defined age-performance specification. This will ensure the turbine performance degradation due to fouling is accounted for during the design stage. A potential future application of the turbine pitch control system and health monitoring system has been suggested to help alleviate potential performance losses from marine biofouling.

Findings for the effect barnacle fouling has on the total blade drag and the subsequent turbine performance are as follows:

- A representative distribution of barnacles on the turbine blade model can be approximated as evenly spread across the blade span and present on approximately half the blade elements. From the limited information available, the occurrence of barnacle fouling on each blade is expected to number approximately fifty individual fouling locations.

- The results demonstrate that the turbine blade drag force and performance is most sensitive to barnacle fouling at the tip region of the blade.

- With reference to the blade baseline design configuration, the blade drag force is estimated to increase by almost 75 % for the defined representative barnacle fouling level and mean local angle of attack variation. Accounting for the local angle of attack variation over the full turbine operating range, the drag increase ranges from 25 % to 110 %.

- The total blade drag increase due to barnacle fouling can be approximated by a linear relationship based on the blade coverage of the fouling.

- The representative level of barnacle fouling on the blade is having a minimal influence on the turbine performance at the optimal operating conditions. In a fully fouled state performance losses have only been identified at tip speed ratios greater than the optimal condition, with reference to the case of microfouling alone. At a tip speed ratio of 8, a power coefficient decrease of up to 20 % and thrust coefficient increase of approximately 10 % could be expected. This is a small improvement from the case of light surface microfouling roughness on the blade surface.

Findings for the effect light surface biofouling has on the turbine blade cavitation inception are as follows:

- It is unlikely that flow cavitation will occur on 19 % tidal turbine blade sections, located at radial positions between $0.7R$ and $0.85R$, unless the turbine blade is experiencing a significant level of flow unsteadiness and stall penetration. For the set of data analysed, at two different water depths, cavitation inception was only identified on the limiting case for the shallower water depth. All other investigated cases were free of flow cavitation.

- At a fixed radial position on the turbine blade, an increase in the level of flow unsteadiness and stall penetration will decrease the minimum cavitation inception margin, making the likelihood of cavitation on the blade more likely. This is due to the maximum peak suction pressure on the blade increasing with increased flow unsteadiness and stall penetration.

- Surface roughness on the blade section generally improves the cavitation inception margin. However, the improvement varies with blade azimuth angle, blade section incidence and flow parameters. If the blade section static stall angle is not exceeded during the blade rotation then a negligible change in the minimum cavitation inception margin, where the difference between the local and vapour pressures is smallest, is identified, even though a larger improvement at other azimuth angles of the blade rotation is observed. For cases where the static stall angle is exceeded the largest improvement to the cavitation inception margin has been identified to occur at an azimuth angle which corresponds to the peak suction pressure, or moment break, on the blade section.

- The results available from this study suggest that for a tidal turbine blade with a light biofouling surface layer, cavitation will not occur at radial positions between $0.7R$ and $0.85R$ during typical turbine operating conditions. However, the results do not allow a relationship between the roughness level and alleviation of cavitation inception to be determined or suggest the role roughness may play in the cavitation process of thinner blade sections at the blade tip where cavitation is more likely to occur. If microfouling is present towards the leading edge of the turbine blade then is would be expected to reduce the suction pressure peak, hence improving the cavitation inception margin as the minimum local pressure on the blade will increase.

- Barnacle fouling is not thought to effect the cavitation behaviour of the turbine blades. The cavitation criteria is based on the aerofoil minimum pressure coefficient, which will occur towards the upper surface leading edge for positive blade incidences, and as no barnacle fouling is expected in this region there will be no change to cavitation inception.

CHAPTER 6

CONCLUSIONS AND FURTHER WORK

The primary objective of this thesis is to determine the impact marine biofouling has on the unsteady hydrodynamic loading and performance of tidal turbine blade sections. To achieve this, a unique set of unsteady experimental data for three different tidal turbine blade sections has been obtained, in a baseline and two surface fouled configurations. It is expected that the conclusions from the presented research work will provide much needed guidance to the marine energy industry and help inform the processes for obtaining estimates of the impact marine biofouling has been shown to have on the performance degradation of tidal turbine blades. Additionally, the results provide an indication of the unsteady blade loading expected through the turbine life cycle and will ultimately contribute towards improving blade fatigue load and life predictions. The final research conclusions and achievements are now outlined, along with recommendations for future work, which it is hoped will all contribute towards the development of robust and economically viable tidal turbine technologies.

6.1 CONCLUSIONS & RESEARCH ACHIEVEMENTS

The approach followed in this work was to experimentally determine the effects of marine biofouling on unsteady tidal turbine blade section loading and, using the obtained data, assess the potential consequences on the tidal turbine performance. It has been shown that the blade sections tested are not insensitive to the surface roughness introduced by marine biofouling and that significant performance losses are to be expected as the fouling species accumulate on the blade during the turbine life cycle.

During turbine operation, the unsteady loads acting on the blade are dependent on the level of unsteadiness in the tidal current and the variation of the local blade section incidence as the turbine rotates. These parameters have in turn been related to

the blade section reduced frequency, through the turbine rotational speed, and the maximum blade section incidence during the pitch cycle, or magnitude of penetration beyond the corresponding static stall condition. The spanwise variation of the local tangential flow speed, with the highest blade section resultant flow at the blade tip, results in a highly unsteady flow conditions for the inboard blade sections and quasi-steady flow conditions for sections towards the blade tip. Similarly, for the blade design to satisfy structural requirements, the inboard blade sections will be thicker and have a larger pre-twist angle resulting in the blade sections operating closer to, or in, the aerofoil stall onset and light dynamic stall regimes. The thinner outboard blade sections are less likely to enter dynamic stall and experience smaller incidences, but will still exhibit the effects of dynamic loading.

The unsteady behaviour exhibited by the tested blade sections is congruous with expectations – a hysteresis load loop with a lift overshoot which increases with increasing levels of flow unsteadiness and fluctuation in the blade section incidence. As with previous unsteady aerofoil investigations, the blade section unsteady loading can be approximated by the equivalent steady behaviour plus the addition of a second-order dynamic effect, which is a function of the reduced frequency and maximum pitch cycle incidence. For the clean baseline configuration, the unsteady peak normal load could be expected to be up to 30 % greater towards the upper limit of the normal operating range for the outboard blade sections, and up to 80 % greater for the inboard blade section, with reference to the corresponding static case.

With the introduction of microfouling to the blade surface, the blade section drag coefficient increases, as would be expected. However, along with the stall delay and reduced maximum lift coefficient, the lift-curve slope is also reduced over the attached flow range, and the indicative kink of gross flow separation is seen in the thicker blade section data. The effect of light surface roughness on the blade section is to increase the drag coefficient by up to 200 % and decrease the lift-to-drag ratio by up to 75 %. In terms of the unsteady blade section loading, the hysteresis load loops do not display a significant change in behaviour, only a decrease in magnitude comparable to the change in the static loading. A negligible difference is seen in the position of the peak load, or moment break, during the pitch cycle, but the the stall process is less abrupt. With respect to the static loading for the roughened blade configuration, the percentage increase of the unsteady peak normal load is of comparable values to the baseline configuration. Further to this, the change in the peak normal load between the baseline and rough blade configurations is shown to be independent of reduced frequency. Therefore, the decrease in the peak normal loading of the blade section when the blade becomes fouled is consistent across the full turbine operating envelope. The impact of blade microfouling is shown to be primarily due to roughness elements at the blade leading edge and roughness towards the aerofoil trailing edge has a reduced influence, especially once the flow in this region has separated.

For the investigation into barnacle macrofouling, it has been shown that a single

barnacle positioned on the blade section upper surface has a negligible impact on the blade section lift coefficient, but will increase the pressure drag coefficient by up to approximately 400 % from the baseline blade configuration. It is also postulated that the position of the barnacle is restricted to aft chordwise locations of the blade due to the higher shear stresses and pressure gradients close to the blade leading edge. An analysis of the spanwise barnacle distribution on the blade indicates that the total blade drag will increase by 75 % for a representative barnacle count and distribution.

When assessing the turbine performance degradation for a fouled device, the change in the turbine rotational speed under the same tidal stream flow conditions must be accounted for. The majority of tidal turbines are lift-based devices and the blade lift-to-drag ratio will decrease as marine biofouling accumulates on the blade surface. For the same flow speed, the torque generated by the turbine blades will decrease in the fouled state, hence a reduced rotational speed and power output. For the baseline rated flow conditions, the impact of light surface microfouling has been assessed as decreasing the power output by over 25 %, but also decreasing the thrust force by approximately 25 %. This indicates that the loss of lift is more significant to the turbine performance than the drag increase. The fouled turbine will still achieve the rated output power conditions, albeit at a higher flow speed, and the turbine loading parameters are similar to those for the baseline case. Although the fouled turbine will still achieve rated power, the cumulative turbine energy production will be reduced, which will have economic consequences for the turbine operator. As the biofouling layer on the turbine blade develops (See Figure 1.5), the turbine performance will change accordingly. For the case of microfouling on the turbine blades, the lift will decrease and drag will increase, resulting in a penalty to the turbine power coefficient and a decrease in the rotor thrust force. However, as macrofouling develops on the initial fouling layer, a negligible change in lift and an increase in the blade drag has been shown to improve the turbine power coefficient to a 20 % decrease from the baseline configuration – a 5 % improvement from the microfouled turbine performance. The turbine thrust loading is also increased, but does not reach the same level as that in the baseline configuration. Nevertheless, any marine biofouling on the turbine blade will negatively affect the turbine performance.

Based on the findings and discussion presented in this thesis, two recommendations have been made (See Sections 3.3.4 and 5.2.5). The first concerns the selection of a suitable design point for the blade section hydrodynamic performance. It is inevitable that tidal turbine blades will become fouled to some extent during their deployment, and it has been shown that the blade section performance is sensitive to the expected level and distribution of marine biofouling. Therefore, the turbine blade will only be operating at the design point for a limited period of time. Once biofouling begins to colonise the blade surface the turbine will be operating in an off-design condition. It is recommended that the blade design point be moved towards the state expected when a light level of marine biofouling is present on the blade surface, which will reflect the blade operating conditions for a wider time frame of the turbine deployment.

The second recommendation concerns the demonstration of compliance with the turbine technical specifications and commercial guarantees. It is recommended that an additional requirement be added to the turbine commissioning process, where the degradation of the turbine performance, at a predefined point in the turbine life cycle, must be confirmed to be within an agreed limit. This would require age-performance curves, based on the anticipated biofouling levels, but could also be used to include the effects mechanical wear and tear in the system. In addition, it has also suggested that a potential strategy worth investigating could be to exploit the blade pitch control and device health monitoring systems to adjust the blade pitch to help counteract the negative impact of marine biofouling on the turbine hydrodynamic loading and performance.

6.2   RECOMMENDATIONS FOR FUTURE WORK

When investigating the effects of marine biofouling on tidal turbine hydrodynamic loading and performance, a major limitation for this work is a lack of knowledge on the fouling process on the turbine blade surface. As discussed in Section 2.6, there have been numerous studies of marine biofouling sampling which report the fouling species found in particular deployment areas, but none have addressed the influence the flow field around the turbine blade is likely to have on the fouling colonisation process on the blade surface. Improved data collection at an appropriate water depth for rotating turbine blades, not just for submerged static structures, is required to help characterise not just the expected fouling species, level and distribution, but also obtain the time frame of the fouling process. This will allow the loading and performance changes at various points through the turbine life cycle to be assessed. Tidal turbines are generally designed to be deployed for 20 to 25 years with 5 year maintenance intervals, so an understanding of fouling accumulation over a 5 year period would be extremely beneficial. This could be from an improved sample collection approach or through the sharing of real life operating experience gained from the deployment of demonstrator devices. However, this would require developers and operators to be willing to disclose commercially sensitive information, particularly if a significant performance degradation could be identified or implied from the supplied data. The current industry guidelines suggest a marine growth thickness of between 60 mm and 150 mm, which may be reasonable for the turbine support structure, but seems unsuitable for the turbine blades. The marine energy industry should work towards defining an agreed set of marine growth profiles for tidal turbine blades. These parameters would allow the effects of marine biofouling to be consistently characterised during the turbine design process and for estimating the turbine life cycle hydrodynamic loading and performance.

In terms of experimental investigations, further ideas for extending the presented work could be explored. The current work has included what is believed to be a representative level and distribution of marine biofouling, based on the available

evidence, and covered a range of motion types and magnitudes spanning the turbine operating envelope. Once additional information of the blade fouling process becomes available, a further set of wind tunnel experiments should be conducted to include an increased set of fouling parameters describing the marine growth profiles at different time points, not just for a fixed case. A reduced set of motions from the experimental test space could be selected and informed by the results in this thesis and would produce age-performance curves quantifying the blade section performance as the marine biofouling develops on the blade surface.

The wind tunnel rig and instrumentation which have been developed as part of this work, along with the operating experience gained, have provided a versatile test facility for unsteady two-dimensional aerofoil experiments. In addition to idealised pitch cycle motions, it would be of interest to obtain the unsteady blade section loading response to an authentic blade section incidence variation over a longer time period. Input data defining the blade incidence is easily extracted from the 10 min Tidal Bladed simulation datasets discussed in Section 2.3, or from a similar tidal turbine design and modelling resource. This would allow the accuracy of the high-level dynamic load estimates in computational modelling tools to be evaluated in both baseline and fouled blade configurations and ensure the overall unsteady blade section loads are being adequately captured, in addition to using the current datasets to evaluate peak loading conditions.

A final consideration for extending the presented work is to use the experimental database to investigate the suitability of existing unsteady semi-empirical models for predicting the unsteady hydrodynamic loads on the tidal turbine blade. The Beddoes-Leishman dynamic stall model, or a variation of, is widely used in turbine performance numerical codes, but has a potential limitation of the model subsystems being based on the investigated behaviour of thinner aerofoil sections and flat plates – not thicker blade sections such as those used for tidal turbine applications. In addition, the unsteady experimental data can be used to determine the model parameters defining the time lags arising from the boundary layer flow separation delay and vortex convection. Using the experimental database, a parametric study of the semi-empirical model would confirm the validity of the numerical model as an engineering tool. It may be that potential improvements to the model subsystems are masked by larger errors inherent to the model, but it would be beneficial for suitable model parameters to be obtained for this class of aerofoil section and provide a level of confidence to this modelling approach. No reference to predicting unsteady blade section loads with a semi-empirical model has been identified in the available literature. It would be of interest to investigate whether the available models can estimate the unsteady loads for a blade section in a roughened fouled state to the same level of confidence as those in the baseline clean configuration.

APPENDIX A

EXPERIMENTAL METHODOLOGY SUPPLEMENT

A.1 HANDLEY PAGE WIND TUNNEL

A.1.1 WIND TUNNEL BENCHMARKING

The flow angularity calibration results are shown in Figure A.1. The longitudinal reference plane is positioned at the pitch axis position and the flow angularity is presented looking upstream.

(A) Downwash Angle Coutours [°]   (B) Yaw Angle Contours [°]
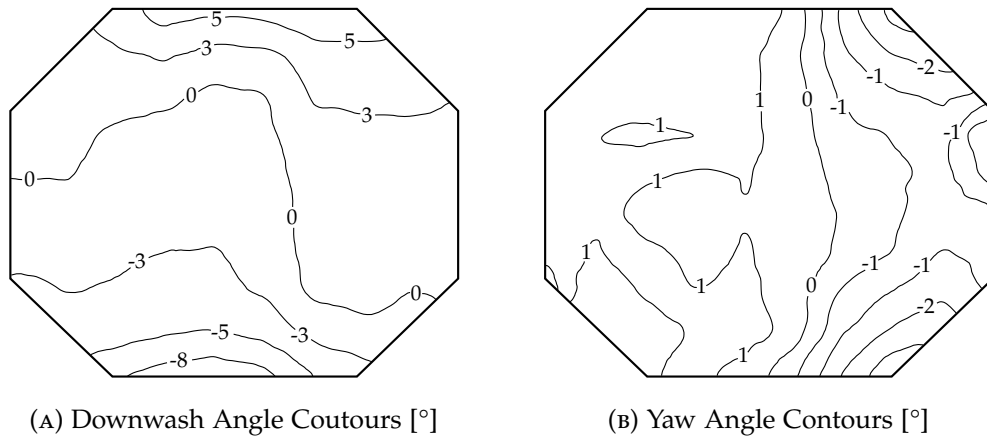
FIGURE A.1: Handley Page wind tunnel flow angularity calibration.

The freestream turbulence intensity results, for four points, are shown in Figure A.2 and described in Equations A.1 and A.2. The reference plane is the same as that for the flow angularity.

$$TI = \frac{\sigma_u}{U_\infty} \tag{A.1}$$

$$\sigma_u^2 = \frac{1}{T} \int_0^T u^2 \, \mathrm{d}t \tag{A.2}$$
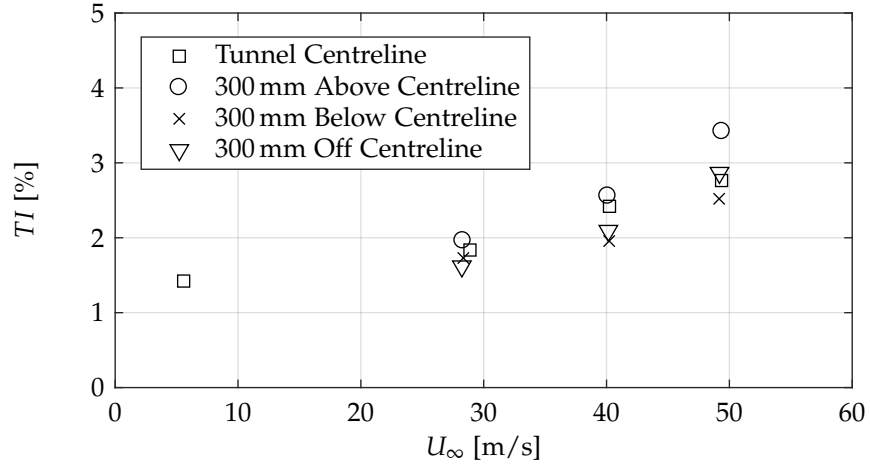
FIGURE A.2: Handley Page wind tunnel flow turbulence intensity calibration.

A.2   DYNAMIC STALL RIG

A.2.1   DYNAMIC STALL RIG CALIBRATION VALUES

TABLE A.1: Dynamic stall rig control calibration parameters.

Aerofoil	$V_{\mathrm{Pos_{Off}}}$ [mV]	S_{Pos} [mV/°]	S_{Com} [mV/°]
NACA 63-619 (Baseline)	44.05	159.99	-158.91
NACA 63-619 (Rough)	48.3	159.4	-158.6
AHH 19 (All Cases)	68.9	159.1	-158.3
AHH 32 (All Cases)	98.7	159.2	-158.4

A.2.2   DYNAMIC STALL RIG CONTROLLER CORRECTION

In Section 2.1.2 the limitations of the dynamic stall rig PID controller were highlighted, with particular mention to the model amplitude during oscillatory test cases. Following completion of the test campaign described in this thesis, the following comments and conclusions can be drawn from the comparison of the rig command (input) and processed position (output) signals for the oscillatory test cases. In all cases a 2nd order polynomial has been fitted to the experimental datasets.

Firstly, the relationship between the required and actual model oscillatory frequency is described in Equation A.3, covering the full range of test settings and

combining the results for all three model test sections.

$$\omega_{\text{Pos}} = -2.8069 \times 10^{-5} \times \omega_{\text{Com}}^2 + 1.0006 \times \omega_{\text{Com}} - 7.7671 \times 10^{-5} \qquad \text{(A.3)}$$

It can be concluded that the desired model oscillatory frequency is being achieved with the current rig configuration.

Secondly, the relationships between the model incidences are described in Equations A.4 and A.5, in terms of the collective and cyclic angles of attack respectively.

$$\alpha_{0_{\text{Pos}}} = C1 \times \alpha_{0_{\text{Pos}}}^2 + C2 \times \alpha_{0_{\text{Pos}}} + C3 \qquad \text{(A.4)}$$

$$\alpha_{1_{\text{Pos}}} = C1 \times \alpha_{1_{\text{Pos}}}^2 + C2 \times \alpha_{1_{\text{Pos}}} + C3 \qquad \text{(A.5)}$$

The polynomial coefficients, $C1$, $C2$ and $C3$, are detailed in Tables A.2 and A.3, for each aerofoil section and test reduced frequency.

Both components of the model incidence are varying as a function of the model thickness and oscillatory frequency. The controller response for the thicker AHH 32 model is worse than that for the two thinner sections and it is thought that this is due to the actuation system reacting to the increased aerodynamic loading on the thicker section. As it is not feasible to change the PID controller gains, these functions could be used as the basis of a lookup table, or similar, to adjust input signals to the rig, which would be beneficial for future work in this facility.

TABLE A.2: Correction functions for model collective angle of attack.

Aerofoil	k	Polynomial Coefficients		
		$C1$	$C2$	$C3$
NACA 63-619	0.025	0.0001	0.9908	-0.0720
	0.05	-0.0007	1.0006	-0.0934
	0.1	0.0014	0.9690	-0.0435
AHH 19	0.025	0.0007	0.9816	-0.0448
	0.05	0.0009	0.9784	-0.0364
	0.1	0.0007	0.9841	-0.0790
AHH 32	0.1	0.0003	0.9902	-0.0959
	0.15	0.0001	0.9889	-0.1158
	0.2	0.0008	0.9799	-0.1313

TABLE A.3: Correction functions for model cyclic angle of attack.

Aerofoil	k	Polynomial Coefficients		
		$C1$	$C2$	$C3$
NACA 63-619	0.025	-0.0021	0.9974	-0.0511
	0.05	-0.0001	0.9612	-0.0370
	0.1	0.0027	0.8696	-0.0540
AHH 19	0.025	0.0004	0.9832	-0.0411
	0.05	-0.0002	0.9608	-0.0356
	0.1	0.0014	0.8648	-0.0464
AHH 32	0.1	0.0033	0.8480	-0.0120
	0.15	0.0011	0.7794	-0.0826
	0.2	0.0006	0.6941	-0.1488

A.3 AEROFOIL MODEL

A.3.1 AEROFOIL COORDINATES

Due to the proprietary nature of the AHH aerofoil designs, the coordinates for the AHH 19 and AHH 32 sections cannot be published. There are numerous online tools available for obtaining coordinates for the NACA 63-619 series aerofoil sections or reference can be made to Abbott and von Doenhoff (1959).

A.3.2 REFERENCE & NUMBERING SYSTEMS

The reference systems describing the experimental arrangement primarily consider the aerofoil loads and the model angular position in the wind tunnel, as summarised in Figure A.3. The arrow denotes the positive direction of the aerofoil load or pitching moment parameter.
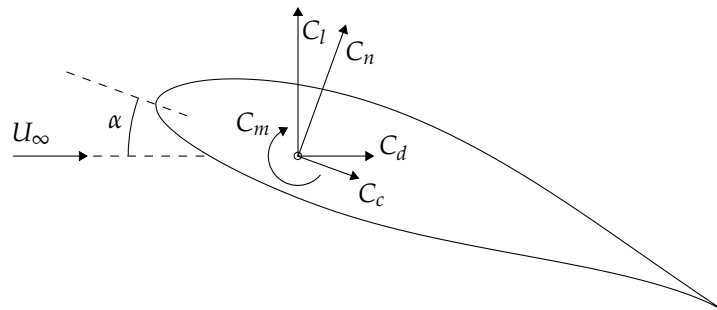
FIGURE A.3: Aerofoil model load, moment and incidence reference systems.

The aerofoil model pressure orifices are numbered from the trailing edge on the upper surface to the trailing edge on the lower surface, as shown in Figure A.4. The

parameter n denotes the total number of pressure sensors installed in the model – 34 for the NACA 63-619 blade section, and 32 for both the AHH aerofoil sections.
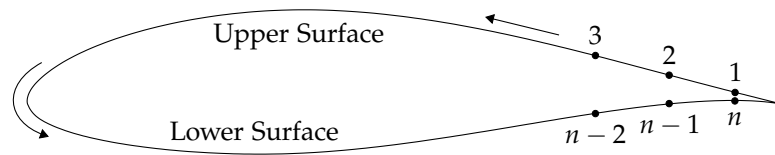
FIGURE A.4: Aerofoil model pressure measurement numbering system.

Similarly, the pressure orifices on the barnacle model are numbered clockwise in concentric rings, starting from the central port and the upstream position thereafter, as shown in Figure A.5.
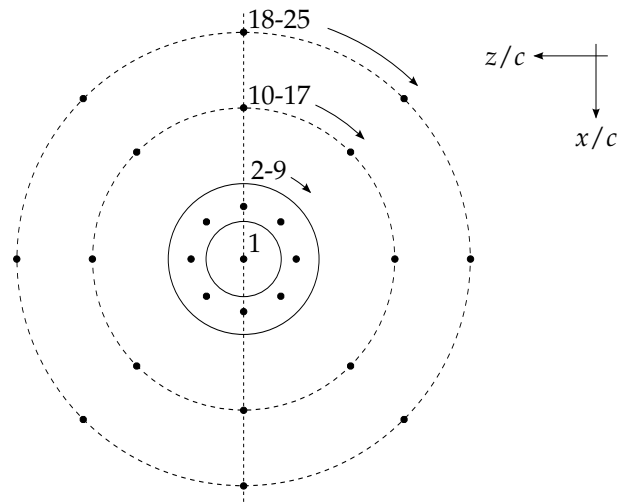
FIGURE A.5: Barnacle model pressure measurement numbering system.

A.3.3 STRUCTURAL CALCULATIONS

TABLE A.4: Wind tunnel model deflection and rotation estimates.

	NACA 63-619	AHH 19	AHH 32
Model Parameters at Model Pitch Axis ($x/c = 0.25$)			
I_x [m^4]	9.00×10^{-6}	5.83×10^{-6}	2.57×10^{-5}
J_x [m^4]	2.51×10^{-4}	2.80×10^{-4}	3.15×10^{-4}
P_x [kg m^2]	0.494	0.512	0.591
Load Case 1: $C_n = 2.2$, $U_\infty = 45$ m/s, 1.5 Safety Factor			
Max Deflection [mm]	0.214	0.331	0.075
Max Deflection [% Span]	0.013	0.021	0.005
Load Case 2: $\omega_{\mathrm{model}} = 10$ Hz, $\alpha = 0° \pm 20°$, 1.5 Safety Factor			
Twist Angle [°]	0.037	0.035	0.036

A.3.4 PRESSURE TRANSDUCER SPECIFICATION & CALIBRATION
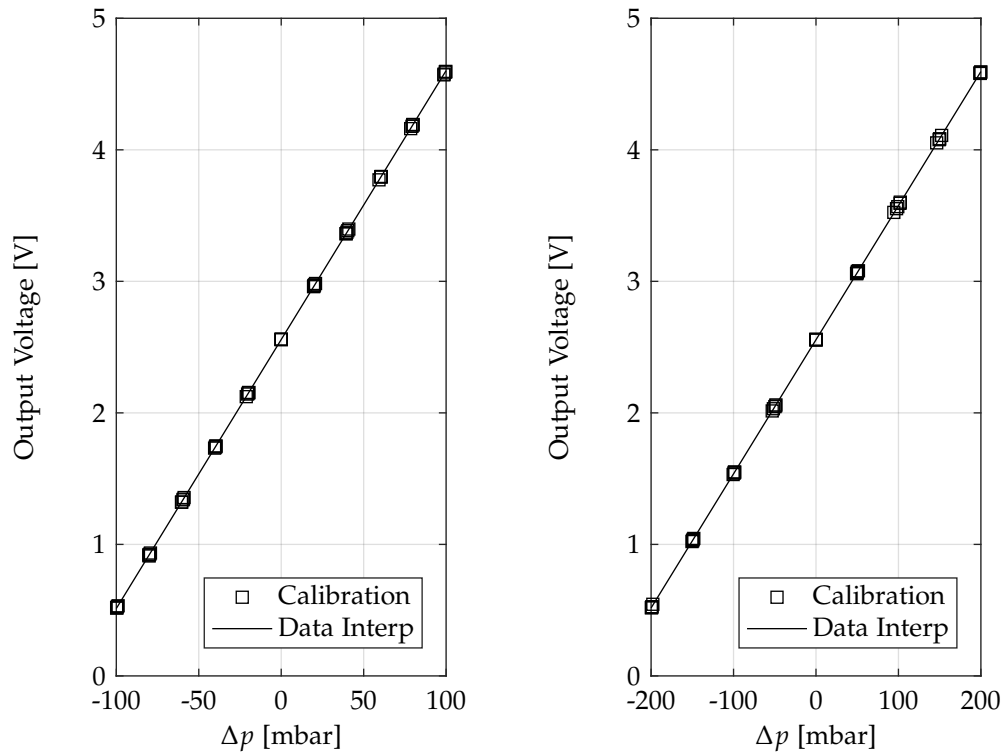
(A) ± 100 mbar Pressure Transducer.

(B) ± 200 mbar Pressure Transducer.

FIGURE A.6: Pressure transducer calibration.

TABLE A.5: Pressure transducer specification and calibration values.

	±100 mbar Sensor	±200 mbar Sensor
Manufacturer	First Sensor	First Sensor
Product Code	HDIM100GBY8P5	HDIM200GBY8H5
Total Accuracy [%FSS]	±0.5	±0.5
Response Delay [ms]	0.5	0.5
FSS [V]	4.0	4.0
D/A Resolution [bit]	11	11
Sensitivity [mV/mbar]	20.45	10.20

A.3.5 PRESSURE TRANSDUCER LOCATIONS

TABLE A.6: Model pressure transducer chordwise locations.

(A) NACA 63-619

Upper Surface		Lower Surface	
x/c [–]	*p* [mbar]	*x/c* [–]	*p* [mbar]
-0.0011		0.005	±200
0.0015	±200	0.025	
0.01		0.0594	
0.025		0.102	
0.0594		0.1482	
0.102		0.191	
0.1482		0.26	
0.191		0.301	
0.26		0.3698	±100
0.301		0.4613	
0.3698	±100	0.567	
0.4613		0.678	
0.567		0.784	
0.678		0.875	
0.784		0.95	
0.875		0.97	
0.95			
0.97			

(B) AHH 19 and AHH 32

Upper Surface		Lower Surface	
x/c [–]	*p* [mbar]	*x/c* [–]	*p* [mbar]
0.0003		0.0003	
0.0025	±200	0.0025	±200
0.01		0.01	
0.025		0.025	
0.05		0.05	
0.1		0.1	
0.17		0.17	
0.26		0.26	
0.37		0.37	
0.49		0.49	
0.6	±100	0.6	±100
0.71		0.71	
0.8		0.8	
0.87		0.87	
0.94		0.94	
0.97		0.97	

A.4 DATA ACQUISITION SYSTEM

TABLE A.7: Data acquisition channel map.

Channel	Description
$1 - 32/34$	Pressure Transducers (p_n to CH_n)
$33/35 - 36$	*Empty*
37	Position Signal (V_{Pos})
38	Command Signal (V_{Com})
$39 - 40$	*Empty*
41	Dynamic Pressure (q)
42	Temperature (T)
43	Atmospheric Pressure (p_{baro})
44	Tunnel Static Pressure (p_s)
$45 - 46$	*Empty*
47	Check Signal
$48 - 96$	*Empty*

A.5 WIND TUNNEL PARAMETER CONVERSION

The conversion of the wind tunnel pressure and temperature from measured voltages to engineering units are described in Equations A.6 to A.9. Pressures are obtained in Pascals and the tunnel air temperature in degree Celsius.

$$q = (q_V - q_{V_{Off}})/0.0255/0.1019716358 \qquad (A.6)$$

$$T = T_V/0.1 \qquad (A.7)$$

$$p_{baro} = (p_{baro_V}/0.0222222 + 600)/0.0075006 \qquad (A.8)$$

$$p_s = (p_{s_V} - p_{s_{V_{Off}}})/0.0198/0.1019716358 \qquad (A.9)$$

Appendix B

1 MW TIDAL TURBINE GEOMETRY & FLOW MODEL

B.1   NREL HARP_OPT INPUTS & CONSTRAINTS

TABLE B.1: HARP_Opt Turbine Configuration Input Parameters.

Number of Blades [–]	3
Rated Power [kW]	1000
Rotor Diameter [m]	20
Hub Diameter [m]	3
Hub Height [m]	16
Rotor Speed [rpm]	$5 - 15$
Water Depth [m]	40
Flow Speed [m/s]	$1 - 4$

TABLE B.2: HARP_Opt Blade Geometry Configuration.

Radius [m]	3.5	3.995	5.404	7.513	10
Twist LB [°]	10	8	5	2	0
Twist UB [°]	20	18	12	10	10
Chord LB [m]	1.8	1.8	1.5	1.0	0.5
Chord UB [m]	2.5	2.2	2.0	1.5	1.0
Min Root Chord [m]		1.0			
Max Root Chord [m]		1.5			
Root Transition [*r/R*]		$0.15 - 0.35$			

Table B.3: HARP_Opt Aerofoil Distribution.

Thickness [%]	30.1	24.1	21.1	15
Lower Bound [r/R]	0.4	0.55	0.75	0.95
Upper Bound [r/R]	0.5	0.7	-	-

B.2 UNSTEADY TURBULENT FLOW MODEL

The turbulent flow measurement from the Sound of Islay (Milne, 2014) used to scale the turbine model flow inputs are presented in Figure B.1 for the axial, lateral and vertical flow directions.

(A) Axial   (B) Lateral   (C) Vertical
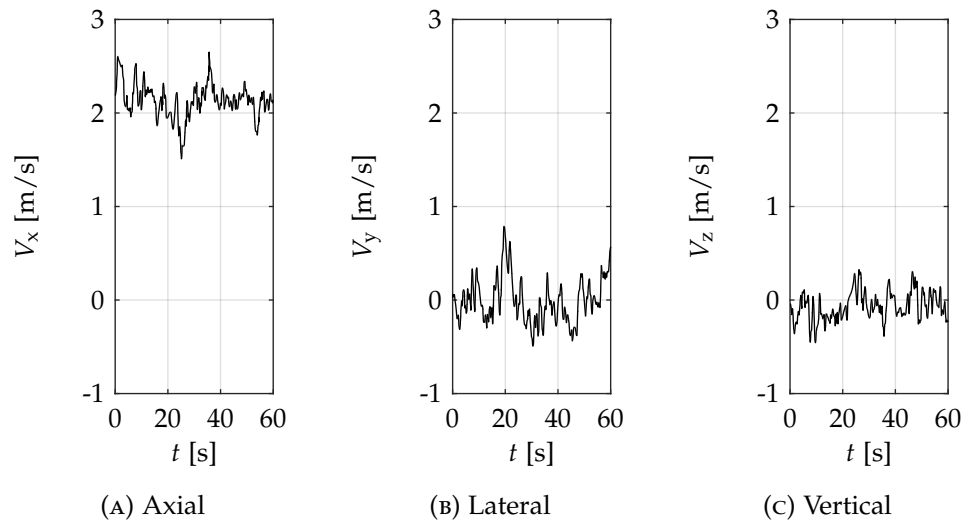
Figure B.1: Turbulent tidal flow measurements from the Sound of Islay. Adapted from Milne (2014).

The flow speed probability distribution (Melville, 2008) used to define the turbine geometry is presented in Figure B.2.
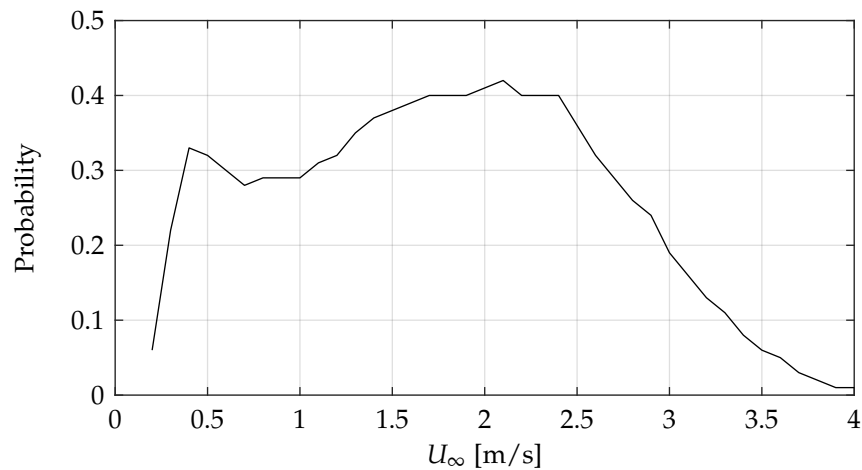
Figure B.2: Flow speed probability at EMEC Falls of Warness tidal test site. Adapted from Melville (2008).

B.3   NREL HARP_OPT DESIGN OUTPUT

(A) Chord

(B) Thickness

(C) Pre-Twist Angle

(D) Blade Pitch
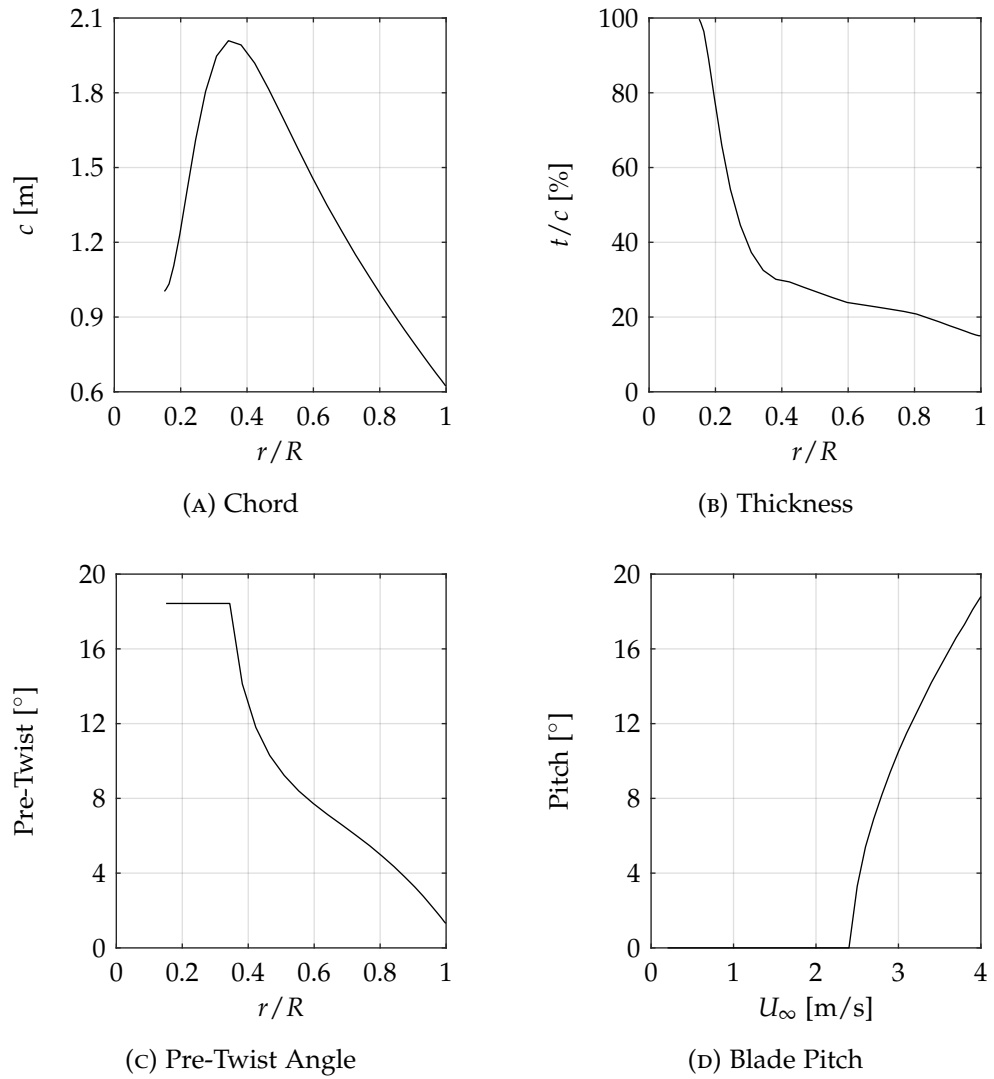
Figure B.3: NREL HARP_Opt tidal turbine blade geometry parameters.

(A) Rotor Speed

(B) Rotor Power

(C) Turbine Torque

(D) Turbine Thrust
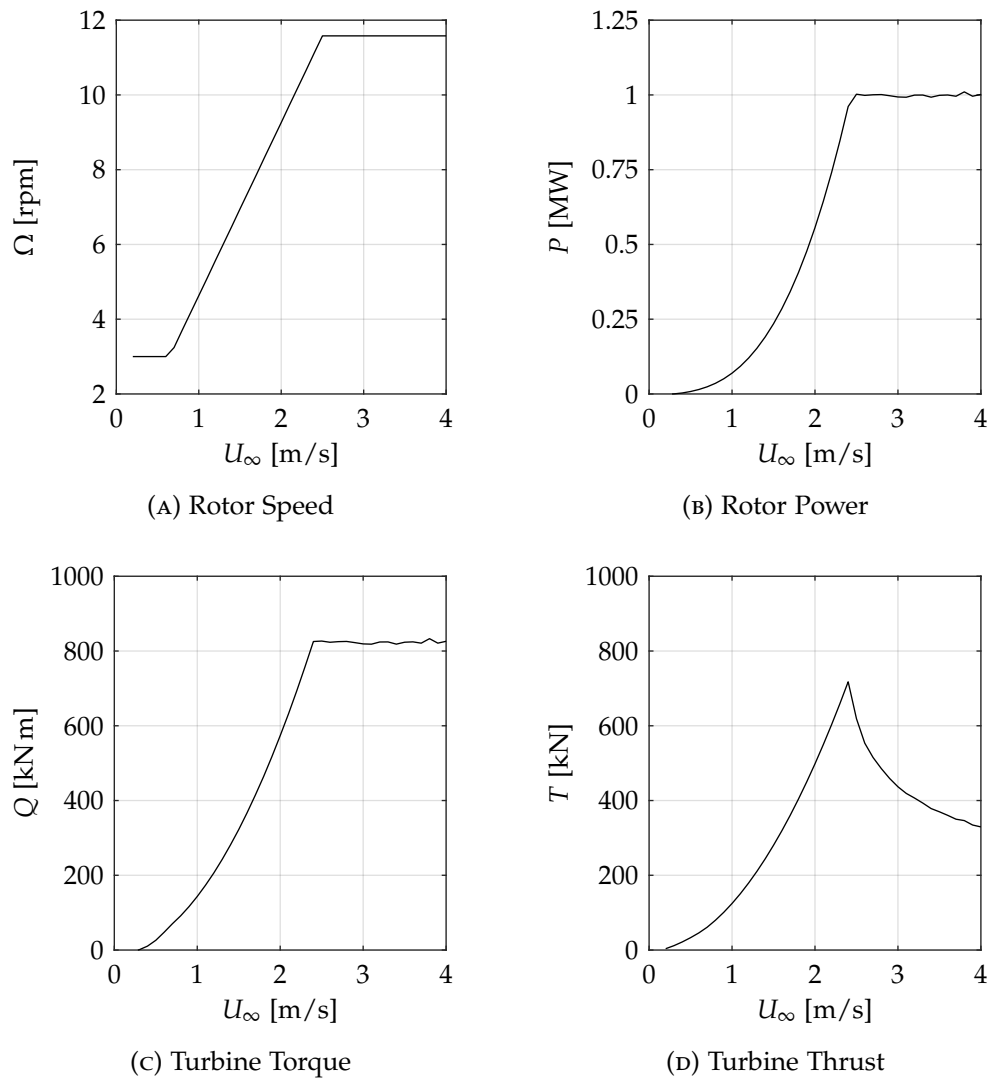
FIGURE B.4: NREL HARP_Opt tidal turbine design output performance.

APPENDIX C

DATA STRUCTURE & FULL TEST MATRIX

C.1 DATA FILE NUMBERING CONVENTION

The data from each experimental test case is assigned and stored to a uniquely numbered (*abcdefgh*) set of data files. Table C.1 summarises the numbering convention which provides basic information on each test cases.

TABLE C.1: Data file numbering convention.

Parameter	Description	Options
ab	Test Aerofoil	20: NACA 63-619 21: AHH 19 22: AHH 32
c	Type of Experiment	0: Baseline 1: Rough
d	Type of Motion	0: Static 1: Oscillatory 2: Ramp Up 3: Ramp Down
efg	Run Number	$001 - 999$
h	Attempt	$1 - 9$

The raw experimental voltage data is stored in MAT-file format (*abcdefgh*.mat), along with a corresponding offset text file (*abcdefgh*.txt). The processed data is stored in text DAT-file format (*abcdefgh*.dat). An event log records all the test parameters, user inputs, and sensitivity files.

C.2   RUN INFORMATION BLOCK FORMAT

Table C.2: Run Information Block structure.

Entry	Static	Oscillatory	Ramps
1		Run Number (*abcdefgh*)	
2		Date of Test: Day	
3		Date of Test: Month	
4		Date of Test: Year	
5		T [°C]	
6		P_{baro} [Pa]	
7		Type of Motion	
8	$\alpha_{\min}$ [°]	α_0 [°]	α_{init} [°]
9	$\alpha_{\max}$ [°]	α_1 [°]	α_{arc} [°]
10	No of Angles	ω [Hz]	$\dot{\alpha}$ [°/s]
11	*Empty*	Cycles	Repeats
12	Sample Time [s]	Samples per Cycle	Samples per Repeat
13 − 16		*Empty*	
17		Sampling Rate [Hz]	
18		Filtered Data Rate [Hz]	
19		q [Pa]	
20		*Re*	
21		*M*	
22	*Empty*	k	$\dot{\alpha}_{\text{red}}$
23		U_∞ [m/s]	
24	Re_{target}	U_{ref} [m/s]	U_{ref} [m/s]
25		*Empty*	
26		Unaveraged Data [0] or Averaged Data [1]	
27 − 29	Combined #	*Empty*	*Empty*
30		Model Number	
31		Type of Experiment	
32		*Empty*	

C.3   DATA FILE FORMAT

The data file containing the processed data (*abcdefgh*.dat) contains the model pressure and wind tunnel flow information at each angle of attack. This structure is described in Table C.3.

Table C.3: Structure of the processed data file.

Run Information Block (RIB)							
α_1	$C_{p_{1,1}}$	$\cdots$	$C_{p_{1,i}}$	q_1	p_{baro_1}	T_1	p_{s_1}
$\vdots$	$\vdots$	$\ddots$	$\vdots$	$\vdots$	$\vdots$	$\vdots$	$\vdots$
α_n	$C_{p_{n,1}}$	$\cdots$	$C_{p_{n,i}}$	q_n	p_{baro_n}	T_n	p_{s_n}

C.4 TEST MATRIX: STATIC CASES

Table C.4: Static Test Cases – Baseline (*Includes Barnacle Configuration).

$\alpha_{\min}$ [°]	$\alpha_{\max}$ [°]	α_{inc} [°]	Aerofoil		
			NACA 63-619	AHH 19	AHH 32
-25	25	2	20000013	21001434*	22001492
-10	24	2	20000022	21001443*	22001501
-7.5	19.5	1	20000033	21001453*	22001511
Combined Dataset			20000000	21000000*	22000000

Table C.5: Static Test Cases – Rough (*Includes Barnacle Configuration).

$\alpha_{\min}$ [°]	$\alpha_{\max}$ [°]	α_{inc} [°]	Aerofoil		
			NACA 63-619	AHH 19	AHH 32
-25	25	2	20100861	21103112*	22102081
-10	24	2	20100871	21103122*	22102091
-7.5	19.5	1	20100881	21103132*	22102101
Combined Dataset			20100000	21100000*	22100000

C.5 TEST MATRIX: OSCILLATORY CASES

Table C.6: Oscillatory Test Cases – Baseline (*Includes Barnacle Configuration).

k	α_0 [°]	α_1 [°]	NACA 63-619	AHH 19	AHH 32
		2	20010043	21011465*	–
	0	4	20010052	21011473*	–
		6	20010063	21011487*	–
		2	20010103	21012682*	–
0.025	5	4	20010113	21012692*	–
		6	20010123	21012702*	–
		2	20010133	21012712*	–
	10	4	20010143	21012722*	–
		6	20010152	21012732*	–

Continued on next page

Table C.6 – *Continued from previous page*

0.05	0	2	20010074	21012742*	–
		4	20010082	21012752*	–
		6	20010092	21012763*	–
	5	2	20010164	21012772*	–
		4	20010172	21012782*	–
		6	20010182	21012792*	–
	10	2	20010193	21012803*	–
		4	20010202	21012812*	–
		6	20010212	21012822*	–
0.1	0	2	20010225	21012832*	–
		4	20010232	21012842*	–
		6	20010242	21012852*	–
	2	2	–	–	22011521
		5	–	–	22011531
		8	–	–	22011541
		10	–	–	22011671
	5	2	20010252	21012862*	–
		4	20010262	21012872*	–
		6	20010272	21012882*	–
	8	2	–	–	22011551
		5	–	–	22011561
		8	–	–	22011571
		10	–	–	22011681
	10	2	20010283	21012892*	–
		4	20010292	21012902*	–
		6	20010303	21012673*	–
	12	2	–	–	22011581
		5	–	–	22011591
		8	–	–	22011601
		10	–	–	22011691
0.15	2	2	–	–	22011611
		5	–	–	22011621
		8	–	–	22011631
		10	–	–	22011701
	8	2	–	–	22011711
		5	–	–	22011721
		8	–	–	22011731
		10	–	–	22011741
	12	2	–	–	22011751
		5	–	–	22011761
		8	–	–	22011641
		10	–	–	22011771

Table C.6 – *Continued from previous page*

0.2	2	2	–	–	22011781
		5	–	–	22011791
		8	–	–	22011801
		10	–	–	22011861
	8	2	–	–	22011811
		5	–	–	22011821
		8	–	–	22011831
		10	–	–	22011871
	12	2	–	–	22011841
		5	–	–	22011851
		8	–	–	22011651
		10	–	–	22011661

TABLE C.7: Oscillatory Test Cases – Rough (*Includes Barnacle Configuration).

k	α_0 [°]	α_1 [°]	NACA 63-619	AHH 19	AHH 32
0.025	0	2	20110894	21113142*	–
		4	20110901	21113152*	–
		6	20110911	21113162*	–
	5	2	20110922	21113172*	–
		4	20110931	21113182*	–
		6	20110941	21113192*	–
	10	2	20110951	21113202*	–
		4	20110961	21113212*	–
		6	20110971	21113222*	–
0.05	0	2	20110981	21113232*	–
		4	20110991	21113242*	–
		6	20111001	21113252*	–
	5	2	20111011	21113262*	–
		4	20111021	21113272*	–
		6	20111031	21113282*	–
	10	2	20111041	21113292*	–
		4	20111051	21113302*	–
		6	20111061	21113312*	–
0.1	0	2	20111071	21113322*	–
		4	20111081	21113332*	–
		6	20111091	21113342*	–
	2	2	–	–	22112111
		5	–	–	22112121
		8	–	–	22112131
		10	–	–	22112141
	5	2	20111104	21113352*	–
		4	20111111	21113362*	–
		6	20111121	21113372*	–

Continued on next page

Table C.7 – *Continued from previous page*

	8	2	–	–	22112151
		5	–	–	22112161
		8	–	–	22112171
		10	–	–	22112181
0.1	10	2	20111131	21113382*	–
		4	20111141	21113392*	–
		6	20111151	21113402*	–
	12	2	–	–	22112191
		5	–	–	22112201
		8	–	–	22112211
		10	–	–	22112221
	2	2	–	–	22112231
		5	–	–	22112241
		8	–	–	22112251
		10	–	–	22112261
0.15	8	2	–	–	22112271
		5	–	–	22112281
		8	–	–	22112291
		10	–	–	22112301
	12	2	–	–	22112311
		5	–	–	22112321
		8	–	–	22112331
		10	–	–	22112341
	2	2	–	–	22112351
		5	–	–	22112361
		8	–	–	22112371
		10	–	–	22112441
0.2	8	2	–	–	22112381
		5	–	–	22112391
		8	–	–	22112401
		10	–	–	22112451
	12	2	–	–	22112411
		5	–	–	22112421
		8	–	–	22112431
		10	–	–	22112461

C.6 TEST MATRIX: RAMP & HOLD CASES

Table C.8: Ramp Up Test Cases – Baseline.

α_{init} [°]	α_{arc} [°]	$\dot{\alpha}_{red}$	NACA 63-619	AHH 19	AHH 32
0	10	0.0025	2020371	–	–
		0.005	20020313	–	–
		0.01	20020381	–	–
		0.025	20020391	–	–
		0.04	20020481	–	–
0	15	0.0025	20020401	–	–
		0.005	20020411	–	–
		0.01	20020421	–	–
		0.025	20020431	–	–
		0.04	20020491	–	–
0	20	0.0025	20020441	21022911	22021881
		0.005	20020451	21022921	22021891
		0.01	20020461	21022931	22021901
		0.025	20020471	21022941	22021911
		0.04	20020501	21022951	22021921
0	25	0.0025	20020511	21022961	22021931
		0.005	20020521	21022971	22021941
		0.01	20020322	21022981	22021951
		0.025	20020332	21022991	22021961
		0.04	20020342	21023001	22021971

Table C.9: Ramp Up Test Cases – Rough.

α_{init} [°]	α_{arc} [°]	$\dot{\alpha}_{red}$	NACA 63-619	AHH 19	AHH 32
0	20	0.0025	20121261	21123411	22122471
		0.005	20121271	21123421	22122481
		0.01	20121281	21123431	22122491
		0.025	20121291	21123441	22122501
		0.04	20121301	21123451	22122511
0	25	0.0025	20121311	21123461	22122521
		0.005	20121321	21123471	22122531
		0.01	20121331	21123481	22122541
		0.025	20121341	21123491	22122551
		0.04	20121351	21123501	22122561

Table C.10: Ramp Down Test Cases – Baseline.

α_{init} [°]	α_{arc} [°]	$\dot{\alpha}_{red}$	NACA 63-619	AHH 19	AHH 32
		-0.0025	20030531	21033011	22031981
		-0.005	20030541	21033021	22031991
20	-20	-0.01	20030551	21033031	22032001
		-0.025	20030561	21033042	22032011
		-0.04	20030571	21033051	22032021
		-0.0025	20030581	21033061	22032031
		-0.005	20030591	21033071	22032041
25	-25	-0.01	20030601	21033081	22032051
		-0.025	20030611	21033091	22032061
		-0.04	20030621	21033101	22032071

Table C.11: Ramp Down Test Cases – Rough.

α_{init} [°]	α_{arc} [°]	$\dot{\alpha}_{red}$	NACA 63-619	AHH 19	AHH 32
		-0.0025	20131161	21133511	22132571
		-0.005	20131171	21133521	22132581
20	-20	-0.01	20131181	21133531	22132591
		-0.025	20131191	21133541	22132601
		-0.04	20131201	21133551	22132611
		-0.0025	20131211	21133561	22132621
		-0.005	20131221	21133571	22132631
25	-25	-0.01	20131231	21133581	22132641
		-0.025	20131241	21133591	22132651
		-0.04	20131251	21133601	22132661

Appendix D

VALIDATION OF EXPERIMENTAL RESULTS

D.1   STATIC DATA (STEADY STATE) VALIDATION

The static lift and drag coefficients obtained during the experimental campaign, in the aerofoil baseline configuration, are compared to reference data available for each of the three test sections.

Firstly, the results for the NACA 63-619 test section are compared with those for the NACA 63-615 and 63-618 aerofoil sections provided by Abbott and von Doenhoff (1959) – the principal reference for NACA aerofoil data – and are shown in Figure D.1. The results from the published datasets are for a Reynolds number of 3×10^6, instead of 1.5×10^6 as tested, so a marginally higher maximum lift coefficient and stall angle are to be expected.

The test data for the present work are in very good agreement with the published data, particularly the lift curve slope, zero-lift angle of attack and design lift coefficient. The peak lift coefficient and static stall angle are also in good agreement, especially considering the reference cases are for a higher Reynolds number and for 15 % and 18 % thick aerofoil sections. Considering the issues inherent with determining aerofoil drag from surface pressure measurements, the drag coefficient agrees well with the published datasets, particularity for angles of attack with separated flow.

A comparison of the AHH 19 and AHH 32 blade sections with CFD datasets supplied by AHH are shown in Figures D.2 and D.3 respectively. The supplied CFD datasets are for a Reynolds number of 1.5×10^6 and turbulence intensity of 2.5 %, which match the wind tunnel test conditions. The CFD datasets have an increased uncertainty for angles of attack greater than 10°.

The measured AHH 19 lift coefficient is in good agreement with the CFD results, matching the lift curve slope and zero-lift angle of attack. No comment can be made on the stall region due to the limitations of the CFD method. The discrepancy in the

(A) Lift Coefficient
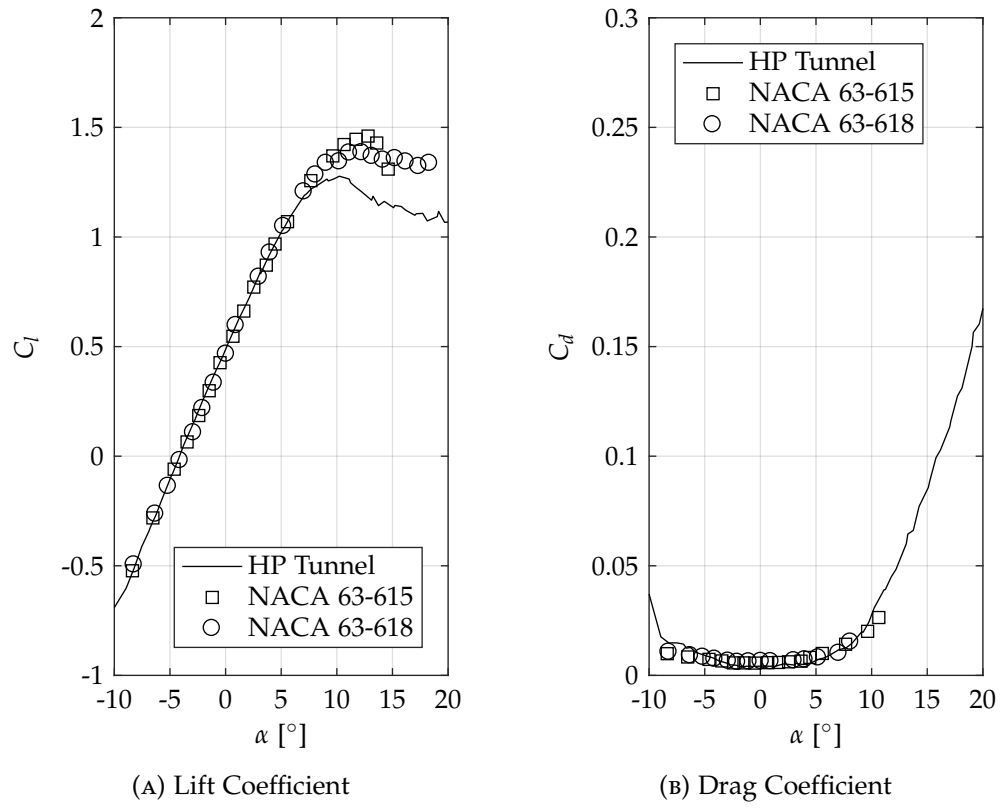
(B) Drag Coefficient

FIGURE D.1: Static test case validation for NACA 63-619 blade section.

(A) Lift Coefficient
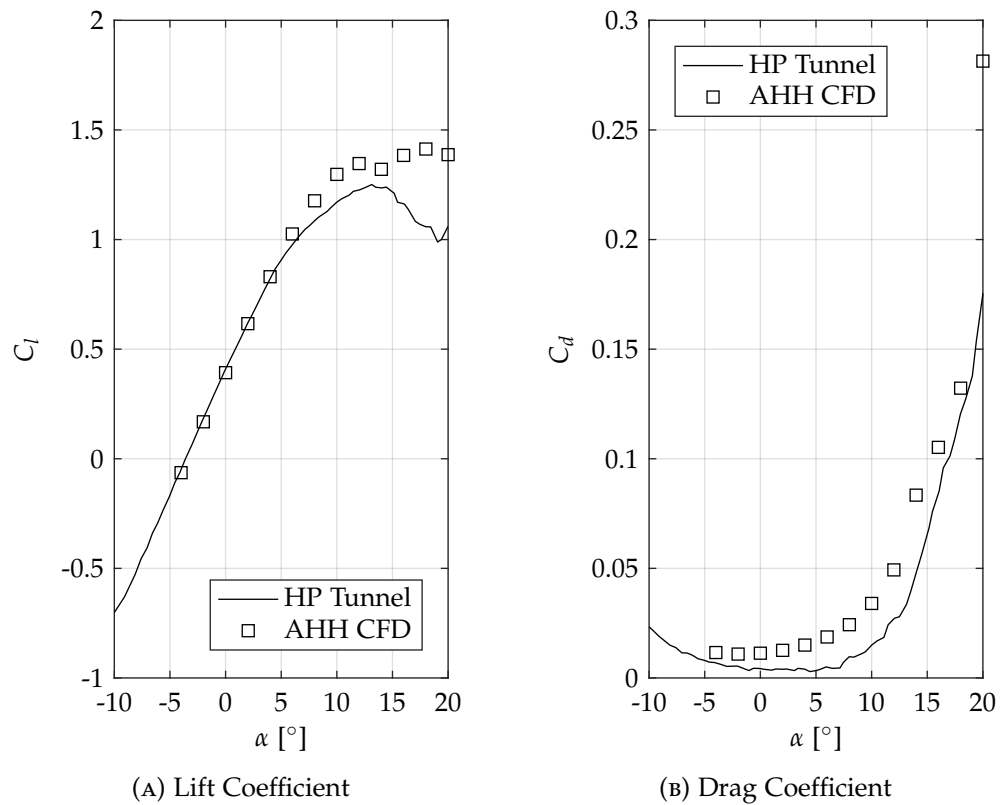
(B) Drag Coefficient

FIGURE D.2: Static test case validation for AHH 19 blade section.

(A) Lift Coefficient
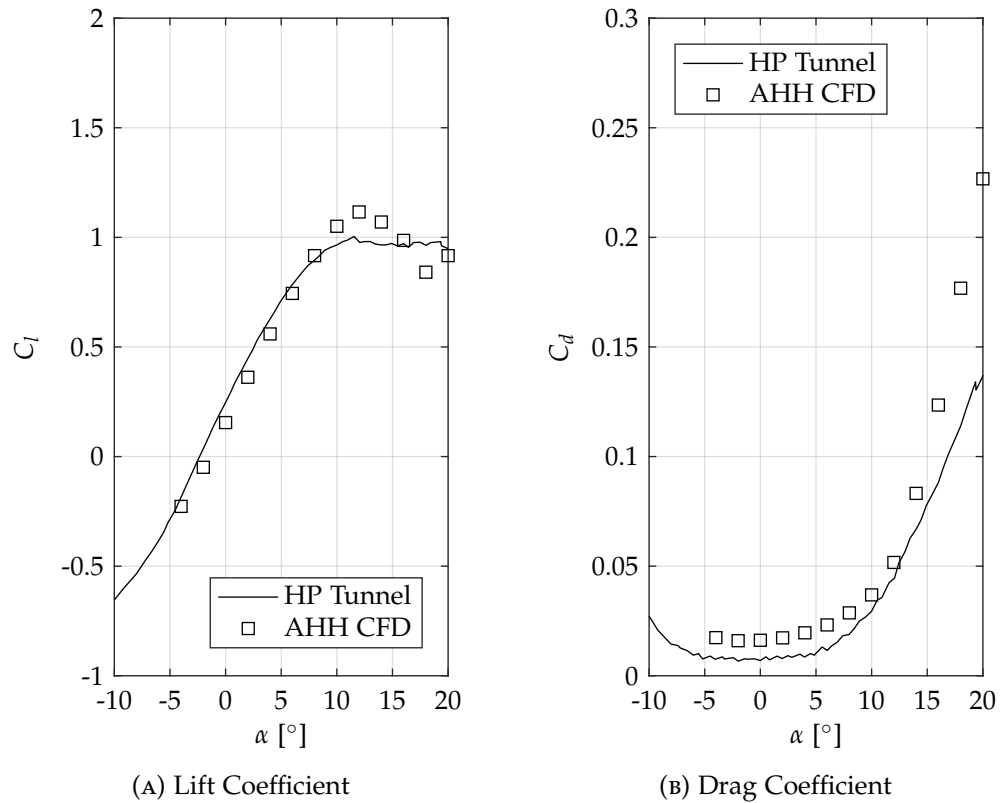
(B) Drag Coefficient

FIGURE D.3: Static test case validation for AHH 32 blade section.

drag coefficient has been discussed and quantified previously in Section 2.5.5 of this thesis. The comparison between the measured forces and CFD results for the AHH 32 blade section are generally in good agreement, particularly the lift curve slope and the drag coefficient at stall.

D.2 DYNAMIC DATA (UNSTEADY) VALIDATION

No unsteady validation datasets are available for the tested blade sections. However, data is available for the NREL S809, a 21 % thick wind turbine blade section, which has been tested in the same UoG facility, using a similar approach as outlined in this thesis, and at Ohio State University (Sheng et al., 2009). A comparison of the integrated force coefficients for similar dynamic stall oscillatory test cases showed a good level of agreement.

At lower angles of attack the model wind tunnel blockage, and flow structures, are of the same order as the model thickness. At higher angles of attack they are of the same order as the model chord, not thickness. Therefore, the test facility is appropriate for the type of testing undertaken. In addition, the static integrated force coefficient data has been shown to be in good agreement with validation cases and the pressure instrumentation response rate is an order of magnitude higher than the fastest pressure fluctuation identified during the tests, hence the test instrumentation is appropriate for purpose.

APPENDIX E

AHH DATA VIEWER

A graphical user interface, shown in Figure E.1, has been created in MATLAB for the analysis and interrogation of the full experimental database. Built-in tools allow: the database to be filtered for selected test variables; plotting of multiple blade section load cases and pressure distributions; exporting of force and pressure data as MS Excel or text files; and a choice of plotting reference systems.
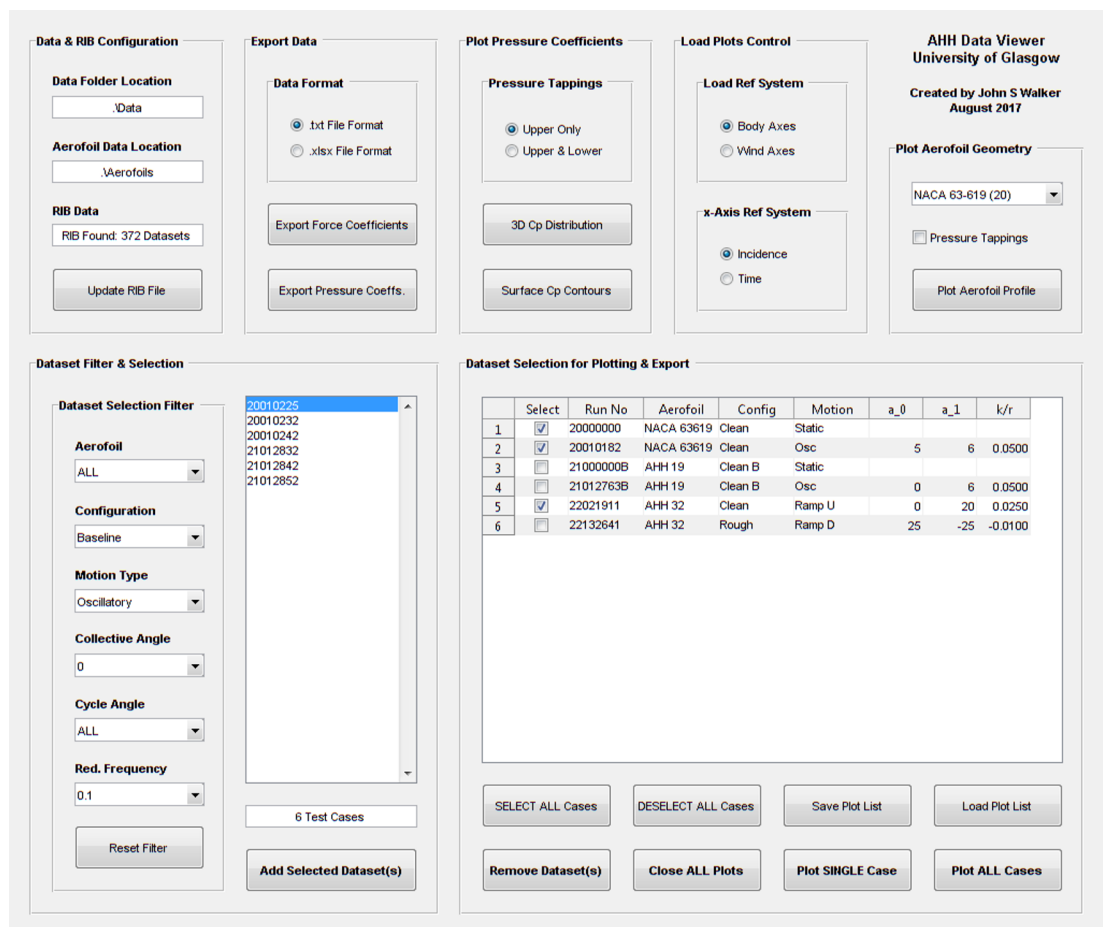
FIGURE E.1: MATLAB graphical user interface for AHH Data Viewer.

BIBLIOGRAPHY

ABBOTT, IH AND VON DOENHOFF, AE (1959). *Theory of Wing Sections: Including a Summary of Airfoil Data*. Dover Publications.

ACHENBACH, E AND HEINECKE, E (1981). On Vortex Shedding from Smooth and Rough Cylinders in the Range of Reynolds Numbers 6×10^3 to 5×10^6. *Journal of Fluid Mechanics*, 109:239–251.

ADCOCK, TA, DRAPER, S, HOULSBY, GT, BORTHWICK, AG, AND SERHADLIOĞLU, S (2013). The Available Power from Tidal Stream Turbines in the Pentland Firth. *Proceedings of the Royal Society A*, 469(2157):20130072.

ADCOCK, TA, DRAPER, S, AND NISHINO, T (2015). Tidal Power Generation – A Review of Hydrodynamic Modelling. *Proceedings of the Institution of Mechanical Engineers Part A: Journal of Power and Energy*, 229(7):755–771.

AHMED, M (2012). Blade Sections for Wind Turbine and Tidal Current Turbine Applications – Current Status and Future Challenges. *International Journal of Energy Research*, 36(7):829–844.

ANDERSON, JD (2001). *Fundamentals of Aerodynamics*. McGraw-Hill, 3rd edition.

ANDRE, H (1978). Ten Years of Experience at the 'La Rance' Tidal Power Plant. *Ocean Management*, 4(2–4):165–178.

ANG, B AND SU, B (2016). Carbon Emission Intensity in Electricity Production: A Global Analysis. *Energy Policy*, 94:56–63.

BAHAJ, A (2011). Generating Electricity from the Oceans. *Renewable and Sustainable Energy Reviews*, 15(7):3399–3416.

BAHAJ, A, BATTEN, W, AND MCCANN, G (2007a). Experimental Verifications of Numerical Predictions for the Hydrodynamic Performance of Horizontal Axis Marine Current Turbines. *Renewable Energy*, 32(15):2479–2490.

BAHAJ, A, MOLLAND, A, CHAPLIN, J, AND BATTEN, W (2007b). Power and Thrust Measurements of Marine Current Turbines Under Various Hydrodynamic Flow Conditions in a Cavitation Tunnel and Towing Tank. *Renewable Energy*, 32(3):407–426.

BAHAJ, A AND MYERS, L (2003). Fundamentals Applicable to the Utilisation of Marine Current Turbines for Energy Production. *Renewable Energy*, 28(14):2205–2211.

BAHAJ, A AND MYERS, L (2013). Shaping Array Design of Marine Current Energy Converters Through Scaled Experimental Analysis. *Energy*, 59:83–94.

BARLOW, JB, RAE JR, WH, AND POPE, A (1999). *Low-Speed Wind Tunnel Testing*. John Wiley & Sons, 3rd edition.

BARLTROP, N, VARYANI, K, CLELLAND, D, AND PHAM, X (2007). Investigation into Wave-Current Interactions in Marine Current Turbines. *Proceedings of the Institution of Mechanical Engineers Part A: Journal of Power and Energy*, 221(2):233–242.

BARNES, H AND POWELL, H (1953). The Growth of *Balanus Balanoides* (L.) and *B. Crenatus* Brug. Under Varying Conditions of Submersion. *Journal of the Marine Biological Association of the United Kingdom*, 32(1):107–127.

BATTEN, W, BAHAJ, A, MOLLAND, A, AND CHAPLIN, J (2006). Hydrodynamics of Marine Current Turbines. *Renewable Energy*, 31(2):249–256.

BATTEN, W, BAHAJ, A, MOLLAND, A, AND CHAPLIN, J (2007). Experimentally Validated Numerical Method for the Hydrodynamic Design of Horizontal Axis Tidal Turbine. *Ocean Engineering*, 34(7):1013–1020.

BATTEN, W, BAHAJ, A, MOLLAND, A, AND CHAPLIN, J (2008). The Prediction of the Hydrodynamic Performance of Marine Current Turbines. *Renewable Energy*, 33(5):1085–1096.

BEDDOES, T (1978). Onset of Leading Edge Separation Effects under Dynamic Conditions and Low Mach Number. In *34th Annual Forum of the American Helicopter Society*.

BEIS (2016). Electricity Generation Costs. Research and Analysis Report, UK Government, Department for Business, Energy and Industrial Strategy, London, UK.

BEIS (2017). Energy Trends: June 2017. National Statistics Publication, UK Government, Department for Business, Energy and Industrial Strategy, London, UK.

BIR, GS, LAWSON, MJ, AND LI, Y (2011). Structural Design of a Horizontal-Axis Tidal Current Turbine Composite Blade. In *ASME 2011 30th International Conference on Ocean, Offshore and Arctic Engineering*, volume 5, pp. 797–808. American Society of Mechanical Engineers.

BJÖRCK, A (1990). Coordinates and Calculations for the FFA-W1-xxx, FFA-W2-xxx and FFA-W3-xxx Series of Airfoils for Horizontal Axis Wind Turbines. Technical Report FFA TN 1990-15, Flygtekniska Försöksanstalten (The Aeronautical Research Institute of Sweden), Stockholm, Sweden.

Blackmore, T, Myers, L, and Bahaj, A (2016). Effects of Turbulence on Tidal Turbines: Implications to Performance, Blade Loads, and Condition Monitoring. *International Journal of Marine Energy*, 14:1–26.

Borthwick, AG (2016). Marine Renewable Energy Seascape. *Engineering*, 2(1):69–78.

Bowles, PO, Corke, TC, Coleman, DG, and Thomas, FO (2014). Improved Understanding of Aerodynamic Damping Through the Hilbert Transform. *AIAA Journal*, 52(11):2384–2394.

Bragg, M, Broeren, A, and Blumenthal, L (2005). Iced-Airfoil Aerodynamics. *Progress in Aerospace Sciences*, 41(5):323–362.

Bryden, I, Couch, S, Owen, A, and Melville, G (2007). Tidal Current Resource Assessment. *Proceedings of the Institution of Mechanical Engineers, Part A: Journal of Power and Energy*, 221(2):125–135.

Buckland, H, Master, I, Orme, J, and Baker, T (2013). Cavitation Inception and Simulation in Blade Element Momentum Theory for Modelling Tidal Stream Turbines. *Proceedings of the Institution of Mechanical Engineers, Part A: Journal of Power and Energy*, 227(4):479–485.

Butterfield, C, Hansen, A, Simms, D, and Scott, G (1991). Dynamic Stall on Wind Turbine Blades. Report NREL/TP-257-4510, National Renewable Energy Laboratory (NREL), Golden (CO), USA.

Callow, ME and Callow, JE (2002). Marine Biofouling: A Sticky Problem. *Biologist*, 49(1):1–5.

Carbon Trust (2011). Accelerating Marine Energy: The Potential for Cost Reduction – Insights From the Carbon Trust Marine Energy Accelerator. Technical Report CTC797, Carbon Trust, London, UK.

Carlton, J (2012). *Marine Propellers and Propulsion*. Butterworth-Heinemann, 3rd edition.

Carr, LW (1988). Progress in Analysis and Prediction of Dynamic Stall. *Journal of Aircraft*, 25(1):6–17.

Carta, F (1971). Effect of Unsteady Pressure Gradient Reduction on Dynamic Stall Delay. *Journal of Aircraft*, 8(10):839–840.

Carta, FO (1967). An Analysis of the Stall Flutter Instability of Helicopter Rotor Blades. *Journal of the American Helicopter Society*, 12(4):1–18.

Charlier, RH and Finkl, CW (2009). *Ocean Energy: Tide and Tidal Power*. Springer.

Choudhry, A, Leknys, R, Arjomandi, M, and Kelso, R (2012). An Insight Into the Dynamic Stall Characteristics. *Experimental Thermal and Fluid Science*, 58:188–208.

COLEMAN, HW AND STEELE, WG (2009). *Experimentation, Validation, and Uncertainty Analysis for Engineers*. John Wiley & Sons, 3rd edition.

CORKE, TC AND THOMAS, FO (2015). Dynamic Stall in Pithcing Airfoils: Aerodyanmic Damping and Compressibility Effects. *Annual Review of Fluid Mechanics*, 47:479–505.

CORTEN, GP AND VELDKAMP, HF (2001). Aerodynamics: Insects can Halve Wind-Turbine Power. *Nature*, 412(6842):41–42.

COWIE, PR (2010). Biofouling Patterns with Depth. In S Dürr and JC Thomson, editors, *Biofouling*, pp. 87–99. Wiley-Blackwell.

CRISP, D AND BOURGET, E (1985). Growth in Barnacles. *Advances in Marine Biology*, 22:199–244.

CUMMINGS, M AND BRAGG, M (1996). Boundary-Layer Transition Due to Isolated Three-Dimensional Roughness of Airfoil Leading Edge. *AIAA Journal*, 34(9):1949–1952.

DECC (2010). National Renewable Energy Action Plan for the United Kingdom. Corporate Report, UK Government, Department of Energy and Climate Change, London, UK.

DECC (2013). UK Renewable Energy Roadmap: 2013 Update. Policy Paper, UK Government, Department of Energy and Climate Change, London, UK.

DNV GL (2015a). DNVGL-ST-0163: Certification of Tidal Turbines and Arrays. Standard DNVGL-ST-0163, DNV GL, Oslo, Norway.

DNV GL (2015b). DNVGL-ST-0164: Tidal Turbines. Standard DNVGL-ST-0164, DNV GL, Oslo, Norway.

DNV GL (2016). Tidal Bladed – Energy – DNV GL. URL `https://www.dnvgl.com/services/tidal-bladed-3799`. Accessed: 10th October 2016.

DRAPER, S, ADCOCK, TA, BORTHWICK, AG, AND HOULSBY, GT (2013). Estimate of the Tidal Stream Power Resource of the Pentland Firth. *Renewable Energy*, 63:650–657.

DRELA, M AND YOUNGREEN, H (2013). XFoil 6.99. URL `http://web.mit.edu/drela/Public/web/xfoil/`. Accessed: 10th October 2016.

ECKERLE, W AND LANGSTON, L (1986). Measurements of a Turbulent Horseshoe Vortex Formed Around a Cylinder. Contractor Report 3986, NASA, Washington (DC), USA.

EMEC (2012). EMEC: European Marine Energy Centre. URL `http://www.emec.org.uk/`. Accessed: 6th July 2017.

EMEC (2017). ANDRITZ HYDRO Hammerfest: EMEC: European Marine Energy Centre. URL `http://www.emec.org.uk/about-us/our-tidal-clients/andritz-hydro-hammerfest/`. Accessed: 22nd February 2017.

ERGIN, F AND WHITE, E (2006). Unsteady and Transitional Flows Behind Roughness Elements. *AIAA Journal*, 44(11):2504–2514.

ERICSSON, L (1967). Comments on Unsteady Airfoil Stall. *Journal of Aircraft*, 4(5):478–480.

EUROPEAN UNION (2009). Directive 2009/28/EC of the European Parliament and of the Coundil of 23 April 2009 on the Promotion of the Use of Energy from Renewable Sources and Amending and Subsequently Repealing Directives 2001/77/EC and 2003/30/EC. *Offical Journal of the European Union*, L(140):16–62.

EWALD, B (1998). Wind Tunnel Wall Corrections. AGARDograph AGARD-AG-336, Advisory Group for Aerospace Research and Development, Neuilly-sur-Seine, France.

FAUDOT, C AND DAHLHAUG, OG (2012). Prediction of Wave Loads on Tidal Turbine Blades. *Energy Procedia*, 20:116–133.

FLACK, KA AND SCHULTZ, MP (2014). Roughness Effects on Wall-Bounded Turbulent Flows. *Physics of Fluids*, 26(10):101305.

FLAY, RG (2013). Bluff Body Aerodynamics. In Y Tamura and A Kareem, editors, *Advanced Structural Wind Engineering*, pp. 59–84. Springer Japan.

FLEMMING, H, MURTHY, P, VENKATESAN, R, AND COOKSEY, K, editors (2009). *Marine and Industrial Biofouling*. Springer Berlin Heidelberg.

FRAENKEL, P (2014). Energy from Tidal Streams: Engineering Issues, State of the Art and Future Prospects. *Underwater Technology*, 32(1):27–37.

FRID, C, ANDONEGI, E, DEPESTELE, J, JUDD, A, RIHAN, D, ROGERS, SI, AND KENCHINGTON, E (2012). The Environmental Interactions of Tidal and Wave Energy Generation Devices. *Environmental Impact Assessment Review*, 32(1):133–139.

FUGLSANG, P, ANTONIOU, I, BAK, C, AND MADSEN, HA (1998a). Wind Tunnel Test of the RISØ-1 Airfoil. Technical Report Risø-R-999(EN), Risø National Laboratory, Roskilde, Denmark.

FUGLSANG, P, ANTONIOU, I, DAHL, KS, AND MADSEN, HA (1998b). Wind Tunnel Tests of the FFA-W3-241, FFA-W3-301 and NACA 63-430 Airfoils. Technical Report Risø-R-1041(EN), Risø National Laboratory, Roskilde, Denmark.

FUGLSANG, P AND BAK, C (2004). Development of the Risø Wind Turbine Airfoils. *Wind Energy*, 7(2):145–162.

GLAUERT, H (1933). Wind Tunnel Interference on Wings, Bodies and Airscrews. Reports and Memoranda ARC R&M 1566, Aeronautical Research Council, London, UK.

GLAUERT, H (1935). Airplane Propellers. In *Aerodynamic Theory*, pp. 169–360. Springer Berlin Heidelberg.

GOOCH, S, THOMSON, J, POLAGYE, B, AND MEGGIT, D (2009). Site Characterization for Tidal Power. In *OCEANS 2009, MTS/IEEE Biloxi-Marine Technology for Our Future: Global and Local Challenges*, pp. 1–10. IEEE.

GRASSO, F (2012). Design and Optimization of Tidal Turbine Airfoil. *Journal of Aircraft*, 49(2):636–643.

GREEN, R AND GALBRAITH, R (1995). Dynamic Recovery to Fully Atatched Aerofoil Flow from Deep Stall. *AIAA Journal*, 33(8):1433–1440.

GREEN, R, GALBRAITH, R, AND NIVEN, A (1992). The Convection Speed of the Dynamic Stall Vortex. Department of Aerospace Engineering Report GU-AERO-9202, University of Glasgow, Glasgow, UK.

GREEN, R, GILLIES, E, AND WANG, Y (2011). Trailing-Edge Flap Flow Control for Dynamic Stall. *The Aeronautical Journal*, 115(1170):493–503.

GROGAN, DM, LEEN, SB, KENNEDY, CR, AND O'BRADAIGH, CM (2013). Design of Composite Tidal Turbine Blades. *Renewable Energy*, 57:151–162.

HAM, ND (1968). Aerodynamic Loading on a Two-Dimensional Airfoil During Dynamic Stall. *AIAA Journal*, 6(10):1927–1934.

HANSEN, A AND BUTTERFIELD, C (1993). Aerodynamics of Horizontal-Axis Wind Turbines. *Annual Review of Fluid Mechanics*, 25(1):115–149.

HEDEVANG, E (2014). Wind Turbine Power Curves Incorporating Turbulence Intensity. *Wind Energy*, 17(2):173–195.

HOFFMAN, M, RAMSAY, RR, AND GREGOREK, G (1996). Effects of Grit Roughness and Pitch Oscillations on the NACA 4415 Airfoil. Airfoil Performance Report NREL/TP-442-7815, National Renewable Energy Laboratory (NREL), Golden (CO), USA. Revised December 1999.

HOLIERHOEK, J, DE VAAL, J, VAN ZUIJLEN, A, AND BIJL, H (2013). Comparing Different Dynamic Stall Models. *Wind Energy*, 16(1):139–158.

HOOKER, RW (1933). The Aerodynamic Characteristics of Airfoils as Affected by Surface Roughness. Technical Note 457, NACA, Washington (DC), USA.

HOUNSFIELD, F (1940). The Handley Page Wind-Tunnel: A Private Tunnel of the Closed-Jet Type with a Single Return Duct. *Aircraft Engineering and Aerospace Technology*, 12(7):202–205.

IEA (2016). World Energy Outlook: Energy and Air Pollution. Special Report, International Energy Agency, Paris, France.

Jacobs, EN (1934). Airfoil Section Characteristics as Affected by Protuberances. Report 446, NACA, Washington (DC), USA.

Janiszewska, J, Ramsay, RR, Hoffman, M, and Gregorek, G (1996). Effects of Grit Roughness and Pitch Oscillations on the S814 Airfoil. Airfoil Performance Report NREL/TP-442-8161, National Renewable Energy Laboratory (NREL), Golden (CO), USA. Revised December 1999.

Johari, H, Henoch, C, Custodio, D, and Levshin, A (2007). Effects of Leading-Edge Protuberances on Airfoil Performance. *AIAA Journal*, 45(11):2634–2642.

Jones, B (1936). Measurement of Profile Drag by the Pivot-Traverse Method. Reports and Memoranda ARC R&M 1688, Aeronautical Research Committee, London, UK.

Jones, R and Williams, D (1936). Effect of Surface Roughness on Characteristics of Aerofoils NACA 0012 and RAF 34. Reports and Memoranda ARC R&M 1708, Aeronautical Research Committee, London, UK.

Keegan, M, Nash, D, and Stack, M (2013). On Erosion Issues Associated with the Leading Edge of Wind Turbine Blades. *Journal of Physics D: Applied Physics*, 46(38):383001.

Kerho, MF and Bragg, MB (1997). Airfoil Boundary-Layer Development and Transition with Large Leading Edge Roughness. *AIAA Journal*, 35(1):75–84.

Khandeparker, L and Anil, AC (2007). Underwater Adhesion: The Barnacle Way. *International Journal of Adhesion and Adhesives*, 27(2):165–172.

Khor, Y and Xiao, Q (2011). CFD Simulations of the Effects of Fouling and Antifouling. *Ocean Engineering*, 38(10):1065–1079.

Klebanoff, P, Cleveland, W, and Tidstrom, K (1992). On the Evolution of a Turbulent Boundary Layer Induced by a Three-Dimensional Roughness Element. *Journal of Fluid Mechanics*, 237:101–187.

Kramer, M (1932). Increase in the Maximum Lift of an Airplane Wing due to a Sudden Increase in its Effective Angle of Attack Resulting from a Gust. *Zeitschrift für Flugtechnik und Motorluftschiffahrt*, 23(7):185–189. (English Translation: NACA TM 678, July 1932).

Küssner, HG (1936). Zusammenfassender Bericht über den instatationären Auftrieb von Flügeln. *Luftfahrtforschung*, 13(12):410–424.

Leishman, J (1990). Dynamic Stall Experiments on the NACA 23012 Aerofoil. *Experiments in Fluids*, 9(1):49–58.

LEISHMAN, JG (1984). *Contributions to the Experimental Investigation and Analysis of Aerofoil Dynamic Stall*. Ph.D. thesis, Faculty of Engineering, University of Glasgow, Glasgow, UK.

LEISHMAN, JG (2000). *Principles of Helicopter Aerodynamics*. Cambridge Aerospace Series. Cambridge University Press.

LEISHMAN, JG AND BEDDOES, T (1989). A Semi-Empirical Model for Dynamic Stall. *Journal of the American Helicopter Society*, 34(3):3–17.

LEWIS, M, NEILL, S, ROBINS, P, HASHEMI, M, AND WARD, S (2017). Characteristics of the Velocity Profile at Tidal Stream Energy Sites. *Renewable Energy*, 114:258–272.

LIIVA, J AND DAVENPORT, FJ (1969). Dynamic Stall of Airfoil Sections for High-Speed Rotors. *Journal of the American Helicopter Society*, 14(2):26–33.

LIU, P AND VEITCH, B (2012). Design and Optimization for Strength and Integrity of Tidal Turbine Rotor Blades. *Energy*, 46(1):393–404.

LUZNIK, L, FLACK, KA, LUST, EE, AND TAYLOR, K (2013). The Effect of Surface Waves on the Performance Charcteristics of a Model Tidal Turbine. *Renewable Energy*, 58:108–114.

MACKAY, DJ (2009). *Sustainable Energy – Without the Hot Air*. UIT Cambridge.

MAGAGNA, D AND UIHLEIN, A (2015). Ocean Energy Development in Europe: Current Status and Future Perspectives. *International Journal of Marine Energy*, 11:84–104.

MAGANGA, F, GERMAIN, G, KING, J, PINON, G, AND RIVOALEN, E (2010). Experimental Characterisation of Flow Effects on Marine Current Turbine Behaviour and on its Wake Properties. *IET Renewable Power Generation*, 4(6):498–509.

MANWELL, JF, MCGOWAN, JG, AND ROGERS, AL (2002). *Wind Energy Explained: Theory, Design and Application*. John Wiley & Sons.

MARTÍN-RODRÍGUEZ, AJ, BABARRO, JM, LAHOZ, F, SANSÓN, M, MARTÍN, VS, NORTE, M, AND FERNÁNDEZ, JJ (2015). From Broad-Spectrum Biocides to Quorum Sensing Disruptors and Mussel Repellents: Antifouling Profile of Alkyl Triphenylphosphoniium Salts. *PLoS ONE*, 10(4):e0123652.

MASON-JONES, A, O'DOHERTY, D, MORRIS, C, AND O'DOHERTY, T (2012). Influence of a Velocity Profile and Support Structure on Tidal Stream Turbine Performance. *Renewable Energy*, 52:23–30.

MASTERS, I, CHAPMAN, J, AND WILLIS, M (2011). A Robust Blade Element Momentum Theory Model for Tidal Stream Turbines Including Tip and Hub Loss Corrections. *Journal of Marine Engineering and Technology*, 10(1):25–35.

MASTERS, I, WILLIAMS, A, CROFT, T, TOGNERI, M, EDMUNDS, M, ZANGIABADI, E, FAIRLEY, I, AND KARUNARATHNA, H (2015). A Comparison of Numerical Modelling Techniques for Tidal Stream Turbine Analysis. *Energies*, 8(8):7833–7853.

MCALISTER, K, PUCCI, S, MCCROSKEY, W, AND CARR, L (1982). An Experimental Study of Dynamic Stall on Advanced Airfoil Sections. Volume 1: Summary of the Experiment. Technical Memorandum 84245, NASA, Washington (DC), USA.

MCALISTER, KW, CARR, LW, AND MCCROSKEY, WJ (1978). Dynamic Stall Experiments on the NACA 0012 Airfoil. Technical Paper 1100, NASA, Washington (DC), USA.

MCCROSKEY, W (1977). Some Current Research in Unsteady Fluid Dynamics. *ASME Journal of Fluids Engineering*, 99(1):8–39.

MCCROSKEY, W (1981). The Phenomenon of Dynamic Stall. Technical Memorandum 81264, NASA, Washington (DC), USA.

MCCROSKEY, W, CARR, L, AND MCALLISTER, K (1976). Dynamic Stall Experiments on Oscillating Airfoils. *AIAA Journal*, 14(1):57–63.

MCCROSKEY, W AND FISHER JR, RK (1972). Detailed Aeodynamic Measurements on a Model Rotor in the Blade Stall Regime. *Journal of the American Helicopter Society*, 17(1):20–30.

MCCROSKEY, W, MCALISTER, K, CARR, L, PUCCI, S, LAMBERT, O, AND INDERGRAND, R (1981). Dynamic Stall on Advanced Airfoil Sections. *Journal of the American Helicopter Society*, 26(3):40–50.

MCCULLOUGH, GB AND GAULT, DE (1951). Examples of Three Respresentative Types of Airfoil-Section Stall at Low Speed. Technical Note TN 2502, NACA, Washington (DC), USA.

MELO, L (2005). Biofilm Physical Structure, Internal Diffusivity and Tortuosity. *Water Science and Technology*, 52(7):77–84.

MELVILLE, GT (2008). *Hydrodynamic and Economic Modelling of Tidal Current Energy Conversion Systems*. Ph.D. thesis, The Robert Gordon University, Aberdeen, UK.

MILLER, RG AND MACLEOD, AK (2016). Marine Growth Mapping and Monitoring: Feasibility of Predictive Mapping of Marine Growth. Technical Report PN000111-SRT-001, Offshore Renewable Energy Catapult, Glasgow, UK.

MILNE, I, DAY, A, SHARMA, R, AND FLAY, R (2013). Blade Loads on Tidal Turbines in Planar Oscillatory Flow. *Ocean Engineering*, 60:163–174.

MILNE, I, DAY, A, SHARMA, R, AND FLAY, R (2015). Blade Loading on Tidal Turbines for Uniform Unsteady Flow. *Renewable Energy*, 77:338–350.

MILNE, I, SHARMA, R, FLAY, R, AND BICKERTON, S (2010). The Role of Onset Turbulence on Tidal Turbine Blade Loads. In *Proceedings of 17ᵗʰ Australasian Fluid Mechanics Conference, Auckland, New Zealand*.

MILNE, I, SHARMA, R, FLAY, R, AND BICKERTON, S (2014). Characteristics of the Turbulence in the Flow at a Tidal Stream Power Site. *Philosophical Transactions of The Royal Society A*, 371(20120196).

MILNE, IA (2014). *An Experimental Investigation of Turbulence and Unsteady Loading on Tidal Turbines*. Ph.D. thesis, University of Auckland, Auckland, New Zealand.

MOLLAND, A, BAHAJ, A, CHAPLIN, J, AND BATTEN, W (2004). Measurements and Predictions of Forces, Pressures and Cavitation on 2-D Sections Suitable for Marine Current Turbines. *Proceedings of the Institution of Mechanical Engineers, Part M: Journal of Engineering for the Maritime Environment*, 218(2):127–138.

MOODY, LF (1944). Friction Factors for Pipe Flow. *Transactions of the ASME*, 66(8):671–684.

MUELLER, M AND WALLACE, R (2008). Enabling Science and Technology for Marine Renewable Energy. *Energy Policy*, 36(12):4376–4382.

MYCEK, P, GAURIER, B, GERMAIN, G, PINON, G, AND RIVOALEN, E (2014). Experimental Study of the Turbulence Intensity Effects on Marine Current Turbines Behaviour. Part 1: One Single Turbine. *Renewable Energy*, 66:729–746.

MYERS, L AND BAHAJ, A (2012). An Experimental Investigation Simulating Flow Effects in First Generation Marine Current Energy Converter Arrays. *Renewable Energy*, 37(1):28–36.

NEILL, SP, VÖGLER, A, GOWARD-BROWN, AJ, BASTON, S, LEWIS, MJ, GILLIBRAND, PA, WALDMAN, S, AND WOOLF, DK (2017). The Wave and Tidal Resource of Scotland. *Renewable Energy*, 114:3–17.

NG, K, LAM, W, AND NG, K (2013). 2002-2012: 10 Years of Research Progress in Horizontal-Axis Marine Current Turbines. *Energies*, 6(3):1497–1526.

NIKURADSE, J (1933). Laws of Flow in Rough Pipes. VDI-Forschungsheft 361, Series B, Vol. 4, The Association of German Engineers (VDI), Berlin, Germany. (English Translation: NACA TM 1292, November 1950).

OFGEM (2016). About the RO. URL `https://www.ofgem.gov.uk/environmental-programmes/ro/about-ro`. Accessed: 29ᵗʰ June 2017.

ORME, J, MASTERS, I, AND GRIFFITHS, R (2001). Investigation of the effect of biofouling on the efficiency of marine current turbines. In *Proceedings of MAREC2001, International Conference on Marine Renewable Energies*, pp. 91–99. Institute of Marine Engineers, London, UK.

Osalusi, E, Side, J, and Harris, R (2009). Structure of Turbulent Flow in EMEC's Tidal Energy Test Site. *International Communications in Heat and Mass Transfer*, 36(5):422–431.

Parkinson, SG and Collier, WJ (2016). Model Validation of Hydrodynamic Loads and Performance of a Full-Scale Tidal Turbine Using Tidal Bladed. *International Journal of Marine Energy*, 16:279–297.

Peters, D (2009). How Dynamic Inflow Survives in the Competitive World of Rotorcraft Aerodynamics. *Journal of the American Helicopter Society*, 54(1):1–15.

Peters, D and HaQuang, N (1988). Dynamic Inflow for Pratical Applications. *Journal of the American Helicopter Society*, 33(4):64–68.

Pires, O, Munduate, X, Ceyhan, O, Jacobs, M, and Snel, H (2016). Analysis of High Reynolds Numbers Effects on a Wind Turbine Airfoil Using 2D Wind Tunnel Test Data. In *Journal of Physics: Conference Series*, volume 753, p. 022047. IOP Publishing.

Polagye, B and Thomson, J (2010). Screening for Biofouling and Corrosion of Tidal Energy Device Materials: In Situ Results for Admiralty Inlet, Puget Sound, Washington. Technical memorandum, Northwest National Marine Renewable Energy Center, Seattle (WA), USA.

Prandtl, L (1933). Recent Results of Turbulence Research. Zeitchrift des Vereines Deutscher Ingenieure Vol. 7, No. 5, The Association of German Engineers (VDI), Berlin, Germany. (English Translation: NACA TM 720, September 1933).

Premalatha, M, Abbasi, T, and Abbasi, S (2014). Wind Energy: Increasing Deploymeny, Rising Environmental Concerns. *Renewable and Sustainable Energy Reviews*, 31:270–288.

Ramsay, RR, Hoffman, M, and Gregorek, G (1995). Effects of Grit Roughness and Pitch Oscillations on the S809 Airfoil. Airfoil Performance Report NREL/TP-442-7817, National Renewable Energy Laboratory (NREL), Golden (CO), USA. Revised December 1999.

Reddy, TA (2011). *Applied Data Analysis and Modeling for Energy Engineers and Scientists*. Springer, 2011 edition.

RenewableUK (2017). UK Marine Energy Database. URL `http://www.renewableuk.com/page/UKMED2`. Accessed: 27th June 2017.

Roberts, A, Thomas, B, Sewell, P, Khan, Z, Balmain, S, and Gilmour, J (2016). Current tidal power technologies and their suitability for applications in coastal and marine areas. *Journal of Ocean Engineering and Marine Energy*, 2:227–245.

Roberts, S and Yaras, M (2005). Boundary-Layer Transition Affected by Surface Roughness and Free-Stream Turbulence. *Journal of Fluids Engineering*, 127(3):449–457.

ROURKE, FO, BOYLE, F, AND REYNOLDS, A (2010). Marine Current Energy Devices: Current Status and Possible Future Applications in Ireland. *Renewable and Sustainable Energy Reviews*, 14(3):1026–1036.

SADIQUE, J, YANG, XI, MENEVEAU, C, AND MITTAL, R (2015). Simulation of Boundary Layer Flows over Biofouled Surfaces. Paper presented at AIAA 22nd Computational Fluid Dynamics Conference, Dallas, TX.

SALE, DC (2014). NWTC Information Portal (HARP_Opt). URL `https://nwtc.nrel.gov/HARP_Opt`. Accessed: 10th October 2016.

SAREEN, A, SAPRE, CA, AND SELIG, MS (2014). Effects of Leading Edge Erosion on Wind Turbine Blade Performance. *Wind Energy*, 17(10):1531–1542.

SCHULTZ, M, BENDICK, J, HOLM, E, AND HERTEL, W (2011). Economic Impact of Biofouling on a Naval Surface Ship. *Biofouling*, 27(1):87–98.

SCOTTISH GOVT (2011). 2020 Routemap for Renewable Energy in Scotland. Report, The Scottish Government, Edinburgh, UK.

SHAW, R (1960). The Influence of Hole Dimensions on Static Pressure Measurements. *Journal of Fluid Mechanics*, 7(4):550–564.

SHENG, W, GALBRAITH, R, AND COTON, F (2006). A New Stall-Onset Criterion for Low Speed Dynamic Stall. *Journal of Solar Energy Engineering*, 128(4):461–471.

SHENG, W, GALBRAITH, RAM, AND COTON, FN (2009). On the S809 Airfoil's Unsteady Aerodynamic Characteristics. *Wind Energy*, 12(8):752–767.

SHI, W, ATLAR, M, ROSLI, R, AKTAS, B, AND NORMAN, R (2016). Cavitation Observations and Noise Measurements of Horizontal Axis Tidal Turbines with Biomimetic Blade Leading-Edge Designs. *Ocean Engineering*, 121:143–155.

SIDDIQUI, M, RASHEED, A, KVAMSDAL, T, AND TABIB, M (2015). Effect of Turbulence Intensity on the Performance of an Offshore Vertical Axis Wind Turbine. *Energy Procedia*, 80:312–320.

SOMERS, D (2005). Effects of Airfoil Thickness and Maximum Lift Coefficient on Roughness Sensitivty. Report NREL/SR-500-36336, National Renewable Energy Laboratory (NREL), Golden (CO), USA.

SOUTHWARD, AJ (2008). *Barnacles: Keys and Notes for the Identification of British Species*. Field Studies Council.

STEPNIEWSKI, W AND KEYS, C (1984). *Rotary-Wing Aerodynamics*. Dover Publications.

SUTHERLAND, W (1893). The Viscosity of Gases and Molecular Force. *The London, Edinburgh and Dublin Philosophical Magazine and Journal of Science*, 36(223):507–531.

TANGLER, J AND SOMERS, D (1995). NREL Airfoil Families for HAWTs. Report NREL/TP-442-7109, National Renewable Energy Laboratory (NREL), Golden (CO), USA.

TANI, I (1969). Boundary-Layer Transition. *Annual Review of Fluid Mechanics*, 1(1):169–196.

TARZANIN JR, F (1972). Prediction of Control Loads Due to Blade Stall. *Journal of the American Helicopter Society*, 17(2):33–46.

TATUM, S, FROST, C, ALLMARK, M, O'DOHERTY, D, MASON-JONES, A, PRICKETT, P, GROSVENOR, R, BYRNE, C, AND O'DOHERTY, T (2015). Wave-Current Interaction Effects on Tidal Stream Turbine Performance and Loading Characteristics. *International Journal of Marine Energy*, 14:161–179.

THEODORSEN, T (1935). General Theory of Aerodynamic Instability and the Mechanism of Flutter. Report 496, NACA, Washington (DC), USA.

THEOPHANATOS, A AND WOLFRAM, J (1989). Hydrodynamic Loading on MAcro-Roughened Cylinders of Various Aspect Ratios. *Journal of Offshore Mechanics and Arctic Engineering*, 111(3):214–222.

THOMSON, J, POLAGYE, B, DURGESH, V, AND RICHMOND, MC (2012). Measurements of Turbulence at Two Tidal Energy Sites in Puget Sound, WA. *IEEE Journal of Oceanic Engineering*, 37(3):363–374.

TIMMER, W AND SCHAFFARCZYK, A (2004). The Effect of Roughness at High Reynolds Numbers on the Performance of Aerofoil DU 97-W-300Mod. *Wind Energy*, 7(4):295–307.

TIMMER, W AND VAN ROOIJ, R (2003). Summary of the Delft University Wind Turbine Dedicated Airfoils. In *ASME 2003 Wind Energy Symposium*, pp. 11–21. American Society of Mechanical Engineers.

UNITED NATIONS (2015). Adoption of the Paris Agreement. Document, United Nations Framework Convention on Climate Change.

UZAWA, K, KAGEYAMA, K, MURAYAMA, H, OHSAWA, I, KANAI, M, NISHIYAMA, T, AND SHICHIRI, A (2008). Study of the Characteristic and Possibility for Applying Composite Materials to the Blades of Tidal Power Generation. In *ASME 2008 27th International Conference on Offshore Mechanics and Arctic Engineering*, pp. 721–728. American Society of Mechanical Engineers.

VAN ROOIJ, R AND TIMMER, W (2003). Roughness Sensitivity Considerations for Thick Rotor Blade Airfoils. *Journal of Solar Energy Engineering*, 125(4):468–478.

VANCE, T, ELLIS, R, AND FILEMAN, T (2014). ETI MA1001 – Reliable Data Acquisition Platform for Tidal (ReDAPT) Project. Technical Report ME8.5 Final Report, Energy Technology Institute, Plymouth, UK.

VON KÁRMÁN, T AND SEARS, W (1938). Airfoil Theory for Non-Uniform Motion. *Journal of the Aeronautical Sciences*, 5(10):379–390.

WAGNER, H (1925). Über die Entstehung des dynamischen Auftriebes von Tragflügeln. *Zeitchrift für Angewandte Mathematik und Mechanik*, 5(1):17–35.

WALKER, JM, FLACK, KM, LUST, EE, SCHULTZ, MP, AND LUZNIK, L (2014). Experimental and Numerical Studies of Blade Roughness and Fouling on Marine Current Turbine Performance. *Renewable Energy*, 66:257–267.

WANG, D, ATLAR, M, AND SAMPSON, R (2007). An Experimental Investigation on Cavitation, Noise, and Slipstream Characteristics of Ocean Stream Turbines. *Proceedings of the Institution of Mechanical Engineers, Part A: Journal of Power and Energy*, 221(2):219–231.

WATERS, S AND AGGIDIS, G (2016). A World First: Swansea Bay Tidal Lagoon in Review. *Renewable and Sustainable Energy Reviews*, 56:916–921.

WERNERT, P, GEISSLER, W, RAFFEL, M, AND KOMPENHANS, J (1996). Experimental and Numerical Investigations of Dynamic Stall on a Pitching Airfoil. *AIAA Journal*, 34(5):982–989.

WHELAN, J (2010). *A Fluid Dynamic Study of Free-Surface Proximity and Inertia Effects of Tidal Turbines*. Ph.D. thesis, Imperial College London, London, UK.

WHITBY, B AND UGALDE-LOO, CE (2014). Performance of Pitch and Stall Regulated Tidal Stream Turbines. *IEEE Transactions on Sustainable Energy*, 5(1):64–72.

WHITMORE, SA, LINDSEY, WT, CURRY, RE, AND GILYARD, GB (1990). Experimental Characterization of the Effects of Pneumatic Tubing on Unsteady Pressure Measurements. Technical Memorandum 4171, NASA, Washington (DC), USA.

WILSON, RE AND LISSAMAN, PB (1974). *Applied Aerodyanmics of Wind Power Machines*. Oregon State University, Corvallis (OR), USA.

WORLD SEA TEMPERATURES (2017). Orkney Sea Temperatture – United Kingdom Water Temperatures. URL `https://www.seatemperature.org/europe/united-kingdom/orkney.htm`. Accessed: 18th August 2017.

ZEINER-GUNDERSEN, DH (2015). Turbine Design and Field Development Concepts for Tidal, Ocean, and River Applications. *Energy Science & Technology*, 3(1):27–42.

ZHOU, Z, SCUILLER, F, FRÉDÉRIC, J, BENBOUZID, M, AND TANG, T (2014). An Up-to-Date Review of Large Marine Tidal Current Turbine Technologies. In *Power Electronics and Application Conference and Exposition (PEAC), 2014 International*, pp. 480–484. IEEE.